

Electrochemical Behavior of Tellurium and Rhenium in LiCl-KCl Eutectic and LiCl-KCl-Li₂O Molten Salt

A Dissertation

Presented in Partial Fulfillment of the Requirements for the

Degree of Doctor of Philosophy

with a

Major in Materials Science and Engineering

in the

College of Graduate Studies

by

Brandon Day

Major Professor: Krishnan Raja, Ph.D.

Committee Members: Vivek Utgikar, Ph.D.; Indrajit Charit, Ph.D.; Thomas Williams, Ph.D.

Department Administrator: Mark Roll, Ph.D.

August 2021

Authorization to Submit Thesis

This dissertation of Brandon Day, submitted for the degree of Doctor of Philosophy with a major in Materials Science and Engineering and titled “Electrochemical Behavior of Tellurium and Rhenium in LiCl-KCl Eutectic and LiCl-KCl-Li₂O Molten Salts,” has been reviewed in in final form. Permission, as indicated by the signatures and dates given below, is now granted to submit final copies to the College of Graduate Studies for approval.

Major Professor _____ Date_____

Krishnan Raja, Ph.D.

Committee Members

_____ Date_____

Indrajit Charit, Ph.D.

_____ Date_____

Vivek Utgikar, Ph.D.

_____ Date_____

Thomas Williams, Ph.D.

Department Administrator

_____ Date_____

Mark Roll, Ph.D.

Abstract

Several radioactive tellurium and technetium isotopes are formed during neutron induced fission of nuclear fuel. These radionuclides are retained within the fuel matrix and by the containment provided by the fuel cladding. During pyroprocessing of used nuclear fuel, tellurium will be present as soluble Te^{2-} and could interfere with the electrorefining of actinides. When present as metallic form, tellurium could lead to liquid embrittlement of structural alloys. Additionally, telluride compounds (such as Cs_2Te , Li_2Te etc.) can be formed during pyroprocessing. These high melting point compounds may form sediments in the molten salt bath and adversely affect the viscosity and flow conditions. Furthermore, technetium can form volatile species with the chloride and oxide salts. In this research, rhenium salt was used as a surrogate for technetium. This study focused on the electrochemistry of tellurium and rhenium species in $\text{LiCl}+\text{KCl}$ eutectic and $\text{LiCl}+\text{KCl} + 1 - 2$ wt% Li_2O electrolytes at $450 - 550$ °C. Multiple electrochemical techniques such as cyclic voltammetry, electrochemical impedance spectroscopy and square wave voltammetry were employed to determine redox potentials of electrochemical reactions, reaction intermediates, number of electrons transferred, and diffusivities of Te^{n+} , Te_x^{2-} , Te^{2-} , TeO_n^{2-} , Re^{n+} , ReO^{n+} , ReO_n^- species as a function of temperature and concentration. From these experiments it was seen that both tellurium and rhenium in $\text{LiCl}-\text{KCl}$ eutectic molten salt went through a 3-step reduction process to reach their metallic neutral state. Additionally, the diffusivity of both Te^{4+} and Re^{3+} increased in relation to a rise in temperature and decreased with increase in the concentration. Formal potentials of different electrochemical reactions of these species, their diffusivities, and number of electrons involved in each reaction steps that were determined from the electrochemical measurements will be presented.

Acknowledgements

I would like to acknowledge my Advisor Dr. Krishnan Raja for accepting me as his graduate student. Additionally, I would like to acknowledge NEUP for funding this project, also all my committee members for taking time out of their busy schedules to help me obtain my doctoral degree in Material Science and Engineering.

Dedication

I would like to thank my family for their support in wanting to pursue higher education. Furthermore, I want to thank all my friends up here for helping me with characterization and Anumat for supplying all of us graduate students with copious amounts of coffee to help keep the energy maintained. Additionally, I want to thank the Lizzie, Emily, Lisa, Brie, Kai, Hailey, Cassandra and the rest of the baristas at Café Artista for providing all the coffee to keep me conscious while working on this project. Furthermore, I want to thank Kassie and all my friends from pottery for their support during this time, along with Jeremy, Megan, Adam, Forest, and the rest of my friends from the chem department. I also want to thank my friends from West Coast Swing and Rachel for helping me stay on task while finishing off my thesis. Also, in memory of Dr. Thomas Bitterwolf who was willing to be on my committee despite everything he had going on in his own life, you will be missed.

Table of Contents

Authorization to Submit Dissertation	ii
Abstract.....	iii
Acknowledgements.....	iv
Dedication.....	v
Table of Contents.....	vi
List of Figures.....	vii
List of Tables	xi
Chapter 1: Introduction.....	1
Chapter 2: Background	5
Chapter 3: Comparing Tellurium Reactions on GC and W Working Electrodes in LiCl-KCl.....	16
Chapter 4: Electrochemical Behavior of TeCl ₄ in LiCl-KCl Eutectic at 500-550 °C.....	37
Chapter 5: Echem Behavior of ReCl ₃ in LiCl-KCl Eutectic at 450-550 °C	57
Chapter 6: Echem Behavior of TeCl ₄ and ReCl ₃ Combination in LiCl-KCl Eutectic at 450 °C.....	79
Chapter 7: Echem Behavior of TeCl ₄ with Li ₂ O addition in LiCl-KCl Eutectic at 550 °C.....	98
Chapter 8: Echem Behavior of ReCl ₃ with Li ₂ O addition in LiCl-KCl Eutectic at 550 °C.....	118
Chapter 9: Conclusions and Future Work.....	137
References.....	141
Appendix: Figures	148

List of Figures

Figure 1: Schematic of Bismuth Phosphate Process at Lab Scale ²	149
Figure 2: Schematic of Electrorefiner ¹²	150
Figure 3: O-Te Phase Diagram ²⁶	150
Figure 4: OCP of Tungsten Electrode	151
Figure 5: OCP of Glassy Carbon Electrode	151
Figure 6: CV in LiCl+KCl TeCl ₄ addition.....	152
Figure 7: CV Cathodic w/wo 1 wt% TeCl ₄	152
Figure 8: CV Full Window 1 wt% TeCl ₄ WE Tungsten	153
Figure 9: CV different scan rates 1 wt% TeCl ₄ WE: Tungsten	153
Figure 10: CV different scan rates 5 wt% TeCl ₄ WE Tungsten.....	154
Figure 11: Current Density vs. Square Root WE Tungsten	155
Figure 12: Current Density vs. Square Root WE Tungsten.....	156
Figure 13: Square Wave 1 wt% TeCl ₄ WE Tungsten.....	156
Figure 14: CV TeCl ₄ WE Glassy Carbon.....	156
Figure 15: EIS 1 wt% TeCl ₄ 450 °C WE Tungsten	158
Figure 16: EIS 5 wt% TeCl ₄ 450 °C WE Tungsten.....	159
Figure 17: EIS 5 wt% TeCl ₄ 450 °C WE GC.....	160
Figure 18: SEM of Te metal sphere deposit.....	161
Figure 19: OCP 0 and 1 wt% TeCl ₄ 500 – 550°C	161
Figure 20: CV Full window 0 wt% TeCl ₄ 500 – 550 °C	162
Figure 21: CV w/wo 1 wt% TeCl ₄ 500 °C.....	162
Figure 22: CV w/wo 1 wt% TeCl ₄ 550 °C.....	163
Figure 23: CV FW vs SW w/wo 1 wt% TeCl ₄ 500 °C.....	163
Figure 24: CV FW vs SW w/wo 1 wt% TeCl ₄ 550 °C.....	164
Figure 25: CV FW 1 wt% TeCl ₄ comparing 500 to 550 °C	164
Figure 26: CV SW 1 wt% TeCl ₄ comparing 500 to 550 °C	165

Figure 27: CV SW 1 wt% TeCl ₄ varying scan rate 500 °C	165
Figure 28: CV SW 1 wt% TeCl ₄ varying scan rate 550 °C	166
Figure 29: Square root scan rate vs. current density	166
Figure 30: SWV 1 wt% TeCl ₄ 500 °C	167
Figure 31: SWV 1 wt% TeCl ₄ 550 °C	167
Figure 32: EIS 1wt% TeCl ₄ WE Tungsten 500 °C	168
Figure 33: EIS 1wt% TeCl ₄ WE Tungsten 550 °C	169
Figure 34: OCP 0 and 1 wt% ReCl ₃ 450-550 °C	170
Figure 35: CV FW 0 and 1 wt% ReCl ₃ 450-550 °C	170
Figure 36: CV comparing SW 0 and 1 wt% ReCl ₃ 450 °C.....	171
Figure 37: CV FW varying scan rate 1 wt% ReCl ₃ 450 °C	171
Figure 38: CV FW varying scan rate 1 wt% ReCl ₃ 500 °C	172
Figure 39: CV FW varying scan rate 1 wt% ReCl ₃ 550 °C	172
Figure 40: CV SW varying scan rate 1 wt% ReCl ₃ 450 °C	173
Figure 41: CV SW varying scan rate 1 wt% ReCl ₃ 500 °C	173
Figure 42: CV SW varying scan rate 1 wt% ReCl ₃ 550 °C	174
Figure 43: Square root scan rate vs. current density ReCl ₃ 450-550 °C	174
Figure 44: SWV 1 wt% ReCl ₃ 450 °C	175
Figure 45: SWV 5 wt% ReCl ₃ 500 °C	175
Figure 46: SWV 5 wt% ReCl ₃ 550 °C	176
Figure 47: EIS 1 wt% ReCl ₃ OCP 450-550 °C	177
Figure 48: OCP comparing 0 and 1 wt% TeRe 450 °C	178
Figure 49: CV FW comparing 0 and 1 wt% TeRe 450 °C	178
Figure 50: CV SW comparing 0 and 1 wt% TeRe 450 °C	179
Figure 51: CV FW varying scan rate 1 wt% TeRe 450 °C	179
Figure 52: CV FW comparing 1 wt% TeCl ₄ vs. 1 wt% TeRe	180
Figure 53: CV FW comparing 1 wt% ReCl ₃ vs. 1 wt% TeRe.....	180

Figure 54: CV SW comparing 1wt% TeRe to 1 wt% TeCl ₄ and 1 wt% ReCl ₃	181
Figure 55: CV SW varying scan rate 1 wt% TeRe	181
Figure 56: Square root scan rate vs. current density 1 wt% TeRe	182
Figure 57: SWV 1 wt% TeRe 450 °C	182
Figure 58: EIS at OCP 1 wt% TeRe	183
Figure 59: OCP comparing 1-2 wt% Li ₂ O w/wo 5 wt% TeCl ₄	184
Figure 60: CV FW 1-2 wt% Li ₂ O without TeCl ₄	184
Figure 61: CV FW 5 wt% TeCl ₄ with 1-2 wt% Li ₂ O.....	185
Figure 62: CV FW 5 wt% Tecl ₄ 1 wt% Li ₂ O varying scan rate	185
Figure 63: CV SW 5 wt% TeCl ₄ 2 wt% Li ₂ O varying scan rate.....	186
Figure 64: CV FW 5 wt% TeCl ₄ 1 wt% Li ₂ O varying scan rate	186
Figure 65: CV FW 5 wt% TeCl ₄ 2 wt% Li ₂ O varying scan rate.....	187
Figure 66: Square root scan rate vs. current density 5 wt% TeCl ₄ 2 wt% Li ₂ O	187
Figure 67: SWV 5 wt% TeCl ₄ 1 wt% Li ₂ O 550 °C	188
Figure 68: SWV 5 wt% TeCl ₄ 2 wt% Li ₂ O 550 °C	188
Figure 69: EIS at OCP 5wt% TeCl ₄ 1 wt% Li ₂ O.....	189
Figure 70: EIS at OCP 5 wt% TeCl ₄ 2 wt% Li ₂ O.....	190
Figure 71: OCP comparing 1-2 wt% w/wo 5 wt% ReCl ₃	191
Figure 72: CV FW 1-2 wt% wo 5 wt% ReCl ₃	191
Figure 73: CV FW 1-2 wt% with 5 wt% ReCl ₃	192
Figure 74: CV SW 5 wt% ReCl ₃ 1 wt% Li ₂ O.....	192
Figure 75: CV SW 5 wt% ReCl ₃ 2 wt% Li ₂ O.....	193
Figure 76: CV SW 5 wt% ReCl ₃ 1 wt% Li ₂ O 200 mV/s scan rate	193
Figure 77: CV SW 5 wt% ReCl ₃ 2 wt% Li ₂ O 200 mV/s scan rate.....	194
Figure 78: CV FW 5 wt% ReCl ₃ 1 wt% Li ₂ O varying scan rate.....	194
Figure 79: CV FW 5 wt% ReCl ₃ 2 wt% Li ₂ O varying scan rate.....	195
Figure 80: Square root scan rate vs. current density 5 wt% ReCl ₃ w/ 1-2 wt% Li ₂ O.....	195

Figure 81: SWV 5 wt% ReCl_3 1 wt% Li_2O 550 °C	196
Figure 82: SWV 5 wt% ReCl_3 2 wt% Li_2O 550 °C	196
Figure 83: EIS at OCP 5 wt% ReCl_3 with 1 wt% Li_2O	197
Figure 84: EIS at OCP 5 wt% ReCl_3 with 2 wt% Li_2O	198

List of Tables

Table I: TeCl ₄ concentration at 450 °C over 4 hour period	18
Table II: SWV TeCl ₄ reactions and number of electron 450 °C WE: Tungsten	28
Table III: Diffusivity of Te species 450 °C.....	29
Table IV: Formal potentials of LiCl-KCl-TeCl ₄ , 450 °C WE: Tungsten	29
Table V: Concentration of TeCl ₄ at 500 and 550 °C over 4 hour period.....	39
Table VI: SWV TeCl ₄ reactions and number of electron 500 °C	49
Table VII: SWV TeCl ₄ reactions and number of electron 550 °C.....	49
Table VIII: Diffusivities of Te species at 500 and 550 °C.....	50
Table IX: Formal potentials of LiCl-KCl-TeCl ₄ , 500 and 550 °C WE: Tungsten	50
Table X: EIS component value at OCP TeCl ₄ for 500 and 550 °C	53
Table XI: Concentration of ReCl ₃ at 450 - 550 °C over 4 hour period.....	58
Table XII: SWV ReCl ₃ reactions and number of electrons 450 °C	70
Table XIII: SWV ReCl ₃ reactions and number of electrons 500 °C.....	71
Table XIV: SWV ReCl ₃ reactions and number of electrons 550 °C	71
Table XV: Diffusivity of Re species 450 – 550 °C.....	72
Table XVI: Formal potentials of LiCl-KCl-ReCl ₃ , 450 - 550 °C WE: Molybdenum.....	73
Table XVII: EIS at OCP circuit component ReCl ₃ 450 – 550 °C.....	76
Table XVIII: Concentration of 1 wt% TeCl ₄ and ReCl ₃ at 450 °C over 4 hour period	82
Table XIX: SWV TeRe reactions and number of electrons 450 °C	92
Table XX: Diffusivity of TeRe at 450 °C	93
Table XXI: Formal potentials of LiCl-KCl-TeCl ₄ -ReCl ₃ , 450 °C WE: Molybdenum.....	94
Table XXII: EIS at OCP circuit components TeRe 450 °C	96
Table XXIII: Concentration of 1 wt% TeCl ₄ at 550 °C over 4 hour period	101

Table XXIV: SWV of 5 wt% TeCl ₄ with 1 wt% Li ₂ O, reactions and electrons.....	111
Table XXV: SWV of 5 wt% TeCl ₄ with 2 wt% Li ₂ O, reactions and electrons	112
Table XXVI: Diffusivity of TeO ₂ for 5 wt% TeCl ₄ with 1 – 2 wt% Li ₂ O.....	113
Table XXVII: Formal potentials of LiCl-KCl-TeCl ₄ -Li ₂ O, 550 °C WE: Tungsten.....	113
Table XXVIII: EIS at OCP circuit components LiCl-KCl-TeCl ₄ -Li ₂ O 550 °C	116
Table XXIX: Concentration of ReCl ₃ at 550 °C over 4 hour period	120
Table XXX: SWV of 5 wt% ReCl ₃ with 1 wt% Li ₂ O, reactions and electrons.....	131
Table XXXI: SWV of 5 wt% ReCl ₃ with 2 wt% Li ₂ O, reactions and electrons.....	131
Table XXXII: Diffusivity of Re species with 1-2 wt% Li ₂ O.....	132
Table XXXIII: Formal potentials of LiCl-KCl-ReCl ₃ -Li ₂ O, 550 °C WE: Tungsten.....	132
Table XXXIV: EIS at OCP circuit component LiCl-KCl-TeCl ₄ -Li ₂ O 550 °C.....	135

Chapter 1: Introduction

As the world population continues to increase, so does the demand for energy consumption. To address this demand nuclear power has been necessary to obtain this goal. One of the concerns with the nuclear fission process is the waste produced from used or decommissioned fuel rods. The radioactive waste will take approximately 10,000 years before it is no longer an environmental hazard. When nuclear weapons and power first came about there was little knowledge about the harmful side effects there would be to the environment. Additionally, there was little to no means to store the waste after its use, resulting in some of the first waste that was generated from the creation of nuclear weapons being disposed in the desert west of Idaho Falls in the 1950s ¹. The barrels cracked and leaked exposing the surrounding environment to the harmful waste. It was not until 2005 where Fluor picked up the contract to start cleaning up the waste from the Rocky Flats weapon plant that was buried in the desert. Before nuclear power plants were created the waste that was generated was the byproducts from extracting the weapons grade plutonium from the rods along with any still usable uranium. Eventually, the waste produced from the need to create nuclear weapons and eventually power plants and medicinal purposes has created an abundance of waste that to this day is still up for debate on how and where to safely store the byproducts until it is no longer harmful.

During WWII, when the idea of using uranium and plutonium as a viable weapon was brought to the forefront, they came up with a way to produce and refine the needed isotopes to implement this new plan to potentially help end the war. One of the first techniques used to refine nuclear fuel rods was the bismuth phosphate process during the 1940's. This method was based upon a series of precipitations and solid-liquid phase separations to extract the

plutonium from spent nuclear fuel components². Figure 1 shows the bismuth phosphate extraction process. From this figure it can be seen that it goes through several washes before it is complete. One drawback is the quantity of steps it takes to finish the refinement process. Another is the hazardous waste that is generated using the bismuth phosphate refinement. Eventually, in 1989 this process that was used at the Hanford site was retired and has been for decades². Other aqueous processes have been used for reprocessing nuclear fuel rods such as Butex process that uses dibutoxy diethylene glycol and PUREX which uses nitric acid and tributyl phosphate (TBP) for extraction³. One of the downsides of using aqueous solution process is that not all the byproducts that are created during the high burn up of the fuel is soluble in nitric acid. Resulting in needing these materials to be filtered out for further treatment or discard to waste. Another aqueous process that was used is known as REDOX. This process was developed to simplify the remote mechanical operations and is based on methyl isobutyl ketone (hexone) extraction. The reason for it being called REDOX process is due to its use of oxidation-reduction separation chemistry. Using the ability of hexone to extract both plutonium and uranium, along with neptunium from oxidizing solutions³. The aqueous feed consisted primarily of molar nitric acid that contained the fission products and transuranic (TRU) elements as nitrate salts. Sodium dichromate oxidant was used to ensure that both plutonium and uranium were in hexavalent state as uranyl and plutonyl ions. In this process essentially all of the radioactive fission products and excess oxidant and reduction product were rejected to waste in the first process step, thus, resulting in minimizing oxidation and radiolysis problems of the solvent and radiolysis of downstream reagents needed for plutonium isolation³.

Another avenue that has been researched for refinement of fuel sources is non-aqueous techniques. A few of these processes are fluoride volatility processing, molten-salt processes, and pyroprocessing³. A benefit that the non-aqueous techniques had over aqueous is that they could be used while the fuel rods were still hot reducing the time needed to store them before they could safely be reprocessed. While the other two techniques mentioned use high temperature molten salts to refine the used or spent fuel, fluoride volatility was created to produce feed for the gaseous diffusion process for uranium enrichment³. This method was developed in several countries from 1950's to 1980's. In the United States research was done at Argonne, Brookhaven and Oak Ridge National Labs to use halogen fluoride (BrF_5 and ClF_3) as fluorination reagents⁴. Fluidized bed reactors housed the actual spent fuels to scale up the capacity resulting in generating 2-10 kg/batch and 40kg/batch tests. Fluoride was used due to some of the compounds it can create with other elements has relatively low boiling point. Example of this is uranium hexafluoride (UF_6) which is a solid that sublimates at atmospheric pressure at $55.2\text{ }^\circ\text{C}$ ⁵. Purifying the UF_6 is done by passing a UF_6 -fluorination gas mixture over a NaF bed at $100\text{ }^\circ\text{C}$. The NaF adsorbs the UF_6 due to the vapor pressure difference between NaF and UF_6 at $100\text{ }^\circ\text{C}$ which is $2 \times 10^{-3}\text{ mm}$ ⁵. The complexed NaF is then heated to $400\text{ }^\circ\text{C}$ while a fluorinated gas stream passes through the bed. This causes a desorption process to occur of the UF_6 which is then collected at another NaF bed at $400\text{ }^\circ\text{C}$. The last step is to cold-trap it at $-60\text{ }^\circ\text{C}$ ⁵. This was a typical way to use fluoride volatility process to refine spent or used fuel rods. A drawback for this process was that it created difficulties in recovering pure Pu, which was not favorable for the use of nuclear weapons which was the original purpose of creating these processes⁴. However now days with more of

a desire to use fission for power instead of weaponizing it, dirty Pu and U are becoming more in favor among the nuclear society.

Molten salt processes were another viable option to refine used or spent nuclear fuels. However, using it for refining fuels was not the first thing high temperature molten salts were used for. The idea was first conceived in the late 1940's and was originally planned to be used as fuel to power long distance airplanes for bombing raids. This first reactor known as the aircraft reactor experiment (ARE) was operated in 1954 at Oakridge National Lab (ORNL). The fuel source was Na-Zr-U salt and generated 96 MW-hours of energy ⁶. When intercontinental ballistic were created the need for such a project was no longer necessary and was promptly canceled. In 1956 ORNL director Alvin Weinberg hired MacPherson to form a group to build a molten salt reactor. They came up with a salt solution known as Flibe which consisted of UF_4 -LiF- BeF_2 and the reactor was brought online in 1966. It was operational for about 3 years before it was shut down due the Atomic Energy Commission not being convinced that it was worth the financial cost. In 1969 at a symposium on reprocessing nuclear fuels R. K. Steunenberg et al., discussed a pyrochemical process that was being used to purify uranium and plutonium. Cycling molten salts between a liquid alloy (donor) to another (acceptor), they were able to separate uranium and plutonium from each other and from nobler metal impurities ⁷. Eventually, these processes evolved into using high temperature molten salts as an electrolyte to electrochemically refine used and spent nuclear fuel rods. This method is known as pyroprocessing and will be further discussed in this thesis.

Chapter 2: Background

In the mid 1960's there was an early version of pyroprocessing that Argonne National Laboratory (ANL) and Landmark Foundation developed to treat domestic light water reactor used nuclear fuel ⁸. During the closure of the Experimental Breeder Reactor-II (EBR-II), they decided to demonstrate the viability of this technique to refine the rods in this reactor. Approximately, 35,000 fuel pins were recycled based on melt-refining and injection-casting fabrication in the adjacent Fuel Cycle Facility (FCF), which had a typical turnaround time of 45 days. However, melt-refining could not remove noble metal fission products and separate higher actinides from uranium ⁸. However, while this used molten salts to refine rods it was a pyrometallurgical process and not what is later on to become known as pyroprocessing ⁹. However, while this was one way to achieve a decent throughput rate of 100 kg a month, it still was not able to successfully separate out the noble fission products which was needed for the burnup rate expected in future fast reactors. In 1983 ANL along with Idaho National Lab (INL) worked together on creating the Integral Fast Reactor (IFR) program ^{8,10}. This process combined the melt-refining method with electrorefining process. EBR-II plant was used as the test reactor for the program, while the FCF (now known as the Fuel Conditioning Facility) was equipped with pyroprocessing equipment to perform the fuel recycle functions of IFR. While the IFR was later stopped in 1994, INL along with other labs has continued to do research and improve upon the pyroprocessing method.

To improve the efficiency of the pyroprocess it is necessary to understand how various elements interact with one another during the electrochemical refinement, which is the key step to this technique. Since this process is done as a batch-mode procedure, the fuel

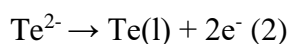
assembly needs to be dismantled so the individual fuel rods can be removed ¹¹. These rods are sent to a chopper to be cut into short 6-7 mm blocks after which they are placed into a perforated steel basket. Once the basket has been filled it is lowered into the electrorefiner where the actinides will be separated and recovered from the other fission products. The electrochemical process is carried out in a high-purity inert gas atmosphere that is contained in a steel vessel. Placed in the bottom of the vessel is a 0.15 m thick layer of cadmium, followed by a 0.3 m thick layer of the electrolyte salt which is a eutectic LiCl-KCl mixture. The process is operated at a temperature of 500 °C. A schematic of the setup is shown in Figure 2 ¹². Once the steel basket filled with the rods is lowered into the molten salt an electric current is ran through the solution. As a result, the actinides from the fuel are drawn from the steel anode basket to two kinds of cathodes. During this process, all the constituents of the chopped fuel, including the cladding, come into chemical equilibrium with the electrolyte salt. Each component of the fuel rod will be melted and mix with the electrolyte to varying degrees. As a result, various elements will be introduced into the salt causing various compounds and species that will be involved in the redox process besides uranium and plutonium that is desired to be collected. A variety of these elements that would be involved in the electrorefining are also desired for various uses. For that reason, most research has gone into understanding the electrochemical behavior of actinides, lanthanides, and alkali/alkaline rare-earths. However, there are still other elements that are created in the fission process that have not been researched to as great of an extent mostly due to its lack of technological or medicinal benefit. Regardless of necessity or low percentage in the molten salt electrolyte they would still have an overall effect on the efficiency of the electrorefining process. The

focus of this thesis will be looking into tellurium and technetium electrochemical behavior in LiCl-KCl eutectic molten salt along with how they will react in the presence of an oxide salt.

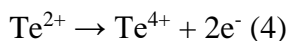
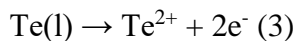
Tellurium/Telluride: Reduction of the used oxide fuels of light water reactors (LWR), fission products such as Cs, Ba, Sr, and Te partition to the salt phase. Reprocessing of mixed oxide (MOX) spent fuels results in elevated concentration of Te in the salt phase¹³. During the electrorefining process the tellurium in the system could result in embrittlement of structural alloys^{14,15}. Tellurides that are in high temperature molten chlorides are dissolved by chlorination reaction¹⁶:



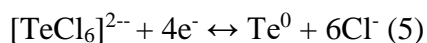
For voloxidation process and electrorefining process, both are done using chloride salts. Voloxidation is the high temperature process by which oxygen or air reacts with oxide spent fuels. With the possibility of reaction, one occurring, and Tellurium chloride salts being created it can create a decrease in efficiency of the solution. According to Poulsen et al, with the addition of Tellurium to a potassium chloride salt the electrical conductivity was $77 \text{ cm}^2/\Omega^{17}$. This is one of the higher rated values amongst molten salts. This increase in electrical conductivity had to do partially with the migration of tellurium in the salt. However, to completely understand all the mechanics of this further research was needed. Lichtenstein et al investigated the behavior of Te^{2-} in LiCl-Li₂Te¹⁸. During anodic deposition, at a value of 2.16 V vs Li⁺/Li(l) in LiCl-Li₂Te they saw the following reaction:



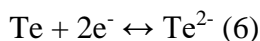
As a result of this reaction Te^{2-} which is soluble in the system, precipitates out as insoluble liquid Te metal. The Te metal is further oxidized to generate the reactions seen below:



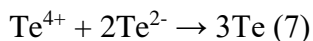
Due to there being no membrane separating the anode from the cathode in the system, the Te^{4+} can be attracted back to the cathode resulting in it being reduced back to Te^{2-} . If in the system $[\text{TeCl}_6]^{2-}$ is created either through the process seen in reaction 1 or by Te^{4+} bonding with chlorine, tellurium could undergo a single 4 electron step as seen in an experiment performed by Eric Gi-Shang et al. They introduced tellurium (IV) to aluminum chloride-1-methyl-3-ethylimidazolium chloride room temperature molten salt in the form of $[\text{TeCl}_6]^{2-}$ using a glassy carbon working electrode and an aluminum wire immersed in AlCl_3 -MEIC melt¹⁹. They saw two cathodic peaks appear, one being around -0.68 V vs. Al. Based on their observation and research they determined that this cathodic peak corresponded to the following reaction:



Further extending the window to more negative potentials, the Te^0 was reduced to Te^{2-} :



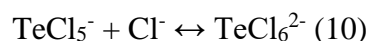
Upon extending the window to a more cathodic potential resulted in an anodic peak that was originally seen during the reverse cycle in the shorter window, no longer existed. It was concluded that when Te (IV) is in the presence of Te (II⁻) or vice versa, that they react with each other immediately by the following equation¹⁹:



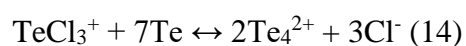
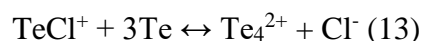
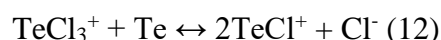
Since the molten salt bath that pyroprocessing occurs in has no membrane separating the electrodes, both Te^{2-} and Te^{4+} can exist in the molten salt. As a result, a higher concentration of Te metal can exist in the solution instead of Te^{2-} or Te^{4+} . Tellurium in the metallic state is highly soluble within molten salts ²⁰. Due to this any tellurium metal that exists will remain within the salt when it is taken for processing.

Depending on the desired ionic state that wants to be created of tellurium in the solution, the type of electrode that is used will greatly affect this. An example of this is what was reported by Bodewig and Plambeck who investigated the behavior between Te and a graphite working electrode in Li-Cl-KCl molten salt at 400 °C. It was observed that the tellurium was oxidized to Te(II) species and remained on the graphite electrode could not be oxidized further ²¹. In another study by Ebe et al. investigated the deposition of Te in $\text{AlCl}_3\text{NaCl-KCl}$ molten salt electrolyte at 423 K. It was seen that pure Te could not be electrodeposited onto a glassy carbon electrode from TeCl_4 ²². Another group reported on the behavior of Te (IV) in KCl-AlCl_3 molten salt at 300 -400 °C using a tungsten working electrode. It was seen that a two-step, two electron transfer reduction occurred with a redox potential in the vicinity of 1.6 V vs. Al/Al(III) in basic melts (high free Cl^- activity), while a three step reaction occurred in neutral melts ²³. Prior to this Poulsen et al., studied the formation of chloro-complexes such as TeCl_3^+ , TeCl_5^- , and $[\text{TeCl}_6]^{2-}$ based on the dissociation reaction of TeCl_4 in the molten salt. Depending on the free chloride activity in the molten salt the following reactions can occur ²⁴:





Another researcher explored the electrodeposition of Te and binary PbTe using room temperature ionic liquid 1-ethyl-3-methylimidazolium chloride (EMIC) – NaBF₄ that contained TeCl₄²⁵. Using two different working electrodes (glassy carbon and platinum) it was seen that nucleation kinetics of Te occurred faster on the platinum electrode than on glassy carbon. The various ionic states that these researchers saw affected the Te species that were created and would result in creating various compounds within the molten salt during electrorefinement of the fuel rods. One study by J. Robinson et al., investigated the electrochemical behavior of Te(IV) in sodium tetrachloroaluminate molten salt. Tellurium was introduced to the salt in the form of TeCl₄. When TeCl₄ is introduced to saturated NaCl it becomes readily soluble and mix with the NaCl melt at temperatures of 175 °C²⁶. Once a few cycles have been completed they noticed that with the presence of Te in the system that complexation reactions occur between Te and Te⁴⁺. From this they were able to deduce the following reactions²⁶.



From these step reactions it was seen that the decomposition of Te₄²⁺ is first order in [Te₄²⁺] and [Cl⁻]. Additionally, in equation 14 Te(IV) existed as TeCl₃⁺, which is created by combining equation 12 with twice that of equation 13 to get the proper ratio²⁶. With Te²⁻ and

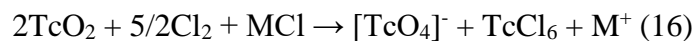
Te⁴⁺ reacting with tellurium metal in various ways it can be seen that in the pyroprocessing method that there will be a higher ratio of Te(0) to other ionic states of tellurium.

With metal oxide fuels being used in reactors and Li₂O salts needed to dissolve the oxide fuel, the reaction between oxygen and tellurium needs to be taken into consideration. However, there is very little research on this subject matter. What research has been done has looked at the crystalline compounds that can be formed. In one article by V. P. Itkin et al., they explored the various O-Te systems at various concentration and temperatures. The phase diagram seen in Figure 3 shows several different phases and compounds of O-Te combination²⁷. A few of these phases that was seen was αO₂Te which has a tetragonal structure. One method that was done to create this was freezing molten O₂Te or by precipitation from a supersaturated acidic aqueous solution of O₂Te. From the phase diagram it was seen that the melting point of this phase was approximately 750 °C Another that was investigated was O₃Te which took both an α amorphous and β crystalline structure, which was prepared by decomposition of H₆O₆Te at about 310 °C. With the quantity of tellurium that exist in the system during fission and pyroprocess, it is possible that αO₂Te could exist in these systems.

Technetium/Rhenium: Little research has been done on technetium especially in nonaqueous solutions. However, it is necessary to understand its electrochemical behavior due to its ability to form volatile species, along with it exhibiting unusual properties that can form anionic species such as [TcO₄]⁻. This compound is a highly mobile species, making it a challenge to safely dispose²⁸. One of the complexes that has been researched in molten salts is the reaction between TcO₂ and HCl in molten salt and is shown in the reactions below²⁹:



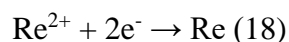
Without the addition of HCl the reaction of TcO_2 with chlorine in molten chloride salt reacts in a different way than what was observed with HCl. These reactions resulted in pertechnetate and volatile TcCl_6 or TcO_3Cl given by the following reactions ²⁹:



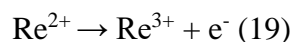
These reactions have a high probability of occurring in the molten salt with both oxide salts and chloride. These products are volatile species within the solution, which can result in vapors being formed and losing electrolyte to the environment. G. Rosner et al., experimented with the solubility of technetium in lithium perchlorate salt. Using lithium perchlorate as a potential solvent was investigated due to its low melting temperature at 236 °C ³⁰. They operated the test between 250-300 °C and determined that technetium was soluble in the solution. Additionally, they saw a loss in activity caused by the volatile oxide or due to the mechanical carry over of the evolution of oxygen. In 2010 V. A. Volkovich et al., performed experiments of metallic Tc in NaCl-2CsCl eutectic molten salt. They observed an anodic dissolution forming Tc(IV) and lower oxidation state species ³¹. Using cyclic voltammogram, two cathodic peaks along with corresponding anodic peaks were seen. One of these pairs were seen around -0.35 V vs. Ag/AgCl reference which was associated with Tc metal deposition.

To further investigate the behaviors of Tc electrochemical behavior that is discussed in this thesis, a surrogate element was used to conduct experiments due to the radioactive nature of technetium. For this reason, rhenium was used due to it having similar electrochemical properties as technetium. Bailey et al. investigated electrochemical studies of rhenium in LiCl-KCl eutectic salts ³². The techniques that were used were potentiometric and

polarographic experiments between a range of 450 – 550°C. They discovered that anodic dissolution of rhenium metal created Re(IV) which is stable indefinitely in the molten salt. Additionally, any lithium metal that was in the system was partly dissolved in the rhenium. With technetium having similar behaviors as rhenium any lithium salts used, if reduced far enough to produce Li⁰ could be dissolved by the technetium in the solution. In another study by O.N. Vinogradov-Zhabrov et al., electrodeposition of rhenium between a temperature range of 680-970 °C at a cathodic current density between 5-250 mA/cm². Part of the experimental procedure was to determine the diffusion coefficient of rhenium ions at temperatures of 790 °C and 840 °C in KCl-NaCl-ReCl₄ solution. It was discovered that at 790 °C the coefficient was 2.8*10⁻⁵ cm²/s and at 840 °C was 3.5*10⁻⁵ cm²/s ³³. In another study done by Danil A. Danilov et al., it was determined that [ReCl₆]⁻² in NaCl-KCl at 750 °C was reduced over a 2 step process from Re(IV) to Re(0) at a potential of -0.5 V vs. Ag/AgCl ³⁴. In another article by A. Affoune et al., they researched the electrochemical properties of Re in fused LiF-NaF-KF eutectic molten salt. It was seen that at a temperature of 650 °C that K₂ReCl₆ decomposed to a stable Re (II) species ³⁵. Upon doing the electrochemical experiments, the following reactions were seen:



Upon return of the cycle it was seen that Re(II) underwent a single electron transfer:

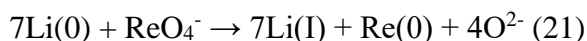
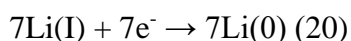


From this it was seen that the Re(II) species was stable in LiF-NaF-KF molten salt before electrochemical process was implemented. R. A. Bailey did a study on the reaction of Re(III) chlorides in molten salts. They started with various Re(III) species and combined it with

diethylammonium chloride and dimethyl sulfone³⁶. It was seen that when the Re(III) species were in the presence of chloride ions the Re_3Cl_9 was converted to $[\text{Re}_2\text{Cl}]^{2-}$. When it was in the presence of LiCl-KCl eutectic, Re(III) disproportionate to Re(0) and $[\text{ReCl}_6]^{2-}$. In another study Re (IV) complexes were explored in basic Aluminum Chloride-1-Methyl-3-ethylimidazolium Chloride room temperature molten salt³⁷. It was seen that the metal-metal-bonded Re(IV) complex $[\text{Re}_2\text{Cl}_9]^-$, was slowly converted to the monomeric Re(IV) complex, $[\text{ReCl}_6]^{2-}$ at room temperature in basic melt through incorporation of chloride ions. In a study by Sandra K. D. Strubinger et al., they saw that the reduction of $[\text{Re}_3\text{Cl}_{12}]^{3-}$ was dependent on the chlorine content within the melt³⁸.

As with tellurium it is needed to understand the behavior of Re when in the presence of oxygen to be able to correlate to that to the behavior of Tc. However, there is little information on this topic and what information that is available is on the benefits of rhenium oxides catalytic abilities. One of the first oxides that was studied using X-ray diffraction was ReO_3 ³⁹. Another structure that they researched was ReO_2 . They combined Re metal with the ReO_3 at 800 °C, resulting in creating an orthorhombic dioxide structure. In another study by M. A. Vuurman et al, the structural surface layer of rhenium oxide on various oxide substrates was investigated. Starting with a 60-70 wt% aqueous solution of perrhenic acid (HReO_4), each substrate was placed in the solution allowing for an impregnation of the rhenium oxide on the substrates. Eventually through several different drying steps they were able to form a Re_2O_7 layer, which was verified using Raman and IR spectroscopy⁴⁰. Brishti Mitra et al., conducted a study to determine the catalytic behavior of Re_2O_7 on TiO_2 and Al_2O_3 substrates. It was seen that the reducibility of Re_2O_7 was dependent on the substrate it was bonded with. The TiO_2 had a weaker Re-O support bond strength than Al_2O_3 , allowing the rhenium oxide

to be reduced more effectively than on the Al_2O_3 substrate ⁴¹. A study that was performed by Leily Majidi et al., researched the viability of ReS_2 as a potential electrode to improve energy efficiency of Li-O_2 batteries. It was discovered that the ReS_2 substrate showed a good current density of 44.37 mA/cm^2 during oxygen reduction reaction and 6.89 mA/cm^2 for oxygen evolution reaction ⁴². In 1972 R.A. Bailey performed electrochemical experiments using ReO_4^- in fused LiCl-KCl eutectic molten salt. Due to the presence of oxygen in the system, the pyrex glass containers were taking damage that is indicative to oxygen attack ³². One of the techniques they used was a constant-current method to deposit rhenium in the system. It was seen that the potential increased immediately to the Li-deposition potential and remained at this value throughout experiment. Having such a process occur indicates that deposition occurs through a secondary mechanism shown below ³²:



In another article by E. Kim et al., they explored the chemistry of rhenium as an analogue to technetium. They wanted to determine the migration of fissiogenic Tc into the environment using rhenium oxides to test the dissolution behavior ⁴³. They discovered that ReO_4^- is highly soluble under the conditions that would be found in radioactive waste. While Re(III) oxides are not stable in aqueous solutions and are not much likely to be found. Re(IV) oxides is weakly soluble which suggests it can be found in noticeable concentrations in aqueous solutions even in anoxic media. Similar results are expected to be seen with Tc ⁴³.

Chapter 3: Comparison of Glassy Carbon and Tungsten Working Electrode of Redox Species of TeCl_4 in LiCl-KCl Eutectic Molten Salt at 450 °C

3.1 Experimental Procedure

Due to the hygroscopic nature of the LiCl-KCl eutectic salt, all experiments were performed in a glove box (MBraun) under an inert argon environment. Oxygen and moisture levels were maintained less than 2 ppm. The eutectic salt was created by thoroughly mixing 44.6wt% LiCl (99.995%, ultra-dry) with 55.4wt% KCl (99.998%, ultra-dry). Due to the high vapor pressure of tellurium tetrachloride (TeCl_4 , 99.9% purity) the following procedure was performed to create the mixture. The eutectic salt was melted in a glassy carbon crucible and left to cool over an 8-h period. Due to the high wetting angle between the salt and glassy carbon crucible, the eutectic ingot was able to be taken from the crucible in one piece. Afterward, varying wt% of TeCl_4 powder was placed in the glassy carbon crucible followed by the eutectic ingot. The entire salt mixture was heated to 10 degrees below the vapor temperature of TeCl_4 (200 °C) and soaked at this temperature for 15 minutes to allow the system to come to equilibrium. The temperature was then brought to 353 °C and let set for 1 hour to allow solution to melt. Once the ingot was created, the completed ingot was broken into half and placed in an alumina crucible for electrochemical testing.

Before bringing the created salt mixture to operating temperatures the furnace was brought to 10 degrees below sublimation temperature of the TeCl_4 (200 °C) for 15 minutes. After soaking at this temperature, the furnace was brought up to 450 °C and equilibrated for 10 minutes before starting the electrochemical measurements. The addition of TeCl_4 was varied

from 1–5wt% or 0.2–1mol%. All chemicals were procured from Alfa Aesar and used without further purification.

The concentration of TeCl_4 retained in the molten salt was determined by using induction coupled plasma- mass spectroscopy (ICP-MS) technique. The sampling of salt for ICP-MS analysis was carried out by dipping a tungsten rod in the molten salt once the furnace had reached operating temperature followed by taking samples at 1 hour intervals. The solidified salts were scraped off the tungsten rod using a stainless steel spatula. The weight of the sampled salt was measured using an analytical balance (Radwag, XA110/2X) capable of measuring a minimum weight of 1mg with a resolution of 0.01mg and dissolved in 30ml of 1% nitric acid. Three samples were extracted for a given condition. The ICP-MS analysis of Te was performed at the Analytical Sciences Laboratory of University of Idaho by following a comprehensive quality management plan that maintains compliance with applicable standards of ISO 17025. The concentration of Te retained in the molten salt was analyzed as a function of time after temperature equilibration, and after completion of electrochemical tests. The amount of TeCl_4 after completion of the tests was significantly lower than the initial amount added which was attributed to the reduction of TeCl_4 to $\text{Te}(0)$ deposited on the working electrode as liquid metal and partially precipitate out of solution which formed as a metal bead upon solidification of the salt which can be seen in Figure 18. Table I summarizes TeCl_4 concentration retained in the molten salt as a function of time after temperature equilibration. The electrochemical results are discussed with reference to the initial addition amount for brevity.

Table I. ICP-MS analyses of TeCl_4 retained in the LiCl-KCl molten salt as a function of time, and after testing.

Initial addition of TeCl_4	Dwelling time at 450 °C, h	TeCl_4 retained in the molten salt, %
1wt%	0	79 ± 0.02
	1	78 ± 0.022
	2	76 ± 0.016
	3	73 ± 0.031
	4	72 ± 0.012
	After testing	46 ± 0.12
5wt%	0.1	4.2 ± 0.2
	2	3.85 ± 0.11
	After testing	3.6 ± 0.25

Open circuit potential measurement, electrochemical impedance spectroscopy (EIS), cyclic voltammetry, and square wave voltammetry, were performed in LiCl+KCl eutectic melt at 450 °C with and without addition of 1–5 wt% TeCl_4 by using a computer controlled potentiostat (Gamry Instruments, model: Reference 1000, software for data generation: Gamry Framework, version 7.03, software for data analysis: Gamry Echem Analyst version 7.03). The temperature stability of the molten salt was ± 2 °C. A fuzzy logic proportional–integral–derivative (PID) controller (Tempco, model: TEC-9100) was used for controlling the temperature of the furnace using a type K (chromel-alumel) thermocouple. The thermocouple of the furnace was NIST calibrated. The temperature of the molten salt was measured by

using a NIST calibrated K-type thermocouple shielded by an alumina tube (99.8% purity, Omega) and a digital thermometer (Omega, model HH91). The working electrode was a 2mm diameter tungsten rod (99.95%, Alfa Aesar) or a 4mm glassy carbon rod (99.95%, Alfa Aesar). The counter electrode was a 4mm diameter glassy carbon rod. The reference electrode was an in-house made AgCl coated Ag wire (99.9%) placed in a borosilicate glass tube that contained LiCl+KCl eutectic thoroughly mixed with 1wt% AgCl (99.997%, ultra-dry). The working and counter electrodes were polished using a series of emery papers down to 2000 grit. The polished surface was wiped down with propanol and acetone and dried in a vacuum oven for 16h at 120 °C. The cleaning, and conditioning protocols were strictly followed for each set of experiments to ensure repeatability. After reaching the set temperature of 450 °C, the electrodes were conditioned in the open circuit potential for 15min before starting the electrochemical tests. The electrodes were placed in an equidistance triangular arrangement. The distance between each electrode was one inch. The surface area ratio of the counter and working electrodes was at least 2.5. The surface area was calculated by physically measuring the diameter and the immersion depth of the working and counter electrodes in the molten salt after the experiments using an inch ruler with 32nd tick mark. The measured depth was compared with the initial set value (typical variation after converting to cm was 0.5 – 0.75cm due to capillary effect). The surface area measured by geometric calculation is prone to error caused by meniscus of the molten salt, and salt built up layer. No effort was taken to address the errors introduced by the geometric surface area calculations which may vary from 7%–12%.

Yoon et al. proposed a relation between the Ag/AgCl reference potential and Cl₂/Cl⁻ potential that was a function of molar fraction of AgCl but independent of temperature between 723–823K and given as⁴⁴:

$$E_{\text{Cl}_2/\text{Cl}^-} = (-0.8726 \pm 0.00486) + (0.05896 \pm 0.00108) \ln(X) \quad (22)$$

Where X = mole fraction of AgCl. Accordingly, the Ag/AgCl potential of this study is -1.197V vs the redox potential of Cl₂/Cl⁻. CV was carried out at different potential windows and at different scan rates. All potentials in this paper are given with reference to the Ag/AgCl electrode whose potential is -1.197 V_{Cl₂/Cl⁻}. The maximum potential window signified decomposition of the LiCl-KCl eutectic by reduction of lithium at the cathodic end and chlorine evolution at the anodic end. Cyclic voltammetry studies were carried out at different scan rates from 100mVs⁻¹ to 5000Mv s⁻¹. The working electrode was cleaned by anodic stripping at +0.3V for 30s between experiments and allowed to relax for 60s without any bias potential to replenish the concentration gradients of ionic species. Electrochemical impedance spectroscopy was carried out at the open circuit condition and at different peak potential conditions (as noted in the cyclic voltammograms) under potentiostatic conditions by superimposing an *ac* signal of 10mV by scanning the frequency from 10kHz to 0.1Hz. Square wave voltammetry was conducted between OCP and -2.5 V_{Ag/AgCl}; and between OCP and 1.2 V_{Ag/AgCl} at a frequency of 25Hz, pulse size of 25mV, step size of 1mV, and pulse time of 0.04s. All the electrochemical tests were either duplicated or triplicated to ensure reproducibility. The average values are presented.

3.2 Results and Discussion

Open circuit potentials (OCP) measurements:

The purpose of OCP measurement is to understand the equilibrium conditions of various redox species present in the molten salt with the surface of the working electrode, which is tungsten or glassy carbon. Figure 4 shows the OCP of tungsten as working electrode in LiCl+KCl eutectic with addition of 1 to 4 wt.% of TeCl₄, while Figure 5 shows OCP of glassy carbon (GC) electrode both performed at 450 °C. In both working electrodes, as the weight percent of TeCl₄ increased the OCP shifted to more positive potentials. Increase in the TeCl₄ concentration will increase the exchange current density (i_0) by following the relation⁴⁵:

$$i_0 = nFk_0C_{Te^{4+}} \quad (23)$$

Where, n = number of electrons, F = Faraday's constant, k_0 = rate constant for electron transfer, and $C_{Te^{4+}}$ is bulk concentration of Te⁴⁺ in the molten salt. The increase in the i_0 value will shift the Tafel plots of the Teⁿ⁺/Te⁽ⁿ⁻¹⁾⁺ redox reactions such that the OCP could increase with the increase in the TeCl₄ concentration. It should be noted that the proposed Te⁴⁺/Te²⁺ redox couple is an example only. There are other possible redox reactions involving tetravalent Te. The standard redox potential of Te is reported to be more positive than that of Pd, Ag, Mo, W, and other transition metals^{15,45}. Even though the glassy carbon electrode may not be electro catalytic and not directly participating in the redox reactions, the OCP observed on the GC followed a similar trend as that of tungsten. The positive OCP values observed on the GC electrode indicated that the GC had significant active sites to support the redox reactions.

Cyclic voltammetry:

A full window CV scan was performed from -2.8V to $1.4\text{ V}_{\text{Ag}/\text{AgCl}}$ as seen in Figure 6. The cyclic voltammogram of pure LiCl-KCl eutectic (without TeCl_4 addition) showed only one cathodic wave corresponding to lithium reduction that started at around $-2.6\text{ V}_{\text{Ag}/\text{AgCl}}$ and an anodic wave associated with chlorine gas evolution that started around 1.2V . No other peaks were observed in between these two potentials on the tungsten electrode. The reduction potentials of lithium reported in the literature vary widely from -2.35V to -2.6V . For example, Koyama et al. reported a value of $-2.353\text{ V}_{\text{Ag}/\text{AgCl}}$ at 723K for the $\text{Li(I)}/\text{Li(0)}$ reaction¹². On the other hand, Bermejo et al. showed lithium reduction occurring at $-2.6\text{ V}_{\text{Ag}/\text{AgCl}}$ at 723K using tungsten as a working electrode⁴⁶. Liu et al. also reported a similar potential of $-2.6\text{ V}_{\text{Ag}/\text{AgCl}}$ for reduction of lithium at 873K ⁴⁷.

Addition of TeCl_4 introduced several additional peaks both in the cathodic and anodic directions. The noise observed could be attributed to the droplets of Te formation on the counter or working electrodes due to crossover of the redox species because the electrodes were not compartmentalized by a micro-porous separator. Crossing of CV occurred at high anodic potentials (between 0.72 and 0.58V in case of $1\text{wt}\%$ TeCl_4 and 0.76 and 0.56V in case of $2\text{wt}\%$ TeCl_4) in all the TeCl_4 additions. It is not evident in the $4\text{wt}\%$ TeCl_4 because the scan was reversed at 1V before reaching the chlorine evolution condition. Therefore, the crossing of CV was considered to be associated with polarizing the electrode to chlorine evolution potentials. Sakamura et al. attributed the anodic wave at 0.7V to the dissolution of Te in the form of Te^{2+} and formation of volatile TeCl_2 ⁴⁹. Generally, double crossing of CV during a reverse scan indicates deposition or adsorption of electroactive species that show nucleation over potential⁵⁰. However, in this case the crossing was attributed to oxidation of Te promoted by the Cl_2 that was adsorbed on the electrode surface. Without Cl_2 adsorption,

no oxidation peak was observed during the reverse scan. Therefore, the proposed reaction steps were: $\text{Cl}_2 \rightarrow 2 \text{Cl}_{(\text{ads})}$; $2 \text{Cl}_{(\text{ads})} + 2 \text{e}^- \rightarrow 2 \text{Cl}^-$; $\text{Te} + 2\text{Cl}^- \rightarrow \text{TeCl}_2 + 2 \text{e}^-$ (anodic peak).

Figure 7 shows cyclic voltammograms on tungsten electrode in the cathodic direction with and without addition of 1wt% TeCl_4 containing LiCl-KCl eutectic at a smaller potential window. The peaks associated with Te species are clearly discerned in Figure 7 in comparison with the CV of LiCl-KCl eutectic without any addition of TeCl_4 . Figure 8 illustrates the full window (both in the cathodic and anodic directions) CV of 1wt% TeCl_4 containing LiCl-KCl molten salt at different scan rates with a tungsten working electrode. The cathodic wave started at potential more negative than $-0.47 \text{ V}_{\text{Ag}/\text{AgCl}}$. Four distinct cathodic peaks were observed at around -0.58V (c_1), -0.95V (c_2), -1.15V (c_3), -2.26V (c_4), and $-2.6 \text{ V}_{\text{Ag}/\text{AgCl}}$ (c_5). During the reverse scan, five anodic peaks were recorded at -2.35V (a_0), -0.78V (a_1), -0.6V (a_2), 0.38V (a_3), and $0.74 \text{ V}_{\text{Ag}/\text{AgCl}}$ (a_4). The first cathodic wave (c_1) was attributed to the reduction of Te^{4+} to Te^{2+} , and the second cathodic wave (c_2) was due to reduction of Te^{2+} to $\text{Te}(0)$. A similar two step reduction reaction was proposed for Te^{4+} ions in the NaCl-2CsCl and 3LiCl-2KCl base molten salts at 823K¹⁶. It was observed that at scan rates of 200–1000 mVs^{-1} , the cathodic wave c_2 showed two peaks (c_2 and c_3) as seen in Figure 8. The cathodic wave (c_4) at a more negative potential was associated with formation of telluride ions (Te_x^{n-}). The number of electrons transferred could be determined from differential square wave pulse voltammetry, which will be discussed in a latter section. The cathodic wave c_5 , which was observed to take off at around $-2.6 \text{ V}_{\text{Ag}/\text{AgCl}}$ was attributed to reduction of lithium. The anodic peaks a_0 , a_1 , a_2 , and a_3 were ascribed as the reverse reactions of cathodic peaks c_4 , c_3 , c_2 , and c_1 , respectively. The anodic wave (a_4) taking off at about 1.2V was associated with evolution of chlorine.

Figures 9 and 10 show the cyclic voltammograms between OCP and $-2.2 V_{\text{Ag}/\text{AgCl}}$ (more positive than the lithium reduction condition) at different scan rates in 1wt% and 5wt% TeCl_4 containing LiCl-KCl using tungsten as a working electrode. The first cathodic wave (c_1) starting at -0.5V evolved clearly at a scan rate of 1Vs^{-1} and higher. The second cathodic wave (c_2) occurred with a peak current at around -0.9V . The peak potential shifted in the negative direction with the increase in the scan rate. The peak shift per decade of the scan rate was observed to be about 0.11V , which is almost equal to the magnitude of $2.3RT/\alpha_c nF$. Assuming that this cathodic wave is associated with a two-electron process, the α_c , transfer coefficient for cathodic reaction shall be estimated as 0.38. The scan rate dependency of the peak potential indicated that the cathodic reaction was not reversible. However, the peak current increased as a function of square root of the scan rate, as seen in Figure 11a. The third wave (c_3) was observed only at particular scan rates (between $0.2\text{--}1\text{Vs}^{-1}$). At lower (0.1Vs^{-1}) and higher scan rates ($> 2\text{Vs}^{-1}$), a broader peak was observed. The cathodic peaks c_2 and c_3 were attributed to formation of zero valent Te on the working electrode. These cathodic peaks were associated with soluble-insoluble species, where soluble Te(II) species were reduced to insoluble Te(0) deposit. A cathodic wave shoulder starting at $-2 V_{\text{Ag}/\text{AgCl}}$ was attributed to the reaction: $n\text{Te}(0) + e^- \rightarrow \text{Te}_n^-$. This cathodic wave was associated with insoluble Te being converted to soluble Te^{2-} species. Since the CV was interrupted at -2.2V no lithium reduction and oxidation peaks were observed. The anodic waves (a_1, a_2) observed at about -0.83 and $-0.7 V_{\text{Ag}/\text{AgCl}}$ were associated with the oxidation of soluble Te anionic species to Te(0). Sakamura et al. reported two anodic peaks at -0.67 , and $-0.5 V_{\text{Ag}/\text{AgCl}}$ in 0.19mol% Na_2Te containing LiCl-KCl molten salt at $500\text{ }^\circ\text{C}$ corresponding to the following reactions (24) and (25) ⁴⁹.



It is noted that the peak potentials of anodic waves a_1 and a_2 were independent of the scan rates indicating reversibility of the reaction. The anodic peaks observed at potentials more positive than $0.3 \text{ V}_{\text{Ag}/\text{AgCl}}$ were attributed to the oxidation of Te to Te^{2+} and Te^{4+} as seen in Figure 9. Oxidation of Te to volatile formation of the TeCl_2 has been:



The anodic peak observed at $0.44 \text{ V}_{\text{Ag}/\text{AgCl}}$ was assigned to reaction (26), which is 0.76V more negative than the chlorine evolution potential. Lichtenstein et al. reported a similar value (0.71V negative to chlorine evolution potential) at $650 \text{ }^\circ\text{C}$ for the Te oxidation to Te^{2+} ¹⁸.

Figures 11a and 11b show the linear relation observed between peak current density and the square root of the scan rate in 1wt% and 5wt% TeCl_4 containing LiCl-KCl eutectic at $450 \text{ }^\circ\text{C}$ at two different potentials using a tungsten electrode. Randles-Sevick equation describes the peak current density as a function of electrode surface area, bulk concentration of the redox species, and square root of the scan rate and diffusivity of redox species ⁵¹. The diffusion coefficient can be calculated from the Randles-Sevick relation as given in (27):

$$D^{1/2} = \left[\frac{i_p}{\sqrt{v}} \right] \left(\frac{1}{0.446nFAc_0} \right) \left(\frac{RT}{nF} \right)^{0.5} \quad (27)$$

Where i_p/\sqrt{v} is the slope of peak current vs square root of scan rate, A is the surface area of electrode, and C_0 is the concentration of the Te species. Using the slopes taken from Figure 11a and (b) the diffusion coefficients of Te^{4+} and Te^{2+} could be calculated for two

different concentrations of TeCl_4 . Figure 12 shows the i_p vs \sqrt{v} plots for the anodic sweep where the soluble Te^{2-} oxidized to insoluble $\text{Te}(0)$ deposit. The peak current of soluble-insoluble redox species can be expressed as a function of \sqrt{v} and \sqrt{D} using the Berzins and Delahay relation⁵²:

$$i_p = 0.611 nFAC_0 \left(\frac{nF\theta D}{RT} \right)^{1/2} \quad (28)$$

The bulk concentration of TeCl_4 retained in the molten salt after two hours of thermal equilibrium was considered to calculate the diffusivities from the slope of the i_p vs \sqrt{v} plots. The number of electrons (n) involved in the reduction reaction was calculated from the square wave voltammetry data as shown in Figure 13 by determining the width of half current peak ($W_{1/2}$) and using the relation^{53,54}:

$$n = 3.5 RT/(W_{1/2}F) \quad (29)$$

Alternately, the number of electrons for reversible soluble-soluble redox system can also be calculated from the CV data using the relations (30) and (31) proposed by Matsuda and Ayabe⁵⁵:

$$E_{p,c} = E_{1/2} - 1.11 \frac{RT}{nF} \quad (30)$$

$$E_{p,a} = E_{1/2} + 1.11 \frac{RT}{nF} \quad (31)$$

Where $E_{p,c}$ and $E_{p,a}$ are cathodic and anodic peak current potentials, respectively; $E_{1/2}$ is a half wave potential and expressed as:

$$E_{1/2} = E_{Te^{4+}/Te^{2+}}^0 + \frac{RT}{nF} \text{Ln} \left(\frac{\gamma_{Te^{4+}}}{\gamma_{Te^{2+}}} \right) + \frac{RT}{nF} \text{Ln} \left(\frac{\sqrt{D_{Te^{2+}}}}{\sqrt{D_{Te^{4+}}}} \right) \quad (32)$$

Formal potential for soluble-soluble system, E^{0*} is expressed as⁵⁶:

$$E_{Te^{4+}/Te^{2+}}^{0*} = E_{Te^{4+}/Te^{2+}}^0 + \frac{RT}{nF} \text{Ln} \left(\frac{\gamma_{Te^{4+}}}{\gamma_{Te^{2+}}} \right) \quad (33)$$

$$E_{Te^{4+}/Te^{2+}}^{0*} = \left(\frac{E_{p,a} + E_{p,c}}{2} \right) - \frac{RT}{nF} \text{Ln} \left(\frac{\sqrt{D_{Te^{2+}}}}{\sqrt{D_{Te^{4+}}}} \right) \quad (34)$$

Formal potential for reversible soluble-insoluble (Te/Te^{2-} , Te^{2+}/Te) system can be expressed as^{18,56}:

$$E_{p,1a} = E_{Te^0/Te^{2-}}^{0*} + \frac{0.854RT}{nF} - \frac{RT}{nF} \text{Ln}(C_{Te^{2-}}) \quad (35)$$

$$E_{p,1c} = E_{Te^{2+}/Te^0}^{0*} - \frac{0.854RT}{nF} + \frac{RT}{nF} \text{Ln}(C_{Te^{2+}}) \quad (36)$$

Table II summarizes the results of square wave voltammograms (SWV) given in Figure 13 and the number of electrons calculated based on the full width half wave of the differential current peaks using the expression given in (29). The peak potentials of different reduction reactions are listed which could be correlated to the formal potentials described in the expressions (33) to (36). The SWV data indicated that the cathodic peaks observed between -0.4 to $-1.2V$ in the CV could be assigned to the three-step reduction process of $Te(IV)$ to $Te(0)$. The three-step process reported in this investigation is different from the two-step process commonly reported in $KCl-AlCl_3$ melts at $300\text{ }^\circ\text{C}$ ⁵². The number of electrons calculated from the SWV data was used for estimation of the diffusivity of species based on

the slopes of i_p vs \sqrt{v} plots given in Figures 8 and 9. Table VII lists the coefficient of diffusion of different species such as Te^{4+} , Te^{2+} , and Te^{2-} in two different TeCl_4 concentrations at 450 °C. Even though a quasi-reversible type reaction was observed, the diffusivity can be estimated based on the Randles–Sevcik equation or Berzins and Delahay relation. Similar approach has been reported by other researchers for calculating the diffusivities of lanthanide ions in the LiCl-KCl eutectic ^{51,57}. Bermejo et al. reported that the corrections required for cylindrical geometry of the working electrode can be neglected to use the semi-infinite relations assumed for the Randles–Sevcik (Eq. 27) or Berzins-Delahay (Eq. 28) relation when the scan rate is higher than 50mV s^{-1} ⁵¹. The diffusivity values, in turn, were used for the estimation of formal potentials based on the relation (34). The formal potentials were determined based on the CV data using the relations (34) (36) and summarized in Table IV.

Table II. Summary of the square wave voltammogram data of tungsten electrode in 1wt% TeCl_4 containing LiCl-KCl at 450 °C.

Peak ID	Peak potential, $V_{\text{Ag}/\text{AgCl}}$	Width at half peak, $(W_{1/2}), V$	Number of electrons	Reaction step
1	-0.48	0.11	1.98	$\text{Te}^{4+} + 2 e^- \rightarrow \text{Te}^{2+}$
2	-0.72	0.21	1.04	$\text{Te}^{2+} + e^- \rightarrow \text{Te}^+$
3	-0.82	0.18	1.2	$\text{Te}^+ + e^- \rightarrow \text{Te}(0)$

Table III. Diffusivities of Te species in LiCl-KCl eutectic at 450 °C.

Working Electrode	Initial concentration of TeCl ₄ , wt%	Diffusing species	Coefficient of diffusion, cm ² /s
Tungsten	1wt% (actual 0.76%)	Te ⁴⁺	$9.2 - 9.8 \times 10^{-6}$
		Te ²⁺	$3.8 - 6.2 \times 10^{-5}$
		Te ²⁻	$1.4 - 1.6 \times 10^{-5}$
	5wt% (actual 3.85%)	Te ⁴⁺	$1.1 - 1.7 \times 10^{-6}$
		Te ²⁺	$9.4 - 13.7 \times 10^{-6}$
		Te ²⁻	$2.0 - 5.2 \times 10^{-6}$
Glassy carbon (GC)	1wt% (actual 0.76%)	Te ⁴⁺	$1.4 - 1.6 \times 10^{-5}$
		Te ²⁻	$5.4 - 7.4 \times 10^{-6}$
	5wt% (actual 3.85%)	Te ⁴⁺	$5.8 - 7.7 \times 10^{-6}$
		Te ²⁻	$1.4 - 2.1 \times 10^{-6}$

Table IV. Formal potentials of LiCl-KCl-TeCl₄ system at 450 °C using tungsten working electrode.

Reaction	Formal potential in 1wt% TeCl ₄ , V _{Ag/AgCl}	Formal potential in 5wt% TeCl ₄ , V _{Ag/AgCl}
Te ⁴⁺ + 2e ⁻ → Te ²⁺	-0.195	-0.161
Te ²⁺ + e ⁻ → Te ⁺	-0.691	-0.78

Reaction	Formal potential in 1wt% TeCl ₄ ,	Formal potential in 5wt% TeCl ₄ ,
	V _{Ag/AgCl}	V _{Ag/AgCl}
Te ⁺ + e ⁻ → Te	-0.82	-0.912
Te ²⁻ → Te + 2e ⁻	-0.934	-0.744

The diffusivity of Te⁴⁺ in LiCl-KCl eutectic at 450 °C decreased with increase in the concentration of TeCl₄ with the tungsten working electrode. The octahedral coordination of Te⁴⁺ with chloride ions as TeCl₆²⁻ could be attributed to the decreased diffusivity with increase in the concentration. The estimated diffusivity of Te⁴⁺ in 1wt% TeCl₄ was about $0.9 \times 10^{-5} \text{ cm}^2 \text{ s}^{-1}$. A similar order of magnitude ($0.54 \times 10^{-5} \text{ cm}^2 \text{ s}^{-1}$) diffusivity was reported for Ce(III) in LiCl-KCl at 723K by Yoon and Phongikharoon⁵⁷. The diffusivity of Te⁴⁺ decreased to $0.1 \times 10^{-5} \text{ cm}^2 \text{ s}^{-1}$ when the concentration of TeCl₄ increased to 5wt%. The diffusivity of Te²⁺ was estimated to be an order of magnitude higher than that of Te⁴⁺ in a given experimental condition. The increased diffusivity of Te²⁺ could be associated with non-cubic coordination with the chloride ions⁵⁸. A planar coordination such as TeCl₃⁻ is reported for Te²⁺²³. The diffusivity of Te²⁺ decreased with the increase in the initial concentration of TeCl₄. The diffusion coefficient of Te²⁻ was estimated to be $\sim 1.4 \times 10^{-5} \text{ cm}^2 \text{ s}^{-1}$ in 1wt% TeCl₄ and $\sim 0.36 \times 10^{-5} \text{ cm}^2 \text{ s}^{-1}$ in 5wt% TeCl₄ at 450 °C. Recently, Lichtenstein et al. reported that the diffusivity of Te²⁻ in 0.07mol% Li₂Te containing LiCl-KCl at 650 °C as $0.73 \times 10^{-5} \text{ cm}^2 \text{ s}^{-1}$ ¹⁸. These authors also reported a decrease in the diffusivity as the mol% of Li₂Te increased to 0.32%. However, the diffusivity reportedly increased when the Li₂Te increased to 0.34 mol%.

Table IV summarizes the formal potentials for different reduction reactions. The formal potentials of Te(IV) reduction reaction and Te^{2-} oxidation reaction shifted in the positive direction with increase in the initial TeCl_4 concentration, while the formal potential of Te^{2+} reduction shifted in the negative direction with increase in the TeCl_4 concentration. Poulsen and Bjerrum reported the reduction potential of $\text{Te(IV)} \rightarrow \text{Te(II)}$ in KCl-AlCl_3 at 300°C to be $1.69 \text{ V}_{\text{Al/Al(III)}}$ and the reduction potential of $\text{Te(II)} \rightarrow \text{Te(0)}$ to be 1.623V ¹⁷. Bae reported the formal potential of Al^{3+} reduction as -1 V Vs Ag/Ag^+ at 450°C in LiCl-KCl eutectic⁵⁹. Because of the difference in temperature and absence of reference data, the potentials measured by Al/Al(III) electrode cannot be directly converted against Ag/AgCl electrode. These reduction potentials are more positive (about $+0.69 - +0.62 \text{ V}_{\text{Ag/AgCl}}$) than what observed in the LiCl-KCl molten salt at 450°C for a quick comparison. Bodewig and Plambeck reported the oxidation potential of Te ($\text{Te} \rightarrow \text{Te}^{2+} + 2\text{e}^-$) to be $-0.45\text{V Vs Cl}_2/\text{Cl}$ in LiCl-KCl at 400°C which is about $0.74 \text{ V}_{\text{Ag/AgCl}}$ ²¹. Probably, this potential corresponds to the reaction: $\text{Te} + 2\text{Cl}^- \rightarrow \text{TeCl}_2 + 2\text{e}^-$ as discussed by Lichtenstein et al¹⁸. These authors observed an anodic peak of the Te^{2-} oxidation at $1.94 \text{ V}_{\text{Li/Li}^+}$ and take-off of the oxidation reaction at $1.65 \text{ V}_{\text{Li/Li}^+}$ which corresponds to about $-0.86 \text{ V}_{\text{Ag/AgCl}}$. The estimated formal potential of the Te^{2-} oxidation of this study closely follows the reported values¹⁸.

Figures 14a and 14b show the cyclic voltammograms carried out using glassy carbon (GC) as a working electrode in 1wt% and 5wt% TeCl_4 conditions, respectively. The shape of the CV of the GC working electrode is significantly different from that observed using a tungsten working electrode. Relatively poor wetting of the GC could be attributed to this different behavior. Poulsen and Bjerrum also reported observation of ill-defined CV peaks using the GC electrode¹⁷. It is observed that the plot of the 1wt% TeCl_4 condition intercepted the

current axis at a non-zero value indicating passage of a non-faradaic current. Error in the calculation of the surface area of the working electrode mainly due to poor wetting could also result in this type of non-zero intercept. The diffusivities calculated based on the slopes of the i_p vs \sqrt{v} plots are listed in the Table III. The diffusivity values estimated from the CV data of GC electrode were smaller than that estimated using the tungsten electrode.

Electrochemical impedance spectroscopy:

Figures 15a and 15b show the EIS of the tungsten electrode in 1wt% TeCl_4 at different potentials in the forms of Nyquist and Bode plots, respectively. The conditioning at -0.9V represented the c_2 peak in Figure 8, application of -1.27V represented deposition of $\text{Te}(0)$, and -2.27V was associated with formation of soluble Te^{2-} species. The highest impedance was recorded at the $-0.9 \text{ V}_{\text{Ag}/\text{AgCl}}$. The lowest impedance spectrum was recorded at the OCP condition, as seen in Figure 16a. The Bode plots in Figure 16b gave a slightly different trend, whereas the -2.2V bias condition showed lower impedance modulus at higher frequencies and the bias condition -1.27V showed higher impedance than that recorded at -0.9V at the two extreme frequency ends.

The rationale behind carrying out EIS measurements was to understand the structural characteristics of the molten salts with and without addition of TeCl_4 . The physical and electrical properties of the molten salt systems depend on the structure and interactions of the constituents. The structural arrangements that are present in molten salts can be viewed as intermediates between discrete chemical bonds and periodic crystalline lattices⁶⁰. The interatomic interactions determine the local ordering of the molten salt. The electrochemical properties are influenced by the structural characteristics of the molten salt. When cations are

present in the molten salt with different sizes and different charge densities, an asymmetric polarization of anions is anticipated which affects the electrostatic stability of the mixture ⁶¹.

In order to better understand the interfacial impedance behavior, the EIS data were fitted into an electrical equivalent circuit (EEC) and the values of the circuit components are summarized in Table SI (supporting information). In general, the impedance spectra showed two time constants. Therefore, the EIS data was modeled using two R||C loops—one embedded into other forming a porous film type model. This EEC showed lower χ^2 values (or better fitting) than 2R||C loops connected in series. In the equivalent circuit, R_s and R_1 represent the electrolyte resistance and resistance to charge transfer, respectively. The R_1 - Q_1 loop represents the electrode/LiCl-KCl electrolyte interface. The embedded R_2 - Q_2 loop represents the interface created by the presence of TeCl_4^{2-} or TeCl_3^- or other redox species. Q_1 represents interfacial leaky capacitance whose impedance (Z) is given by the relation: $Z = 1/[(j\omega)^m Q_F]$ where $j = \sqrt{-1}$, ω = frequency, and the exponent “ m ” represents the surface heterogeneity or continuously distributed time constants for charge transfer when $m < 1$.³³ Q_2 and W_f are constant phase element and diffusion limited charge transfer resistance (Warburg component), respectively that are associated with the redox species other than LiCl-KCl. It should be noted that the values of Q_1 , Q_2 , and W_f are expressed as admittance. Smaller magnitudes of R_1 and R_2 , and larger values of Q_F , Q_P , and W_f will lead to better charge transfer characteristics.

The solution resistance decreased both under the applied potentials in 1wt% TeCl_4 . The charge transfer resistance was given as $R_1 + R_2$ at high frequencies because the resistance due to the constant phase element would be negligible. The impedance due to the constant phase

elements became significant only below 10Hz as seen from the Bode plots. At potentials of -1.28V and -2.2V , the capacitance due to Q_1 increased significantly. This could be attributed to increased concentration of Te species at the electrode/molten salt interface replacing the Cl^- ions that were present in the OCP condition. The magnitude of Q_2 decreased at -0.91 and -1.28V compared to that of OCP condition which could be related to depletion of Te^{4+} ions that were present in the OCP condition, and deposition of $\text{Te}(0)$. On the other hand, an increase in the Q_2 was observed at -2.27V that could be related to the cathodic dissolution of Te in the form of Te^{2-} and replenishment of the interface. The Warburg diffusion component was present only at -1.28V .

Figures 16a and 16b illustrate the EIS data of 5wt% TeCl_4 using tungsten as a working electrode as Nyquist and Bode plots, respectively. The lowest impedance was recorded at the OCP. This could be attributed to very large values of Q_1 and Q_2 . The impedance increased under biased conditions. Not only the solution resistance of the 5wt% TeCl_4 was lower than that of 1wt% TeCl_4 but also the values of $R_1 + R_2$. The diffusion controlled Warburg impedance was observed at the -0.9V condition.

Figures 17a and 17b are the impedance spectra obtained using GC electrode in the 5wt% TeCl_4 solution. The lowest impedance was observed for the -2.16V applied potential condition. The bias condition of -1.1V showed the highest impedance in the intermediate frequencies as seen in Figure 18b. The EIS data were fitted with the EEC as shown in Table SII. The EIS data at OCP showed one time constant and therefore fitted with a single RC loop circuit. No Warburg component could be noticed at applied potential conditions. The values

of Q_1 and Q_2 were significantly higher at -2.16V than that observed at other conditions and that recorded with tungsten electrode as well.

An EEC model consisting of two parallel RC loops connected in series, and each RC loop having a Warburg element was proposed to describe the impedance behavior of LiCl-KCl molten salt at $700\text{ }^\circ\text{C}$ – $800\text{ }^\circ\text{C}$ by Cohen et al ⁶¹. The reported values of solution resistance (R_s), double layer capacitance (Q_1), capacitance due to adsorption of ions (Q_2), and Warburg coefficient were reported as 0.685 ohm , $58\text{--}80\ \mu\text{F}$, $1.8\text{--}2.3\ \text{mF}$, and $2\text{--}4\ \text{mS}$, respectively ⁶². The EIS data of this study was fitted with a different EEC model but the values of the circuit components showed almost similar order of magnitude for the $0\text{wt}\%$ TeCl_4 condition at $450\text{ }^\circ\text{C}$ as given in Table SI. Kim et al ⁶³. reported EIS data of a molybdenum electrode in LiCl-KCl- UCl_3 at 773K and fitted their data to an EEC similar to the one used in this work and the values of the circuit components showed a similar order of magnitude as reported in this work.

Most of the literature on pyroprocessing of used nuclear fuels focuses on the electrochemical behaviors of fission product as cations such as La^{3+} , Nd^{3+} , Sm^{3+} etc.⁶⁴ Not much information is available on the anion type fission products such as Te^{2-} and I^- . It is generally assumed that anions present in the molten salt may not interfere with the cathodic reduction of actinides. This study attempts to fill the knowledge gap and shows that Te^{2-} will be oxidized to $\text{Te}(0)$ and Te^{n+} during the pyroprocessing conditions and adversely affect the stability of the electrodeposits because of the low melting point of Te and volatility of TeCl_n compounds. The electrochemical data presented in this work such as formal potentials of different Te

species (Te^{2-} , Te^{4+} , and Te^{2+}) and their diffusivities are useful in designing more efficient pyrochemical processes.

3.3 Conclusions

The reduction of Te^{4+} to $\text{Te}(0)$ occurred in three steps. The formal potential of Te(IV) reduction to Te(II) was estimated as $-0.21 \text{ V}_{\text{Ag}/\text{AgCl}}$, which was observed to be a two-electron reaction step. The Te(II) reduced to $\text{Te}(0)$ in two steps with one electron reaction at each step. The reduction to $\text{Te}(0)$ completed at around $-1.2 \text{ V}_{\text{Ag}/\text{AgCl}}$. Formation of Te^{2-} was observed at potentials more negative than $-2.2 \text{ V}_{\text{Ag}/\text{AgCl}}$. The redox process of $\text{Te}^{4+}/\text{Te}^{2-}$ system was observed to be quasi-reversible.

The diffusion coefficients of Te^{4+} , Te^{2+} and Te^{2-} were 0.9×10^{-5} , 3.8×10^{-5} , and $1.5 \times 10^{-5} \text{ cm}^2 \text{ s}^{-1}$, respectively in the 1wt% TeCl_4 electrolyte. Increase in the TeCl_4 concentration decreased the diffusion coefficients.

The CV peaks observed on the glassy carbon working electrode were not as clearly defined as that of tungsten working electrode because of poor wetting characteristics.

The electrochemical impedance spectroscopic data could be fitted with an equivalent circuit representing two time constants. Diffusion limited impedance was observed only under certain potential conditions. The charge transfer resistance decreased with increase in the TeCl_4 concentration.

Chapter 4: Electrochemical Behavior of TeCl₄ in LiCl-KCl Eutectic Molten Salt at 500 °C to 550 °C

4.1 Experimental Procedure

Due to the hygroscopic nature of the LiCl-KCl eutectic salt, all experiments were performed in a glove box (MBraun) under an inert argon environment. Oxygen and moisture levels were maintained less than 2 ppm. The eutectic salt was created by thoroughly mixing 44.6wt% LiCl (99.995%, ultra-dry) with 55.4wt% KCl (99.998%, ultra-dry). Due to the high vapor pressure of tellurium tetrachloride (TeCl₄, 99.9% purity) the following procedure was performed to create the mixture. The eutectic salt was melted in a glassy carbon crucible and left to cool over an 8-h period. Due to the high wetting angle between the salt and glassy carbon crucible, the eutectic ingot was able to be taken from the crucible in one piece. Afterward, varying wt% of TeCl₄ powder was placed in the glassy carbon crucible followed by the eutectic ingot. The entire salt mixture was heated to 10 degrees below the vapor temperature of TeCl₄ (200 °C) and soaked at this temperature for 15 minutes to allow the system to come to equilibrium. The temperature was then brought to 353 °C and let set for 1 hour to allow solution to melt. Once the ingot was created, the completed ingot was broken into half and placed in an alumina crucible for electrochemical experiments.

Before bringing the created salt mixture to operating temperatures the furnace was brought to 10 degrees below sublimation temperature of the TeCl₄ (200 °C) for 15 minutes. After soaking at this temperature, the furnace was brought up to 500 to 550 °C and equilibrated for 10 minutes before starting the electrochemical measurements. The addition of TeCl₄ was

varied from 1–5wt% or 0.2–1mol%. All chemicals were procured from Alfa Aesar and used without further purification.

The concentration of TeCl_4 retained in the molten salt was determined by using induction coupled plasma- mass spectroscopy (ICP-MS) technique. The sampling of salt for ICP-MS analysis was carried out by dipping a tungsten rod in the molten salt at 1 hour intervals, ranging from when operating temperature has been reached up to 4 hours. Solidified salt was scrapped off the rod using a stainless steel spatula. The weight of the sampled out salt was measured using an analytical balance (Radwag, XA110/2X) capable of measuring a minimum weight of 1mg with a resolution of 0.01mg, and dissolved in 30ml of 1% nitric acid. Three samples were extracted per condition. The ICP-MS analysis of Te was performed at the Analytical Sciences Laboratory of University of Idaho by following a comprehensive quality management plan that maintains compliance with applicable standards of ISO 17025. The concentration of Te retained in the molten salt was analyzed as a function of time after temperature equilibration, and after completion of electrochemical tests. The amount of TeCl_4 after completion of the tests was significantly lower than the initial amount added which was attributed to the reduction of TeCl_4 to $\text{Te}(0)$ deposited on the working electrode as liquid metal. Table V summarizes TeCl_4 concentration retained in the molten salt as a function of time after temperature equilibration. The difference seen in the 4 hour concentration at 500 °C and 550 °C compared to other sample hours, was potentially due to the dispersion of Te in the salt at the time of test was taken. This could be due to the vapor process of the Te affecting where the greatest concentration of Te was at the time even with mixing the solution upon taking each sample. The electrochemical results are discussed with reference to the initial addition amount for brevity.

Table V. ICP-MS analyses of TeCl₄ retained in the LiCl-KCl molten salt as a function of time.

Initial addition of TeCl ₄	Dwelling time at 500 °C, h	TeCl ₄ retained in the molten salt, %
1wt%	0	100
	1	88.97
	2	88.39
	3	94.48
	4	41.2
Initial addition of TeCl ₄	Dwelling time at 550 °C, h	TeCl ₄ retained in the molten salt, %
1 wt%	0	99.06
	1	100
	2	100
	3	99
	4	1049

Open circuit potential measurement, electrochemical impedance spectroscopy (EIS), cyclic voltammetry, and square wave voltammetry, were performed in LiCl+KCl eutectic melt at 500 and 550 °C with and without addition of 1 wt% TeCl₄ by using a computer controlled potentiostat (Gamry Instruments, model: Reference 1000, software for data generation: Gamry Framework, version 7.03, software for data analysis: Gamry Echem Analyst version 7.03). The temperature stability of the molten salt was ± 2 °C. A fuzzy logic proportional–integral–derivative (PID) controller (Tempco, model: TEC-9100) was used for controlling the

temperature of the furnace using a type K (chromel-alumel) thermocouple. The thermocouple of the furnace was NIST calibrated. The temperature of the molten salt was measured by using a NIST calibrated K-type thermocouple shielded by an alumina tube (99.8% purity, Omega) and a digital thermometer (Omega, model HH91). The working electrode was a 2mm diameter tungsten rod (99.95%, Alfa Aesar). The counter electrode was a 4mm diameter glassy carbon rod. The reference electrode was an in-house made AgCl coated Ag wire (99.9%) placed in a borosilicate glass tube that contained LiCl+KCl eutectic thoroughly mixed with 1wt% AgCl (99.997%, ultra-dry). The working and counter electrodes were polished using a series of emery papers down to 2000 grit. The polished surface was wiped down with propanol and acetone and dried in a vacuum oven for 16h at 120 °C. The cleaning, and conditioning protocols were strictly followed for each set of experiments to ensure repeatability. After reaching the set temperature of 500 or 550 °C, the electrodes were conditioned in the open circuit potential for 15 minutes before starting the electrochemical tests. The electrodes were placed in an equidistance triangular arrangement. The surface area ratio of the counter and working electrodes was at least 2.5. The surface area was calculated by physically measuring the diameter and the immersion depth of the working in the molten salt after the experiments using an inch ruler with 32nd division tick marks. The measured depth was compared with the initial set value (typical variation after converting to cm was 0.5 – 0.75cm due to capillary effect). The surface area measured by geometric calculation is prone to error caused by meniscus of the molten salt, and salt built up layer. No effort was taken to address the errors introduced by the geometric surface area calculations which may vary from 7%–12%.

Yoon et al. proposed a relation between the Ag/AgCl reference potential and Cl₂/Cl⁻ potential that was a function of molar fraction of AgCl but independent of temperature between 723–823K and given as⁴⁴:

$$E_{\text{Cl}_2/\text{Cl}^-} = (-0.8726 \pm 0.00486) + (0.05896 \pm 0.00108) \ln(X) \quad (37)$$

Where X = mole fraction of AgCl. Accordingly, the Ag/AgCl potential of this study is -1.197V vs the redox potential of Cl₂/Cl⁻. CV was carried out at different potential windows and at different scan rates. All potentials in this paper are given with reference to the Ag/AgCl electrode whose potential is -1.197 V_{Cl₂/Cl⁻}. The maximum potential window signified decomposition of the LiCl-KCl eutectic by reduction of lithium at the cathodic end and chlorine evolution at the anodic end. Cyclic voltammetry studies were carried out at different scan rates from 100mVs⁻¹ to 2000Mv s⁻¹. Electrochemical impedance spectroscopy was carried out at the open circuit condition under potentiostatic conditions by super imposing an *ac* signal of 10mV by scanning the frequency from 10kHz to 0.1Hz. Square wave voltammetry was conducted between OCP and -2.5 V_{Ag/AgCl}; and between OCP and 1.2 V_{Ag/AgCl} at a frequency of 25Hz, pulse size of 25mV, step size of 1mV, and pulse time of 0.04s. All the electrochemical tests were either duplicated or triplicated to ensure reproducibility. The average values are presented.

4.2 Results and Discussions

Open Circuit Potential (OCP) Measurements

In the previous chapter, equilibrium measurement of tellurium in the molten salt with the surface of the tungsten and glassy carbon working electrode, at 450 °C was seen to shift the OCP to more positive potentials. This trend was also seen when the temperature was

increased to 500 °C to 550 °C which can be seen in Figure 19. Increase in the TeCl₄ concentration between the two temperatures will increase the exchange current density (i_0) by following the relation⁴⁵:

$$i_0 = nFk_0C_{Te^{4+}} \quad (38)$$

Where, n = number of electrons, F = Faraday's constant, k_0 = rate constant for electron transfer, and $C_{Te^{4+}}$ is bulk concentration of Te⁴⁺ in the molten salt. The increase in the i_0 value will shift the Tafel plots of the Teⁿ⁺/Te⁽ⁿ⁻¹⁾⁺ redox reactions such that the OCP could increase with the increase in the TeCl₄ concentration. It should be noted that the proposed Te⁴⁺/Te²⁺ redox couple is an example only. There are other possible redox reactions involving tetravalent Te. The standard redox potential of Te is reported to be more positive than that of Pd, Ag, Mo, W, and other transition metals^{15,45}. The positive OCP values observed on the tungsten electrode indicated that the tungsten had significant active sites to support the redox reactions. The shift in the OCP between 500 and 550 °C with the 1 wt% TeCl₄ addition is potentially due to a concentration difference between the two temperature that is caused by vapor loss as the temperature increased from 500 to 550 degrees.

Cyclic voltammetry:

A full window CV scan was performed from -2.8V to 1.4 V_{Ag/AgCl} as seen in Figure 20 – 22. The cyclic voltammogram of pure LiCl-KCl eutectic (without TeCl₄ addition) showed only one cathodic wave corresponding to lithium reduction that started at around -2.6 V_{Ag/AgCl} and an anodic wave associated with chlorine gas evolution that started around 1.2V. No other peaks were observed in between these two potentials on the tungsten electrode. The reduction

potentials of lithium reported in the literature vary widely from -2.35V to -2.6V . For example, Koyama et al. reported a value of $-2.353\text{ V}_{\text{Ag}/\text{AgCl}}$ at 723K for the $\text{Li(I)}/\text{Li(0)}$ reaction¹². On the other hand, Bermejo et al. showed lithium reduction occurring at $-2.6\text{ V}_{\text{Ag}/\text{AgCl}}$ at 723K using tungsten as a working electrode⁴⁶. Liu et al. also reported a similar potential of $-2.6\text{ V}_{\text{Ag}/\text{AgCl}}$ for reduction of lithium at 873K ⁴⁷.

Addition of TeCl_4 introduced several additional peaks both in the cathodic and anodic directions. The noise observed could be attributed to the droplets of Te formation on the counter or working electrodes due to crossover of the redox species because the electrodes were not compartmentalized by a micro-porous separator. Crossing of CV occurred at high anodic potentials (between 0.85 and 0.82V for $1\text{wt}\%$ TeCl_4 and $0.$) in all the TeCl_4 additions. Therefore, the crossing of CV was considered to be associated with polarizing the electrode to chlorine evolution potentials. Sakamura et al. attributed the anodic wave at 0.7V to the dissolution of Te in the form of Te^{2+} and formation of volatile TeCl_2 ⁴⁹. Generally, double crossing of CV during a reverse scan indicates deposition or adsorption of electroactive species that show nucleation over potential⁵⁰. However, in this case the crossing was attributed to oxidation of Te promoted by the Cl_2 that was adsorbed on the electrode surface. Without Cl_2 adsorption, no oxidation peak was observed during the reverse scan. Therefore, the proposed reaction steps were: $\text{Cl}_2 \rightarrow 2\text{ Cl}_{(\text{ads})}$; $2\text{ Cl}_{(\text{ads})} + 2\text{ e}^- \rightarrow 2\text{ Cl}^-$; $\text{Te} + 2\text{Cl}^- \rightarrow \text{TeCl}_2 + 2\text{ e}^-$ (anodic peak).

Figure 23 and Figure 24 shows cyclic voltammograms on tungsten electrode in the cathodic direction with and without addition of $1\text{wt}\%$ TeCl_4 containing LiCl-KCl eutectic at a smaller potential window. The peaks associated with Te species are clearly discerned in Figure 23 and

24 in comparison with the CV of LiCl-KCl eutectic without any addition of TeCl₄. Figure 25 illustrates the full window (both in the cathodic and anodic directions) CV of 1wt% TeCl₄ containing LiCl-KCl molten salt at different scan rates with a tungsten working electrode. The cathodic wave started at potential more negative than $-0.47 \text{ V}_{\text{Ag}/\text{AgCl}}$. Four distinct cathodic peaks were observed at around -0.515V (c_1), -0.998V (c_2), -1.92V ($500 \text{ }^\circ\text{C}$) and -2.02V ($550 \text{ }^\circ\text{C}$) (c_3), and 0.678 (c_4). During the reverse scan, five anodic peaks were recorded at -1.18V (a_1), -0.678V (a_2), -0.478V (a_3), 0.558V (a_4), and $1.11 \text{ V}_{\text{Ag}/\text{AgCl}}$ (a_5). The first cathodic wave (c_1) was attributed to the reduction of Te^{4+} to Te^{2+} , and the second cathodic wave (c_2) was due to reduction of Te^{2+} to Te^{1+} . A similar two step reduction reaction was proposed for Te^{4+} ions in the NaCl-2CsCl and 3LiCl-2KCl base molten salts at 823K¹⁶. It was observed that at scan rates of $200\text{--}1000\text{mVs}^{-1}$, the cathodic wave c_2 showed two peaks (c_2 and c_3) as seen in Figure 26. The cathodic wave (c_4) at a more negative potential was associated with formation of telluride ions (Te_x^{n-}). The number of electrons transferred could be determined from differential square wave pulse voltammetry, which will be discussed in a latter section. The anodic peaks a_1 , a_2 , a_3 , and a_4 were ascribed as the reverse reactions of cathodic peaks c_4 , c_3 , c_2 , and c_1 , respectively. The anodic wave (a_4) taking off at about 1.2V was associated with evolution of chlorine.

Figure 26 shows the cyclic voltammograms between OCP and $-2.2 \text{ V}_{\text{Ag}/\text{AgCl}}$ (more positive than the lithium reduction condition) comparing $500 \text{ }^\circ\text{C}$ and $550 \text{ }^\circ\text{C}$. The first cathodic wave (c_1) starting at -0.42V evolved clearly at a scan rate of 1Vs^{-1} and higher. The second cathodic wave (c_2) occurred with a peak current at around -0.762V . A slight shift in peak potential towards the positive direction was seen when the temperature was increased from $500 \text{ }^\circ\text{C}$ to $550 \text{ }^\circ\text{C}$. Additionally, upon doing the smaller windows, it can be seen that a third peak can be

seen around -1.17V for 500 °C and -1.07V for 550 °C. Assuming that the first cathodic wave is associated with a two-electron process, the α_c , transfer coefficient for cathodic reaction shall be estimated as 0.38. Furthermore, as the scan rate increased as seen in Figures 27 and 28, which represents a dependency of the peak potential indicating that the cathodic reaction was not reversible. However, the peak current increased as a function of square root of the scan rate, as seen in Figure 29. The cathodic peaks c_2 and c_3 were attributed to formation of zero valent Te on the working electrode. These cathodic peaks were associated with soluble-insoluble species, where soluble Te(II) species were reduced to insoluble Te(0) deposit. A cathodic wave shoulder starting at $-1.87 V_{Ag/AgCl}$ for 500 °C and $-1.8 V_{Ag/AgCl}$ for 550°C was attributed to the reaction: $nTe(0) + e^- \rightarrow Te_n^-$. This cathodic wave was associated with insoluble Te being converted to soluble Te^{2-} species. Since the CV was interrupted at $-2.2 V$ no lithium reduction and oxidation peaks were observed. The anodic waves (a_1, a_2) observed at about $(-1.27, -0.678) V_{Ag/AgCl}$ for 500 °C and $(-1.27, -0.622) V_{Ag/AgCl}$ for 550 °C were associated with the oxidation of soluble Te anionic species to Te(0). Sakamura et al. reported two anodic peaks at $-0.67, \text{ and } -0.5 V_{Ag/AgCl}$ in 0.19mol% Na_2Te containing LiCl-KCl molten salt at 500 °C corresponding to the following reactions (39) and (40) ⁴⁹.



It is noted that the peak potentials of anodic waves a_2 and a_3 were independent of the scan rates indicating reversibility of the reaction. A small peak (a_1) that is seen around $-1.3 V_{Ag/AgCl}$ could be brought on by Te^{2-} becoming only Te^- . Since this is unstable it bonds with another Te^- to form Te_2^- , while the majority of Te^{2-} undergoes reaction (39) which is marked as (a_2).

The anodic peaks observed at potentials more positive than 0.5 V_{Ag/AgCl} for 500 °C and 0.2 V_{Ag/AgCl} for 550 °C as seen in Figure 26 were due to the oxidation of Te to Te²⁺ and Te⁴⁺.

Oxidation of Te to volatile formation of the TeCl₂ has been:



The anodic peak observed at 0.56 V_{Ag/AgCl} was assigned to reaction (41), which is 0.64V more negative than the chlorine evolution potential. Lichtenstein et al. reported a similar value (0.71V negative to chlorine evolution potential) at 650 °C for the Te oxidation to Te²⁺¹⁸.

Figure 29 shows the linear relation observed between peak current density and the square root of the scan rate in 1wt% TeCl₄ containing LiCl-KCl eutectic at 500 °C and 550 °C using a tungsten electrode. Randles-Sevick equation describes the peak current density as a function of electrode surface area, bulk concentration of the redox species, and square root of the scan rate and diffusivity of redox species⁵¹. The diffusion coefficient can be calculated from the Randles-Sevick relation as given in (42):

$$D^{1/2} = \left[\frac{i_p}{\sqrt{v}} \right] \left(\frac{1}{0.446nFAC_0} \right) \left(\frac{RT}{nF} \right)^{0.5} \quad (42)$$

Where i_p/\sqrt{v} is the slope of peak current vs. square root of scan rate, A is the surface area of electrode, and C₀ is the concentration of the Te species. Using the slopes taken from Figure 29 the diffusion coefficients of Te⁴⁺ could be calculated for the two different temperatures. The peak current of soluble-insoluble redox species can be expressed as a function of \sqrt{v} and \sqrt{D} using the Berzins and Delahay relation⁵²:

$$i_p = 0.611 nFAC_0 \left(\frac{nF\theta D}{RT} \right)^{1/2} \quad (43)$$

The bulk concentration of TeCl_4 retained in the molten salt after two hours of thermal equilibrium was considered to calculate the diffusivities from the slope of the i_p vs \sqrt{v} plots. The number of electrons (n) involved in the reduction reaction was calculated from the square wave voltammetry data as shown in Figure 30 and Figure 31 by determining the width of half current peak ($W_{1/2}$) and using the relation^{53,54}:

$$n = 3.5 RT/(W_{1/2}F) \quad (44)$$

Alternately, the number of electrons for reversible soluble-soluble redox system can also be calculated from the CV data using the relations (45) and (46) proposed by Matsuda and Ayabe⁵⁵:

$$E_{p,c} = E_{1/2} - 1.11 \frac{RT}{nF} \quad (45)$$

$$E_{p,a} = E_{1/2} + 1.11 \frac{RT}{nF} \quad (46)$$

Where $E_{p,c}$ and $E_{p,a}$ are cathodic and anodic peak current potentials, respectively; $E_{1/2}$ is a half wave potential and expressed as:

$$E_{1/2} = E_{\text{Te}^{4+}/\text{Te}^{2+}}^0 + \frac{RT}{nF} \text{Ln} \left(\frac{\gamma_{\text{Te}^{4+}}}{\gamma_{\text{Te}^{2+}}} \right) + \frac{RT}{nF} \text{Ln} \left(\frac{\sqrt{D_{\text{Te}^{2+}}}}{\sqrt{D_{\text{Te}^{4+}}}} \right) \quad (47)$$

Formal potential for soluble-soluble system, E^{0*} is expressed as⁵⁶:

$$E_{\text{Te}^{4+}/\text{Te}^{2+}}^{0*} = E_{\text{Te}^{4+}/\text{Te}^{2+}}^0 + \frac{RT}{nF} \text{Ln} \left(\frac{\gamma_{\text{Te}^{4+}}}{\gamma_{\text{Te}^{2+}}} \right) \quad (48)$$

$$E_{\text{Te}^{4+}/\text{Te}^{2+}}^{0*} = \left(\frac{E_{p,a} + E_{p,c}}{2} \right) - \frac{RT}{nF} \text{Ln} \left(\frac{\sqrt{D_{\text{Te}^{2+}}}}{\sqrt{D_{\text{Te}^{4+}}}} \right) \quad (49)$$

Formal potential for reversible soluble-insoluble (Te/Te^{2-} , Te^{2+}/Te) system can be expressed as^{18,56}:

$$E_{p,1a} = E_{\text{Te}^{0}/\text{Te}^{2-}}^{0*} + \frac{0.854RT}{nF} - \frac{RT}{nF} \ln(C_{\text{Te}^{2-}}) \quad (50)$$

$$E_{p,1c} = E_{\text{Te}^{2+}/\text{Te}^0}^{0*} - \frac{0.854RT}{nF} + \frac{RT}{nF} \ln(C_{\text{Te}^{2+}}) \quad (51)$$

Table VI and Table VII summarizes the results of square wave voltammograms (SWV) given in Figures 30 and 31 and the number of electrons calculated based on the full width half wave of the differential current peaks using the expression given in (44). The peak potentials of different reduction reactions are listed which could be correlated to the formal potentials described in the expressions (48) to (51). The SWV data indicated that the cathodic peaks observed between -0.2 to -1.1V in the CV could be assigned to the three-step reduction process of $\text{Te}(\text{IV})$ to $\text{Te}(0)$. The three-step process reported in this investigation is different from the two-step process commonly reported in KCl-AlCl_3 melts at $300\text{ }^\circ\text{C}$ ⁵². The number of electrons calculated from the SWV data was used for estimation of the diffusivity of species based on the slopes of i_p vs $\sqrt{\nu}$ plots given in Figure 29. Table VIII lists the coefficient of diffusion of Te^{4+} species in two different temperatures at 500 and $550\text{ }^\circ\text{C}$. Even though a quasi-reversible type reaction was observed, the diffusivity can be estimated based on the Randles–Sevcik equation or Berzins and Delahay relation. Similar approach has been reported by other researchers for calculating the diffusivities of lanthanide ions in the LiCl-KCl eutectic^{51,57}. Bermejo et al. reported that the corrections required for cylindrical geometry of the working electrode can be neglected to use the semi-infinite relations assumed for the Randles–Sevcik (Eq. 41) or Berzins-Delahay (Eq. 42) relation when the scan rate is higher

than 50mV s^{-1} . The diffusivity values, in turn, were used for the estimation of formal potentials based on the relation (49). The formal potentials were determined based on the CV data using the relations (49) (51) and summarized in Table IX.

Table VI. Summary of the square wave voltammogram data of tungsten electrode in 1wt% TeCl_4 containing LiCl-KCl at 500 °C.

Peak ID	Peak potential, $V_{\text{Ag}/\text{AgCl}}$	Width at half peak, $(W_{1/2}), \text{V}$	Number of electrons	Reaction step
1	-0.323	-0.273	2.01	$\text{Te}^{4+} + 2\text{e}^- \rightarrow \text{Te}^{2+}$
2	-0.463	-0.463	1	$\text{Te}^{2+} + \text{e}^- \rightarrow \text{Te}^+$
3	-0.63	-0.465	1	$\text{Te}^+ + \text{e}^- \rightarrow \text{Te}(0)$
4	-2	-0.14	1.8	$\text{Te}(0) + 2\text{e}^- \rightarrow \text{Te}^{2-}$

Table VII. Summary of the square wave voltammogram data of tungsten electrode in 1wt% TeCl_4 containing LiCl-KCl at 550 °C.

Peak ID	Peak potential, $V_{\text{Ag}/\text{AgCl}}$	Width at half peak, $(W_{1/2}), \text{V}$	Number of electrons	Reaction step
1	-0.43	-0.211	1.2	$\text{Te}^{4+} + \text{e}^- \rightarrow \text{Te}^{3+}$
2	-0.596	-0.085	2.9	$\text{Te}^{3+} + 3\text{e}^- \rightarrow$

Peak ID	Peak potential, $V_{Ag/AgCl}$	Width at half peak, $(W_{1/2}), V$	Number of electrons	Reaction step
				Te(0)
3	-1.93	-0.14	1.8	Te(0) + 2e ⁻ → Te ²⁻

Table VIII. Diffusivities of Te species in LiCl-KCl eutectic at 500 and 550 °C.

Working Electrode	Temperature, °C	Initial concentration of TeCl ₄ , wt%	Diffusing species	Coefficient of diffusion, cm ² /s
Tungsten	500	1wt% (actual 0.89%)	Te ⁴⁺	9.36×10^{-5}
	550	1 wt% (actual ~1%)	Te ⁴⁺	8.43×10^{-5}

Table IX. Formal potentials of LiCl-KCl-TeCl₄ system at 500 and 550 °C using tungsten working electrode.

Temperature, °C	Reaction	Formal potential in 1wt% TeCl ₄ , $V_{Ag/AgCl}$
500	Te ⁴⁺ + 2e ⁻ → Te ²⁺	-0.412
	Te ²⁻ → 2e ⁻ + Te ⁰	-0.567

Temperature, °C	Reaction	Formal potential in 1wt% TeCl ₄ , V _{Ag/AgCl}
550	$\text{Te}^{4+} + \text{e}^{-} \rightarrow \text{Te}^{3+}$	-0.151
	$\text{Te}^{2-} \rightarrow 2\text{e}^{-} + \text{Te}^0$	-0.483

The diffusivity of Te^{4+} in LiCl-KCl eutectic decreased with an increase in the Temperature of the salt mixture. In the previous chapter as the concentration increased the diffusivity decreased. The same can be seen when comparing diffusivity between 500 and 550 °C. From the concentration analysis, it was seen that 550 °C retained more of the Te^{4+} in the solution than at 500 °C. Due to this, there would be a greater quantity of Te^{4+} at 550 °C to bond with chloride ions to form TeCl_6^{2-} which could attribute to the decrease in diffusivity. A similar order of magnitude ($0.54 \times 10^{-5} \text{ cm}^2 \text{ s}^{-1}$) diffusivity was reported for Ce(III) in LiCl-KCl at 723K by Yoon and Phongikharoon⁵⁷. The diffusivity of Te^{4+} was estimated to be an order of magnitude higher than that of Te^{4+} in a given experimental condition. Recently, Lichtenstein et al. reported that the diffusivity of Te^{2-} in 0.07mol% Li_2Te containing LiCl-KCl at 650 °C as $0.73 \times 10^{-5} \text{ cm}^2 \text{ s}^{-1}$ ¹⁸. These authors also reported a decrease in the diffusivity as the mol% of Li_2Te increased to 0.32%. However, the diffusivity reportedly increased when the Li_2Te increased to 0.34 mol%.

Table IX summarizes the formal potentials for different reduction reactions. The formal potentials of Te(IV) reduction reaction and Te^{2-} oxidation reaction shifted in the positive direction with an increase in temperature. This trend was also seen for the formal potential of Te^{4+} reduction shifted in the positive direction with increase in temperature. Bodewig and Plambeck reported the oxidation potential of Te ($\text{Te} \rightarrow \text{Te}^{2+} + 2\text{e}^{-}$) to be -0.45V Vs Cl_2/Cl in

LiCl-KCl at 400 °C which is about 0.74 V_{Ag/AgCl}²¹. Probably, this potential corresponds to the reaction: $\text{Te} + 2\text{Cl}^- \rightarrow \text{TeCl}_2 + 2\text{e}^-$ as discussed by Lichtenstein et al¹⁸. These authors observed an anodic peak of the Te^{2-} oxidation at 1.94 V_{Li/Li+} and take-off of the oxidation reaction at 1.65 V_{Li/Li+} which corresponds to about -0.86 V_{Ag/AgCl}. The estimated formal potential of the Te^{2-} oxidation of this study closely follows the reported values¹⁸.

Electrochemical impedance spectroscopy:

Figures 32 and Figures 33 show the EIS of the tungsten electrode in 1wt% TeCl_4 at 500 °C and 550 °C potentials in the forms of Nyquist and Bode plots, respectively. These figures are based on open circuit conditions. The Bode plots in Figure 32a gave a slightly different trend, than was seen in Figure 33a for 550 °C. The impedance modulus for 550 °C was higher than at 500 °C for open circuit potentials.

The rationale behind carrying out EIS measurements was to understand the structural characteristics of the molten salts with and without addition of TeCl_4 . The physical and electrical properties of the molten salt systems depend on the structure and interactions of the constituents. The structural arrangements that are present in molten salts can be viewed as intermediates between discrete chemical bonds and periodic crystalline lattices⁶⁰. The interatomic interactions determine the local ordering of the molten salt. The electrochemical properties are influenced by the structural characteristics of the molten salt. When cations are present in the molten salt with different sizes and different charge densities, an asymmetric polarization of anions is anticipated which affects the electrostatic stability of the mixture⁶¹.

In order to better understand the interfacial impedance behavior, the EIS data were fitted into an electrical equivalent circuit (EEC) and the values are shown in Table X. In general, the impedance spectra showed only one time constant. Therefore, the EIS data was modeled using 1 R || \emptyset loops. In the equivalent circuit, R_u and R_p represent the electrolyte resistance and resistance to charge transfer, while the \emptyset (Y is used as a substitute) symbol represents a double layer also known as an imperfect capacitor, respectively. The R_1 - Y_1 loop represents the electrode/LiCl-KCl electrolyte interface. Y_1 represents imperfect capacitance whose impedance (Z) is given by the relation: $Z = 1/[(Q_0 \omega^n)] * e^{-(\pi/2)ni}$ where ω = frequency, and the exponent “n” represents the surface heterogeneity or continuously distributed time constants for charge transfer when $0 < n < 1$.³³ W_d represents a diffusion limited charge transfer resistance (Warburg component), respectively that are associated with the redox species other than LiCl-KCl. It should be noted that the values of Y_0 and W_f are expressed as admittance. Smaller magnitudes of R_u and R_p , and larger values of Y_0 and W_d will lead to better charge transfer characteristics.

Table X. EIS circuit component values of LiCl-KCl-TeCl₄ system at open circuit potentials for 500 °C and 550 °C using tungsten working electrode.

Temperature, °C	Circuit Component	Circuit Component Value
500	R_u	$485 \cdot 10^{-3} \Omega$
	Y_0	$327.4 \cdot 10^{-3} S \cdot s^a$
	α	$860 \cdot 10^{-3}$

Temperature, °C	Circuit Component	Circuit Component Value
	W_d	$237.1 \cdot 10^{-3} \text{ S} \cdot \text{s}^{1/2}$
	R_p	5.026 Ω
550	R_u	$455.2 \cdot 10^{-3} \Omega$
	Y_0	$12.05 \cdot 10^{-3} \text{ S} \cdot \text{s}^a$
	α	$720.1 \cdot 10^{-3}$
	W_d	$148.7 \text{e}^{-3} \text{ S} \cdot \text{s}^{1/2}$
	R_p	44.17 Ω

The solution resistance was approximately the same between 500 and 550 °C. The charge transfer resistance was given as R_p at high frequencies because the resistance due to the constant phase element would be negligible. The impedance due to the constant phase elements became significant only below 10Hz as seen from the Bode plots. As temperature increased, the capacitance due to Y_0 decreased along with its time constant. This could be attributed to increased concentration of Te ions at the electrode/molten salt interface that were present in the OCP condition at 550 °C than 500 °C. The Warburg diffusion component was present in both temperature ranges. However, it was seen to have a higher value at 500 °C.

An EEC model consisting of two parallel RC loops connected in series, and each RC loop having a Warburg element was proposed to describe the impedance behavior of LiCl-KCl molten salt at 700 °C–800 °C by Cohen et al ⁶¹. The reported values of solution resistance

(Rs), double layer capacitance (Q_1), capacitance due to adsorption of ions (Q_2), and Warburg coefficient were reported as 0.685 ohm, 58–80 μF , 1.8–2.3 mF, and 2–4 mS, respectively⁶². The EIS data of this study was fitted with a different EEC model but the values of the solution resistance circuit components showed almost similar order of magnitude as Kim et al.⁶³ reported EIS data of a molybdenum electrode in LiCl-KCl- UCl_3 at 773K and fitted their data to an EEC similar to the one used in this work and the values of the circuit components showed a similar order of magnitude as reported in this work. While the capacitance values due to charged layer had a higher value in this study than the one reported by Kim et al.

Most of the literature on pyroprocessing of used nuclear fuels focuses on the electrochemical behaviors of fission product as cations such as La^{3+} , Nd^{3+} , Sm^{3+} etc.⁶⁴ Not much information is available on the anion type fission products such as Te^{2-} and I^- . It is generally assumed that anions present in the molten salt may not interfere with the cathodic reduction of actinides. This study attempts to fill the knowledge gap and shows that Te^{2-} will be oxidized to $\text{Te}(0)$ and Te^{n+} during the pyroprocessing conditions and adversely affect the stability of the electrodeposits because of the low melting point of Te and volatility of TeCl_n compounds. The electrochemical data presented in this work such as formal potentials of different Te species (Te^{2-} and Te^{4+}) and their diffusivities are useful in designing more efficient pyrochemical processes.

4.3 Conclusions

The reduction of Te^{4+} to $\text{Te}(0)$ occurred in three steps. The formal potential of $\text{Te}(\text{IV})$ reduction to $\text{Te}(\text{II})$ was estimated as -0.412 VAg/AgCl for 500 °C, which was observed to be a two-electron reaction step. For 550 °C Te^{4+} had only gone through a one-electron step

process to Te^{3+} . For 500 °C Te(II) reduced to Te(0) in two steps with one electron reaction at each step. The reduction to Te(0) completed at around $-0.63 \text{ V}_{\text{Ag}/\text{AgCl}}$. Formation of Te^{2-} was observed at potentials around $-2 \text{ V}_{\text{Ag}/\text{AgCl}}$. At 550 °C Te(II) reduced to Te(0) in a single step with a three-electron reaction. The reduction to Te(0) completed at around $-0.596 \text{ V}_{\text{Ag}/\text{AgCl}}$. Formation of Te^{2-} was observed at potentials around $-1.93 \text{ V}_{\text{Ag}/\text{AgCl}}$. The redox process of $\text{Te}^{4+}/\text{Te}^{2-}$ system was observed to be quasi-reversible.

The diffusion coefficients of Te^{4+} were 9.36×10^{-5} (500 °C) and 8.43×10^{-5} (550 °C) cm^2s^{-1} , respectively in the 1wt% TeCl_4 electrolyte.

The electrochemical impedance spectroscopic data could be fitted with an equivalent circuit representing a resistor in series with a 1 loop $\text{R}||\text{CPE}$. Diffusion limited impedance was observed at OCP for both 500 and 550 °C. The charge transfer resistance showed a slight decrease with an increase in temperature.

Chapter 5: Electrochemical Behavior of ReCl_3 in LiCl-KCl Eutectic Molten Salt at 450 to 550 °C

5.1 Experimental Procedure

Due to the hygroscopic nature of the LiCl-KCl eutectic salt, all experiments were performed in a glove box (MBraun) under an inert argon environment. Oxygen and moisture levels were maintained less than 2 ppm. The eutectic salt was created by thoroughly mixing 44.6wt% LiCl (99.995%, ultra-dry) with 55.4wt% KCl (99.998%, ultra- dry). Once the eutectic salt is created, 1 wt% ReCl_3 was placed in a mortar and mixed for 5 minutes with the eutectic salt to make sure the solution was homogenized. Afterward, the completed mixture was placed in an alumina crucible and brought to operating temperatures of 450 – 550 °C. All chemicals were procured from Alfa Aesar and used without further purification.

The concentration of ReCl_3 retained in the molten salt was determined by using induction coupled plasma- mass spectroscopy (ICP-MS) technique. The sampling of salt for ICP-MS analysis was carried out by dipping a tungsten rod in the molten salt at 1 hour intervals, ranging from when operating temperature was reached up to 4 hours. Solidified salt was scrapped off the rod using a stainless-steel spatula. The weight of each sample was measured using an analytical balance (Radwag, XA110/2X) capable of measuring a minimum weight of 1mg with a resolution of 0.01mg and dissolved in 30ml of 1% nitric acid. Three samples were extracted per condition. The ICP-MS analysis of Re was performed at the Analytical Sciences Laboratory of University of Idaho by following a comprehensive quality management plan that maintains compliance with applicable standards of ISO 17025. The concentration of Re retained in the molten salt was analyzed as a function of time after temperature equilibration.

Table XI summarizes ReCl_3 concentration retained in the molten salt as a function of time after temperature equilibration. A trend was seen with the first few samples taken at each temperature. Analysis showed that the initial hour samples had a higher concentration than what was calculated, followed by the remaining time intervals showing a loss in the quantity of Re present in the salt. This could be due to the change in density of the salt mixture as the salt reaches equilibrium over the course of time the samples are taken. During the first few hours samples are collected, there is potentially a greater concentration of Re closer to the bottom and middle of the solution where samples are collected. As time progresses, the Re is potentially rising more to the surface of the solution due to potential vapor pressure difference between ReCl_3 and the eutectic salt as seen with TeCl_4 . Thus, resulting in a higher concentration seen at the beginning of sample collections, followed by a loss towards the end of the time window. The electrochemical results are discussed with reference to the initial addition amount for brevity.

Table XI. ICP-MS analyses of ReCl_3 retained in the LiCl-KCl molten salt as a function of time for 450 to 550 °C.

Initial addition of ReCl_3	Dwelling time at 450 °C, h	ReCl_3 retained in the molten salt, %
1wt%	0	104.24
	1	149.78

	2	126.45
	3	83.43
	4	61.09
Initial addition of ReCl₃	Dwelling time at 500 °C, h	ReCl₃ retained in the molten salt, %
1 wt%	0	196.76
	1	152.86
	2	70.44
	3	56.5
	4	48.68
Initial addition of ReCl₃	Dwelling time at 550 °C, h	ReCl₃ retained in the molten salt, %
1 %	0	170.95
	1	115.42

	2	74.12
	3	45.18
	4	71.12

Open circuit potential measurement, electrochemical impedance spectroscopy (EIS), cyclic voltammetry, and square wave voltammetry, were performed in LiCl+KCl eutectic melt at 450 to 550 °C with and without addition of 1 wt% ReCl₃ by using a computer controlled potentiostat (Gamry Instruments, model: Reference 1000, software for data generation: Gamry Framework, version 7.03, software for data analysis: Gamry Echem Analyst version 7.03). The temperature stability of the molten salt was ± 2 °C. A fuzzy logic proportional–integral–derivative (PID) controller (Tempco, model: TEC-9100) was used for controlling the temperature of the furnace using a type K (chromel–alumel) thermocouple. The thermocouple of the furnace was NIST calibrated. The temperature of the molten salt was measured by using a NIST calibrated K-type thermocouple shielded by an alumina tube (99.8% purity, Omega) and a digital thermometer (Omega, model HH91). The working electrode was a 2mm diameter molybdenum rod (99.95%, Alfa Aesar). The counter electrode was a 4mm diameter glassy carbon rod. The reference electrode was an in-house made AgCl coated Ag wire (99.9%) placed in a borosilicate glass tube that contained LiCl+KCl eutectic thoroughly mixed with 1wt% AgCl (99.997%, ultra-dry). The working and counter electrodes were polished using a series of emery papers down to 2000 grit. The polished surface was wiped down with propanol and acetone and dried in a vacuum oven for 16h at 120 °C. The cleaning,

and conditioning protocols were strictly followed for each set of experiments to ensure repeatability. After reaching the set temperature of 450 to 550 °C, the electrodes were conditioned in the open circuit potential for 15 minutes before starting the electrochemical tests. The electrodes were placed in an equidistance triangular arrangement. The surface area ratio of the counter and working electrodes was at least 2.5. The surface area was calculated by physically measuring the diameter and the immersion depth of the working in the molten salt after the experiments using an inch ruler with 32nd division tick marks. The measured depth was compared with the initial set value (typical variation after converting to cm was 0.5 – 0.75cm due to capillary effect). The surface area measured by geometric calculation is prone to error caused by meniscus of the molten salt, and salt built up layer. No effort was taken to address the errors introduced by the geometric surface area calculations which may vary from 7%–12%.

Yoon et al. proposed a relation between the Ag/AgCl reference potential and Cl₂/Cl⁻ potential that was a function of molar fraction of AgCl but independent of temperature between 723–823K and given as⁴⁴:

$$E_{\text{Cl}_2/\text{Cl}^-} = (-0.8726 \pm 0.00486) + (0.05896 \pm 0.00108) \ln(X) \quad (52)$$

Where X = mole fraction of AgCl. Accordingly, the Ag/AgCl potential of this study is -1.197V vs the redox potential of Cl₂/Cl⁻. CV was carried out at different potential windows and at different scan rates. All potentials in this paper are given with reference to the Ag/AgCl electrode whose potential is -1.197 V_{Cl₂/Cl⁻}. The maximum potential window signified decomposition of the LiCl-KCl eutectic by reduction of lithium at the cathodic end and

chlorine evolution at the anodic end. Cyclic voltammetry studies were carried out at different scan rates from 100mVs^{-1} to 2000Mv s^{-1} . Electrochemical impedance spectroscopy was carried out at the open circuit condition under potentiostatic conditions by super imposing an *ac* signal of 10mV by scanning the frequency from 10kHz to 0.1Hz . Square wave voltammetry was conducted between OCP and $-2.5 V_{\text{Ag}/\text{AgCl}}$; and between OCP and $1.2 V_{\text{Ag}/\text{AgCl}}$ at a frequency of 25Hz , pulse size of 25mV , step size of 1mV , and pulse time of 0.04s . To obtain (SWV) better resolution for calculating electron transfer and rate of diffusion, SWV at $5\text{ wt}\%$ ReCl_3 was used for 500 and $550\text{ }^\circ\text{C}$. All the electrochemical tests were either duplicated or triplicated to ensure reproducibility.

5.2 Results and Discussion

Open circuit potentials (OCP) measurements:

The purpose of OCP measurement is to understand the equilibrium conditions of various redox species present in the molten salt with the surface of the working electrode, which is molybdenum. Figure 34 shows the OCP of molybdenum as working electrode in $\text{LiCl}+\text{KCl}$ eutectic with addition of $1\text{ wt}\%$ of ReCl_3 . As the temperature of ReCl_3 increased from 450 to $500\text{ }^\circ\text{C}$ the OCP shifted to more positive potentials, followed by a shift to more negative potentials at $550\text{ }^\circ\text{C}$. Even though the OCP shifted to more negative potentials compared to 450 and $500\text{ }^\circ\text{C}$, it was still at a more positive potential than eutectic salt with no ReCl_3 as seen in Figure 35. A reason for $550\text{ }^\circ\text{C}$ OCP being more negative could be due to the loss of some of the ReCl_3 as vapors to the environment at these temperatures. Due to the difference in concentration levels at each temperature, OCP value can shift based on the exchange current density (i_0) by following the relation⁴⁵:

$$i_0 = nFk_0C_{Re^{3+}} \quad (53)$$

Where, n = number of electrons, F = Faraday's constant, k_0 = rate constant for electron transfer, and $C_{Re^{3+}}$ is bulk concentration of Re^{3+} in the molten salt. The increase in the i_0 value will shift the Tafel plots of the $Re^{n+}/Re^{(n-1)+}$ redox reactions such that the OCP could increase or decrease with a change in the $ReCl_3$ concentration. The standard redox potential of Re is reported to be more positive than that of Pd, Ag, Mo, W, and other transition metals⁴⁵.

Cyclic voltammetry:

A full window CV scan was performed from $-2.8V$ to $1.4 V_{Ag/AgCl}$ as seen in Figure 35. The cyclic voltammogram of pure LiCl-KCl eutectic (without $ReCl_3$ addition) showed only one cathodic wave corresponding to lithium reduction that started at around $-2.6 V_{Ag/AgCl}$ and an anodic wave associated with chlorine gas evolution that started around $1.2V$. No other peaks were observed in between these two potentials on the molybdenum electrode. The reduction potentials of lithium reported in the literature vary widely from $-2.35V$ to $-2.6V$. For example, Koyama et al. reported a value of $-2.353 V_{Ag/AgCl}$ at $723K$ for the $Li(I)/Li(0)$ reaction¹². On the other hand, Bermejo et al. showed lithium reduction occurring at $-2.6 V_{Ag/AgCl}$ at $723K$ using tungsten as a working electrode⁴⁶. Liu et al. also reported a similar potential of $-2.6 V_{Ag/AgCl}$ for reduction of lithium at $873K$ ⁴⁷.

Addition of $ReCl_3$ introduced several additional peaks both in the cathodic and anodic directions.

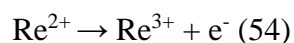
Figure 36 shows cyclic voltammograms on molybdenum electrode in the cathodic direction with and without addition of 1wt% $ReCl_3$ containing LiCl-KCl eutectic at a smaller potential

window. The peaks associated with Re species are clearly discerned in Figure 36 in comparison with the CV of LiCl-KCl eutectic without any addition of ReCl_3 . Figures 37 to 39 illustrates the full window (both in the cathodic and anodic directions) CV of 1wt% ReCl_3 containing LiCl-KCl molten salt at different scan rates with a molybdenum working electrode. The cathodic wave started at potential more negative than $-0.02 \text{ V}_{\text{Ag}/\text{AgCl}}$. Three distinct cathodic peaks were seen for each temperature range. For $450 \text{ }^\circ\text{C}$ these peaks were observed at around -0.202V (c_1), -1.67V (c_2), and -2.79V (c_3). At $500 \text{ }^\circ\text{C}$ they were seen around -2.02V (c_1), -2.14V (c_2), and -2.79V (c_3). For $550 \text{ }^\circ\text{C}$ the peaks were seen around -1.79V (c_1), -2.02V (c_2), and -2.79V (c_3). During the reverse scan for $450 \text{ }^\circ\text{C}$ and $500 \text{ }^\circ\text{C}$, 4 anodic peaks were recorded. However, $550 \text{ }^\circ\text{C}$ saw an additional fifth peak arise between lithium reduction and chlorine gas evolution. The anodic peaks for $450 \text{ }^\circ\text{C}$ were seen at -2.21V (a_0), -0.642V (a_1), 0.638V (a_2), and $1.3\text{V}_{\text{Ag}/\text{AgCl}}$ (a_3). For $500 \text{ }^\circ\text{C}$ the peak potentials were seen at -2.27V (a_0), -1.67 (a_1), -0.65V (a_2), and $1.06\text{V}_{\text{Ag}/\text{AgCl}}$. At $550 \text{ }^\circ\text{C}$ their following potential values were seen at -2.14V (a_0), -1.46V (a_1), -0.99V (a_2), -0.57 (a_3), and $0.79\text{V}_{\text{Ag}/\text{AgCl}}$. In a study performed by Bailey et al., saw that when Re(III) was present in LiCl-KCl it disproportionated into Re(IV) and Re(0) ⁶⁵. Due to this the first cathodic peak that is denoted by (c_1) at $450 \text{ }^\circ\text{C}$ was attributed to the reduction of Re^{4+} to Re^{2+} , and the second cathodic wave (c_2) was due to reduction of Re^{2+} to Re^+ . However, the (c_1) peak for both $500 \text{ }^\circ\text{C}$ and $550 \text{ }^\circ\text{C}$ seen in Figures 38 and 39, did not arise until more negative potentials than (c_1) at $450 \text{ }^\circ\text{C}$. This could potentially be due to a higher quantity of Re(III) that disproportionated to Re(0) . For this reason a peak was not noticeable in the full window cyclic voltammetry until Re(0) was reduced to Re^{2-} . This 2-step electron transfer differs from what is seen in most literature. In one study by Danilov et al. saw Re(IV) in $3\text{LiCl}-2\text{KCl}$ molten salt at $500 \text{ }^\circ\text{C}$

being reduced to Re(III), followed by Re(III) being reduced to Re metal⁶⁶. In another study by E.M. Hondrogiannis et al., they saw $[\text{Re}_2\text{Cl}_8]^{2-}$ in $\text{AlCl}_3\text{-NaCl}_{\text{sat}}$ at 175 °C undergo a single electron transfer step to $[\text{Re}_2\text{Cl}_8]^{3-}$ ⁶⁷. It was observed that at scan rates of 1000–2000 mVs^{-1} , the cathodic wave c_1 showed two peaks (c_1 and c_2) as seen in Figure 38 and Figure 39. The cathodic wave (c_2) at a more negative potential for all temperature ranges was associated with formation of Re(0) to Re_x^{n-} states. The number of electrons transferred could be determined from differential square wave pulse voltammetry, which will be discussed in a latter section. The cathodic wave c_3 , which was observed to take off at around $-2.5 \text{ V}_{\text{Ag}/\text{AgCl}}$ was attributed to reduction of lithium. The anodic peaks a_0 , a_1 , a_2 , and a_3 were ascribed as the reverse reactions of cathodic peaks c_3 , c_2 , and c_1 , respectively. The anodic wave following anodic peak (a_3) or (a_4) that started taking off around 1.2V was associated with evolution of chlorine.

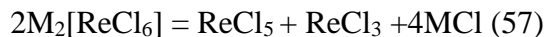
Figures 40 - 42 shows the cyclic voltammograms between OCP and $-2 \text{ V}_{\text{Ag}/\text{AgCl}}$ (more positive than the lithium reduction condition) at different scan rates in 1wt% ReCl_3 containing LiCl-KCl using molybdenum as a working electrode. The first cathodic wave (c_1) starting at -0.17V for 450 °C evolved clearly at a scan rate of 1Vs^{-1} and higher. For 500 and 550 °C the first cathodic wave was seen at -2.03 and -1.77V were clearly seen at a scan rate of 1Vs^{-1} and higher. The second cathodic wave (c_2) occurred with a peak current at around -1.67V for 450 °C, while for 500 °C and 550 °C was seen at -2.15 and -2.02V . The peak potential shifted in the negative direction with the increase in the scan rate. The peak shift per decade of the scan rate was observed to be about 0.19V, which is almost equal to the magnitude of $2.3RT/\alpha_c nF$. Assuming that this cathodic wave is associated with a two-electron process, the α_c , transfer coefficient for cathodic reaction shall be estimated as 0.38. The scan rate dependency of the peak potential indicated that the cathodic reaction was not reversible. However, the peak

current increased as a function of square root of the scan rate, as seen in Figure 43. The cathodic peaks c_1 and c_2 for 500 °C and 550 °C were attributed to formation of zero valent Re to Re^n . These cathodic peaks were associated with soluble-insoluble species, where insoluble Re(IV) species were reduced to soluble Re(0) deposit. A cathodic wave shoulder starting at $-1.5 \text{ V}_{\text{Ag}/\text{AgCl}}$ for 450 °C, $-1.69 \text{ V}_{\text{Ag}/\text{AgCl}}$ for 500 °C, and $-1.46 \text{ V}_{\text{Ag}/\text{AgCl}}$ for 550 °C was attributed to the reaction: $n\text{Re}(0) + e^- \rightarrow \text{Re}_n^-$. This cathodic wave could potentially be associated with soluble Re being converted to soluble Re^{2-} species. Since the CV was interrupted at -2 V no lithium reduction and oxidation peaks were observed. The anodic waves (a_1 , a_2) observed at about -1.44 and $-0.66 \text{ V}_{\text{Ag}/\text{AgCl}}$ for 450 °C were associated with the oxidation of soluble Re anionic species to Re(0). The corresponding anodic peaks for 500 °C seen at -1.37 and $-0.54 \text{ V}_{\text{Ag}/\text{AgCl}}$ were associated with the same anodic reaction as 450 °C. At 500 °C a third anodic peak was seen at a potential of -0.47 V , resulting in the Re(0) potentially being further oxidized to Re(IV). Loiseau et al. reported three anodic peaks at -1.078 , 0.151 , and $0.972 \text{ V}_{\text{Ag}/\text{AgCl}}$ in $0.1 \text{ M NBu}_4\text{ClO}_4\text{-DMF}$ at room temperature using a double junction saturated calomel reference electrode that corresponded to the following reactions (54), (55), and (56)⁶⁸.



The anodic peaks observed at potentials more positive than $0.3 \text{ V}_{\text{Ag}/\text{AgCl}}$ before reaching chlorine evolution were attributed to the oxidation of Re^{3+} to Re^{4+} as seen in full potential

windows shown in Figures 37 to 39 Potentially, oxidation of Re(III) could form a volatile formation of ReCl_5 through the following reaction:



This reaction was seen in one study done by Danilov et al.⁶⁶ This could occur at the anodic peak observed at -0.69 V for 450 °C, -0.52V for 500 °C, and -0.47V_{Ag/AgCl} for 550 °C was assigned to reaction (56). Additionally, if Re(V) is formed during oxidation as was seen in the study that Loiseau et al. saw in their cyclic voltammograms it could also form volatile ReCl_5 ⁶⁸.

Figure 43 shows the linear relation observed between peak current density and the square route of the scan rate in 1wt% ReCl_3 containing LiCl-KCl eutectic at 450 to 550 °C at peak denoted as (c₁) using a molybdenum electrode. Randles-Sevick equation describes the peak current density as a function of electrode surface area, bulk concentration of the redox species, and square root of the scan rate and diffusivity of redox species⁵¹. The diffusion coefficient can be calculated from the Randles-Sevick relation as given in (58):

$$D^{1/2} = \left[\frac{i_p}{\sqrt{v}} \right] \left(\frac{1}{0.446nFAc_0} \right) \left(\frac{RT}{nF} \right)^{0.5} \quad (58)$$

Where i_p/\sqrt{v} is the slope of peak current vs square root of scan rate, A is the surface are of electrode, and C_0 is the concentration of the Re species. Using the slopes taken from Figure 43 the diffusion coefficients of Re^{4+} could be calculated for 450 to 550 °C of the ReCl_3 salt mixture. The peak current of soluble-insoluble redox species can be expressed as a function of \sqrt{v} and \sqrt{D} using the Berzins and Delahay relation⁵²:

$$i_p = 0.611 nFAC_0 \left(\frac{nF\theta D}{RT} \right)^{1/2} \quad (59)$$

The bulk concentration of ReCl_3 retained in the molten salt after two hours of thermal equilibrium was considered to calculate the diffusivities from the slope of the i_p vs \sqrt{v} plots. The number of electrons (n) involved in the reduction reaction was calculated from the square wave voltammetry data as shown in Figure 44 to Figure 46 by determining the width of half current peak ($W_{1/2}$) and using the relation^{53,54}:

$$n = 3.5 RT/(W_{1/2}F) \quad (60)$$

Figure 44 shows a square wave voltammetry at 1 wt% ReCl_3 addition, while Figures 45 and 46 showed more obvious peaks using a 5 wt% addition of ReCl_3 to the molten salt mixture. Alternately, the number of electrons for reversible soluble-soluble redox system can also be calculated from the CV data using the relations (61) and (62) proposed by Matsuda and Ayabe⁵⁵:

$$E_{p,c} = E_{1/2} - 1.11 \frac{RT}{nF} \quad (61)$$

$$E_{p,a} = E_{1/2} + 1.11 \frac{RT}{nF} \quad (62)$$

Where $E_{p,c}$ and $E_{p,a}$ are cathodic and anodic peak current potentials, respectively; $E_{1/2}$ is a half wave potential and expressed as:

$$E_{1/2} = E_{\text{Re}^{4+}/\text{Re}^{2+}}^0 + \frac{RT}{nF} \text{Ln} \left(\frac{\gamma_{\text{Re}^{4+}}}{\gamma_{\text{Re}^{2+}}} \right) + \frac{RT}{nF} \text{Ln} \left(\frac{\sqrt{D_{\text{Re}^{2+}}}}{\sqrt{D_{\text{Re}^{4+}}}} \right) \quad (63)$$

Formal potential for soluble-soluble system, E^{0*} is expressed as⁵⁶:

$$E_{Re^{4+}/Re^{2+}}^{0*} = E_{Re^{4+}/Re^{2+}}^0 + \frac{RT}{nF} \ln \left(\frac{\gamma_{Re^{4+}}}{\gamma_{Re^{2+}}} \right) \quad (64)$$

$$E_{Re^{4+}/Re^{2+}}^{0*} = \left(\frac{E_{p,a} + E_{p,c}}{2} \right) - \frac{RT}{nF} \ln \left(\frac{\sqrt{D_{Re^{2+}}}}{\sqrt{D_{Re^{4+}}}} \right) \quad (65)$$

Formal potential for reversible soluble-insoluble (Re^{3+}/Re^0 , Re^-/Re^0) system can be expressed as^{18,56}:

$$E_{p,1a} = E_{Re^0/Re^-}^{0*} + \frac{0.854RT}{nF} - \frac{RT}{nF} \ln(C_{Re^-}) \quad (66)$$

$$E_{p,1c} = E_{Re^{3+}/Re^0}^{0*} - \frac{0.854RT}{nF} + \frac{RT}{nF} \ln(C_{Re^{3+}}) \quad (67)$$

Tables XII to XIV summarizes the results of square wave voltammograms (SWV) given in Figures 44 to 46 and the number of electrons calculated based on the full width half wave of the differential current peaks using the expression given in (60). The peak potentials of different reduction reactions are listed which could be correlated to the formal potentials described in the expressions (64) to (67). The SWV data indicated that the cathodic peaks observed between -0.49 to $-1.92V$ in the CV could be assigned to the three-step reduction process of $Re(IV)$ to $Re(0)$ at 450 °C. For 500 and 550 °C a four-step process was seen in the SWV data, while only 3 peaks could be seen in the CV between -0.5 to -2 V. A reason for more peaks appearing in the SWV is due to the square wave signal providing greater peak resolution than CV. The three-step process that is reported in this investigation for $Re(IV)$ to reduce to $Re(0)$ is different from the one-step process reported in $LiCl-KCl$ melts at $450-550$ °C where they started with $Re(IV)$ in the form of K_2ReCl_6 and used rhenium metal rod or foil as the working electrode⁶⁵. The number of electrons calculated from the SWV data was used

for estimation of the diffusivity of species based on the slopes of i_p vs \sqrt{v} plots given in Figure 43. Table XV lists the coefficient of diffusion of different species such as Re^{4+} , Re^{3+} , Re^{2+} , and Re^- in ReCl_3 melts at temperatures ranging from 450 to 550 °C. Due to time, concentration loss for 5 wt% was not able to be performed. For that reason, the amount of loss for 1 wt% at 2 hour test was taken for 5 wt% to account for some of the loss that occurred. Even though a quasi-reversible type reaction was observed, the diffusivity can be estimated based on the Randles–Sevcik equation or Berzins and Delahay relation. Similar approach has been reported by other researchers for calculating the diffusivities of lanthanide ions in the LiCl-KCl eutectic^{51,57}. Bermejo et al. reported that the corrections required for cylindrical geometry of the working electrode can be neglected to use the semi-infinite relations assumed for the Randles–Sevcik (Eq. 58) or Berzins-Delahay (Eq. 59) relation when the scan rate is higher than 50mV s^{-1} ⁵¹. The diffusivity values, in turn, were used for the estimation of formal potentials based on the relation (65). The formal potentials were determined based on the CV data using the relations (65) (67) and summarized in Table XVI.

Table XII. Summary of the square wave voltammogram data of molybdenum electrode in 1wt% ReCl_3 containing LiCl-KCl at 450 °C.

Peak ID	Peak potential, $V_{\text{Ag}/\text{AgCl}}$	Width at half peak, $(W_{1/2}), \text{V}$	Number of electrons	Reaction step
1	-0.475	0.618	0.43	$\text{Re}^{4+} + \text{e}^- \rightarrow \text{Re}^{3+}$
2	-2.07	0.199	1.17	$\text{Re}^{3+} + \text{e}^- \rightarrow \text{Re}^{2+}$

Peak ID	Peak potential, $V_{Ag/AgCl}$	Width at half peak, $(W_{1/2}), V$	Number of electrons	Reaction step
3	-2.51	0.114	2.05	$Re^{2+} + 2e^{-} \rightarrow Re(0)$

Table XIII. Summary of the square wave voltammogram data of molybdenum electrode in 5wt% $ReCl_3$ containing LiCl-KCl at 500 °C.

Peak ID	Peak potential, $V_{Ag/AgCl}$	Width at half peak, $(W_{1/2}), V$	Number of electrons	Reaction step
1	-0.186	0.122	1.91	$Re^{4+} + 2e^{-} \rightarrow Re^{2+}$
2	-0.683	0.241	0.97	$Re^{2+} + e^{-} \rightarrow Re^{+}$
3	-0.868	0.16	1.46	$Re^{+} + e^{-} \rightarrow Re(0)$
4	-1.237	0.11	2.12	$Re(0) + 2e^{-} \rightarrow Re^{2-}$

Table XIV. Summary of the square wave voltammogram data of molybdenum electrode in 5wt% $ReCl_3$ containing LiCl-KCl at 550 °C.

Peak ID	Peak potential, $V_{Ag/AgCl}$	Width at half peak, $(W_{1/2}), V$	Number of electrons	Reaction step
1	-0.14	0.618	1.5	$Re^{4+} + e^{-} \rightarrow Re^{3+}$

Peak ID	Peak potential, $V_{Ag/AgCl}$	Width at half peak, $(W_{1/2}), V$	Number of electrons	Reaction step
2	-0.57	0.199	1	$Re^{3+} + e^{-} \rightarrow Re^{2+}$
3	-0.61	0.114	2.1	$Re^{2+} + 2e^{-} \rightarrow Re(0)$
4	-1.625	0.593	0.4	$Re(0) + e^{-} \rightarrow Re^{-}$

Table XV. Diffusivity of Re species in LiCl-KCl eutectic at 450 to 550 °C, WE: Molybdenum.

Temperature, °C	Initial concentration of $ReCl_3$, wt%	Diffusing species	Coefficient of diffusion, cm^2/s
450	1wt%	Re^{4+}	12.86×10^{-5}
		Re^{3+}	7.56×10^{-5}
500	5wt% (actual 4.75%)	Re^{4+}	12.3×10^{-5}
		Re^{2+}	5.03×10^{-5}
550	5wt% (actual 4.75%)	Re^{4+}	0.033×10^{-5}
		Re^{3+}	5.93×10^{-5}

Table XVI. Formal potentials of LiCl-KCl-ReCl₃ system at 450 °C using molybdenum working electrode.

Temperature, °C	Concentration, wt%	Reaction	Formal potential ReCl ₃ , V _{Ag/AgCl}
450	1	Re ⁴⁺ + e ⁻ → Re ³⁺	-0.113
	5	Re ⁴⁺ + e ⁻ → Re ³⁺	0.131
500	5	Re ⁴⁺ + 2e ⁻ → Re ²⁺	-0.428
550	5	Re ⁴⁺ + e ⁻ → Re ³⁺	-0.678

The diffusivity of Re⁴⁺ in LiCl-KCl eutectic decreased with increase in temperature as can be seen between 500 °C and 550 °C. The decrease in diffusivity from 450 to 500 °C can be due to both increase in temperature along with the increase in concentration. The octahedral coordination of Re⁴⁺ with chloride ions as ReCl₆²⁻ could be attributed to the decreased diffusivity with increase in the concentration and temperature. The estimated diffusivity of Re⁴⁺ in 1wt% ReCl₄ at 450 °C was about 12.86 × 10⁻⁵ cm² s⁻¹. The diffusivity of Re⁴⁺ decreased to 0.3 × 10⁻⁵ cm² s⁻¹ for 5 wt% when the temperature of ReCl₃ increased to 500 °C, then to 0.03 × 10⁻⁵ cm² s⁻¹ at 550 °C. A similar order of magnitude (0.063 × 10⁻⁵ cm² s⁻¹) diffusivity was reported for Re(IV) in AlCl₃-MeEtimCl room temperature molten salt by Sandra Strubinger et al. ⁶⁹ In another paper by O.N. Vinogradov-Zhabrov et al., they saw a few orders of magnitude higher in value for diffusivity at 840 °C around 3.5 × 10⁻⁵ cm² s⁻¹ for 7 wt% Re⁴⁺ ⁷⁰. The diffusivity of Re²⁺ and Re³⁺ was estimated to be an order of magnitude higher than that of Re⁴⁺ for 500 and 550 °C. The increased diffusivity of Re²⁺ for 500 and 550 °C could be associated with greater solubility in the salt mixture than Re⁴⁺.

Table XVI summarizes the formal potentials for different reduction reactions. The formal potentials of Re(IV) reduction reaction shifted in the positive direction with increase in the initial ReCl_3 concentration. Additionally, as the temperature increased from 450 to 550 °C, the formal potential shifted in the negative direction. Danilov et al. reported the reduction potential of $\text{Re(IV)} \rightarrow \text{Re(III)}$ in NaCl-2CsCl at 750 °C to be 0.52 $V_{\text{Ag/AgCl}}$ and the reduction potential of $\text{Re(III)} \rightarrow \text{Re(0)}$ to be -0.48V⁶⁶. These reduction potentials are more positive (+1.2V (550 °C) to +0.6V (450 °C)) than what was observed in the LiCl-KCl molten salt at 450 to 550 °C for a quick comparison. Loiseau et al. reported the reduction potential of $\text{Re} (\text{Re}^{4+} \rightarrow \text{Re}^{3+} + e^-)$ to be 0.5V Vs saturated calomel reference in $\text{NBu}_4\text{ClO}_4\text{-DMF}$ at room temperature which is about 0.486 $V_{\text{Ag/AgCl}}$ ⁶⁸. Probably, this potential corresponds to the reaction: $2\text{Re}^{4+} + 8\text{Cl}^- \rightarrow \text{Re}_2\text{Cl}_8^{2-} + e^-$ which was one of the compounds seen by Volkovich et al.²⁹

Electrochemical impedance spectroscopy:

Figures 47a and 47b show the EIS of the molybdenum electrode in 1wt% ReCl_3 at different temperatures in the forms of Nyquist and Bode plots, respectively. The potential for each temperature was taken at open circuit conditions. The highest impedance was taken at a 450 °C, while the lowest was recorded at 500 °C. Impedance value for 550 °C was appeared in between 450 and 500 °C. This same trend was also seen in both the Bode plot (48a) and Nyquist plot (48b).

The rationale behind carrying out EIS measurements was to understand the structural characteristics of the molten salts with and without addition of TeCl_4 . The physical and electrical properties of the molten salt systems depend on the structure and interactions of the

constituents. The structural arrangements that are present in molten salts can be viewed as intermediates between discrete chemical bonds and periodic crystalline lattices⁶⁰. The interatomic interactions determine the local ordering of the molten salt. The electrochemical properties are influenced by the structural characteristics of the molten salt. When cations are present in the molten salt with different sizes and different charge densities, an asymmetric polarization of anions is anticipated which affects the electrostatic stability of the mixture⁶¹.

In order to better understand the interfacial impedance behavior, the EIS data were fitted into an electrical equivalent circuit (EEC) and the values are shown in Table XVII. In general, the impedance spectra showed only one time constant. Therefore, the EIS data was modeled using 1 R|| \emptyset loop for every temperature. In the equivalent circuit, R_u and R_p represent the electrolyte resistance and resistance to charge transfer, while the \emptyset (Y is used as a substitute) symbol represents a double layer also known as an imperfect capacitor, respectively. The R_1 - Y_1 loop represents the electrode/LiCl-KCl electrolyte interface. Y_1 represents imperfect capacitance whose impedance (Z) is given by the relation: $Z = 1/[(Q_0 \omega^n)] * e^{-(\pi/2)ni}$ where ω = frequency, and the exponent “n” represents the surface heterogeneity or continuously distributed time constants for charge transfer when $0 < n < 1$.³³ Smaller magnitudes of R_u and R_p , and larger values of Y_0 will lead to better charge transfer characteristics.

Table XVII. EIS circuit component values of LiCl-KCl-ReCl₃ system at open circuit potentials for 450 to 550 °C using molybdenum working electrode and 1 wt% ReCl₃.

Temperature, °C	Circuit Component	Circuit Component Value
450	R _u	698.2 * 10 ⁻³ Ω
	Y ₀	8.797 * 10 ⁻³ S*s ^a
	α	793.7 * 10 ⁻³
	R _p	846.9 Ω
500	R _u	923.1*10 ⁻³ Ω
	Y ₀	27.22*10 ⁻³ S*s ^a
	α	704.9*10 ⁻³
	R _p	64.07 Ω
550	R _u	620.3 * 10 ⁻³ Ω
	Y ₀	13.77 * 10 ⁻³ S*s ^a
	α	795.6 * 10 ⁻³
	R _p	249.3 Ω

The electrolyte resistance for all three temperature tests were of the same order of magnitude. However, the solution resistance was highest at 500 °C and the lowest at 550 °C. The charge transfer resistance was given as R_p at high frequencies because the resistance due to the

constant phase element would be negligible. The impedance due to the constant phase elements became significant only below 10Hz as seen from the Bode plots. As temperature increased, the capacitance denoted by Y_0 increased, while the time constant staid relatively consistent for 450 and 550 °C, while the time constant was seen to decrease at 500 °C even though it showed the greatest capacitance value. The increase in capacitance value could be attributed to increased concentration of Re^{3+} ions dissociating into Re^{4+} at the higher temperatures, resulting in a greater ratio difference of $\text{Re}^{3+}/\text{Re}^{4+}$ at the electrode/molten salt interface that existed in the OCP condition at 500 °C and 550 °C than was present at 450 °C.

An EEC model consisting of two parallel RC loops connected in series, and each RC loop having a Warburg element was proposed to describe the impedance behavior of LiCl-KCl molten salt at 700 °C–800 °C by Cohen et al.⁶¹. The reported values of solution resistance (R_s), double layer capacitance (Q_1), capacitance due to adsorption of ions (Q_2), and Warburg coefficient were reported as 0.685 ohm, 58–80 μF , 1.8–2.3 mF, and 2–4 mS, respectively⁶². The EIS data of this study was fitted with a different EEC model but the values of the solution resistance circuit components showed almost similar order of magnitude for electrolyte resistance and capacitance as Kim et al.⁶³ reported. Their EIS data of a molybdenum electrode in LiCl-KCl- UCl_3 at 773K and their fitted data to an EEC similar to the one used in this work and the values of the circuit components showed a similar order of magnitude as reported in this work. While the resistance to charge transfer values had a higher value in this study than the one reported by Kim et al.

Most of the literature on pyroprocessing of used nuclear fuels focuses on the electrochemical behaviors of fission product as cations such as La^{3+} , Nd^{3+} , Sm^{3+} etc.⁶⁴ Not much information

is available on the anion type fission products such as $[\text{ReCl}_6]^{2-}$ (as a surrogate for Tc). It is generally assumed that anions present in the molten salt may not interfere with the cathodic reduction of actinides. This study attempts to fill the knowledge gap and shows that Re^{3+} will dissociate into Re(IV) and Re(0) before any redox reaction occurs. Resulting in potentially Tc existing in the same ionic states in the molten salt solution before pyroprocessing begins. Once the process starts various states of Tc^{n+} could exist and result in creating the volatile compounds such as TcCl_6 . The electrochemical data presented in this work such as formal potentials of different Re species (Re^{4+} and Re(0)) and their diffusivities are useful in understanding Tc behaviors that can lead to designing more efficient pyrochemical processes.

5.3 Conclusions

The reduction of Re^{4+} to Re(0) occurred in three steps for all temperatures. The formal potential of Re(IV) reduction to Re(III) for 450 °C was estimated as $-0.113 \text{ V}_{\text{Ag}/\text{AgCl}}$, for 1 wt% ReCl_3 and 0.131 V for 5 wt% ReCl_3 . For 500 °C formal potential of Re(IV) to Re(II) at 5 wt% was seen to be $-0.428 \text{ V}_{\text{Ag}/\text{AgCl}}$, while 550 °C formal potential of Re(IV) to Re(III) was seen to be $-0.678 \text{ V}_{\text{Ag}/\text{AgCl}}$. The Re(III) for 450 and 550 °C reduced to Re(0) in two steps with one electron reaction at one step, followed by a two electron transfer. The reduction to Re(0) completed at around $-1.237 \text{ V}_{\text{Ag}/\text{AgCl}}$ for 500 °C, while it completed at $-1.625 \text{ V}_{\text{Ag}/\text{AgCl}}$ for 550 °C. Formation of Re(0) was observed for 450 to 550°C. The redox process of $\text{Re}^{4+}/\text{Re}^0$ system was observed to be quasi-reversible.

The diffusion coefficients of Re^{4+} and Re^{3+} at 450 °C were 12.86×10^{-5} and $7.56 \times 10^{-5} \text{ cm}^2 \text{ s}^{-1}$, respectively in the 1wt% ReCl_3 electrolyte. While Re^{4+} for 5 wt% for 450 to 550 °C

was seen to be 12.3×10^{-5} , 0.304×10^{-5} , and $0.033 \times 10^{-5} \text{ cm}^2\text{s}^{-1}$. Increase in the ReCl_3 concentration and temperature decreased the diffusion coefficients.

The electrochemical impedance spectroscopic data could be fitted with an equivalent circuit representing one time constant. The charge transfer resistance for 1 wt% ReCl_3 decreased with increase in temperature, with the lowest being at 500 °C.

Chapter 6: Electrochemical Behavior of TeCl_4 and ReCl_3 Combination in LiCl-KCl Eutectic at $450\text{ }^\circ\text{C}$

6.1 Experimental Procedure

Due to the hygroscopic nature of the LiCl-KCl eutectic salt, all experiments were performed in a glove box (MBraun) under an inert argon environment. Oxygen and moisture levels were maintained less than 2 ppm. The eutectic salt was created by thoroughly mixing 44.6wt% LiCl (99.995%, ultra-dry) with 55.4wt% KCl (99.998%, ultra-dry). Due to the high vapor pressure of tellurium tetrachloride (TeCl_4 , 99.9% purity) the following procedure was performed to create the mixture. Half of the eutectic salt was melted in a glassy carbon crucible and left to cool over an 8-h period. Due to the high wetting angle between the salt and glassy carbon crucible, the eutectic ingot was able to be taken from the crucible in one piece. Afterward, 1 wt% of TeCl_4 powder was placed in the glassy carbon crucible followed by the eutectic ingot. The remaining eutectic salt was mixed with 1 wt% ReCl_3 . Once mixed it was placed on top of the eutectic ingot. The entire salt mixture was heated to 10 degrees below the vapor temperature of TeCl_4 ($200\text{ }^\circ\text{C}$) and soaked at this temperature for 15 minutes to allow the system to come to equilibrium. The temperature was then brought to $353\text{ }^\circ\text{C}$ and let set for 1 hour to allow solution to melt and was mixed periodically to combine the ReCl_3 and TeCl_4 with the entire mixture. Once the ingot was created, the completed ingot was broken into half and placed in an alumina crucible for electrochemical experiments.

Before bringing the created salt mixture to operating temperatures the furnace was brought to 10 degrees below sublimation temperature of the TeCl_4 ($200\text{ }^\circ\text{C}$) for 15 minutes. After soaking at this temperature, the furnace was brought up to 500 to $550\text{ }^\circ\text{C}$ and equilibrated for

10 minutes before starting the electrochemical measurements. The addition of TeCl_4 and ReCl_3 was varied from 1wt% or 0.2mol%. All chemicals were procured from Alfa Aesar and used without further purification.

Due to time constraints and funding limitation, the concentration of $\text{TeCl}_4/\text{ReCl}_3$ mixture was not analyzed to determine how much was retained in the molten salt. For the purpose of this chapter the concentration for 2 hour analysis for Te and Re that was used in previous chapters will be used for concentration values and are shown in Table XVIII. These concentrations were determined by using induction coupled plasma- mass spectroscopy (ICP-MS) technique. The sampling of salt for ICP-MS analysis was carried out by dipping a tungsten rod in the molten salt at 1 hour intervals, ranging from when operating temperature has been reached up to 4 hours. Solidified salt was scrapped off the rod using a stainless steel spatula. The weight of the sampled out salt was measured using an analytical balance (Radwag, XA110/2X) capable of measuring a minimum weight of 1mg with a resolution of 0.01mg, and dissolved in 30ml of 1% nitric acid. Three samples were extracted per condition. The ICP-MS analysis of Te and Re was performed at the Analytical Sciences Laboratory of University of Idaho by following a comprehensive quality management plan that maintains compliance with applicable standards of ISO 17025. The concentration of Te and Re retained in the molten salt was analyzed as a function of time after temperature equilibration. The difference seen in the 4 hour concentration at 500 °C and 550 °C compared to other sample hours, was potentially due to the dispersion of Te in the salt at the time of test was taken. This could be due to the vapor process of the Te affecting where the greatest concentration of Te was at the time even with mixing the solution upon taking each sample. The electrochemical results are discussed with reference to the initial addition amount for brevity.

Table XVIII. ICP-MS analyses of TeCl_4 and ReCl_3 retained in the LiCl-KCl molten salt as a function of time at $450\text{ }^\circ\text{C}$.

Initial addition of TeCl_4	Dwelling time at $450\text{ }^\circ\text{C}$, h	TeCl_4 retained in the molten salt, %
1wt%	0	79
	1	78
	2	76
	3	73
	4	72
Initial addition of ReCl_3	Dwelling time at $450\text{ }^\circ\text{C}$, h	ReCl_3 retained in the molten salt, %
1 wt%	0	104.24
	1	149.78
	2	126.45
	3	83.43
	4	61.09

Open circuit potential measurement, electrochemical impedance spectroscopy (EIS), cyclic voltammetry, and square wave voltammetry, were performed in LiCl+KCl eutectic melt at $450\text{ }^\circ\text{C}$ with and without addition of 1 wt% TeCl_4 and ReCl_3 by using a computer controlled potentiostat (Gamry Instruments, model: Reference 1000, software for data generation: Gamry Framework, version 7.03, software for data analysis: Gamry Echem Analyst version 7.03). The temperature stability of the molten salt was $\pm 2\text{ }^\circ\text{C}$. A fuzzy logic proportional–integral–derivative (PID) controller (Tempco, model: TEC-9100) was used for controlling the

temperature of the furnace using a type K (chromel-alumel) thermocouple. The thermocouple of the furnace was NIST calibrated. The temperature of the molten salt was measured by using a NIST calibrated K-type thermocouple shielded by an alumina tube (99.8% purity, Omega) and a digital thermometer (Omega, model HH91). The working electrode was a 2mm diameter molybdenum rod (99.95%, Alfa Aesar). The counter electrode was a 4mm diameter glassy carbon rod. The reference electrode was an in-house made AgCl coated Ag wire (99.9%) placed in a borosilicate glass tube that contained LiCl+KCl eutectic thoroughly mixed with 1wt% AgCl (99.997%, ultra-dry). The working and counter electrodes were polished using a series of emery papers down to 2000 grit. The polished surface was wiped down with propanol and acetone and dried in a vacuum oven for 16h at 120 °C. The cleaning, and conditioning protocols were strictly followed for each set of experiments to ensure repeatability. After reaching the set temperature of 450 °C, the electrodes were conditioned in the open circuit potential for 15 minutes before starting the electrochemical tests. The electrodes were placed in an equidistance triangular arrangement. The surface area ratio of the counter and working electrodes was at least 2.5. The surface area was calculated by physically measuring the diameter and the immersion depth of the working in the molten salt after the experiments using an inch ruler with 32nd division tick marks. The measured depth was compared with the initial set value (typical variation after converting to cm was 0.5 – 0.75cm due to capillary effect). The surface area measured by geometric calculation is prone to error caused by meniscus of the molten salt, and salt built up layer. No effort was taken to address the errors introduced by the geometric surface area calculations which may vary from 7%–12%.

Yoon et al. proposed a relation between the Ag/AgCl reference potential and Cl_2/Cl^- potential that was a function of molar fraction of AgCl but independent of temperature between 723–823K and given as⁴⁴:

$$E_{\text{Cl}_2/\text{Cl}^-} = (-0.8726 \pm 0.00486) + (0.05896 \pm 0.00108) \ln(X) \quad (68)$$

Where X = mole fraction of AgCl. Accordingly, the Ag/AgCl potential of this study is -1.197V vs the redox potential of Cl_2/Cl^- . CV was carried out at different potential windows and at different scan rates. All potentials in this paper are given with reference to the Ag/AgCl electrode whose potential is $-1.197 \text{ V}_{\text{Cl}_2/\text{Cl}^-}$. The maximum potential window signified decomposition of the LiCl-KCl eutectic by reduction of lithium at the cathodic end and chlorine evolution at the anodic end. Cyclic voltammetry studies were carried out at different scan rates from 100mVs^{-1} to 2000Mv s^{-1} . Electrochemical impedance spectroscopy was carried out at the open circuit condition under potentiostatic conditions by super imposing an *ac* signal of 10mV by scanning the frequency from 10kHz to 0.1Hz . Square wave voltammetry was conducted between OCP and $-2.5 \text{ V}_{\text{Ag}/\text{AgCl}}$; and between OCP and $1.2 \text{ V}_{\text{Ag}/\text{AgCl}}$ at a frequency of 25Hz , pulse size of 25mV , step size of 1mV , and pulse time of 0.04s . All the electrochemical tests were either duplicated or triplicated to ensure reproducibility. The average values are presented.

6.2 Results and Discussions

Open Circuit Potential (OCP) Measurements

In the previous chapters, equilibrium measurement of tellurium and rhenium in the molten salt with the surface of the tungsten/molybdenum and glassy carbon working electrode, at 450°C was seen to shift the OCP to more positive potentials. This trend was also seen when rhenium

and tellurium were combined in the same solution, which can be seen in Figure 48. The shift in OCP with TeCl_4 and ReCl_3 addition will increase the exchange current density (i_0) by following the relation⁴⁵:

$$i_0 = nFk_0C_{\text{Te}^{4+}} \quad (69)$$

Where, n = number of electrons, F = Faraday's constant, k_0 = rate constant for electron transfer, and $C_{\text{Te}^{4+}}$ is bulk concentration of Te^{4+} in the molten salt. The increase in the i_0 value will shift the Tafel plots of the $\text{Te}^{n+}/\text{Te}^{(n-1)+}$ redox reactions such that the OCP could increase with the increase in the TeCl_4 and ReCl_3 concentration. It should be noted that the proposed $\text{Te}^{4+}/\text{Te}^{2+}$ redox couple is an example only. There are other possible redox reactions involving tetravalent Te and tetravalent Re that occurs from the disproportionation of Re(III) in the molten salt. The standard redox potential of Te and Re is reported to be more positive than that of Pd, Ag, Mo, W, and other transition metals^{15,45}. The positive OCP values observed on the molybdenum electrode indicated that the molybdenum had significant active sites to support the redox reactions. The shift in the OCP between with and without the 1 wt% TeCl_4 and ReCl_3 addition is due to the mixed potentials of Re and Te having a more positive potential than chlorine.

Cyclic voltammetry:

A full window CV scan was performed from -2.8V to $1.4 \text{V}_{\text{Ag}/\text{AgCl}}$ as seen in Figure 49. The cyclic voltammogram of pure LiCl-KCl eutectic (without $\text{TeCl}_4/\text{ReCl}_3$ addition) showed only one cathodic wave corresponding to lithium reduction that started at around $-2.6 \text{V}_{\text{Ag}/\text{AgCl}}$ and an anodic wave associated with chlorine gas evolution that started around 1.2V . No other

peaks were observed in between these two potentials on the molybdenum electrode. The reduction potentials of lithium reported in the literature vary widely from -2.35V to -2.6V . For example, Koyama et al. reported a value of $-2.353\text{ V}_{\text{Ag}/\text{AgCl}}$ at 723K for the $\text{Li(I)}/\text{Li(0)}$ reaction¹². On the other hand, Bermejo et al. showed lithium reduction occurring at $-2.6\text{ V}_{\text{Ag}/\text{AgCl}}$ at 723K using tungsten as a working electrode⁴⁶. Liu et al. also reported a similar potential of $-2.6\text{ V}_{\text{Ag}/\text{AgCl}}$ for reduction of lithium at 873K ⁴⁷.

Addition of $\text{TeCl}_4/\text{ReCl}_3$ introduced several additional peaks both in the cathodic and anodic directions that can be seen in Figures 50 and 51, where Figure 50 is a small potential window comparing both with and without 1 wt% addition. The peaks associated with Te/Re species are clearly discerned in Figure 50 and 51 in comparison with the CV of LiCl-KCl eutectic without any addition of $\text{TeCl}_4/\text{ReCl}_3$. Figure 51 illustrates the full window (both in the cathodic and anodic directions) CV of 1wt% TeCl_4 and 1 wt% ReCl_3 containing LiCl-KCl molten salt at different scan rates with a molybdenum working electrode. The cathodic wave started at potential more negative than $-0.47\text{ V}_{\text{Ag}/\text{AgCl}}$. Five distinct cathodic peaks were observed at around -0.793V (c_1), -1.33V (c_2), -1.55V (c_3), -2.09V (c_4), and -2.8V (c_5). During the reverse scan, five anodic peaks were recorded at -2.12V (a_0), -1.52V (a_1), -0.96V (a_2), -0.353V (a_3), 0.287V (a_4), and $0.537\text{ V}_{\text{Ag}/\text{AgCl}}$ (a_5). To determine if the peaks that are seen relate to either rhenium or tellurium depositions, full window CV of Te and Re are compared to TeRe combination shown in Figures 52 and 53. From overlaying the graphs of 1 wt% TeCl_4 and 1 wt% ReCl_3 with 1 wt% Te/Re combination, the only peaks to a line in the cathodic direction was c_1 and c_4 with 1 wt% Te, while in the anodic direction a_1 lined up with 1 wt% Re graph while a_2 and a_3 coincided with peaks in the TeCl_4 graph. From this it can be inferred that the first cathodic wave (c_1) was attributed to the reduction of Te^{4+} to Te^{2+} for 1

wt% TeCl₄/ReCl₃, and the fourth cathodic wave (c₄) was due to reduction of Te⁰ to Te²⁻. The additional peaks between c₁ and c₄ were mostly observed at scan rates of 200–1000mVs⁻¹. The cathodic wave (c₄) at a more negative potential could be associated with formation of telluride ions (Te_xⁿ⁻). The number of electrons transferred could be determined from differential square wave pulse voltammetry, which will be discussed in a latter section. The anodic peaks a₁ could be associated with Re⁰ being oxidized, while a₂ and a₃, could correlate to Te metal being oxidized to Te⁺ and Te²⁺. The anodic wave taking off at about 1.2V was associated with evolution of chlorine.

Figure 54 shows the cyclic voltammograms between OCP and -2.2 V_{Ag/AgCl} (more positive than the lithium reduction condition) comparing 1 wt% TeCl₄ and 1 wt% ReCl₃, with 1 wt% TeCl₄/ReCl₃ mixture. To obtain a better resolution of peaks for analysis, the scan rate for Te/Re combination was taken at 200 mV/s, while the others were taken at 1000 mV/s. The first cathodic wave (c₁) starting at -0.67V overlapped with the reaction of Te⁴⁺ being reduced to Te²⁺. The second cathodic wave (c₂) occurred with around -1.68V. When comparing the Te/Re combination this potential aligned with reduction of Re²⁺ to Re⁰. For the anodic peaks a₁ and a₂, which closely a line with the appearance and potential of Te⁰ oxidizing to Te⁺ followed by Te⁺ undergoing a two electron transfer to Te³⁺. However, there is a slight potential shift with a₂ when compared to 1 wt% TeCl₄ without Re addition. This peak is seen to appear at a potential of -0.283V while Te without Re is seen around -0.683V. Assuming that the first cathodic wave is associated with a two-electron process, the α_c , transfer coefficient for cathodic reaction shall be estimated as 0.38. Furthermore, as the scan rate increased as seen in Figures 55, which represents a dependency of the peak potential indicating that the cathodic reaction was not reversible. However, the peak current increased

as a function of square root of the scan rate, as seen in Figure 56. Little research has been done on this topic to cross reference the peaks seen with other sources. However, in one article by E.A. Salakhova et al. used electrochemistry to deposit a thin film of a tellurium rhenium alloy ⁷¹. Using a chloride-borate acid electrolyte, E.A. Salakhova added 0.003 M TeO₂ and 0.05 M NH₄ReO₄ at room temperature up to 80 °C to create the co-deposition in respect to a silver chloride reference electrode. At room temperature they saw three maximums. The first two peaks at 0.6V and 0.3V were correlated with the dissolution of rhenium and tellurium, while the third was seen to be ReTe₂. When rhenium and tellurium were separate, they both were reduced to a metallic state. When combined, ReTe₂ was created by rhenium reacting with tellurides in the system to form ReTe₂. It was seen that this reaction occurred at a more positive potential than rhenium stand-alone. E.A. Salakhova et al. stated that the chemical activity of freshly deposited tellurium with respect to given metal ions and ability of telluride ions undergo profound cathode reduction ⁷¹. Using the information from E.A. Salakhova et al., cathodic peaks c₁ and c₂ shown in Figure 54 could be attributed to the reduction of Re(IV) to Re(III) and Te(IV) to Te(II) on the working electrode. These cathodic peaks were associated with soluble-soluble species, where soluble Te(IV) species were reduced to soluble Te(II) deposit and Re(IV) was reduced to Re(III). The cathodic wave shoulder starting at -0.523 V_{Ag/AgCl} could be attributed to the reaction: $n\text{Re}^{4+} + e^{-} \rightarrow \text{Re}_n^{3+}$. While the cathodic wave shoulder starting at -0.933 V_{Ag/AgCl} could be attributed to the reaction: $n\text{Te}^{4+} + 2e^{-} \rightarrow \text{Te}_n^{2+}$. Since the CV was interrupted at -2 V no lithium reduction and oxidation peaks were observed. The anodic waves (a₁, a₂) observed at about (-0.743, -0.403) V_{Ag/AgCl} were associated with the oxidation of Te(II) species to Te(IV) and Re(III)

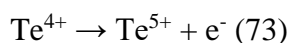
species to Re(IV). Poulsen et al. performed experiments in KCl-AlCl₃ with TeCl₄ addition in the molten salt at 300 to 400 °C and saw the corresponding reactions (70) ²³.



For rhenium, Loiseau et al. reported the following reaction in 0.1 M NBu₄ClO₄-DMF at room temperature using a double junction saturated calomel reference electrode (71) ⁶⁸.



It is noted that the peak potentials of anodic waves a₁ and a₂ were independent of the scan rates indicating reversibility of the reaction. The anodic peaks observed at potentials more positive than -0.063 V_{Ag/AgCl} seen in Figure 51, could be due to the oxidation of Re(IV) to Re⁵⁺ as seen by Loiseau et al.⁶⁸ Also, of Te(IV) being oxidized to Te(V) seen in the following reactions.



The anodic peak observed at 0.296 V_{Ag/AgCl} and 0.527V_{Ag/AgCl} was assigned to reaction (72) and (73).

Figure 56 shows the linear relation observed between peak current density and the square root of the scan rate in 1wt% TeCl₄/ReCl₃ containing LiCl-KCl eutectic at 450 °C using a molybdenum electrode. Randles-Sevick equation describes the peak current density as a function of electrode surface area, bulk concentration of the redox species, and square root of

the scan rate and diffusivity of redox species ⁵¹. The diffusion coefficient can be calculated from the Randles-Sevcik relation as given in (74):

$$D^{1/2} = \left[\frac{i_p}{\sqrt{v}} \right] \left(\frac{1}{0.446nFAC_0} \right) \left(\frac{RT}{nF} \right)^{0.5} \quad (74)$$

Where i_p/\sqrt{v} is the slope of peak current vs. square root of scan rate, A is the surface area of electrode, and C_0 is the concentration of the Te species. Using the slope taken from Figure 56 the diffusion coefficients of Te^{4+} and Re^{4+} could be calculated. The peak current of soluble-insoluble redox species can be expressed as a function of \sqrt{v} and \sqrt{D} using the Berzins and Delahay relation⁵²:

$$i_p = 0.611 nFAC_0 \left(\frac{nF\vartheta D}{RT} \right)^{1/2} \quad (75)$$

The bulk concentration of $\text{TeCl}_4/\text{ReCl}_3$ retained in the molten salt after two hours of thermal equilibrium was considered to calculate the diffusivities from the slope of the i_p vs \sqrt{v} plots. The number of electrons (n) involved in the reduction reaction was calculated from the square wave voltammetry data as shown in Figure 57 by determining the width of half current peak ($W_{1/2}$) and using the relation^{53,54}:

$$n = 3.5 RT/(W_{1/2}F) \quad (76)$$

Alternately, the number of electrons for reversible soluble-soluble redox system can also be calculated from the CV data using the relations (77) and (78) proposed by Matsuda and Ayabe⁵⁵:

$$E_{p,c} = E_{1/2} - 1.11 \frac{RT}{nF} \quad (77)$$

$$E_{p,a} = E_{1/2} + 1.11 \frac{RT}{nF} \quad (78)$$

Where $E_{p,c}$ and $E_{p,a}$ are cathodic and anodic peak current potentials, respectively; $E_{1/2}$ is a half wave potential and expressed as:

$$E_{1/2} = E_{Te^{4+}/Te^{2+}}^0 + \frac{RT}{nF} \ln \left(\frac{\gamma_{Te^{4+}}}{\gamma_{Te^{2+}}} \right) + \frac{RT}{nF} \ln \left(\frac{\sqrt{D_{Te^{2+}}}}{\sqrt{D_{Te^{4+}}}} \right) \quad (79)$$

Formal potential for soluble-soluble system, E^{0*} is expressed as⁵⁶:

$$E_{Te^{4+}/Te^{2+}}^{0*} = E_{Te^{4+}/Te^{2+}}^0 + \frac{RT}{nF} \ln \left(\frac{\gamma_{Te^{4+}}}{\gamma_{Te^{2+}}} \right) \quad (80)$$

$$E_{Te^{4+}/Te^{2+}}^{0*} = \left(\frac{E_{p,a} + E_{p,c}}{2} \right) - \frac{RT}{nF} \ln \left(\frac{\sqrt{D_{Te^{2+}}}}{\sqrt{D_{Te^{4+}}}} \right) \quad (81)$$

Formal potential for reversible soluble-insoluble (Te^{4+}/Te , Re^{4+}/Re) system can be expressed as^{18,56}:

$$E_{p,1a} = E_{Te^0/Te^{2-}}^{0*} + \frac{0.854RT}{nF} - \frac{RT}{nF} \ln(C_{Te^{2-}}) \quad (82)$$

$$E_{p,1c} = E_{Te^{2+}/Te^0}^{0*} - \frac{0.854RT}{nF} + \frac{RT}{nF} \ln(C_{Te^{2+}}) \quad (83)$$

Table XIX summarizes the results of square wave voltammograms (SWV) given in Figure 57 and the number of electrons calculated based on the full width half wave of the differential current peaks using the expression given in (76). The peak potentials of different reduction reactions are listed which could be correlated to the formal potentials described in the expressions (80) to (83). The SWV data indicated that the cathodic peaks observed

between -0.2 to -1.9V in the CV could be assigned to the one and two-step reduction process of Re(IV) to Re(III) and Te(IV) to Te(II). The last two reactions denoted by peaks 5 and 6 in the SWV are possible reactions that can occur, and further analysis would need to be done in the future to verify this. The number of electrons calculated from the SWV data was used for estimation of the diffusivity of species based on the slopes of i_p vs \sqrt{v} plots given in Figure 56. Table XX lists the coefficient of diffusion of Te^{4+} and Re^{4+} species. Even though a quasi-reversible type reaction was observed, the diffusivity can be estimated based on the Randles–Sevcik equation or Berzins and Delahay relation. Similar approach has been reported by other researchers for calculating the diffusivities of lanthanide ions in the LiCl-KCl eutectic^{51,57}. Bermejo et al. reported that the corrections required for cylindrical geometry of the working electrode can be neglected to use the semi-infinite relations assumed for the Randles–Sevcik (Eq. 75) or Berzins-Delahay (Eq. 76) relation when the scan rate is higher than 50mV s^{-1} ⁵¹. The diffusivity values, in turn, were used for the estimation of formal potentials based on the relation (81). The formal potentials were determined based on the CV data using the relations (81) (83) and summarized in Table XXI.

Table XIX. Summary of the square wave voltammogram data of molybdenum electrode in 1wt% $\text{TeCl}_4/\text{ReCl}_3$ containing LiCl-KCl at $450\text{ }^\circ\text{C}$.

Peak ID	Peak potential, $V_{\text{Ag}/\text{AgCl}}$	Width at half peak, $(W_{1/2}), \text{V}$	Number of electrons	Reaction step
1	-0.606	-0.41	0.53	$\text{Re}^{4+} + \text{e}^- \rightarrow \text{Re}^{3+}$
2	-1.03	-0.12	1.81	$\text{Te}^{4+} + 2\text{e}^- \rightarrow \text{Te}^{2+}$

Peak ID	Peak potential, $V_{\text{Ag/AgCl}}$	Width at half peak, $(W_{1/2}), V$	Number of electrons	Reaction step
3	-1.36	-0.13	1.68	$\text{Re}^{3+} + 2e^- \rightarrow \text{Re}^+$
4	-1.42	-0.02	10.9	$2\text{Te}^{2+} + \text{Re}^+ + 11e^- \rightarrow \text{ReTe}_2$
5	-1.56	-0.07	3.12	$\text{ReTe}_2 + 3e^- \rightarrow [\text{ReTe}_2]^{3-}$
6	-1.79	-1.2	1.2	$\text{ReTe}_2 + e^- \rightarrow [\text{ReTe}_2]^{4-}$

Table XX. Diffusivities of Te and Re species in LiCl-KCl eutectic at 450 °C.

Working Electrode	Temperature, °C	Initial concentration, wt%	Diffusing species	Coefficient of diffusion, cm^2/s
Molybdenum	450	1 wt% ReCl_3	Re^{4+}	5.17×10^{-5}
	450	1 wt% TeCl_4 (0.76%)	Te^{4+}	684.5×10^{-5}

Table XXI. Formal potentials of LiCl-KCl-TeCl₄-ReCl₃ system at 450 °C using molybdenum working electrode.

Temperature, °C	Reaction	Formal potential in 1wt% TeCl ₄ /ReCl ₃ , V _{Ag/AgCl}
450	$\text{Re}^{4+} + \text{e}^{-} \rightarrow \text{Re}^{3+}$	0.032
	$\text{Te}^{4+} + 2\text{e}^{-} \rightarrow \text{Te}^{2+}$	0.376

The diffusivity of Te⁴⁺ to Re⁴⁺ in LiCl-KCl eutectic had a vast difference between them as can be seen in table XX. A reason for Te having a higher diffusivity than rhenium is due to Te⁴⁺ being less stable and more soluble than rhenium as was noted by Bailey et al.³² Additionally, Salakhova et al. that tellurium has a certain role by the chemical activity of freshly deposited tellurium in respect to the given metals. Furthermore, the high number of electron transfer seen in Table XIX can be due the profound cathode reduction that any telluride ions present might undergo at this potential to create ReTe₂.⁷¹

Table XXI summarizes the formal potentials for different reduction reactions. The formal potentials of Te(IV) reduction reaction is shifted to a more positive potential than Re(IV). The formal potential of Te is close to what Salakhova report (0.4V) at room temperature conditions.⁷¹ However, there is an order of magnitude difference between Re potentials. This could be due to tellurium having a more positive OCP value (0.4V) than rhenium (0.12V) resulting in LiCl-KCl, resulting in a more positive formal potential.

Electrochemical impedance spectroscopy:

Figures 58 show the EIS of the tungsten electrode in 1wt% TeCl₄/ReCl₃ at 450 potentials in the forms of Nyquist and Bode plots, respectively. These figures are based on open circuit conditions.

The rationale behind carrying out EIS measurements was to understand the structural characteristics of the molten salts with and without addition of TeCl₄/ReCl₃. The physical and electrical properties of the molten salt systems depend on the structure and interactions of the constituents. The structural arrangements that are present in molten salts can be viewed as intermediates between discrete chemical bonds and periodic crystalline lattices⁶⁰. The inter-atomic interactions determine the local ordering of the molten salt. The electrochemical properties are influenced by the structural characteristics of the molten salt. When cations are present in the molten salt with different sizes and different charge densities, an asymmetric polarization of anions is anticipated which affects the electrostatic stability of the mixture⁶¹.

In order to better understand the interfacial impedance behavior, the EIS data were fitted into an electrical equivalent circuit (EEC) and the values are shown in Table XXII. In general, the impedance spectra showed only one time constant. Therefore, the EIS data was modeled using 1 R || Ø loops. In the equivalent circuit, R_u and R_p represent the electrolyte resistance and resistance to charge transfer, while the Ø (Y is used as a substitute) symbol represents a double layer also known as an imperfect capacitor, respectively. The R₁-Y₁ loop represents the electrode/LiCl-KCl electrolyte interface. Y₁ represents imperfect capacitance whose impedance (Z) is given by the relation: $Z = 1/[(Q_0 \omega^n)] * e^{-(\pi/2)ni}$ where ω = frequency, and the exponent “n” represents the surface heterogeneity or continuously distributed time constants for charge transfer when $0 < n < 1$.³³ W_d represents a diffusion limited charge transfer

resistance (Warburg component), respectively that are associated with the redox species other than LiCl-KCl. It should be noted that the values of Y_0 and W_f are expressed as admittance. Smaller magnitudes of R_u and R_p , and larger values of Y_0 and W_d will lead to better charge transfer characteristics.

Table XXII. EIS circuit component values of LiCl-KCl-TeCl₄-ReCl₃ system at open circuit potentials for 450 °C using molybdenum working electrode.

Temperature, °C	Circuit Component	Circuit Component Value
450	R_u	$455.2 \cdot 10^{-3} \Omega$
	Y_0	$12.05 \cdot 10^{-3} S \cdot s^a$
	α	$720.1 \cdot 10^{-3}$
	W_d	$148.7 \cdot 10^{-3} S \cdot s^{1/2}$
	R_p	44.17Ω

The overall behavior of the system favored more of the solution with only tellurium added to it than rhenium. The charge transfer resistance was given as R_p at high frequencies because the resistance due to the constant phase element would be negligible. The impedance due to the constant phase elements became significant only below 10Hz as seen from the Bode plots. The capacitance due to Y_0 had the same order of magnitude as the pure rhenium mixture, while the time constant fitted more with pure tellurium solution. The overall behavior of the system favoring more of the pure tellurium experiments could be attributed to Te ions having

better solubility in solution, resulting in the electrode/molten salt interface having a greater presence than rhenium ions at OCP potentials. The Warburg diffusion component was present which was also seen when tellurium was present in the molten salt.

An EEC model consisting of two parallel RC loops connected in series, and each RC loop having a Warburg element was proposed to describe the impedance behavior of LiCl-KCl molten salt at 700 °C–800 °C by Cohen et al.⁶¹ The reported values of solution resistance (R_s), double layer capacitance (Q_1), capacitance due to adsorption of ions (Q_2), and Warburg coefficient were reported as 0.685 ohm, 58–80 μF , 1.8–2.3 mF, and 2–4 mS, respectively⁶². The EIS data of this study was fitted with a different EEC model but the values of the solution resistance circuit components showed almost similar order of magnitude as Kim et al.⁶³ reported EIS data of a molybdenum electrode in LiCl-KCl- UCl_3 at 773K and fitted their data to an EEC similar to the one used in this work and the values of the circuit components showed a similar order of magnitude as reported in this work. While the capacitance values due to charged layer had a higher value in this study than the one reported by Kim et al.

Most of the literature on pyroprocessing of used nuclear fuels focuses on the electrochemical behaviors of fission product as cations such as La^{3+} , Nd^{3+} , Sm^{3+} etc.⁶⁴ Not much information is available on the anion type fission products such as Te^{2-} and Γ^- . It is generally assumed that anions present in the molten salt may not interfere with the cathodic reduction of actinides. This study attempts to fill the knowledge gap and shows that Te^{2-} will be oxidized to $\text{Te}(0)$ and Te^{n+} during the pyroprocessing conditions and adversely affect the stability of the electrodeposits because of the low melting point of Te and volatility of TeCl_n compounds. The electrochemical data presented in this work such as formal potentials of different Te

species (Te^{2-} and Te^{4+}) and their diffusivities are useful in designing more efficient pyrochemical processes.

6.3 Conclusions

The reduction of Re^{4+} and Te^{4+} to ReTe_2 potentially occurred in four steps, where rhenium was reduced first followed by tellurium. The formal potential of Re(IV) to Re(III) reduction at $450\text{ }^\circ\text{C}$ was estimated as 0.032 VAg/AgCl , while the formal potential of Te(IV) to Te(II) was estimated as 0.376 VAg/AgCl for $1\text{ wt\% TeCl}_4/\text{ReCl}_3$. The further reduction of ReTe_2 was seen to undergo 2 more reduction steps. It was first reduced to a $3e^-$ state, followed by a single electron transfer before lithium reduction occurred.

The diffusion coefficients of Re^{4+} and Te^{4+} at $450\text{ }^\circ\text{C}$ were 5.17×10^{-5} and $684.51 \times 10^{-5}\text{ cm}^2\text{ s}^{-1}$, respectively in the $1\text{wt\% TeCl}_4/\text{ReCl}_3$ electrolyte.

The electrochemical impedance spectroscopic data could be fitted with an equivalent circuit representing one time constant. The overall electrochemical system resembled more of pure tellurium addition, while the capacitance value was closer to rhenium mixture than tellurium.

Chapter 7: Electrochemical Behavior of Te in LiCl-KCl with Li₂O addition at 550 °C

7.1 Experimental Procedure

Due to the hygroscopic nature of the LiCl-KCl eutectic salt, all experiments were performed in a glove box (MBraun) under an inert argon environment. Oxygen and moisture levels were maintained less than 2 ppm. The eutectic salt was created by thoroughly mixing 44.6wt% LiCl (99.995%, ultra-dry) with 55.4wt% KCl (99.998%, ultra- dry). Once the eutectic salt was made, 1-2 wt% Li₂O was added to the solution. To add TeCl₄ to the solution the following procedure was used due to the high vapor pressure of tellurium tetrachloride (TeCl₄, 99.9% purity) to create the mixture. The eutectic salt was melted in a glassy carbon crucible and left to cool over an 8-h period. Due to the high wetting angle between the salt and glassy carbon crucible, the eutectic ingot was able to be taken from the crucible in one piece. Afterward, 5 wt% of TeCl₄ powder was placed in the glassy carbon crucible followed by the eutectic ingot. The entire salt mixture was heated to 10 degrees below the vapor temperature of TeCl₄ (200 °C) and soaked at this temperature for 15 minutes to allow the system to come to equilibrium. The temperature was then brought to 353 °C and let set for 1 hour to allow solution to melt. Once the ingot was created, the completed ingot was broken into half and placed in an alumina crucible for electrochemical testing.

Before bringing the created salt mixture to operating temperatures the furnace was brought to 10 degrees below sublimation temperature of the TeCl₄ (200 °C) for 15 minutes. After soaking at this temperature, the furnace was brought up to 450 °C and equilibrated for 10 minutes before starting the electrochemical measurements. The addition of TeCl₄ was 5wt%

or 1mol%. All chemicals were procured from Alfa Aesar and used without further purification.

Due to the lack of time and funding the concentration values of TeCl_4 retained in the molten salt that was used in chapter 3 that was determined by using induction coupled plasma- mass spectroscopy (ICP-MS) technique was also used for this chapter. The sampling of salt for ICP-MS analysis was carried out by dipping a tungsten rod in the molten salt once the furnace had reached operating temperature followed by taking samples at 1 hour intervals. The solidified salts were scraped off the tungsten rod using a stainless steel spatula. The weight of the sampled salt was measured using an analytical balance (Radwag, XA110/2X) capable of measuring a minimum weight of 1mg with a resolution of 0.01mg and dissolved in 30ml of 1% nitric acid. Three samples were extracted for a given condition. The ICP-MS analysis of Te was performed at the Analytical Sciences Laboratory of University of Idaho by following a comprehensive quality management plan that maintains compliance with applicable standards of ISO 17025. The concentration of Te retained in the molten salt was analyzed as a function of time after temperature equilibration, and after completion of electrochemical tests. The amount of TeCl_4 after completion of the tests was significantly lower than the initial amount added which was attributed to the reduction of TeCl_4 to $\text{Te}(0)$ deposited on the working electrode as liquid metal and partially precipitate out of solution. Table XXIII summarizes TeCl_4 concentration retained in the molten salt as a function of time after temperature equilibration. The electrochemical results are discussed with reference to the initial addition amount for brevity.

Table XXIII. ICP-MS analyses of TeCl_4 retained in the LiCl-KCl molten salt as a function of time, and after testing.

Initial addition of TeCl_4	Dwelling time at 450 °C, h	TeCl_4 retained in the molten salt, %
1wt%	0	79 ± 0.02
	1	78 ± 0.022
	2	76 ± 0.016
	3	73 ± 0.031
	4	72 ± 0.012
	After testing	46 ± 0.12
5wt%	0.1	4.2 ± 0.2
	2	3.85 ± 0.11
	After testing	3.6 ± 0.25

Open circuit potential measurement, electrochemical impedance spectroscopy (EIS), cyclic voltammetry, and square wave voltammetry, were performed in LiCl+KCl eutectic melt at 550 °C with and without addition of 5 wt% TeCl_4 while containing 1 to 2 wt% Li_2O by using a computer controlled potentiostat (Gamry Instruments, model: Reference 1000, software for data generation: Gamry Framework, version 7.03, software for data analysis: Gamry Echem Analyst version 7.03). The temperature stability of the molten salt was ± 2 °C. A fuzzy logic proportional–integral–derivative (PID) controller (Tempco, model: TEC-9100) was used for controlling the temperature of the furnace using a type K (chromel-alumel) thermocouple. The thermocouple of the furnace was NIST calibrated. The temperature of the molten salt was

measured by using a NIST calibrated K-type thermocouple shielded by an alumina tube (99.8% purity, Omega) and a digital thermometer (Omega, model HH91). The working electrode was a 2mm diameter tungsten rod (99.95%, Alfa Aesar). The counter electrode was a 2 mm diameter molybdenum rod (99.95%, Alfa Aesar). The reference electrode was an in-house made AgCl coated Ag wire (99.9%) placed in a borosilicate glass tube that contained LiCl+KCl eutectic thoroughly mixed with 1wt% AgCl (99.997%, ultra-dry). The working and counter electrodes were polished using a series of emery papers down to 2000 grit. The polished surface was wiped down with propanol and acetone and dried in a vacuum oven for 16h at 120 °C. The cleaning, and conditioning protocols were strictly followed for each set of experiments to ensure repeatability. After reaching the set temperature of 550 °C, the electrodes were conditioned in the open circuit potential for 15min before starting the electrochemical tests. The electrodes were placed in an equidistance triangular arrangement. The distance between each electrode was one inch. The surface area ratio of the counter and working electrodes was at least 2.5. The surface area was calculated by physically measuring the diameter and the immersion depth of the working and counter electrodes in the molten salt after the experiments using an inch ruler with 32nd tick mark. The measured depth was compared with the initial set value (typical variation after converting to cm was 0.5 – 0.75cm due to capillary effect). The surface area measured by geometric calculation is prone to error caused by meniscus of the molten salt, and salt built up layer. No effort was taken to address the errors introduced by the geometric surface area calculations which may vary from 7%–12%.

Yoon et al. proposed a relation between the Ag/AgCl reference potential and Cl₂/Cl⁻ potential that was a function of molar fraction of AgCl but independent of temperature between 723–823K and given as⁴⁴:

$$E_{\text{Cl}_2/\text{Cl}^-} = (-0.8726 \pm 0.00486) + (0.05896 \pm 0.00108) \ln(X) \quad (84)$$

Where X = mole fraction of AgCl. Accordingly, the Ag/AgCl potential of this study is -1.197V vs the redox potential of Cl₂/Cl⁻. CV was carried out at different potential windows and at different scan rates. All potentials in this paper are given with reference to the Ag/AgCl electrode whose potential is -1.197 V_{Cl₂/Cl⁻}. The maximum potential window signified decomposition of the LiCl-KCl eutectic by reduction of lithium at the cathodic end and chlorine evolution at the anodic end. Cyclic voltammetry studies were carried out at different scan rates from 100mVs⁻¹ to 5000mVs⁻¹. Electrochemical impedance spectroscopy was carried out at the open circuit condition and at different peak potential conditions (as noted in the cyclic voltammograms) under potentiostatic conditions by super imposing an *ac* signal of 10mV by scanning the frequency from 10kHz to 0.1Hz. Square wave voltammetry was conducted between OCP and -2.5 V_{Ag/AgCl}; and between OCP and 1.2 V_{Ag/AgCl} at a frequency of 25Hz, pulse size of 25mV, step size of 1mV, and pulse time of 0.04s. All the electrochemical tests were either duplicated or triplicated to ensure reproducibility. The average values are presented.

7.2 Results and Discussions

Open Circuit Potential (OCP) Measurements

In the previous chapters, equilibrium measurement of tellurium in the molten salt with the surface of the tungsten electrode, at 550 °C was seen to shift the OCP to more positive

potentials. However, with the addition of Li₂O added both with and without tellurium the OCP shifted towards more negative potentials. Increase in the Li₂O concentration between 1 and 2 wt% resulted in a negative shift due to the exchange current density (i_0) by following the relation⁴⁵:

$$i_0 = nFk_0C_{O^{2-}} \quad (85)$$

Where, n = number of electrons, F = Faraday's constant, k_0 = rate constant for electron transfer, and $C_{O^{2-}}$ is bulk concentration of O²⁻ in the molten salt. The decrease in the i_0 value will shift the Tafel plots of the Teⁿ⁺/Te⁽ⁿ⁻¹⁾⁺ redox reactions such that the OCP could decrease with the increase in the Li₂O concentration. It is to be noted that even with the addition of Li₂O shifting the OCP to more negative potentials, the OCP with tellurium addition is still more positive than the OCP without the presence of TeCl₄, following the same trend that was seen in the previous chapters. The standard redox potential of Te is reported to be more positive than that of Pd, Ag, Mo, W, and other transition metals^{15,45}. The positive OCP values observed on the tungsten electrode indicated that the tungsten had significant active sites to support the redox reactions.

Cyclic voltammetry:

A full window CV scan was performed from -2.8V to 1.4 V_{Ag/AgCl} as seen in Figures 60 and 61. The cyclic voltammogram of LiCl-KCl eutectic with Li₂O addition (without TeCl₄ addition) showed two cathodic waves corresponding to lithium reduction that started at around -1.7V_{Ag/AgCl} and -2.6 V_{Ag/AgCl} and two anodic wave associated with oxygen gas evolution seen around 0 V_{Ag/AgCl} and chlorine gas evolution that started around 1.2V. No other

peaks were observed in between these two potentials on the tungsten electrode. The reduction potentials of lithium reported in the literature vary widely from -1.5V to -2.6V . For example, SEO et al. reported a value of -1.7 V at $650\text{ }^\circ\text{C}$ for the $\text{Li(I)}/\text{Li(0)}$ reaction with Li_2O addition⁷². On the other hand, Hur et al. showed lithium reduction occurring at $-0.4\text{ V}_{\text{LiPb}}$ at $650\text{ }^\circ\text{C}$ using stainless steel as a working electrode⁷³. There is still a lithium reduction peak that occurs at the same value that Liu et al. reported at a potential of $-2.6\text{ V}_{\text{Ag}/\text{AgCl}}$ for reduction of lithium at 873K ⁴⁷. The additional lithium peak that is seen is potentially due to the lithium attached to the oxygen being reduced.

Addition of TeCl_4 seen in Figure 61 introduced several additional peaks both in the cathodic and anodic directions. These additional peaks are due to the reduction and oxidation of tellurium. However, with the addition of oxygen to the system various tellurium oxide compounds could potentially form, resulting in the reaction that occurs at each peak being an oxide compound instead of just tellurium being reduced as was seen in previous chapters. Referring to a phase diagram of a tellurium oxygen system seen in a paper by V.P. Itkin et al., it can be seen that before any electrochemistry occurs that at $550\text{ }^\circ\text{C}$ TeO_2 can form with in the salt mixture⁷⁴.

Figure 62 and Figure 63 shows cyclic voltammograms on tungsten electrode in the cathodic direction with 5wt% TeCl_4 containing 1 and 2 wt% Li_2O in the LiCl-KCl eutectic salt at a smaller potential window. These peaks associated with Te species are clearly discerned in Figure 62 and 63 in comparison with the CV of LiCl-KCl eutectic without any addition of TeCl_4 . Figures 64 and 65 illustrates the full window (both in the cathodic and anodic directions) CV of 5wt% TeCl_4 containing LiCl-KCl molten salt at different scan rates with a

tungsten working electrode. The cathodic wave started at potential more negative than $-0.1V_{\text{Ag}/\text{AgCl}}$ for 1 wt% Li_2O addition, while it was more negative than $-0.47 V_{\text{Ag}/\text{AgCl}}$ when 2 wt% Li_2O was added. Five distinct cathodic peaks were observed for both 1 and 2 wt% Li_2O with Te addition. For 1 wt% Li_2O they were seen around $-0.787V$ (c_1), $-1.276V$ (c_2), $-1.558V$ (c_3), $-2.318V$ (c_4), and $-2.538V$ (c_5). During the reverse scan, five anodic peaks were recorded at $-1.307V$ (a_1), $-0.767V$ (a_2), $-0.478V$ (a_3), $0.623V$ (a_4), and $1.19 V_{\text{Ag}/\text{AgCl}}$ (a_5). For 2 wt% Li_2O they were seen around $-0.861V$ (c_1), $-1.15V$ (c_2), $-1.89V$ (c_3), $-2.361V$ (c_4), and $-2.561V$ (c_5). During the reverse scan, five anodic peaks were recorded at $-1.59V$ (a_1), $-1.33V$ (a_2), $-0.881V$ (a_3), $-0.411V$ (a_4), $-0.001V$ (a_5), and $0.53V_{\text{Ag}/\text{AgCl}}$ (a_6). The first cathodic wave (c_1) was attributed to the reduction of TeO_2 to TeO_2^- , and the second cathodic wave (c_2) was potentially due to reduction of TeO_2^- to TeO_3^{2-} . TeO_3^{2-} can potentially form in the solution and has been seen and used in various applications such as transparent coatings for thin film applications⁷⁵. In this application they saw TeO_3^{2-} taking a pyramidal structure in the pentahydrate compound. When comparing Figures 64 and 65 (1 and 2 wt% Li_2O), an additionally anodic peak arises in the 2 wt% that was not seen in 1 wt% addition. This peak that is seen around $-0.001V$ in Figure 65 is due to oxygen gas evolution. A reason for this not being seen in Figure 64 is the oxygen content was low enough that it was creating tellurium oxide compounds and there was not enough oxygen left to be oxidized where that was not the case for the 2 wt% addition. The cathodic wave (c_4) at a more negative potential was associated with formation of telluride ions (Te_x^{n-}). The number of electrons transferred could be determined from differential square wave pulse voltammetry, which will be discussed in a latter section. The anodic peaks a_1 , a_2 , a_3 , a_4 , and a_5 or a_6 were ascribed as the

reverse reactions of cathodic peaks c_5 , c_4 , c_3 , c_2 , and c_1 , respectively. The anodic wave (a_5 or a_6) taking off at about 1.2V was associated with evolution of chlorine.

Figures 62 and 63 shows the cyclic voltammograms between OCP and $-2.2 V_{Ag/AgCl}$ (more positive than the lithium reduction condition) where Figure 62 is 1 wt% Li_2O and Figure 63 is 2 wt% Li_2O . The first cathodic wave (c_1) starting at $-0.787 V$ for 1 wt% Li_2O and $-0.861 V$ evolved clearly at a scan rate of $0.2Vs^{-1}$ and higher. The second cathodic wave (c_2) occurred with a peak current at around $-1.276V$ for 1 wt% Li_2O and $-1.15V$ for 2 wt% Li_2O . A slight shift in OCP potential towards the negative direction was seen when the concentration of Li_2O was increased from 1 to 2 wt%. Additionally, upon doing the smaller windows, a third peak can be seen around $-2.17V$ for 1 wt% Li_2O and $-1.8V$ for 2 wt% Li_2O . Furthermore, as the scan rate increased as seen in Figures 62 and 63, which represents a dependency of the peak potential indicating that the cathodic reaction was not reversible. However, the peak current increased as a function of square root of the scan rate, as seen in Figure 66. The cathodic peaks c_2 and c_3 could be attributed to TeO_2 reducing to TeO_2^- and TeO_3^{2-} on the working electrode. These cathodic peaks were associated with soluble-soluble species, where soluble TeO_2 species were reduced to soluble TeO_3^{2-} ⁷⁶. Since the CV was interrupted at $-2.2 V$ no lithium reduction and oxidation peaks were observed. The anodic waves (a_1 , a_2) observed at about $(-1.58, -0.847) V_{Ag/AgCl}$ for 1 wt% Li_2O and $(-1.45, -0.989) V_{Ag/AgCl}$ for 2 wt% Li_2O were associated with the oxidation of soluble TeO_3^{2-} anionic species to TeO_2 . The following reactions (84) and (85) are what is potentially occurring at cathodic peaks (a_2) and (a_3) seen in Figure 62 and Figure 63.





It is noted that the peak potentials of anodic waves a_2 and a_3 were independent of the scan rates indicating reversibility of the reaction. A small peak (a_1) that is seen around $-1.59 \text{ V}_{\text{Ag}/\text{AgCl}}$ could potentially, due to Te^{2+} becoming Te^{4+} . This reaction could be creating TeO being oxidized back to TeO_3^{2-} . The anodic peaks observed at potentials more positive than $0.5 \text{ V}_{\text{Ag}/\text{AgCl}}$ for 1 and 2 wt% Li_2O for $550 \text{ }^\circ\text{C}$ as seen in Figures 64 and 65 could be due to the oxidation of Te^{4+} creating TeCl_4 as chlorine gas evolution occurs after oxygen evolution begins. Oxidation of Te to volatile formation of TeCl_4 has been:



The anodic peak observed at $0.63 \text{ V}_{\text{Ag}/\text{AgCl}}$ for 1 wt% Li_2O and $0.47 \text{ V}_{\text{Ag}/\text{AgCl}}$ for 2 wt% Li_2O was assigned to reaction (86), which is 0.55V more negative for 2 wt% and 0.71V for 1 wt% than the chlorine evolution potential. Lichtenstein et al. reported a similar value (0.71V negative to chlorine evolution potential) at $650 \text{ }^\circ\text{C}$ for the Te oxidation to Te^{2+} ¹⁸. At the temperatures these experiments were performed, TeCl_4 is volatile and can escape over time.

Figure 66 shows the linear relation observed between peak current density and the square root of the scan rate in 1 and 2 wt% Li_2O with 5 wt% addition of TeCl_4 containing LiCl-KCl eutectic at $550 \text{ }^\circ\text{C}$ using a tungsten electrode. Randles-Sevick equation describes the peak current density as a function of electrode surface area, bulk concentration of the redox species, and square root of the scan rate and diffusivity of redox species ⁵¹. The diffusion coefficient can be calculated from the Randles-Sevick relation as given in (87):

$$D^{1/2} = \left[\frac{i_p}{\sqrt{v}} \right] \left(\frac{1}{0.446nFAC_0} \right) \left(\frac{RT}{nF} \right)^{0.5} \quad (89)$$

Where i_p/\sqrt{v} is the slope of peak current vs. square root of scan rate, A is the surface area of electrode, and C_0 is the concentration of the Te species. Using the slopes taken from Figure 66 the diffusion coefficients of TeO_2 could be calculated for the two different weight percent of Li_2O . The peak current of soluble-insoluble redox species can be expressed as a function of \sqrt{v} and \sqrt{D} using the Berzins and Delahay relation⁵²:

$$i_p = 0.611 nFAC_0 \left(\frac{nF\vartheta D}{RT} \right)^{1/2} \quad (90)$$

The bulk concentration of TeCl_4 retained in the molten salt after two hours of thermal equilibrium was considered to calculate the diffusivities from the slope of the i_p vs \sqrt{v} plots. The number of electrons (n) involved in the reduction reaction was calculated from the square wave voltammetry data as shown in Figure 67 and Figure 68 by determining the width of half current peak ($W_{1/2}$) and using the relation^{53,54}:

$$n = 3.5 RT/(W_{1/2}F) \quad (91)$$

Alternately, the number of electrons for reversible soluble-soluble redox system can also be calculated from the CV data using the relations (92) and (93) proposed by Matsuda and Ayabe⁵⁵:

$$E_{p,c} = E_{1/2} - 1.11 \frac{RT}{nF} \quad (92)$$

$$E_{p,a} = E_{1/2} + 1.11 \frac{RT}{nF} \quad (93)$$

Where $E_{p,c}$ and $E_{p,a}$ are cathodic and anodic peak current potentials, respectively; $E_{1/2}$ is a half wave potential and expressed as:

$$E_{1/2} = E_{Te^{4+}/Te^{2+}}^0 + \frac{RT}{nF} \ln \left(\frac{\gamma_{Te^{4+}}}{\gamma_{Te^{2+}}} \right) + \frac{RT}{nF} \ln \left(\frac{\sqrt{D_{Te^{2+}}}}{\sqrt{D_{Te^{4+}}}} \right) \quad (94)$$

Formal potential for soluble-soluble system, E^{0*} is expressed as⁵⁶:

$$E_{Te^{4+}/Te^{2+}}^{0*} = E_{Te^{4+}/Te^{2+}}^0 + \frac{RT}{nF} \ln \left(\frac{\gamma_{Te^{4+}}}{\gamma_{Te^{2+}}} \right) \quad (95)$$

$$E_{Te^{4+}/Te^{2+}}^{0*} = \left(\frac{E_{p,a} + E_{p,c}}{2} \right) - \frac{RT}{nF} \ln \left(\frac{\sqrt{D_{Te^{2+}}}}{\sqrt{D_{Te^{4+}}}} \right) \quad (96)$$

Formal potential for reversible soluble-insoluble system can be expressed as^{18,56}:

$$E_{p,1a} = E_{Te^0/Te^{2-}}^{0*} + \frac{0.854RT}{nF} - \frac{RT}{nF} \ln(C_{Te^{2-}}) \quad (97)$$

$$E_{p,1c} = E_{Te^{2+}/Te^0}^{0*} - \frac{0.854RT}{nF} + \frac{RT}{nF} \ln(C_{Te^{2+}}) \quad (98)$$

Table XXIV and Table XXV summarizes the results of square wave voltammograms (SWV) given in Figures 67 and 68 and the number of electrons calculated based on the full width half wave of the differential current peaks using the expression given in (91). The peak potentials of different reduction reactions are listed which could be correlated to the formal potentials described in the expressions (96) to (98). The SWV data indicated that the cathodic peaks observed between -0.5 to $-1.9V$ in the CV could be assigned to the three-step reduction process of TeO_2 . For 1 wt% Li_2O this could potentially correlate to TeO_2 being reduced to TeO , while 2 wt% Li_2O resulted in the product of TeO^- due to a total of five electron transfer occurring over the three step process instead of four which was seen when only 1 wt% Li_2O was added. The number of electrons calculated from the SWV data was used for estimation of

the diffusivity of species based on the slopes of i_p vs \sqrt{v} plots given in Figure 66. Table XXVI lists the coefficient of diffusion of TeO_2 species in two different weight percent at 550 °C. Even though a quasi-reversible type reaction was observed, the diffusivity can be estimated based on the Randles–Sevcik equation or Berzins and Delahay relation. Similar approach has been reported by other researchers for calculating the diffusivities of lanthanide ions in the LiCl-KCl eutectic ^{51,57}. Bermejo et al. reported that the corrections required for cylindrical geometry of the working electrode can be neglected to use the semi-infinite relations assumed for the Randles–Sevcik (Eq. 87) or Berzins-Delahay (Eq. 88) relation when the scan rate is higher than 50mV s⁻¹ ⁵¹. The diffusivity values, in turn, were used for the estimation of formal potentials based on the relation (94). The formal potentials were determined based on the CV data using the relations (94) (96) and summarized in Table XXVII.

Table XXIV. Summary of the square wave voltammogram data of tungsten electrode in 5wt% TeCl_4 containing 1 wt% Li_2O in LiCl-KCl at 550 °C.

Peak ID	Peak potential, $V_{\text{Ag/AgCl}}$	Width at half peak, $(W_{1/2}), V$	Number of electrons	Reaction step
1	-0.55	0.35	0.709	$\text{TeO}_2 + e^- \rightarrow \text{TeO}_2^-$
2	-0.625	0.2	1.241	$\text{TeO}_2^- + e^- \rightarrow \text{TeO}_3^{2-}$
3	-1.05	0.14	1.773	$\text{TeO}_3^{2-} + 2e^- \rightarrow \text{TeO} + \text{O}_2$
4	-1.85	0.7	0.355	$\text{TeO} + e^- \rightarrow \text{TeO}^-$

Peak ID	Peak potential, $V_{\text{Ag/AgCl}}$	Width at half peak, $(W_{1/2}), V$	Number of electrons	Reaction step
5	-2.3	0.65	0.382	$2\text{TeO}^- + e^- \rightarrow 2\text{Te}(0) + \text{O}_2$

Table XXV. Summary of the square wave voltammogram data of tungsten electrode in 5wt% TeCl_4 containing 2 wt% Li_2O in LiCl-KCl at 550 °C.

Peak ID	Peak potential, $V_{\text{Ag/AgCl}}$	Width at half peak, $(W_{1/2}), V$	Number of electrons	Reaction step
1	-0.66	-0.088	2.82	$\text{TeO}_2 + 3e^- \rightarrow \text{TeO}_3^{3-}$
2	-0.985	-0.171	1.45	$\text{TeO}_3^{3-} + e^- \rightarrow \text{TeO} + \text{O}_2$
3	-1.71	-0.19	1.31	$\text{TeO} + e^- \rightarrow \text{TeO}^-$
4	-1.9	-0.08	3.1	$2\text{TeO} + 3e^- \rightarrow 2\text{Te}^- + \text{O}_2$
5	-2.09	-0.21	1.18	$\text{Te}^- + e^- \rightarrow \text{Te}^{2-}$

Table XXVI. Diffusivities of TeO₂ species in LiCl-KCl eutectic with 5 wt% TeCl₄ and 1 to 2 wt% addition of Li₂O at 550 °C.

Working Electrode	Li ₂ O Concentration, wt%	Initial concentration of TeCl ₄ , wt%	Diffusing species	Coefficient of diffusion, cm ² /s
Tungsten	1	5wt% (actual 3.85%)	TeO ₂	7.81×10^{-5}
	2	5wt% (actual 3.85%)	TeO ₂	3.58×10^{-5}

Table XXVII. Formal potentials of LiCl-KCl-TeCl₄-Li₂O system at 550 °C using tungsten working electrode.

Li ₂ O Concentration, wt%	Reaction	Formal potential in 1wt% TeCl ₄ , V _{Ag/AgCl}
1	$\text{TeO}_2 + e^- \rightarrow \text{TeO}_2^-$	0.247
2	$\text{TeO}_2 + 3e^- \rightarrow \text{TeO}_3^-$	0.039

The diffusivity of TeO₂ in LiCl-KCl eutectic with Li₂O addition decreased with an increase in the concentration of Li₂O. With the increase in Li₂O, there is more oxygen present with the solution. Due to this, there would be a greater quantity of TeO₂ present within the mixture resulting in an abundant amount of larger coordinated species within the solution that are diffusing to the surface of the electrode which could attribute to the decrease in diffusivity at

the higher concentration. A similar order of magnitude ($8.43 \times 10^{-5} \text{ cm}^2 \text{ s}^{-1}$) diffusivity was seen for pure tellurium at 550 °C in previous chapters for 1 wt% TeCl_4 . When the concentration was increased of Li_2O the diffusivity decreased. With this trend the addition of oxygen to the system affected the diffusivity of tellurium within the molten salt mixture.

Table XXVII summarizes the formal potentials for different reduction reactions. The formal potentials of TeO_2 reduction reaction in 1 and 2 wt% Li_2O oxidation reactions shifted in the negative direction with an increase in Li_2O . These values are more negative than what was reported by Bodewig and Plambeck who reported the oxidation potential of Te ($\text{Te} \rightarrow \text{Te}^{2+} + 2\text{e}^-$) to be -0.45V Vs Cl_2/Cl in LiCl-KCl at 400 °C which is about $0.74 \text{ V}_{\text{Ag}/\text{AgCl}}$ ²¹. Which follows the same trend that has been seen with the addition of oxygen to the overall system.

Electrochemical impedance spectroscopy:

Figure 69 and Figure 70 show the EIS of the tungsten electrode in 5wt% TeCl_4 with 1 and 2 wt% addition of Li_2O at 550 °C potentials in the forms of Nyquist and Bode plots, respectively. These figures are based on open circuit conditions. The Bode plots in Figure 69a gave a slightly different trend, than was seen in Figure 70a for 2 wt% addition. The impedance modulus for 1 wt% was slightly higher than at 2 wt% for open circuit potentials.

The rationale behind carrying out EIS measurements was to understand the structural characteristics of the molten salts with the addition of TeCl_4 and Li_2O . The physical and electrical properties of the molten salt systems depend on the structure and interactions of the constituents. The structural arrangements that are present in molten salts can be viewed as intermediates between discrete chemical bonds and periodic crystalline lattices⁶⁰. The inter-

atomic interactions determine the local ordering of the molten salt. The electrochemical properties are influenced by the structural characteristics of the molten salt. When cations are present in the molten salt with different sizes and different charge densities, an asymmetric polarization of anions is anticipated which affects the electrostatic stability of the mixture⁶¹.

In order to better understand the interfacial impedance behavior, the EIS data were fitted into an electrical equivalent circuit (EEC) and the values are shown in Table XXVIII. In general, the impedance spectra showed only one time constant. Therefore, the EIS data was modeled using 1 R|| \emptyset loops. In the equivalent circuit, R_u and R_p represent the electrolyte resistance and resistance to charge transfer, while the \emptyset (Y is used as a substitute) symbol represents a double layer also known as an imperfect capacitor, respectively. The R_1 - Y_1 loop represents the electrode/LiCl-KCl electrolyte interface. Y_1 represents imperfect capacitance whose impedance (Z) is given by the relation: $Z = 1/[(Q_0 \omega^n)] * e^{-(\pi/2)ni}$ where ω = frequency, and the exponent “ n ” represents the surface heterogeneity or continuously distributed time constants for charge transfer when $0 < n < 1$.³³ W_d represents a diffusion limited charge transfer resistance (Warburg component), respectively that are associated with the redox species other than LiCl-KCl. It should be noted that the values of Y_0 and W_d are expressed as admittance. Smaller magnitudes of R_u and R_p , and larger values of Y_0 and W_d will lead to better charge transfer characteristics.

Table XXVIII. EIS circuit component values of LiCl-KCl-TeCl₄-Li₂O system at open circuit potentials for 550 °C using tungsten working electrode.

Li ₂ O Concentration, wt%	Circuit Component	Circuit Component Value
1	R _u	577.4*10 ⁻³ Ω
	Y ₀	1.345*10 ⁻³ S*s ^a
	α	839.4*10 ⁻³
	W _d	5.648*10 ⁻³ S*s ^{1/2}
	R _p	92.62 Ω
2	R _u	709.8*10 ⁻³ Ω
	Y ₀	167.7*10 ⁻³ S*s ^a
	α	768.2*10 ⁻³
	R _p	41.67 Ω

The solution resistance increased between 1 and 2 wt% addition of Li₂O. The charge transfer resistance was given as R_p at high frequencies because the resistance due to the constant phase element would be negligible, which decreased with an increase in Li₂O concentration. The impedance due to the constant phase elements became significant only below 10Hz as seen from the Bode plots. As concentration increased, the capacitance due to Y₀ also increase along with its time constant. This could be attributed to increased concentration of oxygen ions at the electrode/molten salt interface that were present in the OCP condition at 2 wt%

than 1 wt% Li₂O. The Warburg diffusion component was present in only the 1 wt% addition of Li₂O.

An EEC model consisting of two parallel RC loops connected in series, and each RC loop having a Warburg element was proposed to describe the impedance behavior of LiCl-KCl molten salt at 700 °C–800 °C by Cohen et al.⁶¹ The reported values of solution resistance (R_s), double layer capacitance (Q₁), capacitance due to adsorption of ions (Q₂), and Warburg coefficient were reported as 0.685 ohm, 58–80 μF, 1.8–2.3 mF, and 2–4 mS, respectively.⁶² The EIS data of this study was fitted with a different EEC model but the values of the solution resistance circuit components showed almost similar order of magnitude as Kim et al.⁶³ reported EIS data of a molybdenum electrode in LiCl-KCl-UCl₃ at 773K and fitted their data to an EEC similar to the one used in this work and the values of the circuit components showed a similar order of magnitude as reported in this work for the 2 wt% Li₂O, while the 1 wt% showed higher values in this study than the one reported by Kim et al.

Most of the literature on pyroprocessing of used nuclear fuels focuses on the electrochemical behaviors of fission product as cations such as La³⁺, Nd³⁺, Sm³⁺ etc.⁶⁴ Not much information is available on the anion type fission products such as Te²⁻ and I⁻. It is generally assumed that anions present in the molten salt may not interfere with the cathodic reduction of actinides. This study attempts to fill the knowledge gap and shows that with the addition of oxygen will affect the oxidation behaviors of tellurium during the pyroprocessing conditions and adversely affect the stability of the electrodeposits because of the low melting point of Te and the readily more soluble oxide compounds that could form. The electrochemical data presented in

this work such as formal potentials of different TeO_2 species and their diffusivities are useful in designing more efficient pyrochemical processes.

7.3 Conclusions

The reduction of TeO_2 resulted in a total of five electrochemical peaks arising before lithium reduction occurred. The formal potential of TeO_2 was estimated as 0.247 $\text{V}_{\text{Ag}/\text{AgCl}}$ for 1 wt%, while it was estimated to be 0.039 for 2 wt% addition which was observed to be a one-electron reaction step for 1 wt% and a three-electron reaction step for 2 wt%. For 1 wt% TeO_2 was potentially reduced to $\text{Te}(0)$ in five steps with varying electron transfer depending on the step which occurred at -2.3V. The reduction of TeO_2 completed at around $-2.09 \text{ V}_{\text{Ag}/\text{AgCl}}$ and was potential reduced to Te^{2-} .

The diffusion coefficients of TeO_2 were 7.81×10^{-5} (550 °C) and 3.58×10^{-5} (550 °C) cm^2s^{-1} , respectively in the 1wt% and 2wt% Li_2O electrolyte with the 5wt% TeCl_4 addition.

The electrochemical impedance spectroscopic data could be fitted with an equivalent circuit representing a resistor in series with a 1 loop $\text{R}||\text{CPE}$. Diffusion limited impedance was observed at OCP for 1wt% Li_2O . The charge transfer resistance showed a decrease with an increase in Li_2O concentration.

Chapter 8: Electrochemical Behavior of Re in LiCl-KCl with Li₂O addition at 550 °C

8.1 Experimental Procedure

Due to the hygroscopic nature of the LiCl-KCl eutectic salt, all experiments were performed in a glove box (MBraun) under an inert argon environment. Oxygen and moisture levels were maintained less than 2 ppm. The eutectic salt was created by thoroughly mixing 44.6wt% LiCl (99.995%, ultra-dry) with 55.4wt% KCl (99.998%, ultra-dry). Once the eutectic salt was made, 1-2 wt% Li₂O was added to the solution. The eutectic salt was created by thoroughly mixing 44.6wt% LiCl (99.995%, ultra-dry) with 55.4wt% KCl (99.998%, ultra-dry). Once the eutectic salt is created, 5 wt% ReCl₃ was placed in a mortar and mixed for 5 minutes along with 1 to 2 wt% Li₂O with the eutectic salt to make sure the solution was homogenized. Afterward, the completed mixture was placed in an alumina crucible and brought to operating temperature of 550 °C. All chemicals were procured from Alfa Aesar and used without further purification.

Due to the lack of time and funding the concentration values of ReCl₃ retained in the molten salt that was used in chapter 5 that was determined by using induction coupled plasma- mass spectroscopy (ICP-MS) technique was also used for this chapter. The sampling of salt for ICP-MS analysis was carried out by dipping a tungsten rod in the molten salt once the furnace had reached operating temperature followed by taking samples at 1 hour intervals. The solidified salts were scraped off the tungsten rod using a stainless steel spatula. The weight of the sampled salt was measured using an analytical balance (Radwag, XA110/2X) capable of measuring a minimum weight of 1mg with a resolution of 0.01mg and dissolved in 30ml of 1% nitric acid. Three samples were extracted for a given condition. The ICP-MS analysis of Te

was performed at the Analytical Sciences Laboratory of University of Idaho by following a comprehensive quality management plan that maintains compliance with applicable standards of ISO 17025. The concentration of Re retained in the molten salt was analyzed as a function of time after temperature equilibration, and after completion of electrochemical tests. Table XXIX summarizes ReCl_3 concentration retained in the molten salt as a function of time after temperature equilibration. The electrochemical results are discussed with reference to the initial addition amount for brevity. With this test containing 5 wt% ReCl_3 the quantity of the two hour test lost was used in respect to how much would be an equivalent retainment for 5 wt% ReCl_3 .

Table XXIX. ICP-MS analyses of ReCl_3 retained in the LiCl-KCl molten salt as a function of time, and after testing.

Initial addition of ReCl_3	Dwelling time at 550 °C, h	ReCl_3 retained in the molten salt, %
1 %	0	170.95
	1	115.42
	2	74.12
	3	45.18
	4	71.12

Open circuit potential measurement, electrochemical impedance spectroscopy (EIS), cyclic voltammetry, and square wave voltammetry, were performed in LiCl+KCl eutectic melt at 550 °C with and without addition of 5 wt% ReCl_3 while containing 1 to 2 wt% Li_2O by using a computer controlled potentiostat (Gamry Instruments, model: Reference 1000, software for

data generation: Gamry Framework, version 7.03, software for data analysis: Gamry Echem Analyst version 7.03). The temperature stability of the molten salt was ± 2 °C. A fuzzy logic proportional–integral–derivative (PID) controller (Tempco, model: TEC-9100) was used for controlling the temperature of the furnace using a type K (chromel-alumel) thermocouple. The thermocouple of the furnace was NIST calibrated. The temperature of the molten salt was measured by using a NIST calibrated K-type thermocouple shielded by an alumina tube (99.8% purity, Omega) and a digital thermometer (Omega, model HH91). The working electrode was a 2mm diameter tungsten rod (99.95%, Alfa Aesar). The counter electrode was a 2 mm diameter molybdenum rod (99.95%, Alfa Aesar). The reference electrode was an in-house made AgCl coated Ag wire (99.9%) placed in a borosilicate glass tube that contained LiCl+KCl eutectic thoroughly mixed with 1wt% AgCl (99.997%, ultra-dry). The working and counter electrodes were polished using a series of emery papers down to 2000 grit. The polished surface was wiped down with propanol and acetone and dried in a vacuum oven for 16h at 120 °C. The cleaning, and conditioning protocols were strictly followed for each set of experiments to ensure repeatability. After reaching the set temperature of 550 °C, the electrodes were conditioned in the open circuit potential for 15min before starting the electrochemical tests. The electrodes were placed in an equidistance triangular arrangement. The distance between each electrode was one inch. The surface area ratio of the counter and working electrodes was at least 2.5. The surface area was calculated by physically measuring the diameter and the immersion depth of the working and counter electrodes in the molten salt after the experiments using an inch ruler with 32nd tick mark. The measured depth was compared with the initial set value (typical variation after converting to cm was 0.5 – 0.75cm due to capillary effect). The surface area measured by geometric calculation is prone to error

caused by meniscus of the molten salt, and salt built up layer. No effort was taken to address the errors introduced by the geometric surface area calculations which may vary from 7%–12%.

Yoon et al. proposed a relation between the Ag/AgCl reference potential and Cl₂/Cl⁻ potential that was a function of molar fraction of AgCl but independent of temperature between 723–823K and given as⁴⁴:

$$E_{\text{Cl}_2/\text{Cl}^-} = (-0.8726 \pm 0.00486) + (0.05896 \pm 0.00108) \ln(X) \quad (99)$$

Where X = mole fraction of AgCl. Accordingly, the Ag/AgCl potential of this study is -1.197V vs the redox potential of Cl₂/Cl⁻. CV was carried out at different potential windows and at different scan rates. All potentials in this paper are given with reference to the Ag/AgCl electrode whose potential is -1.197 V_{Cl₂/Cl⁻}. The maximum potential window signified decomposition of the LiCl-KCl eutectic by reduction of lithium at the cathodic end and chlorine evolution at the anodic end. Cyclic voltammetry studies were carried out at different scan rates from 100mVs⁻¹ to 5000mVs⁻¹. Electrochemical impedance spectroscopy was carried out at the open circuit condition and at different peak potential conditions (as noted in the cyclic voltammograms) under potentiostatic conditions by super imposing an *ac* signal of 10mV by scanning the frequency from 10kHz to 0.1Hz. Square wave voltammetry was conducted between OCP and -2.8 V_{Ag/AgCl}; and between OCP and 1.2 V_{Ag/AgCl} at a frequency of 25Hz, pulse size of 25mV, step size of 1mV, and pulse time of 0.04s. All the electrochemical tests were either duplicated or triplicated to ensure reproducibility. The average values are presented.

8.2 Results and Discussions

Open Circuit Potential (OCP) Measurements

In the previous chapters, equilibrium measurement of rhenium in the molten salt with the surface of the tungsten electrode, at 550 °C was seen to shift the OCP to more positive potentials. However, with the addition of Li₂O added both with and without rhenium the OCP shifted towards more negative potentials. Increase in the Li₂O concentration between 1 and 2 wt% resulted in a negative shift due to the exchange current density (*i*₀) by following the relation⁴⁵:

$$i_0 = nFk_0C_{O^{2-}} \quad (100)$$

Where, *n* = number of electrons, *F* = Faraday's constant, *k*₀ = rate constant for electron transfer, and *C*_{O²⁻} is bulk concentration of O²⁻ in the molten salt. The decrease in the *i*₀ value will shift the Tafel plots of the Re^{*n*+}/Re^{(*n*-1)+} redox reactions such that the OCP could decrease with the increase in the Li₂O concentration. It is to be noted that even with the addition of Li₂O shifting the OCP to more negative potentials, the OCP with rhenium addition is still more positive than the OCP without the presence of ReCl₃, following the same trend that was seen in the previous chapters. The standard redox potential of Re is reported to be more positive than that of Pd, Ag, Mo, W, and other transition metals^{15,45}. The positive OCP values observed on the tungsten electrode indicated that the tungsten had significant active sites to support the redox reactions.

Cyclic voltammetry:

A full window CV scan was performed from -2.8V to $1.4\text{ V}_{\text{Ag}/\text{AgCl}}$ as seen in Figures 72 and 73. The cyclic voltammogram of LiCl-KCl eutectic with Li_2O addition (without ReCl_3 addition) showed two cathodic waves corresponding to lithium reduction that started at around $-1.7\text{V}_{\text{Ag}/\text{AgCl}}$ and $-2.6\text{ V}_{\text{Ag}/\text{AgCl}}$ and two anodic wave associated with oxygen gas evolution seen around $0\text{ V}_{\text{Ag}/\text{AgCl}}$ and chlorine gas evolution that started around 1.2V . No other peaks were observed in between these two potentials on the tungsten electrode. The reduction potentials of lithium reported in the literature vary widely from -1.5V to -2.6V . For example, SEO et al. reported a value of -1.7 V at $650\text{ }^\circ\text{C}$ for the $\text{Li(I)}/\text{Li(0)}$ reaction with Li_2O addition⁷². On the other hand, Hur et al. showed lithium reduction occurring at $-0.4\text{ V}_{\text{LiPb}}$ at $650\text{ }^\circ\text{C}$ using stainless steel as a working electrode⁷³. There is still a lithium reduction peak that occurs at the same value that Liu et al. reported at a potential of $-2.6\text{ V}_{\text{Ag}/\text{AgCl}}$ for reduction of lithium at 873K ⁴⁷. The additional lithium peak that is seen is potentially due to the lithium attached to the oxygen being reduced.

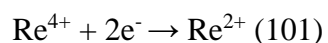
Addition of ReCl_3 seen in Figure 73 introduced several additional peaks both in the cathodic and anodic directions. However, when comparing 1 to 2 wt% Li_2O addition with ReCl_3 that more peaks are seen with only 1 wt% than with 2 wt% Li_2O . These additional peaks are due to the reduction and oxidation of rhenium. With the addition of oxygen to the system various rhenium oxide compounds could potentially form, resulting in the reaction that occurs at each peak being an oxide compound instead of just rhenium being reduced as was seen in previous chapters. With rhenium disproportionate into Re(IV) , as was seen with tellurium ReO_2 could potentially form before any electrochemistry occurs.

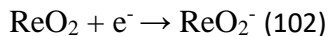
Figure 74 and Figure 75 shows cyclic voltammograms on tungsten electrode in the cathodic direction with 5wt% ReCl_3 containing 1 and 2 wt% Li_2O in the LiCl-KCl eutectic salt at a smaller potential window. It can be seen in these figures that as the scan rate increased the peak resolution decreased. This could be due to the reactions not having enough time to occur at higher scan rates. For this reason, Figures 76 and 77 show only the 200 mV/s scan rate so the peaks can be discerned for rhenium redox. Figures 78 and 79 illustrates the full window (both in the cathodic and anodic directions) CV of 5wt% ReCl_3 containing LiCl-KCl molten salt at different scan rates with a tungsten working electrode. The cathodic wave started at potential more negative than $-0.5V_{\text{Ag/AgCl}}$ for 1 wt% Li_2O addition, while it was more negative than $-1.5 V_{\text{Ag/AgCl}}$ when 2 wt% Li_2O was added. Two distinct cathodic peaks were observed for both 1 and 2 wt% Li_2O with Re addition. For 1 wt% Li_2O they were seen around $-0.686V$ (c_1) and $-1.89V$ (c_2). During the reverse scan, five anodic peaks were recorded at $-1.57V$ (a_1), $-1.266V$ (a_2), $-1.01V$ (a_3), $-0.655V$ (a_4), and $-0.329 V_{\text{Ag/AgCl}}$ (a_5). For 2 wt% Li_2O , two cathodic peaks were seen around $-2.07V$ (c_1) and $-2.25V$ (c_2). During the reverse scan, two additional anodic peaks were recorded passed lithium reduction which was seen at $-2.39V$ (a_1), $-0.968V$ (a_2), and $-0.04V$ (a_3). The first cathodic wave (c_1) for 1 wt% Li_2O addition could be attributed to the reduction of Re(IV) being reduced to Re(III) instead of a rhenium oxide compound, and the second cathodic wave (c_2) was potentially due to reduction of Re(III) . The electron transfer that is occurring will be discussed later with SWV. However, for 2 wt% Li_2O reduction of Re did not start until $-2V$. With a higher concentration of oxygen in the system the probability of rhenium oxide compounds forming increased. This can be seen by the fact that no reduction was seen until a more negative potential. For 2wt% Li_2O , the compound that is potentially being reduced is ReO_2 . Benjamin P. Hahn et al.

experimented on the deposition of ReO_4^- in an aqueous solution. During this process they saw the formation of $\text{Re}^{\text{III}}_2\text{O}_3$. However, this compound is unstable and disproportionated into $\text{Re}^{\text{IV}}\text{O}_2$ and $\text{Re}(0)$ ⁷⁷. If ReO_2 is being reduced to the $\text{Re}^{\text{III}}_2\text{O}_3$, then (c₂) with 2 wt% Li_2O addition could be attributed to the reduction of $\text{Re}(0)$ from this disproportionation. When comparing Figures 78 and 79 (1 and 2 wt% Li_2O), an additionally anodic peak arises in the 2 wt% that was not seen in 1 wt% addition. This peak that is seen around 0.04V in Figure 79 is due to oxygen gas evolution. A reason for this not being seen in Figure 78 is the oxygen content was low enough that any available oxygen formed rhenium oxide compounds during anodic cycle and there was not enough oxygen left to create an oxygen gas evolution peak which was not the case for the 2 wt% addition. The cathodic wave (c₄) seen in Figure 78 at a potential of 0.159V could be due a rhenium oxide compound that was formed during anodic sweep being reduced before the CV reached the starting potential that was taken at open circuit value. The number of electrons transferred could be determined from differential square wave pulse voltammetry, which will be discussed in a latter section. The anodic peaks a₁, a₂, a₃, a₄, and a₅ for 1 wt% were ascribed as the reverse reactions of cathodic peaks c₂, and c₁, while for 2 wt% a₂ corresponded to c₁, respectively. The anodic wave that occurred past a₅ for 1 wt% and a₃ for 2 wt% that began taking off at about 1.2V was associated with evolution of chlorine.

Figures 76 and 77 shows the cyclic voltammograms between OCP and $-2.2 \text{ V}_{\text{Ag}/\text{AgCl}}$ (more positive than the lithium reduction condition) where Figure 76 is 1 wt% Li_2O and Figure 77 is 2 wt% Li_2O . The first cathodic wave (c₁) starting at -0.786 V for 1 wt% Li_2O and -1.496 V for 2 wt% evolved clearly at a scan rate of 0.2 Vs^{-1} . The second cathodic wave (c₂) occurred with a peak current at around -1.414 V for 1 wt% Li_2O and -1.748 V for 2 wt% Li_2O . A shift

in OCP potential towards the negative direction was seen when the concentration of Li_2O was increased from 1 to 2 wt%. Additionally, upon doing the smaller windows, a third peak can be seen around -1.97V for 1 wt% Li_2O and -2.096V for 2 wt% Li_2O . Furthermore, as the scan rate increased as seen in Figures 76 and 77, which represents a dependency of the peak potential indicating that the cathodic reaction was not reversible. However, the peak current increased as a function of square root of the scan rate, as seen in Figure 80. The cathodic peaks c_2 and c_3 could be attributed to Re^{2+} reducing to Re^+ then Re^- on the working electrode for 1 wt% Li_2O . For 2 wt% Li_2O addition c_2 could be ReO_2^- being reduced to $\text{Re}(0)$ and c_3 relating to $\text{Re}(0)$ reduced to Re^- . These cathodic peaks were associated with soluble-soluble species, where soluble ReO_2 species were reduced to soluble ReO_2^- for 2 wt% Li_2O . Lennart Sandbrink et al. researched the stability of ReO_x as a potential catalyst on TiO_2 substrates⁷⁸. It was seen that the composition of ReO_x underwent little change during the catalytic process. With this it could lead to assume that is one reason why for 2 wt% addition a reduction did not occur until a more negative potential along with not seeing very strong peaks, since little of the ReO_2 would have went through a redox reaction. Since the CV was interrupted at -2.2 V no lithium reduction and oxidation peaks were observed. The anodic waves (a_1 , a_2) observed at about (-1.67, -1.11) $V_{\text{Ag}/\text{AgCl}}$ for 1 wt% Li_2O and (-1.8, -1.45) $V_{\text{Ag}/\text{AgCl}}$ for 2 wt% Li_2O were associated with the oxidation of anionic species to $\text{Re}(0)$ for 1 wt% Li_2O and soluble Re^- for 2 wt% Li_2O . The following reactions (101) and (102) could potentially be what is occurring at cathodic peaks (c_1) for 1 wt% Li_2O and (c_1) for 2 wt% Li_2O seen in Figure 76 and Figure 77.





For the anodic peaks observed at potentials more positive than $-0.1 \text{ V}_{\text{Ag}/\text{AgCl}}$ for 1 and 2 wt% Li_2O for $550 \text{ }^\circ\text{C}$ as seen in Figures 78 and 79 are due to oxygen and chlorine evolution for 2 wt% and only chlorine evolution for 1 wt%.

Figure 80 shows the linear relation observed between peak current density and the square root of the scan rate in 1 and 2 wt% Li_2O with 5 wt% addition of ReCl_3 containing LiCl-KCl eutectic at $550 \text{ }^\circ\text{C}$ using a tungsten electrode. Randles-Sevick equation describes the peak current density as a function of electrode surface area, bulk concentration of the redox species, and square root of the scan rate and diffusivity of redox species⁵¹. The diffusion coefficient can be calculated from the Randles-Sevick relation as given in (103):

$$D^{1/2} = \left[\frac{i_p}{\sqrt{v}} \right] \left(\frac{1}{0.446nFAC_0} \right) \left(\frac{RT}{nF} \right)^{0.5} \quad (103)$$

Where i_p/\sqrt{v} is the slope of peak current vs. square root of scan rate, A is the surface area of electrode, and C_0 is the concentration of the Te species. Using the slopes taken from Figure 80 the diffusion coefficients of Re(IV) and ReO_2 could be calculated for the two different weight percent of Li_2O . The peak current of soluble-insoluble redox species can be expressed as a function of \sqrt{v} and \sqrt{D} using the Berzins and Delahay relation⁵²:

$$i_p = 0.611 nFAC_0 \left(\frac{nF\theta D}{RT} \right)^{1/2} \quad (104)$$

The bulk concentration of ReCl_3 retained in the molten salt after two hours of thermal equilibrium was considered to calculate the diffusivities from the slope of the i_p vs \sqrt{v} plots. The number of electrons (n) involved in the reduction reaction was calculated from the square

wave voltammetry data as shown in Figure 81 and Figure 82 by determining the width of half current peak ($W_{1/2}$) and using the relation^{53,54}:

$$n = 3.5 RT/(W_{1/2}F) \quad (105)$$

Alternately, the number of electrons for reversible soluble-soluble redox system can also be calculated from the CV data using the relations (106) and (107) proposed by Matsuda and Ayabe⁵⁵:

$$E_{p,c} = E_{1/2} - 1.11 \frac{RT}{nF} \quad (106)$$

$$E_{p,a} = E_{1/2} + 1.11 \frac{RT}{nF} \quad (107)$$

Where $E_{p,c}$ and $E_{p,a}$ are cathodic and anodic peak current potentials, respectively; $E_{1/2}$ is a half wave potential and expressed as:

$$E_{1/2} = E_{Re^{4+}/Re^{2+}}^0 + \frac{RT}{nF} \ln \left(\frac{\gamma_{Re^{4+}}}{\gamma_{Re^{2+}}} \right) + \frac{RT}{nF} \ln \left(\frac{\sqrt{D_{Re^{2+}}}}{\sqrt{D_{Re^{4+}}}} \right) \quad (108)$$

Formal potential for soluble-soluble system, E^{0*} is expressed as⁵⁶:

$$E_{Re^{4+}/Re^{2+}}^{0*} = E_{Re^{4+}/Re^{2+}}^0 + \frac{RT}{nF} \ln \left(\frac{\gamma_{Re^{4+}}}{\gamma_{Re^{2+}}} \right) \quad (109)$$

$$E_{Re^{4+}/Re^{2+}}^{0*} = \left(\frac{E_{p,a} + E_{p,c}}{2} \right) - \frac{RT}{nF} \ln \left(\frac{\sqrt{D_{Re^{2+}}}}{\sqrt{D_{Re^{4+}}}} \right) \quad (110)$$

Formal potential for reversible soluble-insoluble system can be expressed as^{18,56}:

$$E_{p,1a} = E_{\text{Re}^0/\text{Re}^-}^{0*} + \frac{0.854RT}{nF} - \frac{RT}{nF} \text{Ln}(C_{\text{Re}^-}) \quad (111)$$

$$E_{p,1c} = E_{\text{Re}^{2+}/\text{Re}^0}^{0*} - \frac{0.854RT}{nF} + \frac{RT}{nF} \text{Ln}(C_{\text{Re}^{2+}}) \quad (112)$$

Table XXX and Table XXXI summarizes the results of square wave voltammograms (SWV) given in Figures 81 and 82 and the number of electrons calculated based on the full width half wave of the differential current peaks using the expression given in (105). The peak potentials of different reduction reactions are listed which could be correlated to the formal potentials described in the expressions (110) to (112). The SWV data indicated that the cathodic peaks observed between -0.4 to -2V in the CV for 1 wt% Li_2O and between -1.3 to -2.2V for 2 wt% Li_2O could be assigned to the three-step reduction process of Re(IV) for 1 wt% and ReO_2 for 2 wt% Li_2O . For 1 wt% Li_2O this could potentially correlate to Re(IV) being reduced to Re^- , while 2 wt% Li_2O potentially resulted in Re(0) before lithium reduction occurred. The number of electrons calculated from the SWV data was used for estimation of the diffusivity of species based on the slopes of i_p vs \sqrt{v} plots given in Figure 80. Table XXXII lists the coefficient of diffusion of Re species in two different weight percent at 550°C . Even though a quasi-reversible type reaction was observed, the diffusivity can be estimated based on the Randles–Sevcik equation or Berzins and Delahay relation. Similar approach has been reported by other researchers for calculating the diffusivities of lanthanide ions in the LiCl-KCl eutectic^{51,57}. Bermejo et al. reported that the corrections required for cylindrical geometry of the working electrode can be neglected to use the semi-infinite relations assumed for the Randles–Sevcik (Eq. 87) or Berzins-Delahay (Eq. 88) relation when the scan rate is higher than 50mV s^{-1} ⁵¹. The diffusivity values, in turn, were used for the estimation of formal potentials based on the relation (94). The formal potentials were

determined based on the CV data using the relations (94) (96) and summarized in Table XXXIII.

Table XXX. Summary of the square wave voltammogram data of tungsten electrode in 5wt% ReCl_3 containing 1 wt% Li_2O in LiCl-KCl at 550 °C.

Peak ID	Peak potential, $V_{\text{Ag/AgCl}}$	Width at half peak, $(W_{1/2}), \text{V}$	Number of electrons	Reaction step
1	-0.611	-0.104	2.387	$\text{Re}^{4+} + 2e^- \rightarrow \text{Re}^{2+}$
2	-1.462	-0.588	0.874	$\text{Re}^{2+} + e^- \rightarrow \text{Re}^+$
3	-1.751	-0.173	1.773	$\text{Re}^+ + 2e^- \rightarrow \text{Re}^-$

Table XXXI. Summary of the square wave voltammogram data of tungsten electrode in 5wt% ReCl_3 containing 2 wt% Li_2O in LiCl-KCl at 550 °C.

Peak ID	Peak potential, $V_{\text{Ag/AgCl}}$	Width at half peak, $(W_{1/2}), \text{V}$	Number of electrons	Reaction step
1	-1.83	-0.31	0.8	$\text{ReO}_2 + e^- \rightarrow \text{ReO}_2^-$
2	-2.02	-0.07	3.55	$\text{ReO}_2^- + 3e^- \rightarrow \text{Re}^0 + \text{O}_2$
3	-1.71	-0.18	1.38	$\text{Re}^0 + e^- \rightarrow \text{Re}^-$

Table XXXII. Diffusivities of Re species in LiCl-KCl eutectic with 1 and 2 wt% Li₂O at 550°C.

Working Electrode	Li ₂ O Concentration, wt%	Initial concentration of TeCl ₄ , wt%	Diffusing species	Coefficient of diffusion, cm ² /s
Tungsten	1	5wt% (actual 4.74%)	Re ⁴⁺	0.034 × 10 ⁻⁵
	2	5wt% (actual 4.74%)	ReO ₂	0.0127 × 10 ⁻⁵

Table XXXIII. Formal potentials of LiCl-KCl-ReCl₃-Li₂O system at 550 °C using tungsten working electrode.

Li ₂ O Concentration, wt%	Reaction	Formal potential in 1wt% TeCl ₄ , V _{Ag/AgCl}
1	Re ⁴⁺ + 2e ⁻ → Re ²⁺	-0.245
2	ReO ₂ + e ⁻ → ReO ₂ ⁻	-0.342

The diffusivity of Re in LiCl-KCl eutectic with Li₂O addition decreased with an increase in the concentration of Li₂O. One reason for this is in the 1 wt% there is potentially more rhenium that has not created oxygen compounds, resulting in mostly rhenium species being reduced. When comparing diffusivity of rhenium without Li₂O addition compared to with, there is no noticeable difference in the rate of diffusivity. However, when 2 wt% Li₂O is

added to the solution, diffusivity decreases. With the increase in Li_2O , there is more oxygen present within the solution potentially resulting in forming ReO_2 . Due to this, there would be a decrease in diffusivity due to the larger coordination number that is present around the rhenium ion.

Table XXXIII summarizes the formal potentials for 1 and 2 wt% Li_2O addition. The formal potentials of Re(IV) and ReO_2 reduction reaction in 1 and 2 wt% Li_2O oxidation reactions shifted in the negative direction with an increase in Li_2O . Additionally, for diffusivity a similar order of magnitude ($0.063 \times 10^{-5} \text{ cm}^2 \text{ s}^{-1}$) diffusivity was reported for Re(IV) in $\text{AlCl}_3\text{-MeEtimCl}$ room temperature molten salt by Sandra Strubinger et al. ⁶⁹ In another paper by O.N. Vinogradov-Zhabrov et al., they saw a few orders of magnitude higher in value for diffusivity at 840 °C around $3.5 \times 10^{-5} \text{ cm}^2 \text{ s}^{-1}$ for 7 wt% Re^{4+} ⁷⁰.

Electrochemical impedance spectroscopy:

Figure 83 and Figure 84 show the EIS of the tungsten electrode in 5wt% ReCl_3 with 1 and 2 wt% addition of Li_2O at 550 °C potentials in the forms of Nyquist and Bode plots, respectively. These figures are based on open circuit conditions. The Bode plots in Figure 83a gave a slightly different trend, than was seen in Figure 84a for 2 wt% addition. The impedance modulus for 1 wt% started off at a higher impedance value before decreasing over the frequency range, while 2 wt% started off lower it increased and had the same impedance as 1 wt% started at a frequency of approximately 0.025 Hz before it decreased.

The rationale behind carrying out EIS measurements was to understand the structural characteristics of the molten salts with the addition of ReCl_3 and Li_2O . The physical and

electrical properties of the molten salt systems depend on the structure and interactions of the constituents. The structural arrangements that are present in molten salts can be viewed as intermediates between discrete chemical bonds and periodic crystalline lattices⁶⁰. The interatomic interactions determine the local ordering of the molten salt. The electrochemical properties are influenced by the structural characteristics of the molten salt. When cations are present in the molten salt with different sizes and different charge densities, an asymmetric polarization of anions is anticipated which affects the electrostatic stability of the mixture⁶¹.

In order to better understand the interfacial impedance behavior, the EIS data were fitted into an electrical equivalent circuit (EEC) and the values are shown in Table XXXIV. In general, the impedance spectra showed only one time constant. Therefore, the EIS data was modeled using 1 R|| \emptyset loops. In the equivalent circuit, R_u and R_p represent the electrolyte resistance and resistance to charge transfer, while the \emptyset (Y is used as a substitute) symbol represents a double layer also known as an imperfect capacitor, respectively. The R_1 - Y_1 loop represents the electrode/LiCl-KCl electrolyte interface. Y_1 represents imperfect capacitance whose impedance (Z) is given by the relation: $Z = 1/[(Q_0 \omega^n)] * e^{-(\pi/2)ni}$ where ω = frequency, and the exponent “ n ” represents the surface heterogeneity or continuously distributed time constants for charge transfer when $0 < n < 1$.³³ W_d represents a diffusion limited charge transfer resistance (Warburg component), respectively that are associated with the redox species other than LiCl-KCl. It should be noted that the values of Y_0 and W_d are expressed as admittance. Smaller magnitudes of R_u and R_p , and larger values of Y_0 and W_d will lead to better charge transfer characteristics.

Table XXXIV. EIS circuit component values of LiCl-KCl-ReCl₃-Li₂O system at open circuit potentials for 550 °C using tungsten working electrode.

Li ₂ O Concentration, wt%	Circuit Component	Circuit Component Value
1	R _u	878.3*10 ⁻³ Ω
	Y ₀	11.51*10 ⁻³ S*s ^a
	α	897*10 ⁻³
	W _d	21.42*10 ⁻³ S*s ^{1/2}
	R _p	135.7 Ω
2	R _u	620.9*10 ⁻³ Ω
	Y ₀	2.970*10 ⁻³ S*s ^a
	α	779.1*10 ⁻³
	R _p	236.8 Ω

The solution resistance increased by several orders of magnitude between 1 and 2 wt% addition of Li₂O. The charge transfer resistance was given as R_p at high frequencies because the resistance due to the constant phase element would be negligible. The impedance due to the constant phase elements became significant only below 10Hz as seen from the Bode plots. As concentration increased, the capacitance due to Y₀ decreased along with its time constant. This could be attributed to increased concentration of oxygen creating rhenium oxide compounds, resulting in lowering the amount of Re(IV) ions that were present in the solution

at the electrode/molten salt interface that were present in the OCP condition at 2 wt% than 1 wt% Li_2O . The Warburg diffusion component was present in only the 1 wt% addition of Li_2O .

An EEC model consisting of two parallel RC loops connected in series, and each RC loop having a Warburg element was proposed to describe the impedance behavior of LiCl-KCl molten salt at 700 °C–800 °C by Cohen et al.⁶¹ The reported values of solution resistance (R_s), double layer capacitance (Q_1), capacitance due to adsorption of ions (Q_2), and Warburg coefficient were reported as 0.685 ohm, 58–80 μF , 1.8–2.3 mF, and 2–4 mS, respectively.⁶² The EIS data of this study was fitted with a different EEC model but the values of the solution resistance circuit components showed almost similar order of magnitude as Kim et al.⁶³ reported EIS data of a molybdenum electrode in LiCl-KCl- UCl_3 at 773K and fitted their data to an EEC similar to the one used in this work and the values of the circuit components showed a similar order of magnitude as reported in this work for the 2 wt% Li_2O , while the 1 wt% showed higher values in this study than the one reported by Kim et al.

Most of the literature on pyroprocessing of used nuclear fuels focuses on the electrochemical behaviors of fission product as cations such as La^{3+} , Nd^{3+} , Sm^{3+} etc.⁶⁴ Not much information is available on the anion type fission products such as Te^{2-} and I^- . It is generally assumed that anions present in the molten salt may not interfere with the cathodic reduction of actinides. This study attempts to fill the knowledge gap and shows that with the addition of oxygen will affect the oxidation behaviors of technetium during the pyroprocessing conditions using rhenium as a surrogate and adversely affect the stability of the electrodeposits because of the oxide compounds that could form. The electrochemical data presented in this work such as

formal potentials of different Re and ReO₂ species and their diffusivities are useful in designing more efficient pyrochemical processes.

8.3 Conclusions

The reduction of Re resulted in a total of 2 electrochemical peaks arising before lithium reduction occurred. The formal potential of Re in 1 wt% Li₂O was estimated as -0.245 V_{Ag/AgCl}, while it was estimated to be -0.342V_{Ag/AgCl} for 2 wt% addition with the species that is reacting is ReO₂. The number of electron transfer that was observed for 1 wt% was a two-electron reaction step and a one-electron reaction step for 2 wt%. For 1 wt% Re(IV) was potentially reduced to Re(0) in three steps with varying electron transfer depending on the step which occurred at -1.75V. The reduction of ReO₂ completed at around -1.71 V_{Ag/AgCl} and was potential reduced to Re⁻.

The diffusion coefficients of Re(IV) were 0.034×10^{-5} (1 wt% Li₂O) and ReO₂ was 0.0127×10^{-5} (2 wt% Li₂O) cm²s⁻¹, respectively in the 1wt% and 2wt% Li₂O electrolyte with the 5wt% ReCl₃ addition.

The electrochemical impedance spectroscopic data could be fitted with an equivalent circuit representing a resistor in series with a 1 loop R||Ø. Diffusion limited impedance was observed at OCP for 1wt% Li₂O. The charge transfer resistance showed an increase with an increase in Li₂O concentration.

Chapter 9: Conclusion and Future Works

Over the course of this dissertation various topics were discussed in determining the behaviors of tellurium and rhenium in LiCl-KCl eutectic salt at various temperatures and with the addition of Li₂O in later chapters. For tellurium at 450 °C, two different electrodes were compared to determine the reactivity behavior between tungsten and glassy carbon electrodes. It was seen that more reactions occurred on the tungsten electrode than glassy carbon due to the high wetting angle that happens between the salt and electrode. This results in less of the salt adhering to the electrode during the redox process.

The diffusivity of tellurium was seen to increase as temperature was raised from 450 to 550 °C. Diffusivity at 450 °C was $0.9 \times 10^{-5} \text{ cm}^2/\text{s}$ and was seen to increase to $9 \times 10^{-5} \text{ cm}^2/\text{s}$ for 500 °C and $8.43 \times 10^{-5} \text{ cm}^2/\text{s}$ for 550 °C. Additionally, formal potentials were seen to shift as well to more positive potentials where it was seen for 450 °C to be -0.161 and shift to -0.151 V_{Ag/AgCl} for 550 °C. Additionally, electrochemical impedance spectroscopy was performed to help understand more of the reactions that occurred between the electrolyte and the electrode. It was seen that the electron transfer resistance increased with temperature. Additionally, each temperature could be modeled using a similar circuit diagram of a resistor in series with a resistor and capacitor in parallel with a Warburg coefficient being in the parallel circuit as well.

With rhenium investigation, it was seen that when Re³⁺ is added to the solution it disproportionates into Re⁴⁺ and Re(0). Thus, resulting in Re⁴⁺ being reduced instead of Re³⁺. It was seen that as temperature increased the rate of diffusivity decreased at 450 °C from 12.3 to $0.033 \times 10^{-5} \text{ cm}^2/\text{s}$ at 550 °C for 5 wt% addition of ReCl₃. Additionally, formal potential

shifted in a more negative direction with temperature increase. At 450 °C the formal potential was 0.131. When the temperature was raised to 550 °C it shifted to -0.678. Which was opposite of what was seen with open circuit values, that as the temperature increased OCP shifted towards more positive potentials. Furthermore, when electrochemical impedance spectroscopy was performed at open circuit conditions the circuit models were similar to tellurium. Additionally, with the rise in temperature the charge transfer resistance decreased. One difference between rhenium and tellurium in the circuit model is that there was no diffusion control occurring which can be seen from the lack of a Warburg coefficient appearing in the circuit model.

To simulate more of what it would be like during the pyroprocess both tellurium and rhenium were added to the electrolyte to see what the behaviors would be when they were combined. From literature studies, what potentially could have been occurring is that tellurium and rhenium reduced separately without forming any ionic bonds before any electrochemical reaction occurred. The first element to be reduced was Re^{4+} at a potential of -0.606V followed by tellurium at -1.03V. A reaction that could have possibly occurred at a potential of -1.36 was tellurium and rhenium reacting to create ReTe_2 . Further analysis would need to be done to verify if this is what occurred. Additionally, what was seen is that tellurium had a higher rate of diffusion than rhenium, which tracks with what was seen when comparing pure rhenium and tellurium solutions to the mixture. The formal potentials for this combined mixture were in the positive direction. For electrochemical impedance spectroscopy, Warburg coefficient appeared which is potentially due to the addition of tellurium to the system.

Lastly, each solution had Li_2O added to the mixture to determine what effect oxygen would have on the system. This is to simulate when metal oxide fuels are being refined. For

tellurium it could potentially be determined that before any redox reaction occurred that oxygen and tellurium reacted creating TeO_2 . After which, this would be the species that would be involved in the redox process. These experiments were performed at $550\text{ }^\circ\text{C}$. It was seen that as the weight percent of Li_2O increased the diffusivity decreased. This was possibly caused by there being a higher quantity of TeO_2 existing with the more abundant quantity of oxygen present. This can be further verified by the fact that an oxygen gas evolution peak was seen in the 2 wt% addition and was missing in only 1 wt% addition. Additionally, the formal potentials shifted to more negative potentials when 2 wt% Li_2O was added. The open circuit potential due to the presence of oxygen shifted to more negative potentials when compared to tellurium without the addition of Li_2O . For electrochemical impedance spectroscopy the charge transfer resistance was seen to decrease between the 1 and 2 wt% Li_2O . The diffusion controlled constant was also seen to decrease in the oxygen addition, due to the larger coordination number that TeO_2 would have.

For rhenium with oxide addition, there was potentially no oxide formation occurring as was seen in tellurium for 1 wt% addition due to some of the same reactions being the same without any oxygen added to it. However, at 2 wt% there was a lack of redox peaks that could be seen during the full window cyclic voltammetry. Even when comparing the smaller potential windows, a redox peak did not occur until -1.86V as to where in the 1 wt% a reaction occurred at -0.611V . A similar trend was also seen with the rate of diffusivity as was seen with tellurium, that as the concentration of Li_2O increased the diffusivity decreased. Furthermore, the formal potential shifted towards negative potentials as was also seen with the open circuit potential. The electrochemical impedance spectroscopy showed a similar model at open circuit conditions as the rest of the experiments performed. One thing to note is

that a Warburg coefficient appeared for 1 wt% Li_2O which was not seen in pure rhenium addition. However, when the concentration increased to 2 wt% the Warburg coefficient disappeared. Additionally, the resistance to charge transfer also increased. This aligns with the theory that ReO_2 was created with 2 wt% addition since rhenium oxides seem to be more stable in the solution resulting in a decrease in its ability to be reduced.

Some future characterization that could be performed to verify these findings would be raman spectroscopy in an inert environment to prevent atmosphere conditions from affecting the salt. Additionally, for comparing results of technetium to the rhenium surrogate would be to perform electrochemical experiments on technetium in a more controlled condition due to the radioactive nature of technetium, then compare the results together. Furthermore, since uranium is one of the more desirable elements to be recovered from fuel rods, experiments would need to be performed with uranium or a uranium surrogate with tellurium and technetium (rhenium). This would help to determine if these elements could possibly form compounds with uranium during the pyroprocess. This would result in limiting the amount of uranium that could be recovered from the overall system. These are just a few of many experiments that could be performed to gain a better understanding of how these elements would affect the total electrochemical behavior during the pyroprocess.

References

1. *Fluor says*, 2019, https://www.postregister.com/news/government/fluor-says-just-69-acres-of-waste-left-at-desert-complex/article_331be9c7-02ee-5f79-bd4b-6e8027984e42.html
2. Schwantes, J.M., et. al, Contaminants of the Bismuth Phosphate Process as Signifiers of Nuclear Reprocessing History, *PNNL-21057 FY-2010 Report*, pp. 1-18
3. National Research Council. 1996. *Nuclear Wastes: Technologies for Separations and Transmutation*. Washington, DC: The National Academies Press. <https://doi.org/10.17226/4912>
4. Takahashi, M., et al, Improved Fluoride Volatility Reprocessing, *Atlalante*, 2000 P3.13
5. Szulinski, M.J., Fluoride Volatility Processing of Reactor Fuels, *Chemical Processing Division, Isochem Inc., Richland Washington*, 14 Jan. 1966, pp. 1-11
6. Touran, Nick. "Molten Salt Reactors." *What is Nuclear?*, <https://whatisnuclear.com/msr.html#:~:text=The%20first%20molten%20salt%20reactor,tubes%20in%20blocks%20of%20Beryllium>
7. Steunenberg, R.K., et al., Uranium and Plutonium Purification: Salt Transport Method, *Symposium Reprocessing of Nuclear Fuels*, vol. 15, Fused Salt-Liquid Section, 25-37 Aug. 1969, pp. 337
8. Chang, Y. II, et al., Conceptual Design of Pilot-scale Pyroprocessing Facility, *Nuclear Technology ANS*, 14 Aug. 2018, pp. 1-19
9. Till, Charles, Chang, Yoon II. *Plentiful Energy: The Story of Integral Fast Reactor*. Library of Congress, 2011 by Charles Till (book)
10. Simpson, M., Developments of Spent Nuclear Fuel Pyroprocessing Technology, *Idaho National Lab*, INL/EXT-12-25124, March. 2012, pp. 1-23
11. Laidler, J.J, et al., Development of pyroprocess Technology, *Progress in Nuclear Energy*, vol. 31, No ½, 1997, pp 131-140

12. Koyama, T., et al., Experimental Study of Molten Salt Electrorefining of Uranium...., *Journal of Nuclear Science and Technology*, vol. 34, No. 4, April. 1997, pp. 384-393
13. Simpson, M., Developments of Spent Nuclear Fuel Pyroprocessing Technology, *Idaho National Lab*, INL/EXT-12-25124, March. 2012, pp. 1-23
14. Chu, X.W., et al., Effect of Thermal Exposure Time on Tellurium-induced Embrittlement..., *Nucl Sci Tech*, 2017, pp. 1-6
15. Cheng, H., et al., Intergranular Diffusion and Embrittlement of a Ni-16-Mo-7Cr alloy..., *Journal of Nuclear Materials*, vol. 467, No. 1, Dec. 2015, pp 341-348
16. Volkovich, V. A., et al., Electrochemical and Spectroscopic Properties of Tellurium in..., *ECS Transactions*, vol. 16, No. 49, 2009, pp. 335-341
17. Poulsen F. W., et al., Electrical Conductivity of Molten Bismuth Chloride-Aluminum Chloride..., *Journal of Physical Chemistry*, vol. 79, No. 15, 1975, pp 1610-1614
18. Lichtenstein, T., et al., Electrochemical Behavior of Te^{2-} in Molten $\text{LiCl-Li}_2\text{Te}$..., *Inorg. Chem.*, vol. 58, No. 2, 2019, pp. 1548-1554
19. Gi-Shong, E., et al., Electrochemistry of Tellurium in Basic Aluminum Chloride..., *J. Electrochem. Soc.*, vol. 144, No. 7, July. 1997, pp. 2369-2374
20. Li, H., et al., Tellurium-tin Based Electrodes Enabling Liquid Metal Batteries..., *Energy Storage Materials*, 13, April. 2018, pp. 1-17
21. Bodewing, F.G., et al., Electrochemical Behavior of Selenium and Tellurium in Fused LiCl-KCl Eutectic, *J. Electrochem. Soc.*, vol. 117, No. 5, May. 1970, pp. 618-621
22. Ebe, H., et al., Electrodeposition of Sb, Ti, Te, and Their Alloys in...., *Electrochimica Acta*, vol. 53, 2007, pp. 100-105
23. Poulsen, F. W., et al., Electrochemistry of Te (IV) in KCl-AlCl_3 Melts..., *Journal of Electroanalytical Chemistry and Interfacial Electrochemistry*, vol. 79, No. 2, 24 June. 1977, pp 327-336

24. Poulsen, F. W., et al., Electrical Conductivity of Molten ..., Tellurium Chloride-Aluminum Chloride..., *Journal of Physical Chemistry*, vol. 79, No. 15, 1975, pp 1610-1614
25. Tsai, R. W., et al., Voltammetric Study and Electrodeposition of Tellurium, Lead,...., *Electrochimica Acta*, vol. 137, No. 10, Aug. 2014, pp. 49-56
26. Robinson, J., et al., Electrochemical Behavior of Te(IV) in Sodium Tetrachloroaluminate Melts, *J. Electrochem. Soc.*, vol. 125, No. 11, Nov. 1978, pp. 1784-1789
27. Itkin, V. P., et al., The O-Te (Oxygen Tellurium) System, *Journal of Phase Equilibria*, Vol. 17, No. 6, 1996, pp. 533-538
28. Serrano, P.N., et al., Electrochemistry of Technetium Analogues Rhenium..., *Graduate College in Chemistry University of Nevada*, Master of Science, June. 2011, pp. 1-106
29. Volkovich, V. A., et al., Reactions and Speciation of Technetium and Rhenium..., *Phys. Chem. Chem. Phys.*, vol. 4, 2002, pp. 5753-5760
30. Rosner, G., et al., The Reaction of Rhenium and Technetium Metals with Molten Lithium..., *I. Inorg. Nucl. Chem.*, vol. 33, 1971, pp. 2687 - 2688
31. Volkovich, V. A., et al., Electrochemical and Spectroscopic Properties of Technetium..., *ECS Transactions*, vol. 33, No. 7, 2010, pp. 381 - 390
32. Bailey, R. A., et al., Electrochemical Studies on Rhenium in Fused LiCl-KCl Eutectic, *Electrochimica Acta*, vol 17, 1972, pp. 1139 - 1149
33. Vinogradov-Zhabrov, O. N., et al., Electrodeposition of Rhenium from Chloride Melts:..., *Journal of Mining and Metallurgy, Section B: Metallurgy*, vol. 39, No.1-2, 2003, pp. 149-166
34. Danilov, D. A., et al., Speciation of Rhenium in Chloride Melts: Spectroscopic..., *Zeitschrift fur Naturforschung A*, 2008, pp. 371-376
35. Affoune, A., et al., Study of Some Rhenium Electrochemical Properties in The Fused..., *Electrochemical Society*, vol. 1990-17 471, 1990, pp. 471-480
36. Bailey, R. A., et al., Spectroscopic Study of the Behavior of Re(III) Chlorides in Molten Salts, *Inorganic Chemistry*, vol. 5, No. 11, Nov. 1966, pp. 1940-1942

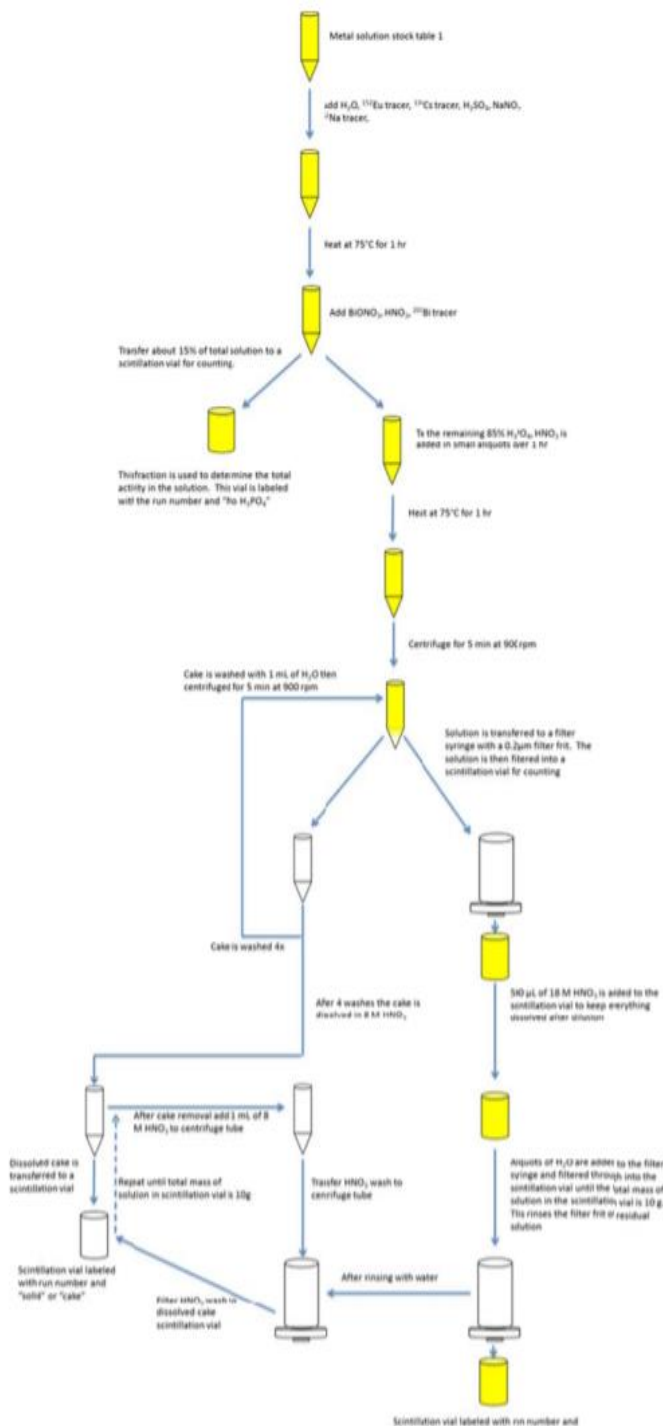
37. Strubinger, S. K. D., et al., Electrochemical and Spectroscopic studies of Rhenium (IV)..., *Inorg. Chem*, vol. 29, No. 21, 1990, pp. 4246-4252
38. Strubinger, S. K. D., et al., Electrochemical and Spectroelectrochemistry of Polynuclear Rhenium..., *Inorg. Chem*, vol. 29, No. 5, 1990, pp. 993-999
39. Magneli, A., Studies on Rhenium Oxides, *Acta Chem. Scand.*, vol. 11, No. 1 1957, pp. 28-33
40. Vurrman, M. A., et al., Structural Determination of Surface Rhenium Oxide, *Journal of Molecular Catalysis*, vol. 76, No. 1-3, 15 Oct. 1992, pp. 263-285
41. Mitra, B., et al., Characterization of Supported Rhenium Oxide, *Phys. Chem. Chem. Phys.*, vol. 3, 20, Feb. 2001, pp. 1144-1152
42. Majidi, L., et al., Highly Active Rhenium, Ruthenium, and Iridium Based Dichal..., *Chem. Mater.*, vol. 32, No. 7, 19 March. 2020, pp. 2764-2773
43. Kim, E., et al., Chemistry of Rhenium as an Analogue of Technetium: Experi..., *Radiochimica Acta*, vol. 91, No. 4, 2003, pp. 211-216
44. Yoon, D., et al., Fundamental Data Acquisition toward Silver-Silver Chloride..., *Journal of the Electrochemical Society*, vol. 166, No. 6, 3 April. 2019, pp. E159-E164
45. Guo, S., et al., Corrosion in the Molten Fluoride and Chloride Salts and Materials..., *Progress in Materials Science*, vol. 97, Aug. 2018, pp. 448-487
46. Bermejo, M. R., et al., The Electrochemistry of Gadolinium in eutectic LiCl-KCl..., *Journal of Electroanalytical Chemistry*, vol. 588, 2006, pp. 253-266
47. Liu, Y. L., et al., Electrochemical Extraction of Samarium from LiCl-KCl Melt..., vol. 120, 20 Feb. 2014, pp. 369-378
48. Eliz, N. et al., Physical Electrochemistry: Fundamentals, techniques..., *Wiley-VCH*, 2nd Edition, 21 Sep. 2018, pp. 1-481
49. Sakamura, Y., et al., Electrochemical Behavior of Selenide and Telluride Ions, *Journal of The Electrochemical Society*, vol. 167, No. 8, 13 May. 2020, pp. 1-10

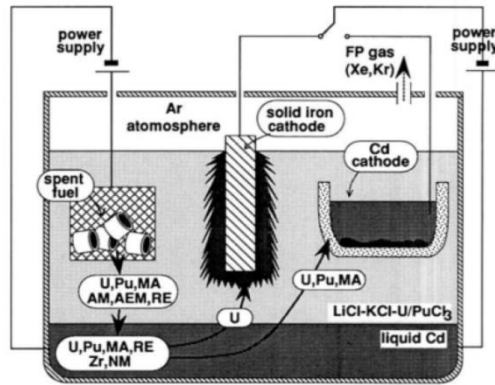
50. Greff, R., et al., Instrumental Methods in Electrochemistry, *Woodhead Publishing*, 1 April. 2001, pp. 1-442
51. Bermejo, M. R., et al., Cathodic Behavior of Europium (III) on Glassy Carbon..., *Journal of Electroanalytical Chemistry*, vol. 603, No. 1, 1 May. 2007, pp. 81-95
52. Berzins, T. et al., Oscillographic Polarographic Waves Reversible Deposition of Metals..., *ACS Publication*, 5 Feb. 1953, pp. 555-559
53. Ramaley, L., et al., Theory of Square Wave Voltammetry, *Analytical Chemistry*, vol. 41, No. 11, Sept. 1969, pp. 1362 - 1365
54. Osteryoung, J. G., et al., Square Wave Voltammetry, *Analytical Chemistry*, vol. 57, No. 1, Jan. 1985, pp. 101A – 110A
55. Matsuda, H., et al., The Theory of Cathode-ray Polarography of Randles-Sevik..., *Zeitschrift fur Elektrochemie and Angewandte Physikalische Chemie*, vol. 59, 1955, pp. 494-503
56. Masset, P., et al., Electrochemistry of Uranium in Molten LiCl-KCl Eutectic, *Journal of The Electrochemical Society*, vol. 152, No. 6, 4 May. 2005, pp. A1109 – A1115
57. Yoon, D., et al., Electrochemical Properties and Analysis of CeCl₃ in LiCl-KCl..., *Journal of The Electrochemical Society*, vol. 162, No. 10, 24 July. 2015, pp. E237-E243
58. Bjerrum, N., et al., Lower Oxidation States of Tellurium Tellurium(II) in Chloroaluminate..., *Inorganic Chemistry*, vol. 10, No. 11, 1971, pp. 2578 - 2580
59. Bae, S.E., et al., Aluminum Assisted Electrodeposition of Europium in LiCl-KCl Molten Salt, *Electrochimica Acta*, vol. 55, No. 8, 1 March. 2010, pp. 3022-3025
60. Martin J. D., et al., Designing Intermediate-range Order in Amorphous Materials, *Nature*, vol. 419, 2002, pp. 381-384
61. Cohen Y. S., et al., Temperature-dependent Impedance Spectroscopy of Molten..., *ECS Electrochemistry Letters*, vol. 4, No. 1, 2015, pp. H1-H4

62. Orazem, M. E., et al. Electrochemical Impedance Spectroscopy, *Electrochemical Society*, 2nd Edition, 13 Jun. 2017, pp. 1-712
63. Kim G. Y., et al., A Study on the Electrochemical Deposition Behavior of Uranium Ion, *Journal of Electroanalytical Chemistry*, vol. 682, 15 Aug. 2012, pp. 128-135
64. Zhang, J., Electrochemistry of Actinides and Fission Products in Molten Salts..., *J. Nucl. Mater.*, vol. 447, No. 1-3, April. 2014, pp. 271-284
65. Bailey, R. A., et al., Electrochemical Studies on Rhenium in Fused LiCl-KCl, *Electrochimica Acta*, vol 17., No. 6, June 1972, pp. 1139-1149
66. Danilov, D. A., et al., Speciation of Rhenium in Chloride Melts: Spectroscopic and..., *Verlag der Zeitschrift für Naturforschung*, 2008, pp. 371-376
67. Hondrogiannis, E. M., et al., Spectroscopy, Electrochemistry, and Spectroelectrochemistry of Rhenium..., *Journal of The Electrochemical Society*, vol. 142, No. 8, 1995, pp. 2532-2538
68. Loiseau F., et al., Bidentate phosphinophenol ligands, preparation and echem of Re(III), *Inorganica Chimica Acta*, vol. 306, No. 1, 11 Aug. 2000, pp 94-100
69. Strubinger, K. D. S, et al., Electrochemical and Spectroscopic studies of Rhenium(IV) Monomeric, *Inorg. Chem.*, 1990, pp. 4246-4252
70. Vinogradov-Zhabrov, O.N., et al., Electrodeposition of Rhenium from chloride melts, *Journal of Mining and Metallurgy*, vol. 39, No. 1-2, 2003, pp. 149-166
71. Salakhova, E. A., et al., Electrochemical Preparation of Thin Rhenium-Tellurium Coating..., *Russian Journal of Electrochemistry*, vol.47, No. 8, 2011, pp. 877-882
72. Seo, C. E., et al., Electrochemical Study on Reduction Mechanism of Uranium Oxide...., *Journal of Nuclear Science and Technology*, vol. 43, No. 5, 2006, pp. 587-595
73. Hur, J.M., et al., Underpotential Deposition of Li in Molten LiCl-Li₂O, *Electrochemistry Communications*, vol. 12, No. 5, May. 2010, pp. 706-709

74. Itkin, V. P., et al., The O-Te (Oxygen Tellurium) System, *Journal of Phase Equilibria*, Vol. 17, No. 6, 1996, pp. 533-538
75. Mohammed, M. I., et al., Synthesis, Optical Properties, and Impedance Spectroscopy..., *Optical and Quantum Electronics*, vol. 53, 2021, pp. 1-25
76. Grundler, P. V., et al., Speciation of Aqueous Tellurium(IV) in Hydrothermal Solutions..., *Geochimica et Cosmochimica Acta*, vol. 120, 1 Nov. 2013, pp. 298 -325
77. Hahn, B. P., et al., Electrochemical Deposition and Characterization Mixed Valent Rhenium..., *ACS Society*, vol. 23, No. 21, 2007, pp. 10837-10845
78. Sandbrink, L., et al., $\text{ReO}_x/\text{TiO}_2$: A Recyclable Solid Catalyst for Deoxydehydration, *ACS Catal*, vol. 6, No. 2, 2016, pp. 677-680

Appendix A:

Figure 1: Schematic of Bismuth Phosphate Process at Lab Scale²



AM: Alkali metal FP NM: Noble metal FP&Zr
 AEM: Alkaline earth metals FP RE: Rare earth FP
 MA: Np, Am, Cm Operated at 773 K

Figure 2: Schematic of Electrorefiner¹²

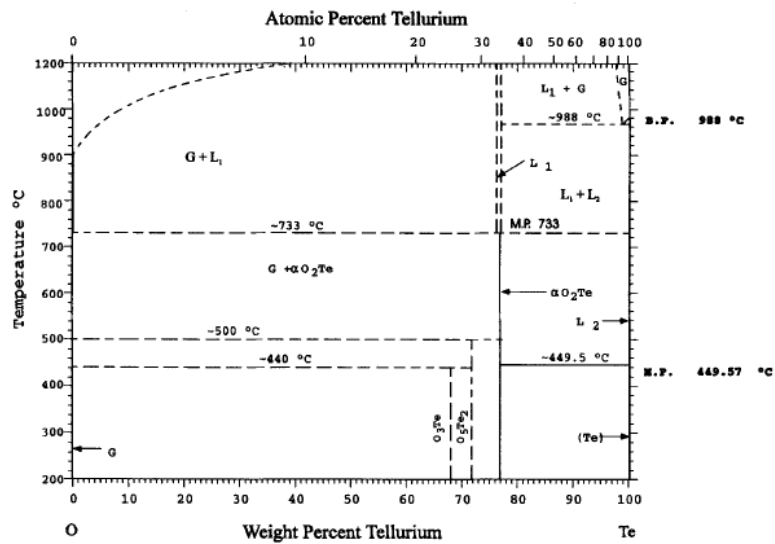
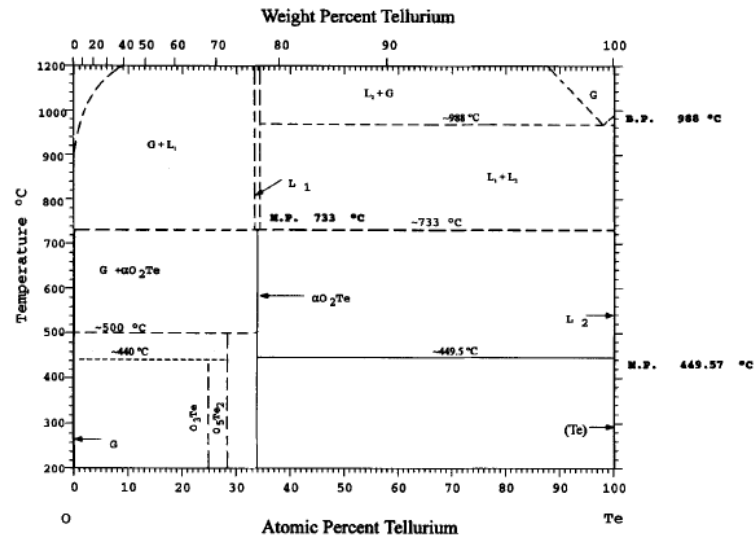


Figure 3: O-Te Phase Diagram²⁶

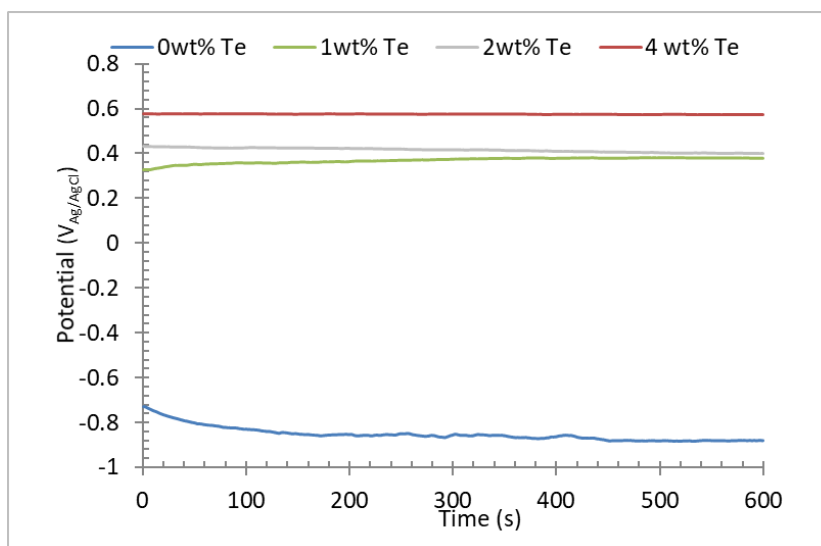


Figure 4: OCP of tungsten electrode in LiCl-KCl eutectic containing different concentration of TeCl_4 at 450 °C.

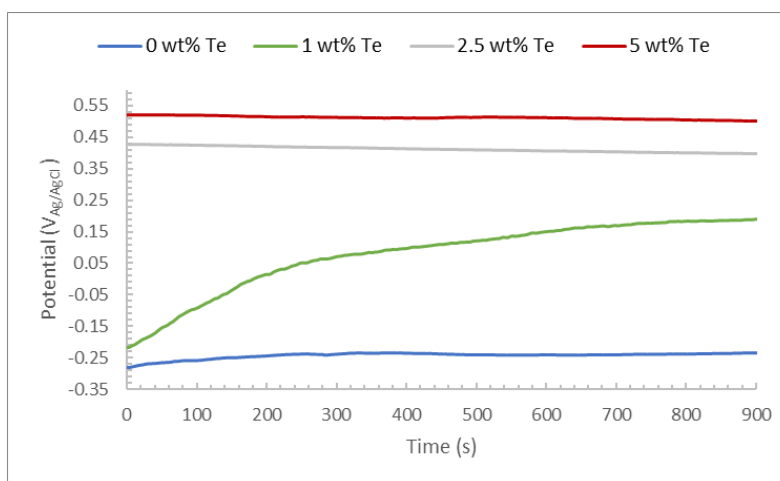


Figure 5: OCP of glassy carbon (GC) electrode in LiCl-KCl eutectic containing different concentration of TeCl_4 at 450 °C.

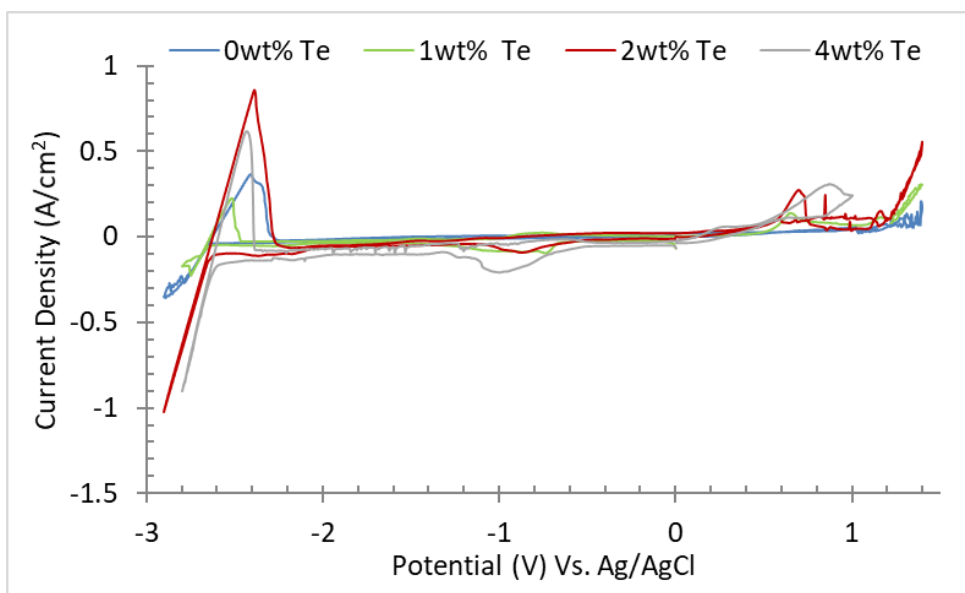


Figure 6: Cyclic voltammogram (CV) in LiCl+KCl eutectic with the addition of 0, 1, 2 and 4 wt% TeCl_4 at 450 °C using tungsten as a working electrode at a scan rate of 100 mV/s.

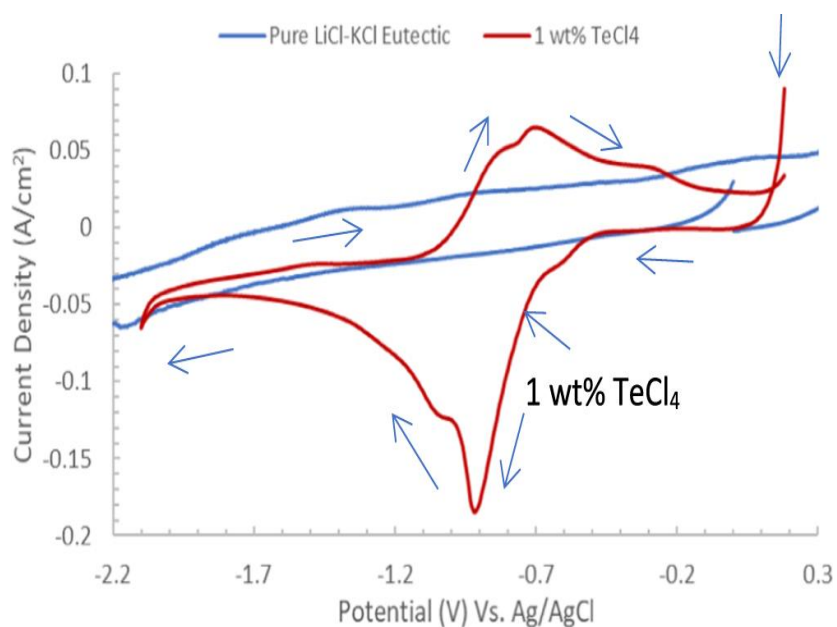


Figure 7: Cyclic voltammograms at cathodic potentials with reference to OCP in LiCl-KCl eutectic with and without 1 wt% TeCl_4 addition at 450 °C. Reduction and oxidation waves of Te species are revealed. Test conditions: scan rate: 500 mV s⁻¹, WE: Tungsten

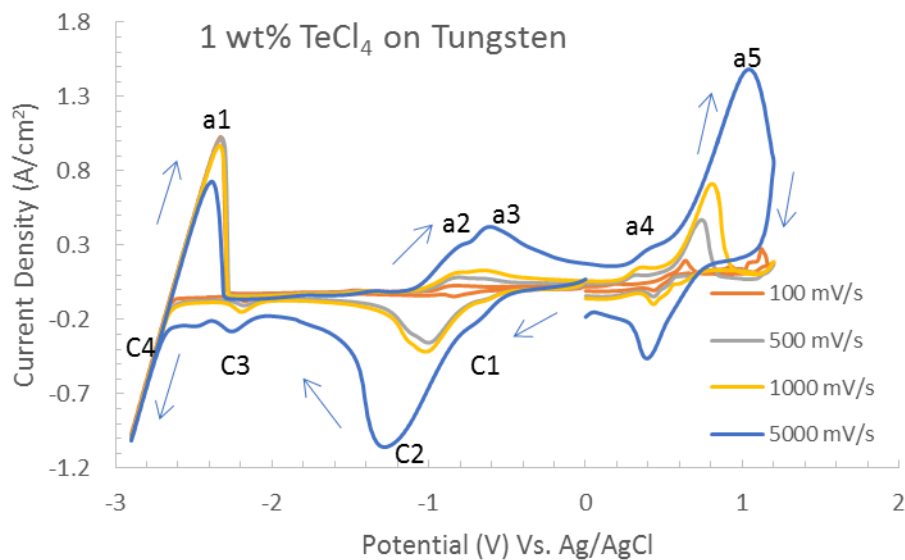


Figure 8: Cyclic voltammograms in LiCl-KCl eutectic with 1 wt% TeCl_4 addition at 450 °C at different scan rates using tungsten as working electrode.

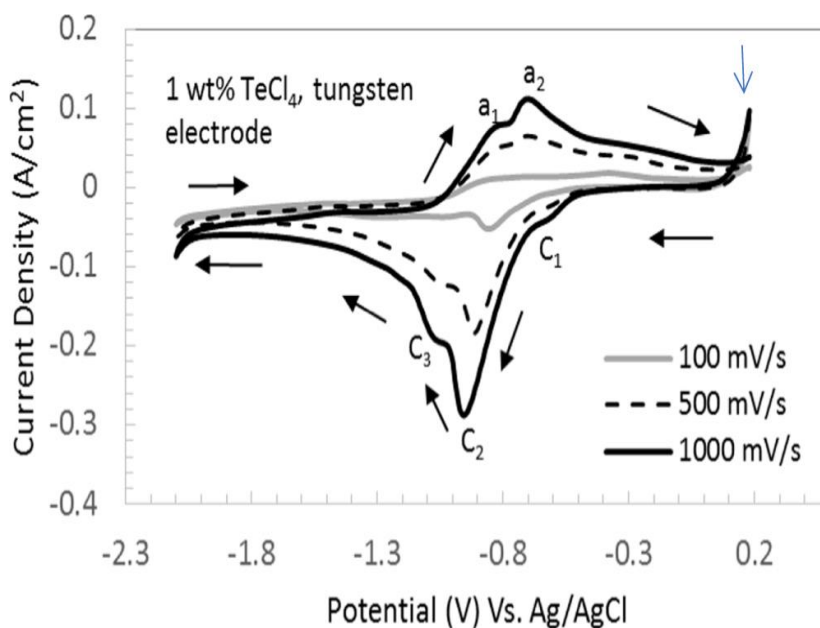


Figure 9: Cyclic voltammograms at different scan rates in 1 wt% TeCl_4 containing LiCl-KCl eutectic molten salt at 450 °C. The working electrode was tungsten

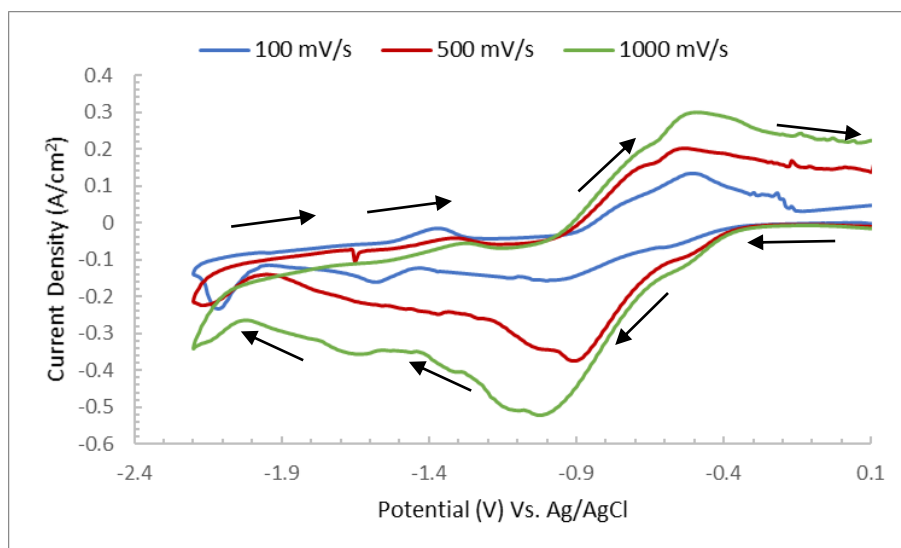
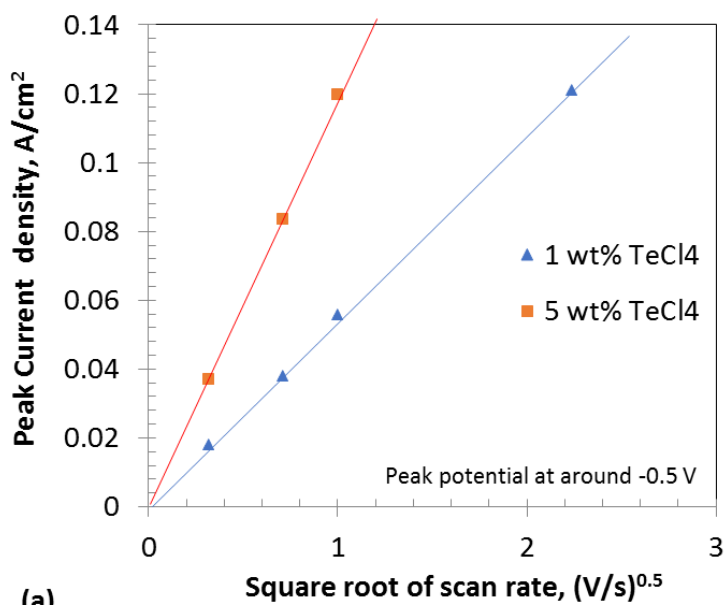
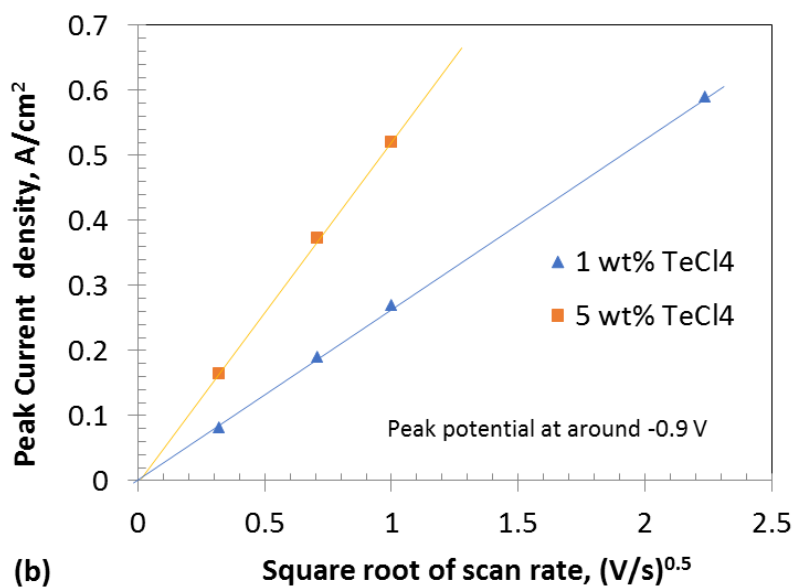


Figure 10: Cyclic voltammograms at different scan rates in 5 wt% TeCl_4 containing LiCl-KCl eutectic molten salt at 450 °C. The working electrode was tungsten.



(a)



(b)

Fig. 11: Plots of peak current density versus square root of scan rate in 1 and 5 wt% TeCl₄ containing LiCl-KCl melt at 450 °C observed at two different reduction conditions: a) at about -0.5 V_{Ag/AgCl} and b) -0.9 V_{Ag/AgCl}. Note that the reduction current is considered positive. Tungsten is the working electrode.

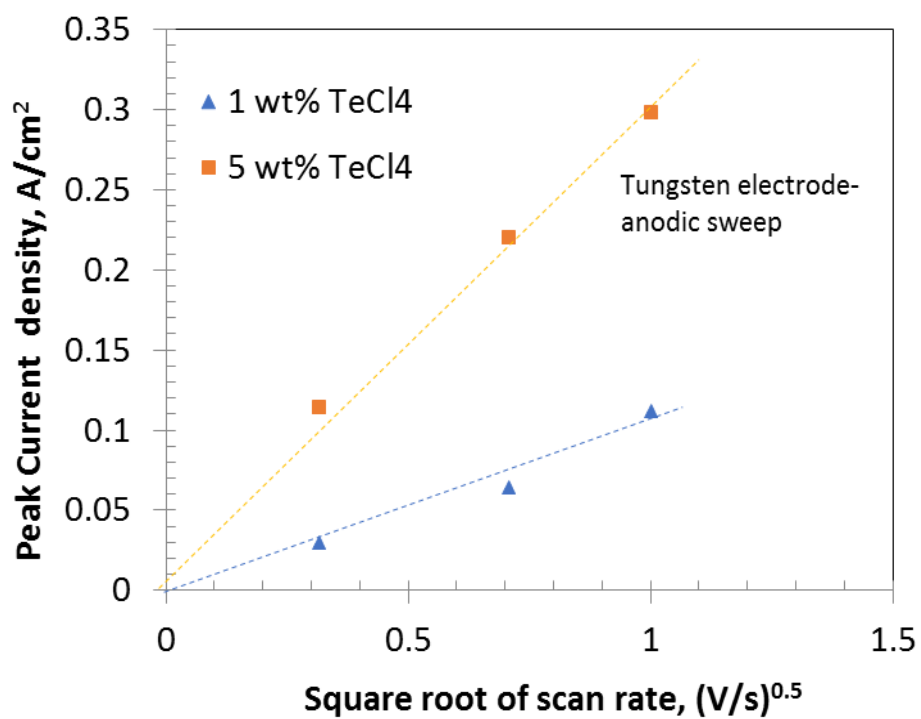


Fig. 12: Plots of oxidation peak current density versus square root of scan rate in 1 and 5 wt% TeCl₄ containing LiCl-KCl melt at 450 °C observed during the anodic sweep

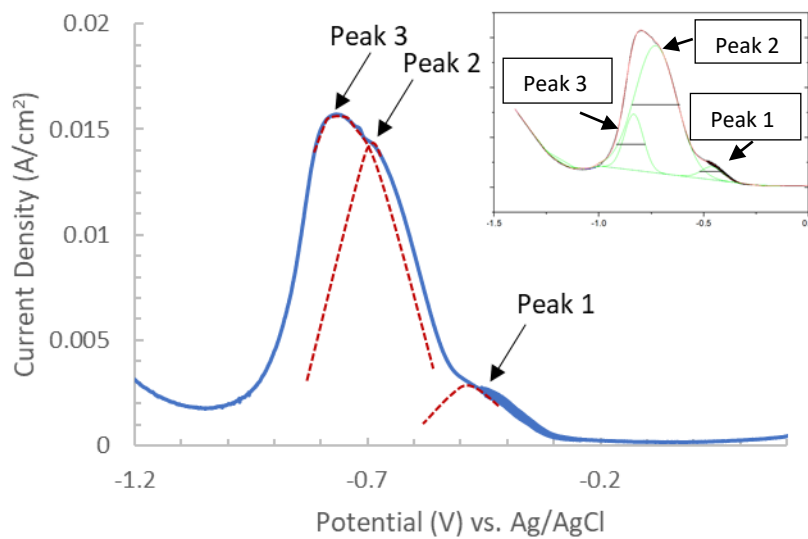


Figure 13: SWV of 1 wt% TeCl₄ in LiCl-KCl melt at 450 °C, WE: Tungsten Rod

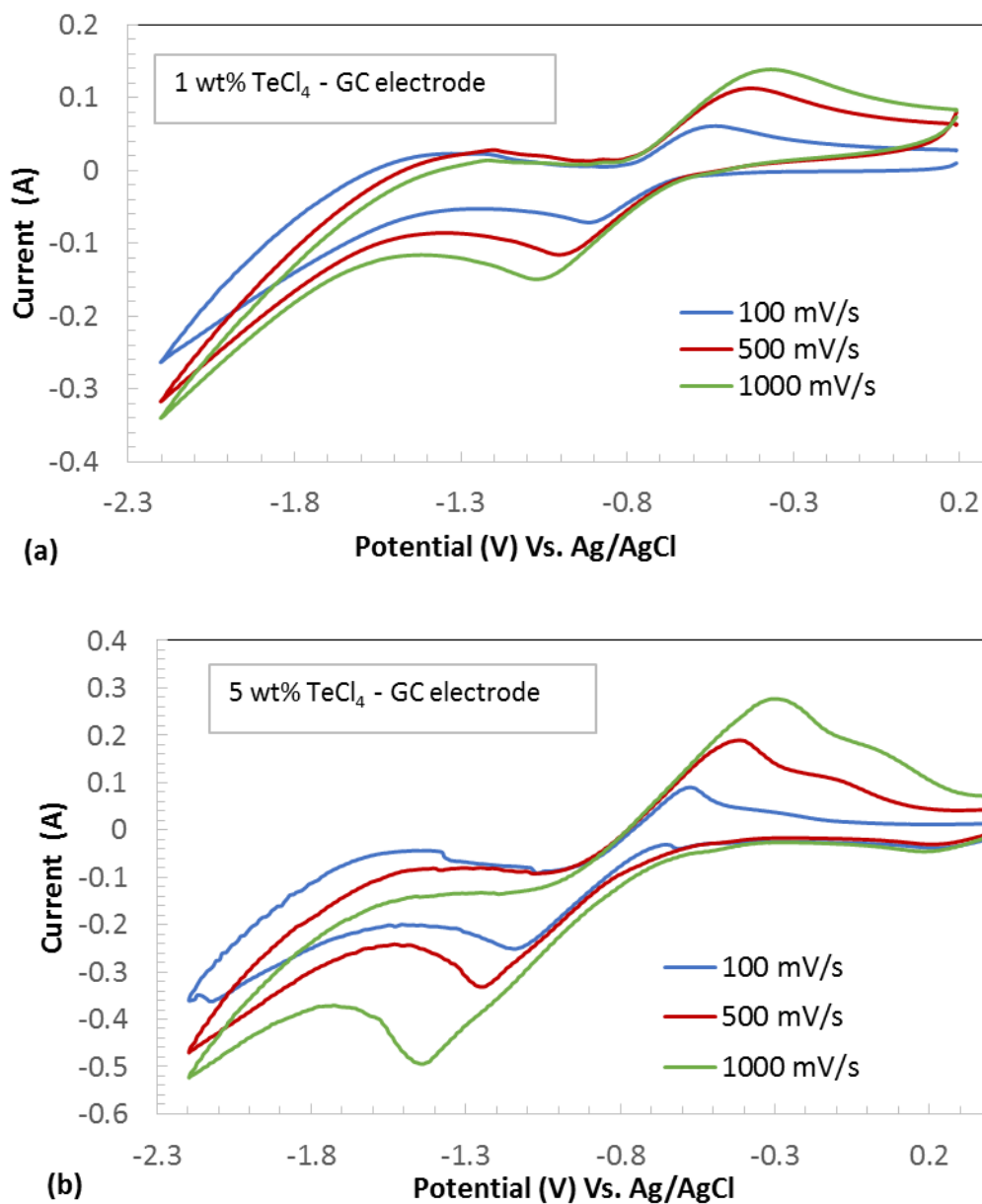


Figure 14: Cathodic portion of cyclic voltammograms at different scan rates in TeCl₄ containing LiCl-KCl eutectic molten salt at 450 °C. The working electrode was glassy carbon (GC): (a) 1 wt% TeCl₄ addition; and (b) 5 wt% TeCl₄ addition.

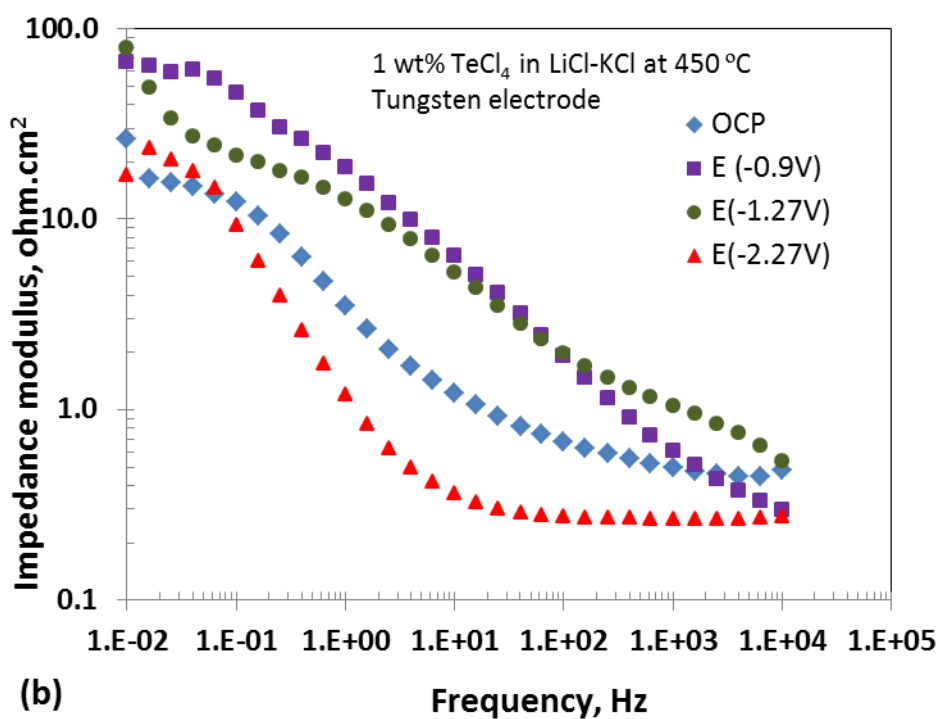
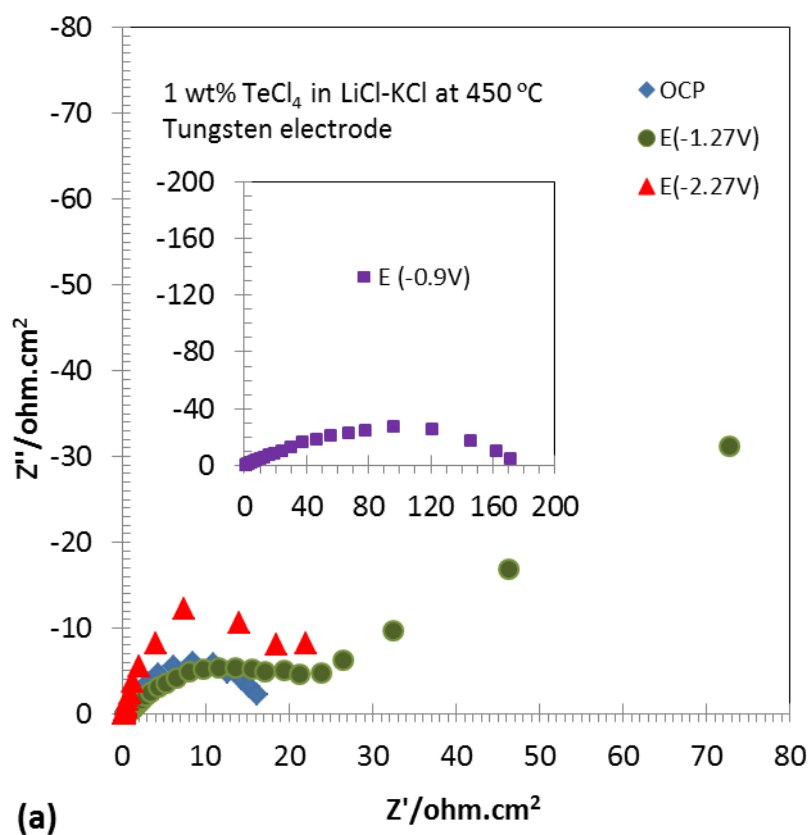


Figure 15: Impedance spectra of tungsten electrode in 1 wt% TeCl_4 containing LiCl-KCl melt at 450 °C at different potential conditions: a) Nyquist plots; and b) Bode plots.

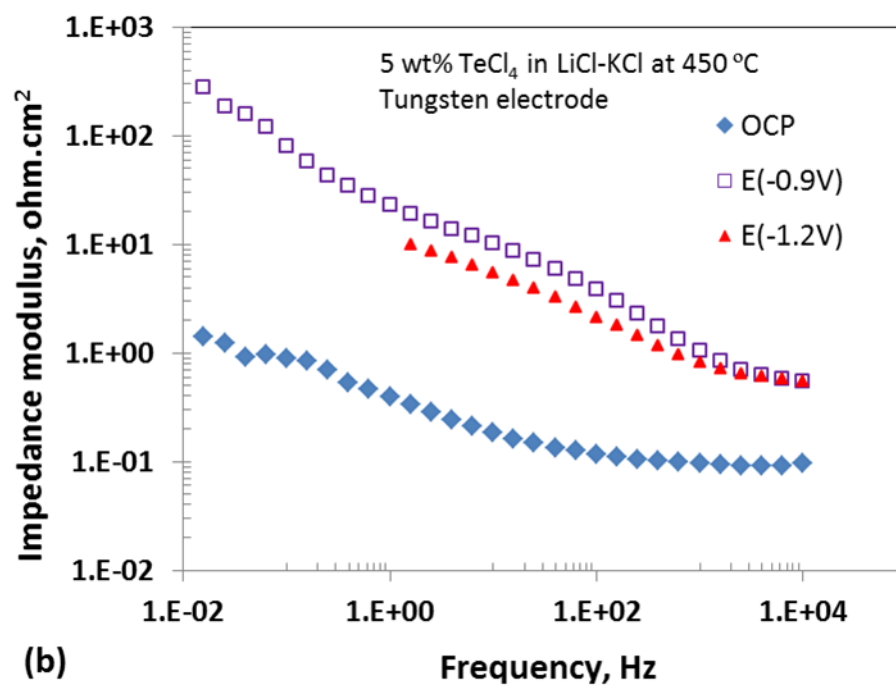
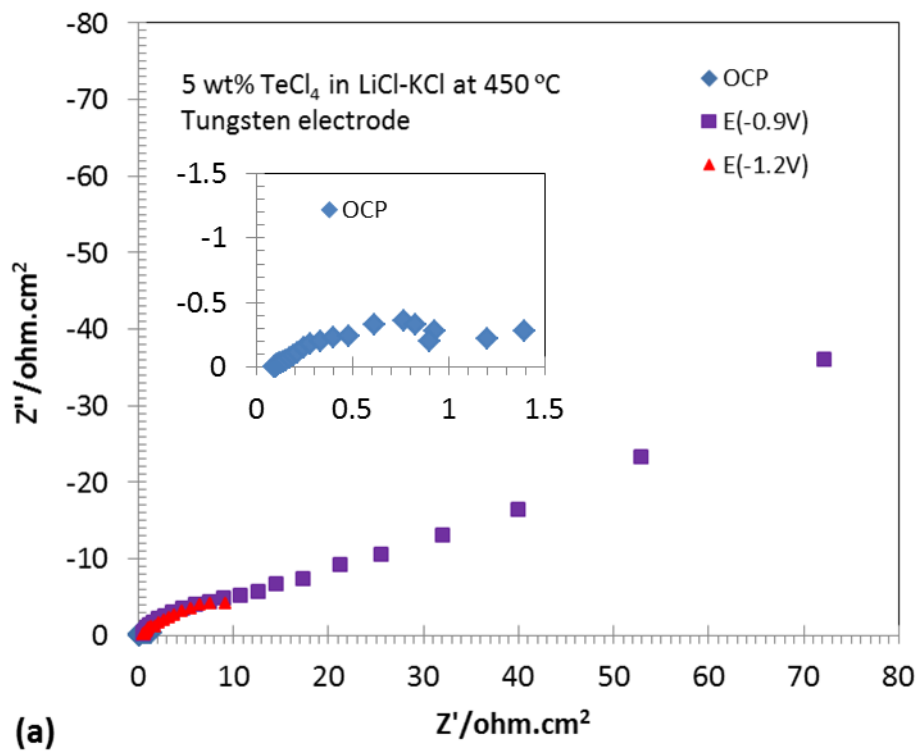


Figure 16: Impedance spectra of tungsten electrode in 5 wt% TeCl_4 containing LiCl-KCl melt at 450 °C at different potential conditions: a) Nyquist plots; and (b) Bode plots.

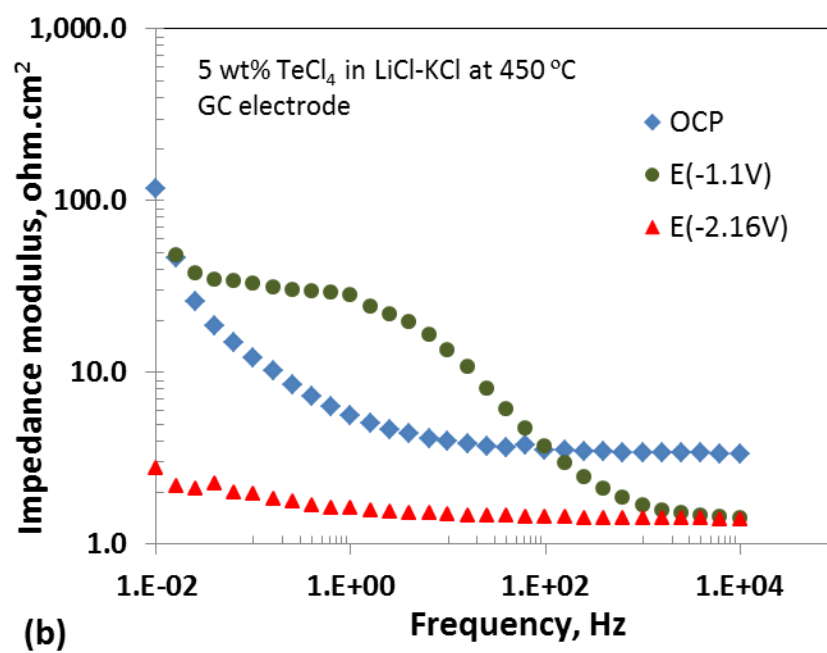
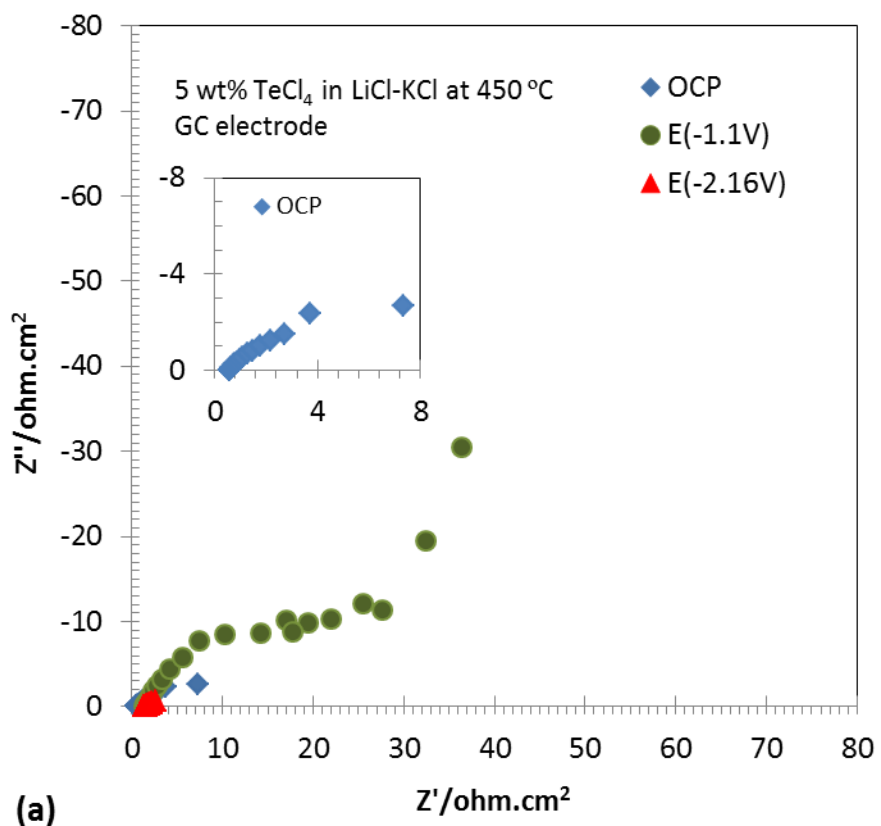


Figure 17: Impedance spectra of glassy carbon electrode in 5 wt% TeCl_4 containing LiCl-KCl melt at 450 °C at different potential conditions: a) Nyquist plots; and (b) Bode plots.

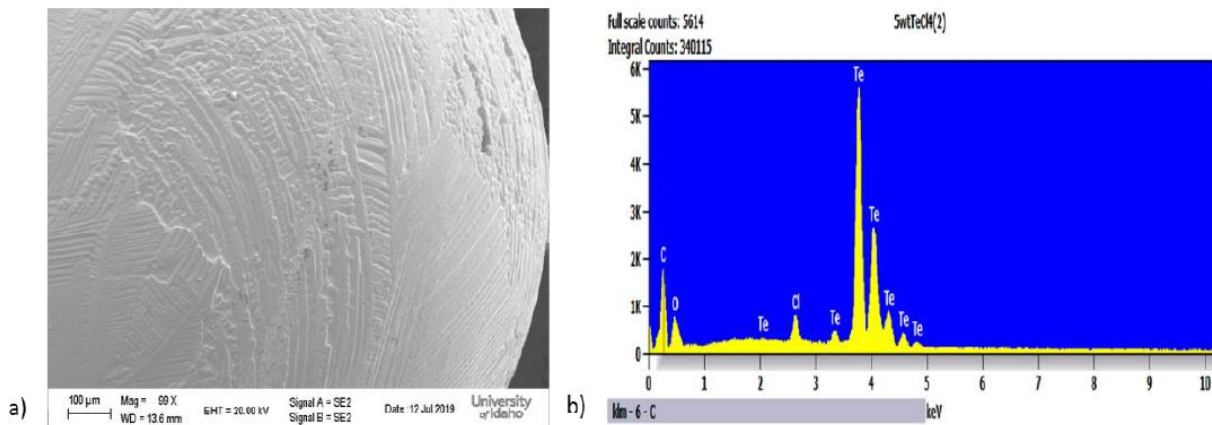


Figure 18: a) SEM image of the Te metal sphere formed at -1.27 V, b) Energy dispersive analysis of the deposit

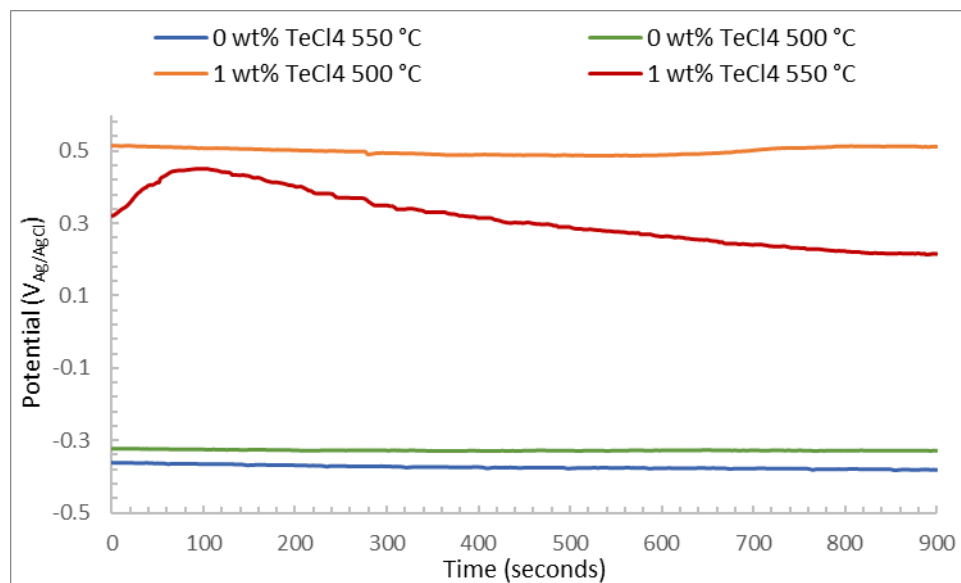


Figure 19: OCP comparing 0 and 1 wt% TeCl₄ at 500 - 550 °C, WE: Tungsten Rod

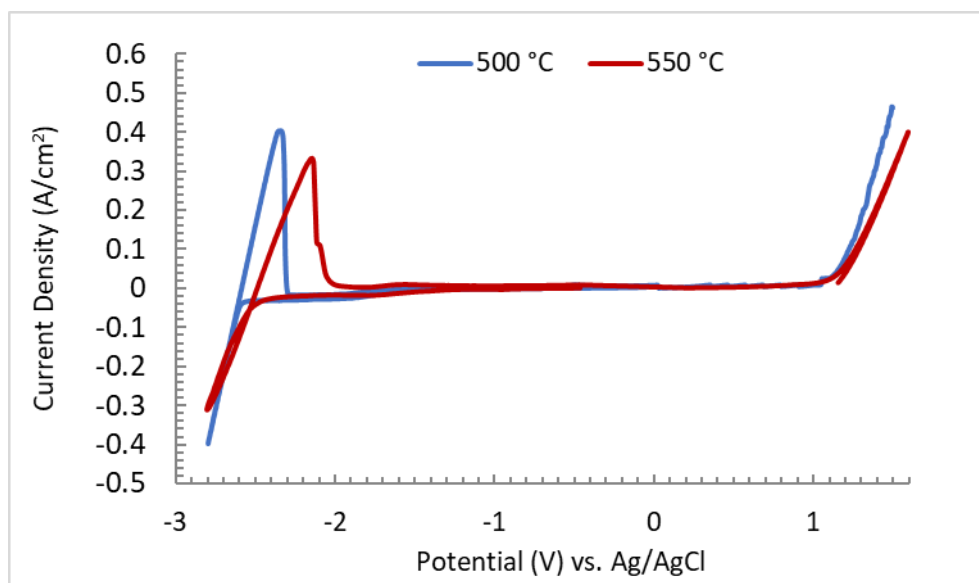


Figure 20: Cyclic Voltammogram Full Window LiCl-KCl Eutectic Molten Salt without TeCl₄ Addition Temperature Comparison, Scan Rate: 100 mV/s, Working Electrode: Tungsten Rod

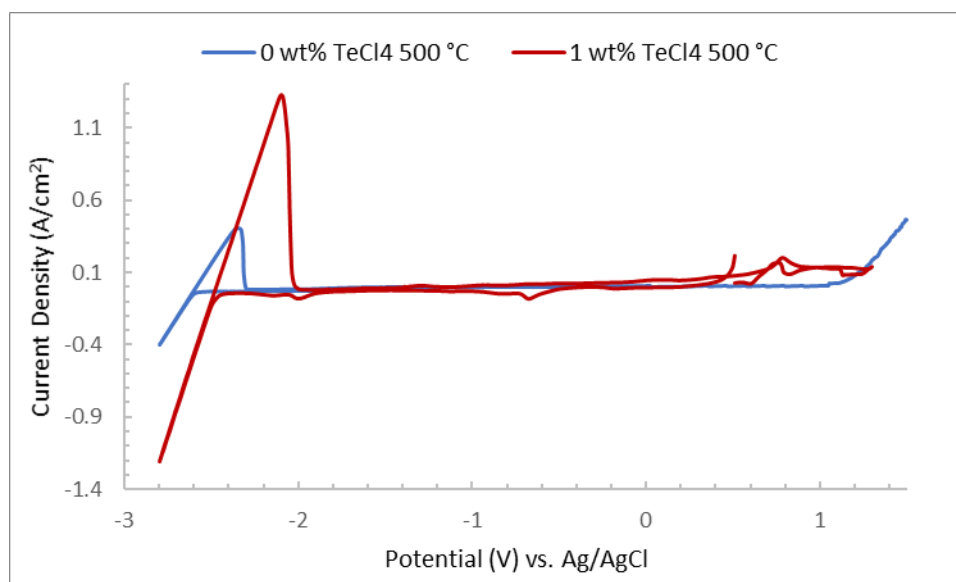


Figure 21: Cyclic Voltammogram Full Window LiCl-KCl Molten Salt w/wo 1 wt% TeCl₄ Addition 500 °C, Scan Rate: 100 mV/s, Working Electrode: Tungsten Rod

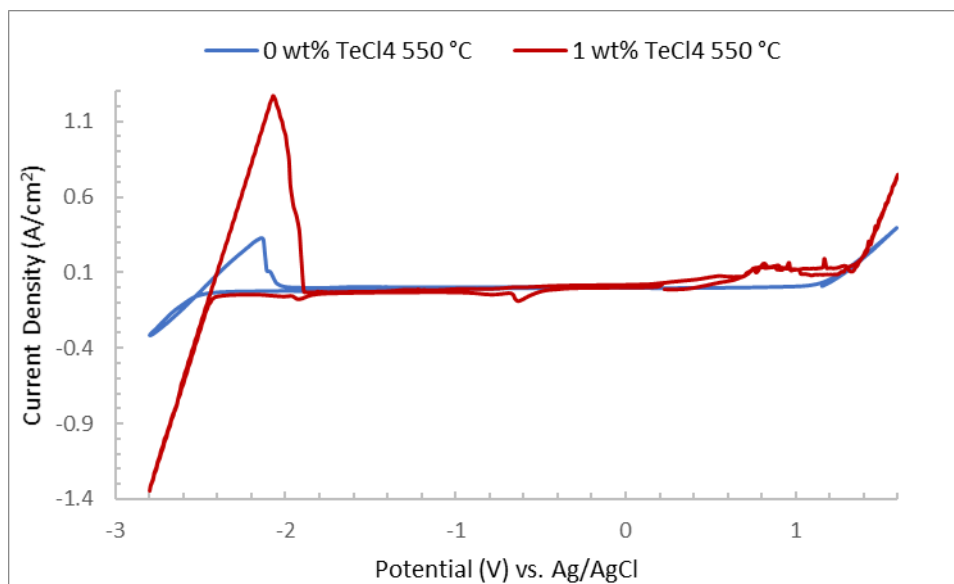


Figure 22: Cyclic Voltammogram Full Window LiCl-KCl Molten Salt w/wo 1 wt% TeCl₄ Addition 500 °C, Scan Rate: 100 mV/s, Working Electrode: Tungsten Rod

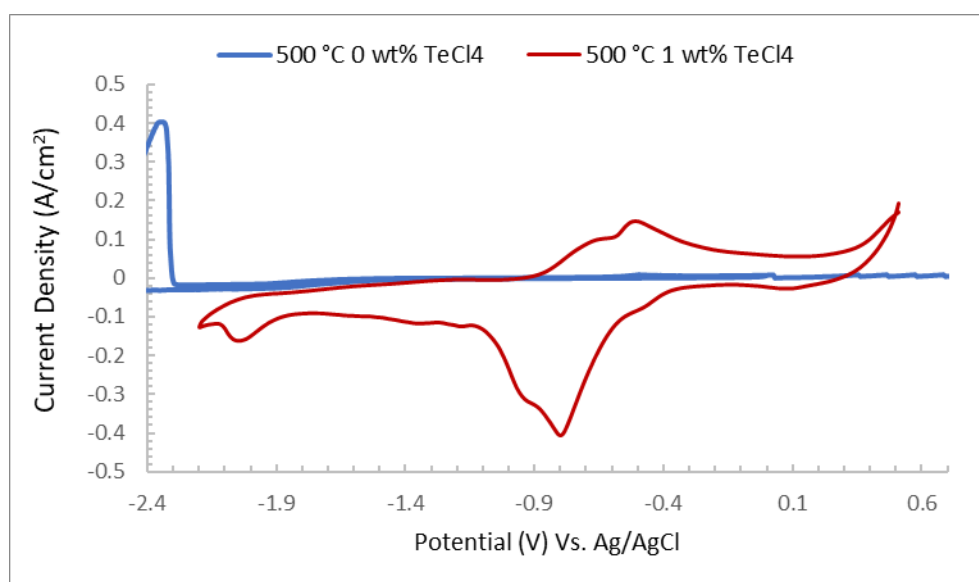


Figure 23: Cyclic voltammograms at cathodic potentials with reference to OCP in LiCl-KCl eutectic with and without 1 wt% TeCl₄ addition at 500 °C. Reduction and oxidation waves of Te species. Test conditions: 0 wt% Scan Rate: 100 mV/s, 1 wt% Scan Rate: 1000 mV/s, Working Electrode: Tungsten

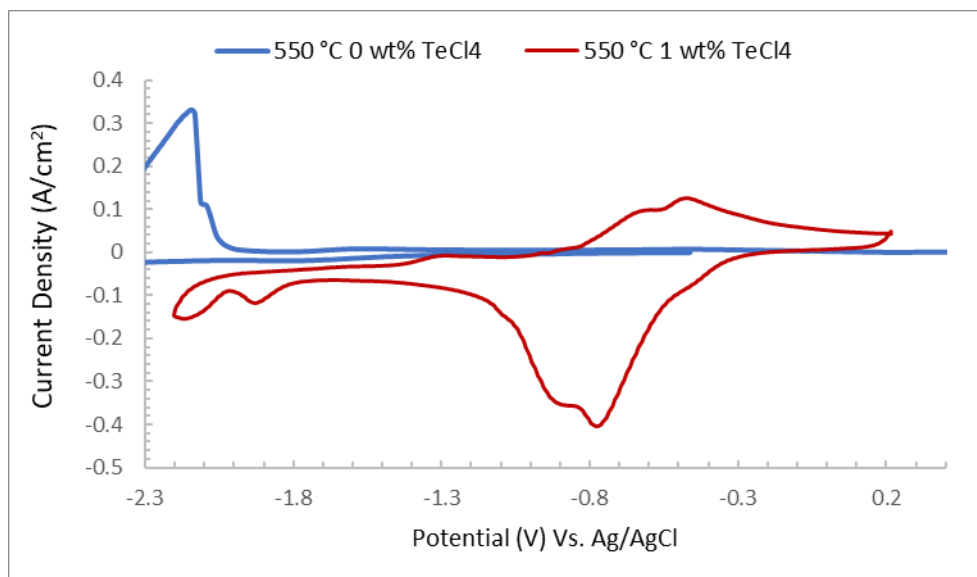


Figure 24: Cyclic voltammograms at cathodic potentials with reference to OCP in LiCl-KCl eutectic with and without 1 wt% TeCl₄ addition at 550 °C. Reduction and oxidation waves of Te species. Test conditions: 0 wt% Scan Rate: 100 mV/s, 1 wt% Scan Rate: 1000 mV/s, Working Electrode: Tungsten

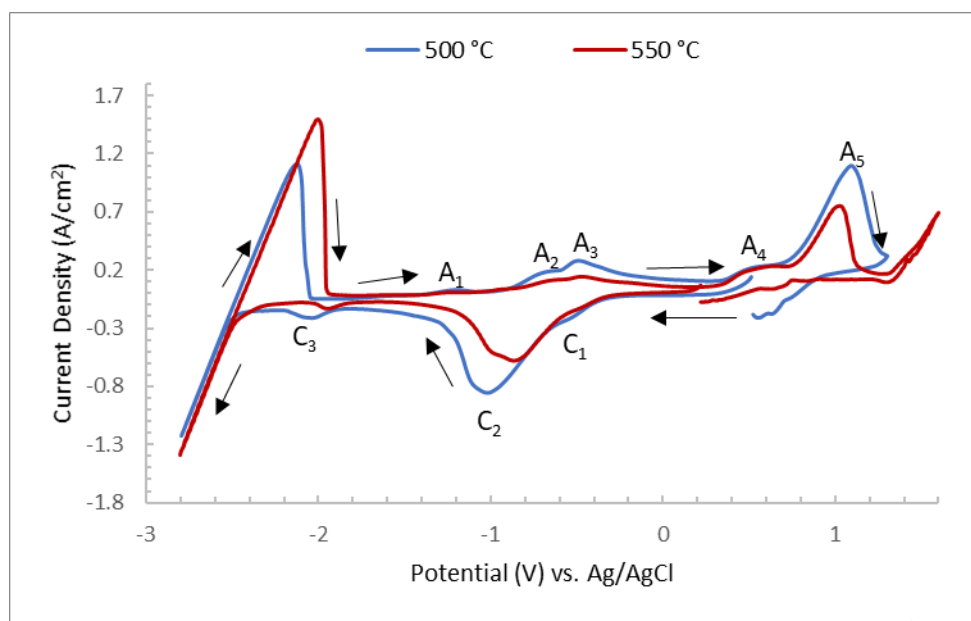


Figure 25: Cyclic Voltammogram Full Window of 1 wt% TeCl₄ in LiCl-KCl Eutectic Molten Salt Temperature Comparison, Scan Rate: 1000 mV/s, Working Electrode: Tungsten Rod

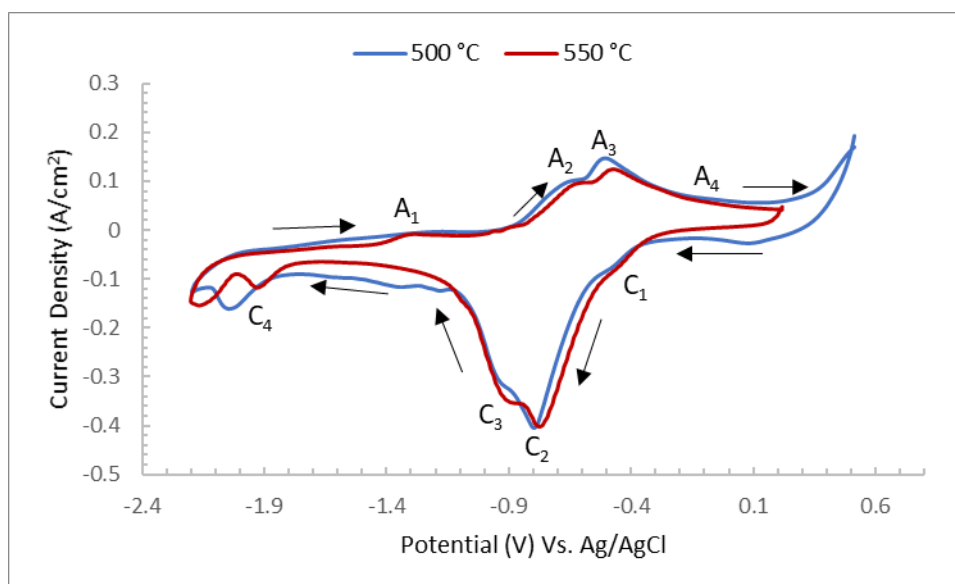


Figure 26: Cyclic voltammograms at different scan rates in 1 wt% TeCl_4 in LiCl-KCl eutectic molten salt Temperature Comparison, Scan Rate: 1000 mV/s, Working Electrode: Tungsten Rod

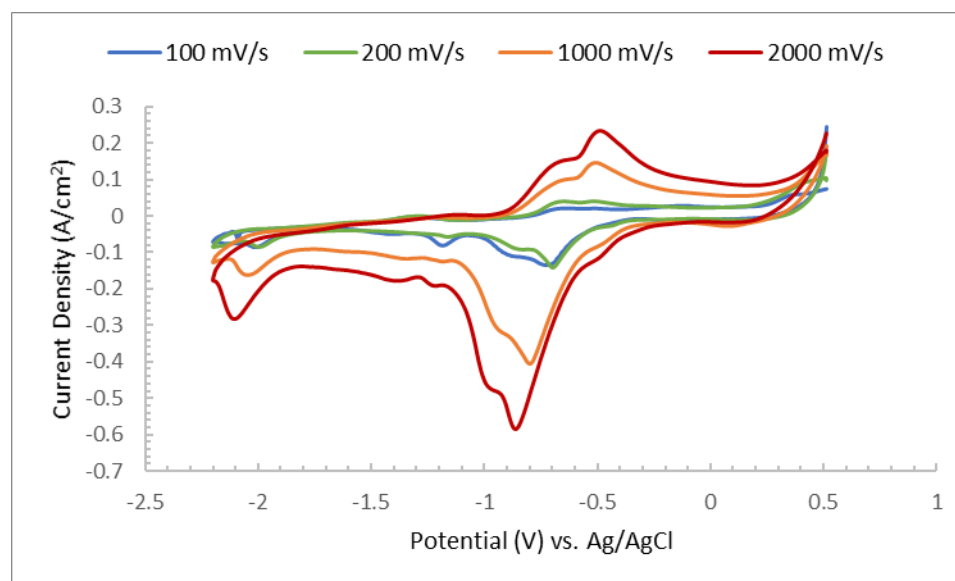


Figure 27: Cyclic Voltammogram (OCP to -2.2 V) 1 wt% TeCl_4 500 °C Scan Rates: 100-2000 mV/s, Working Electrode: Tungsten Rod

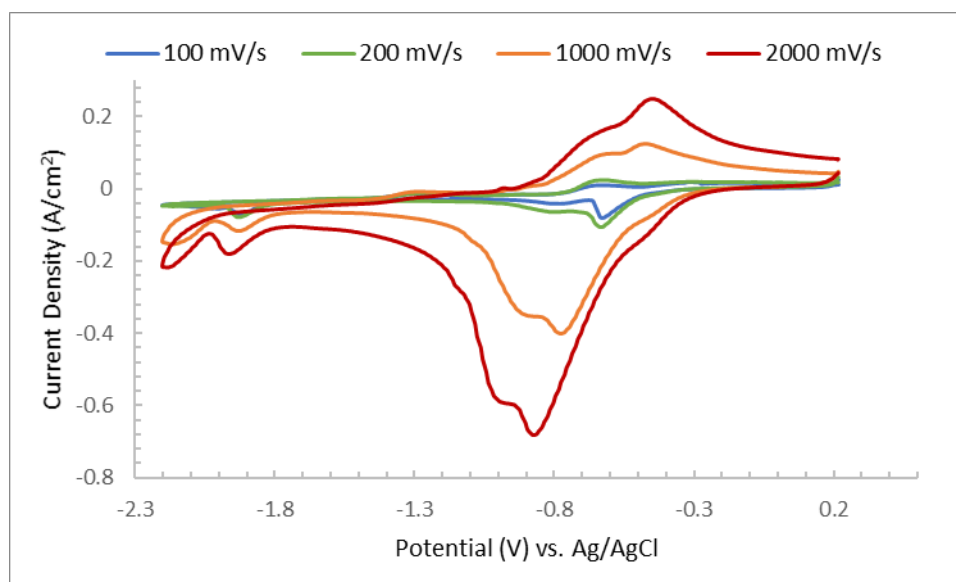


Figure 28: Cyclic Voltammogram (OCP to -2.2V) 1 wt% TeCl_4 , 550 °C, Scan Rate: 100 -1000 mV/s, Working Electrode: Tungsten Rod

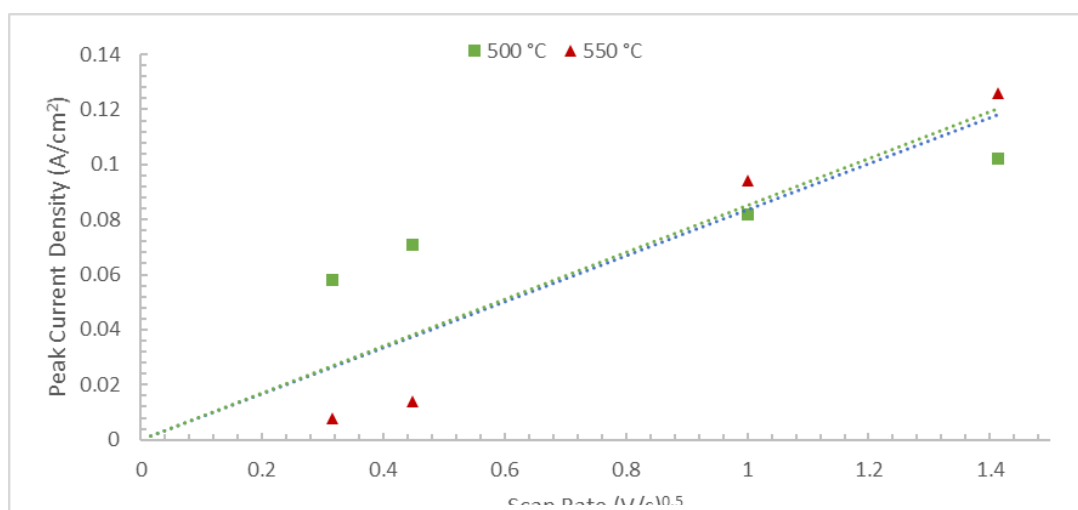


Figure 29: Comparing Square Root of Scan Rate vs. Peak Current Density for Te^{4+} to Te^{2+} at 500 and 550 °C, Working Electrode: Tungsten

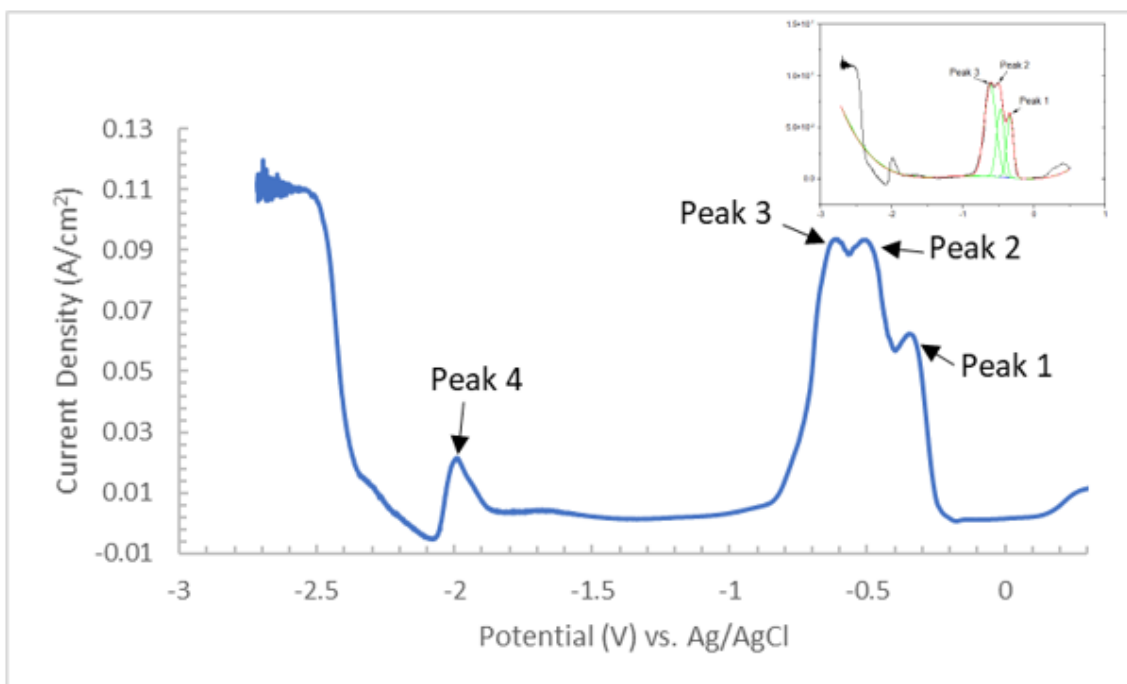


Figure 30: SWV 1 wt% TeCl₄ in LiCl-KCl molten salt at 500 and 550 °C, Working Electrode: Tungsten Rod

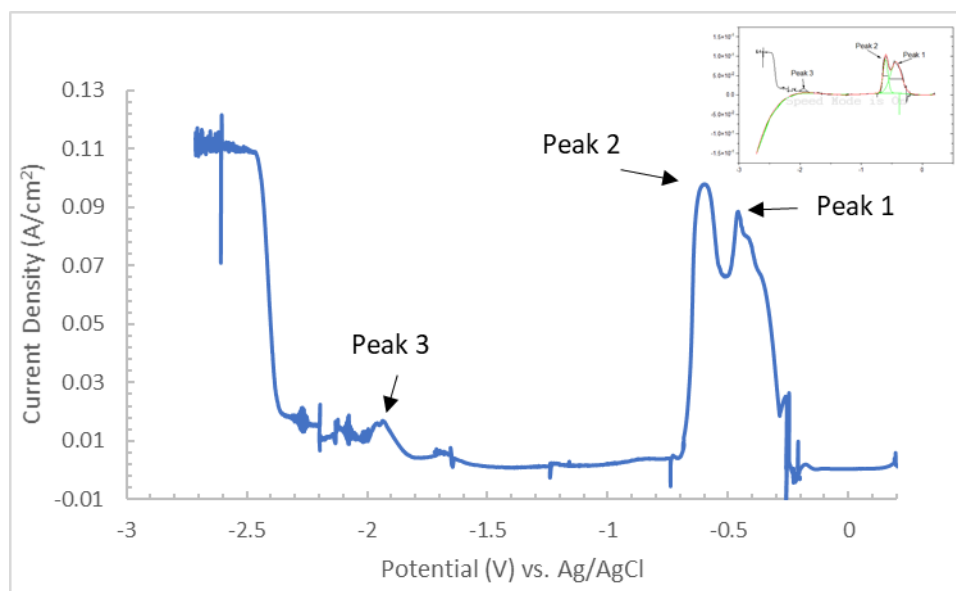


Figure 31: SWV 1 wt% TeCl₄ in LiCl-KCl molten salt at 550 °C, Working Electrode: Tungsten Rod

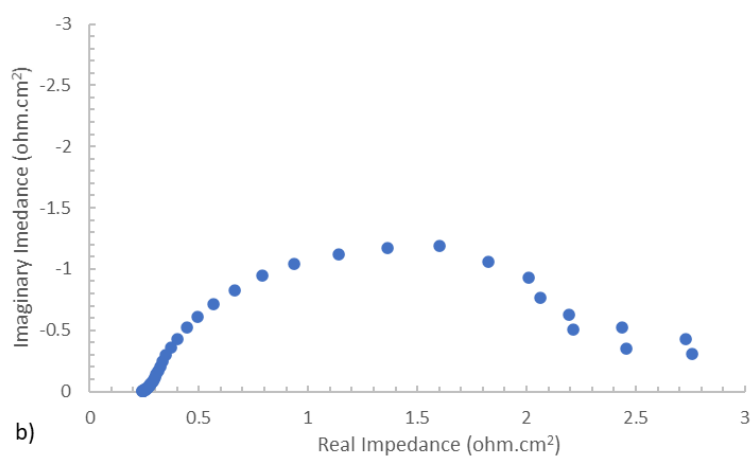
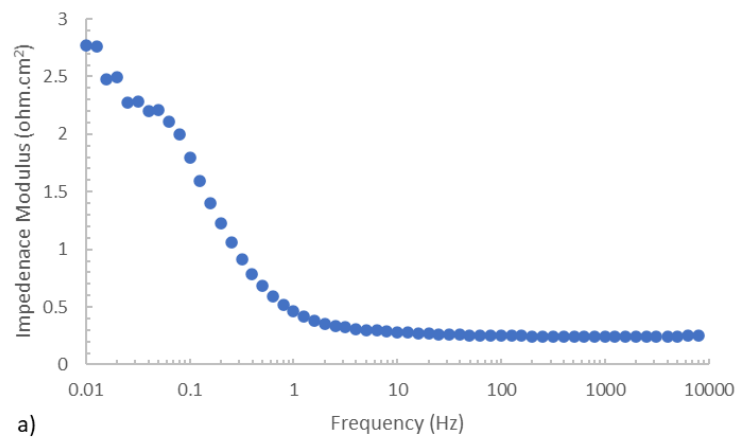


Figure 32: EIS of 1 wt% TeCl₄ at Open Circuit Potential for 500 °C:
a) Bode Plot, b) Nyquist, WE: Tungsten

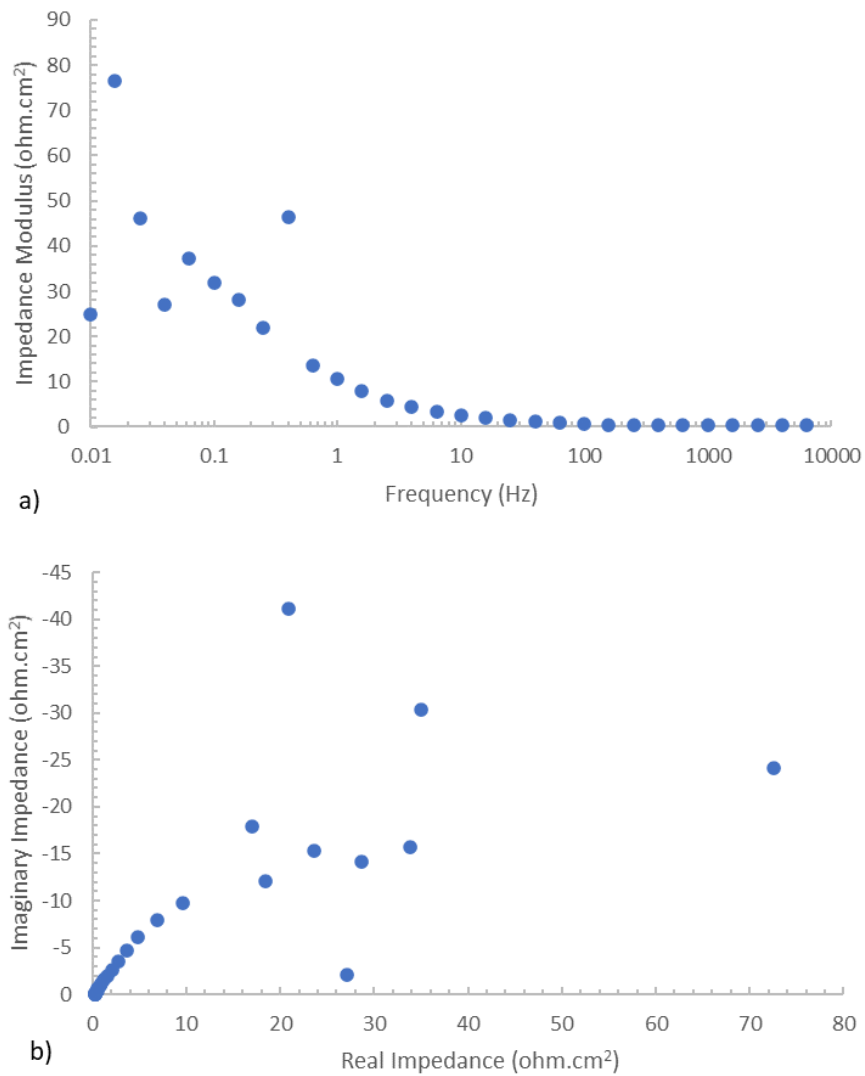


Figure 33: EIS of 1 wt% TeCl_4 at Open Circuit Potential for 550 °C: a) Bode Plot, b) Nyquist, WE: Tungsten

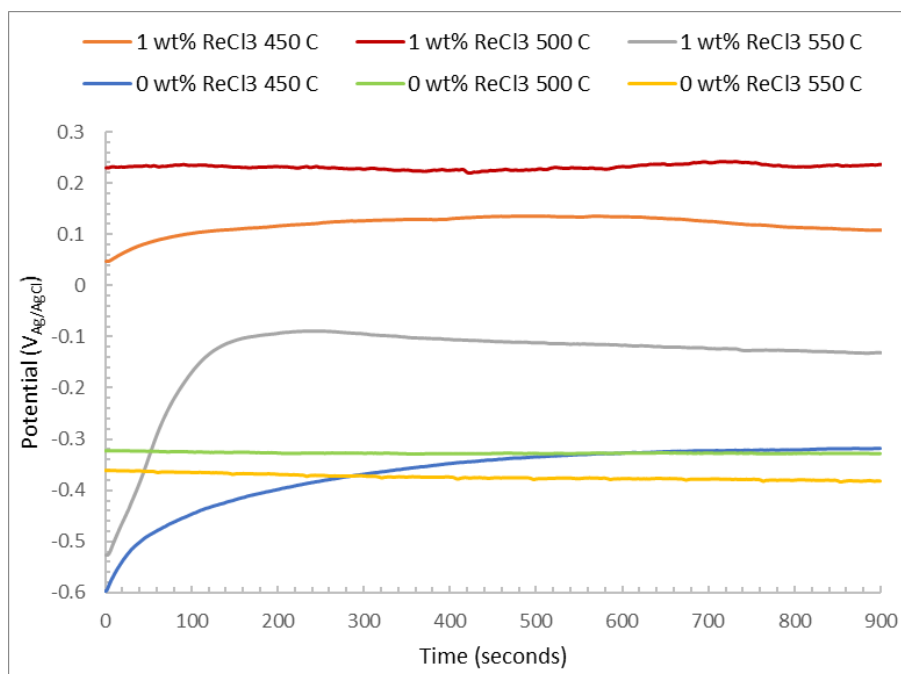


Figure 34: OCP comparing 0 and 1 wt% ReCl₃ at 450 - 550 °C, WE: Tungsten Rod

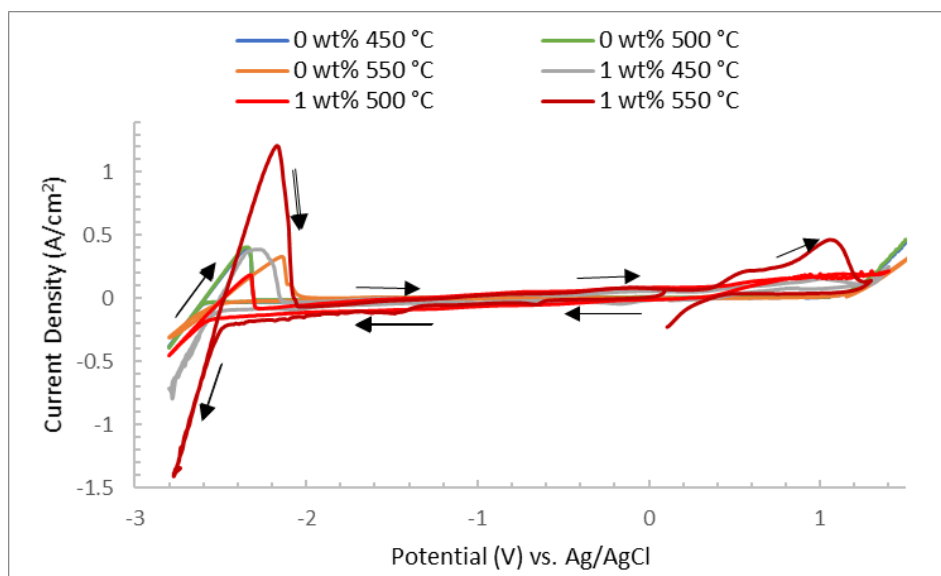


Figure 35: Cyclic voltammogram (CV) in LiCl+KCl eutectic with the addition of 0 and 1 wt% ReCl₃ at 450 to 550 °C using molybdenum rod as a working electrode, scan rate: 100 mV/s

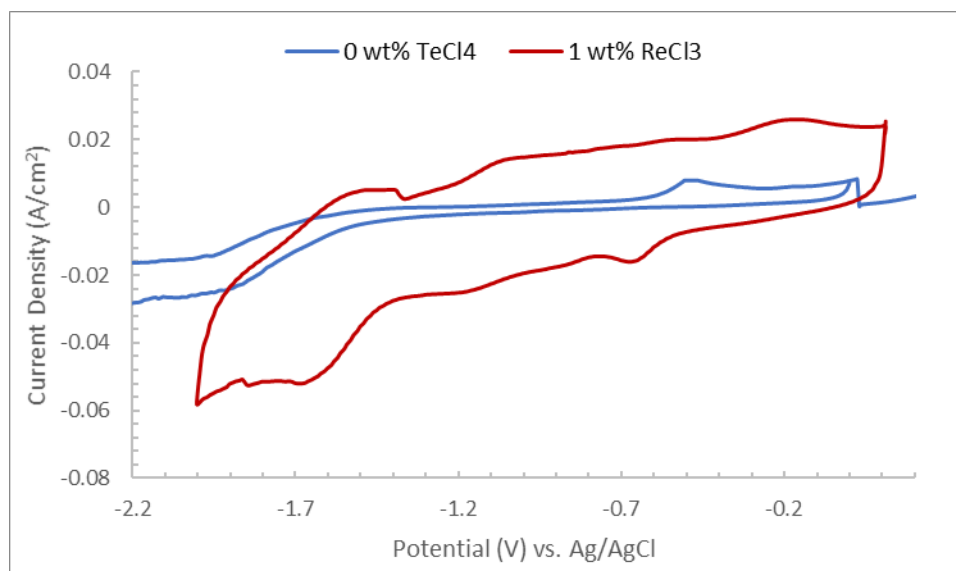


Figure 36: Cyclic voltammograms at cathodic potentials with reference to OCP in LiCl-KCl eutectic with and without 1 wt% ReCl_3 addition at 450 °C. Reduction and oxidation waves of Re species are revealed. Test conditions: scan rate: 100 mV s^{-1} , WE: Molybdenum

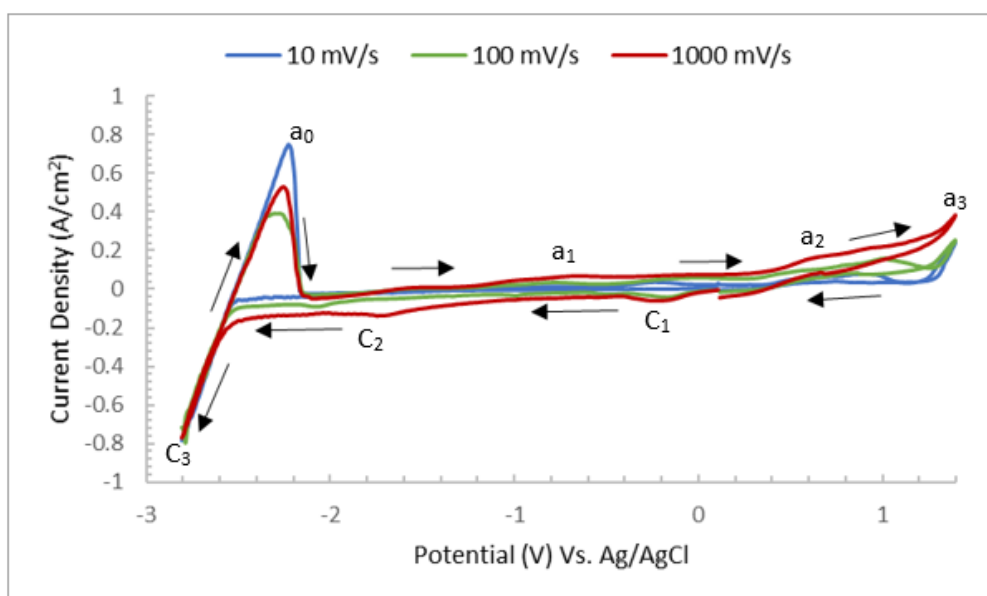


Figure 37: Cyclic voltammograms in LiCl-KCl eutectic with 1 wt% ReCl_3 addition at 450 °C at different scan rates, WE: Molybdenum Rod

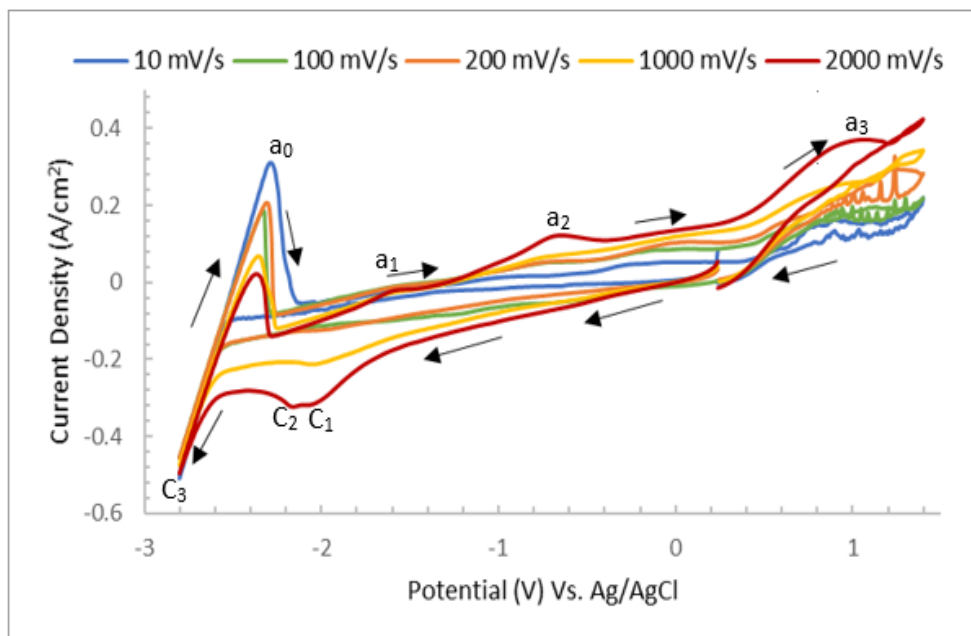


Figure 38: Cyclic voltammograms in LiCl-KCl eutectic with 1 wt% ReCl_3 addition at 500 °C at different scan rates, WE: Molybdenum Rod

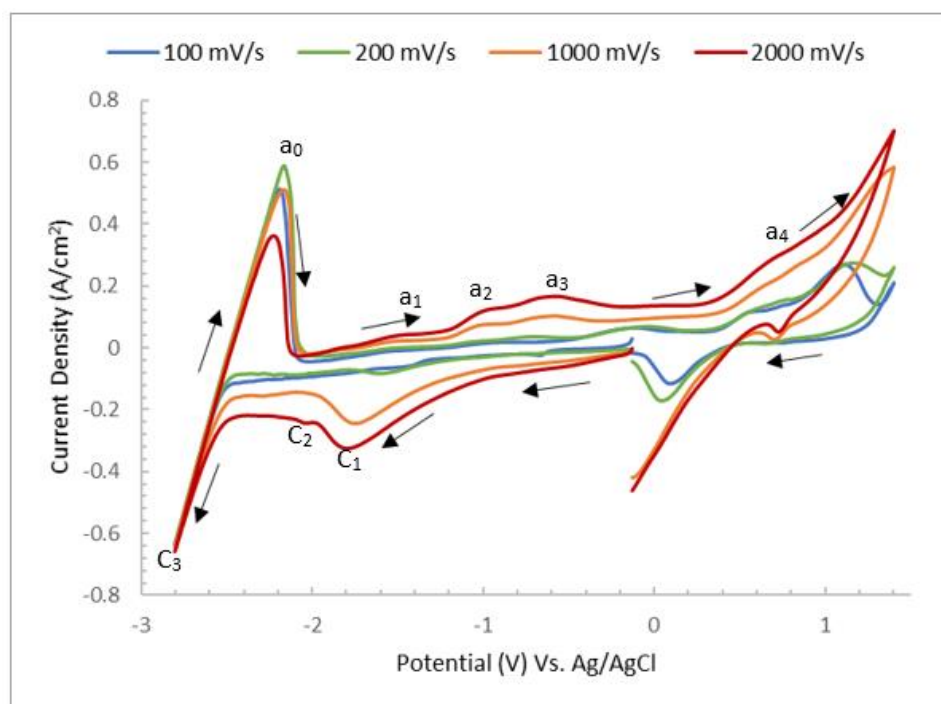


Figure 39: Cyclic voltammograms in LiCl-KCl eutectic with 1 wt% ReCl_3 addition at 550 °C at different scan rates, WE: Molybdenum Rod

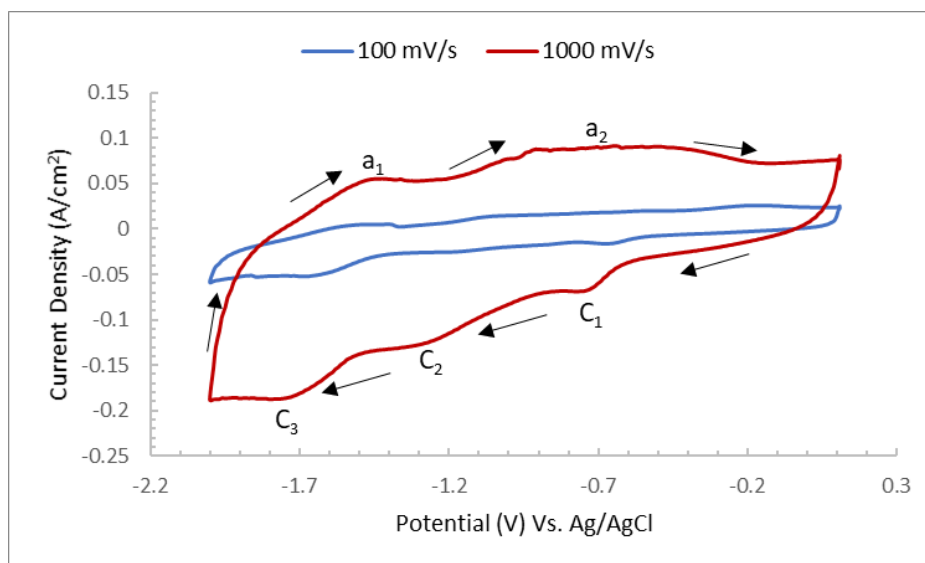


Figure 40: Cyclic voltammograms at different scan rates in 1 wt% ReCl_3 containing LiCl-KCl eutectic molten salt at 450°C , WE: Molybdenum Rod

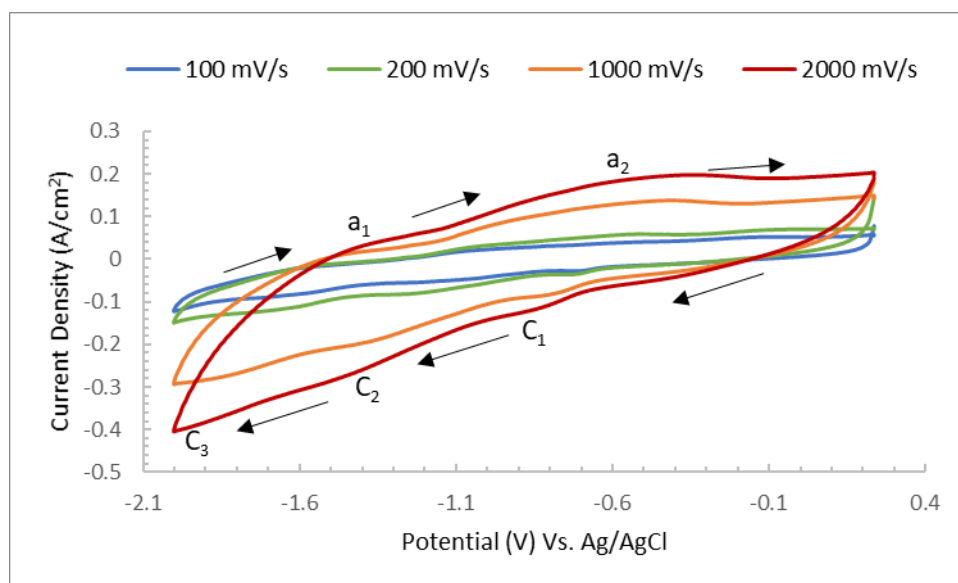


Figure 41: Cyclic voltammograms at different scan rates in 1 wt% ReCl_3 containing LiCl-KCl eutectic molten salt at 500°C , WE: Molybdenum Rod

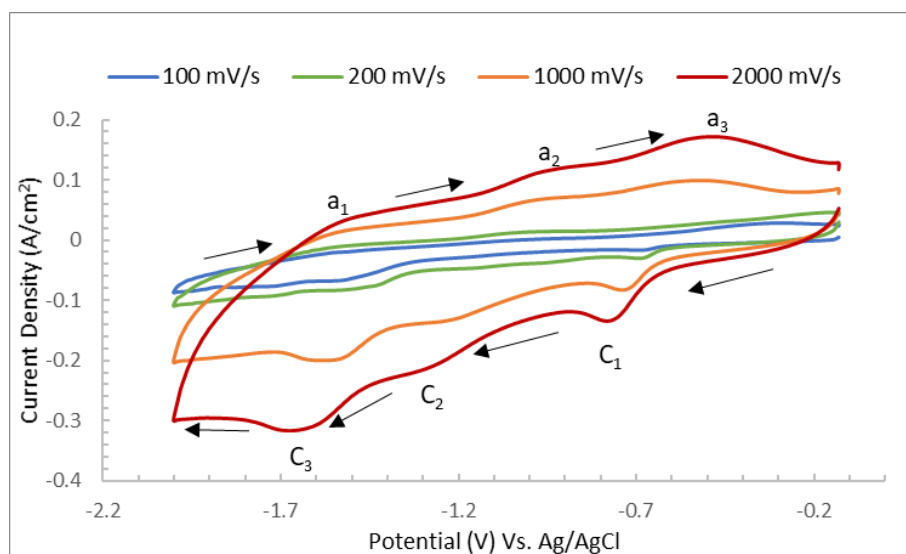


Figure 42: Cyclic voltammograms at different scan rates in 1 wt% ReCl_3 containing LiCl-KCl eutectic molten salt at 550 °C, WE: Molybdenum Rod

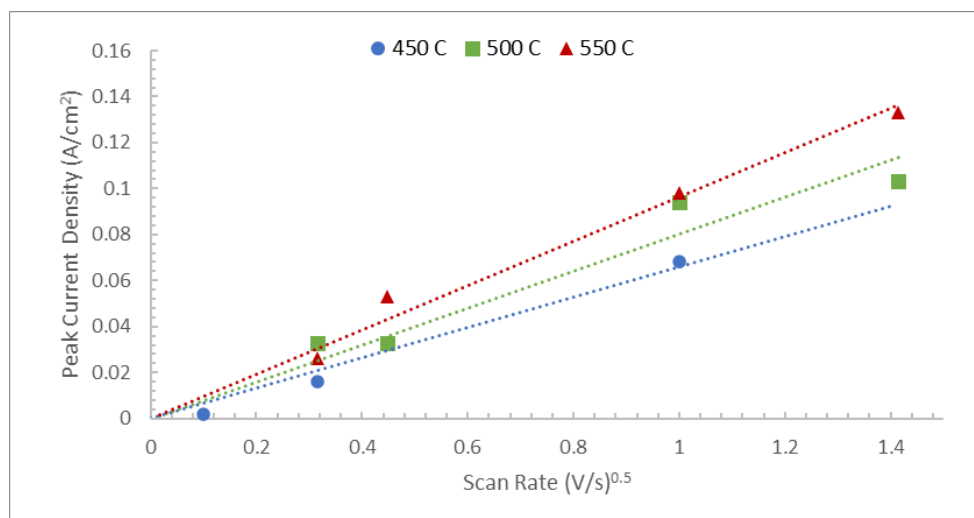


Figure 43: Plots of peak current density versus square root of scan rate in 1 wt% ReCl_3 containing LiCl-KCl melt at 450 °C to 550 °C

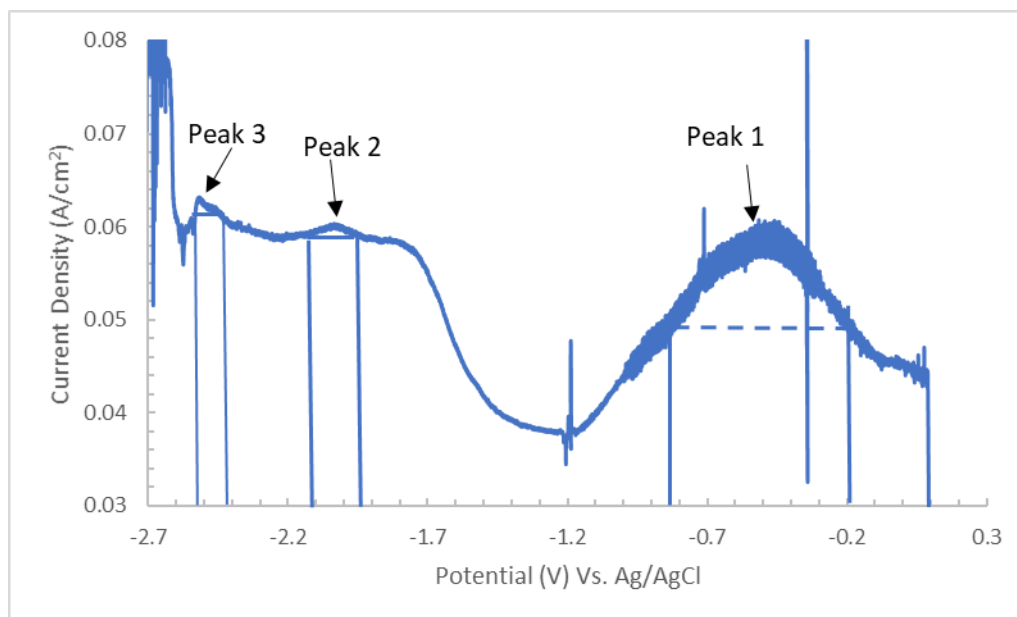


Figure 44: SWV 1 wt% ReCl_3 in LiCl-KCl molten salt at 450 °C, Working Electrode Molybdenum Rod

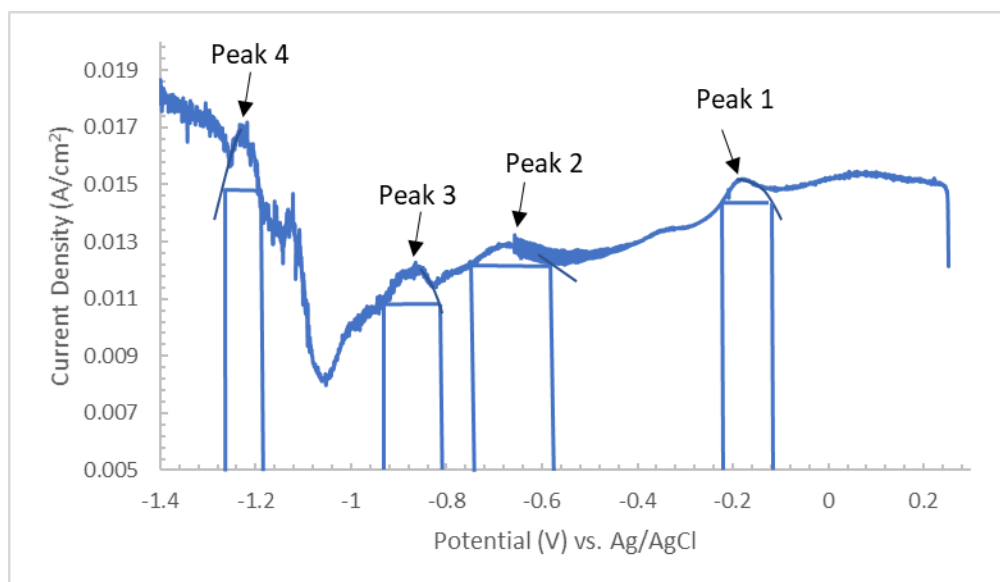


Figure 45: SWV 5 wt% ReCl_3 in LiCl-KCl molten salt at 500 °C, Working Electrode Molybdenum Rod

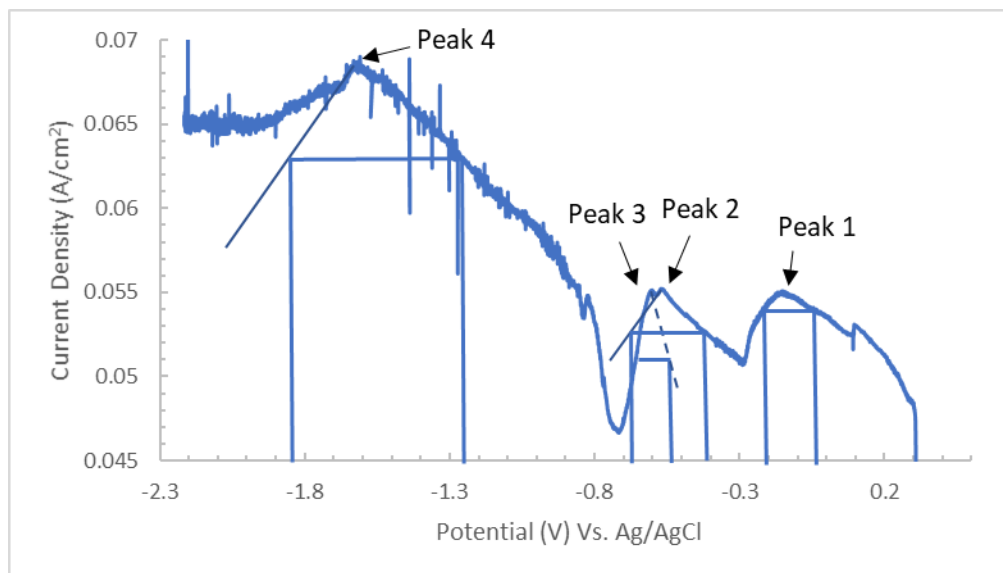


Figure 46: SWV 5 wt% ReCl₃ in LiCl-KCl molten salt at 550 °C, Working Electrode Molybdenum Rod

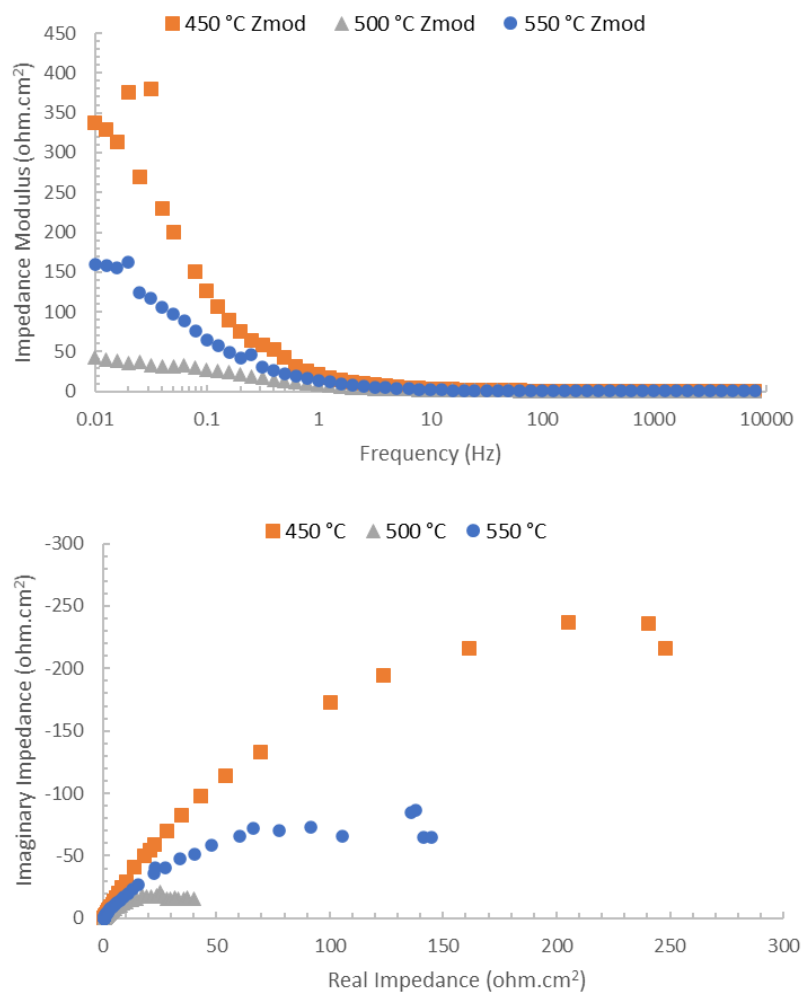


Figure 47: EIS of 1 wt% ReCl_3 at Open Circuit Potential for 450 to 550 °C: a) Bode Plot, b) Nyquist, WE: Molybdenum

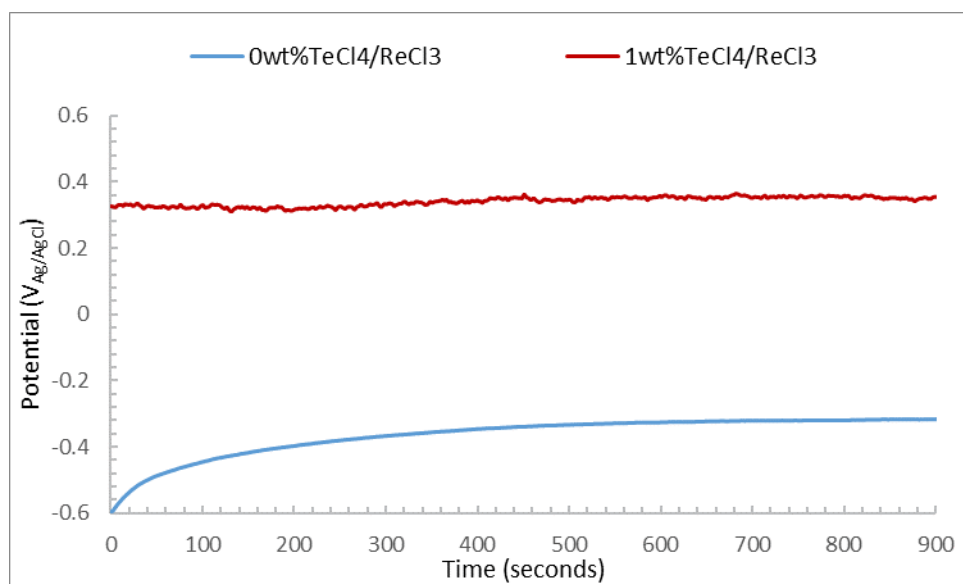


Figure 48: OCP comparing 0 and 1 wt% $\text{TeCl}_4/\text{ReCl}_3$ at 450°C , WE: Molybdenum Rod

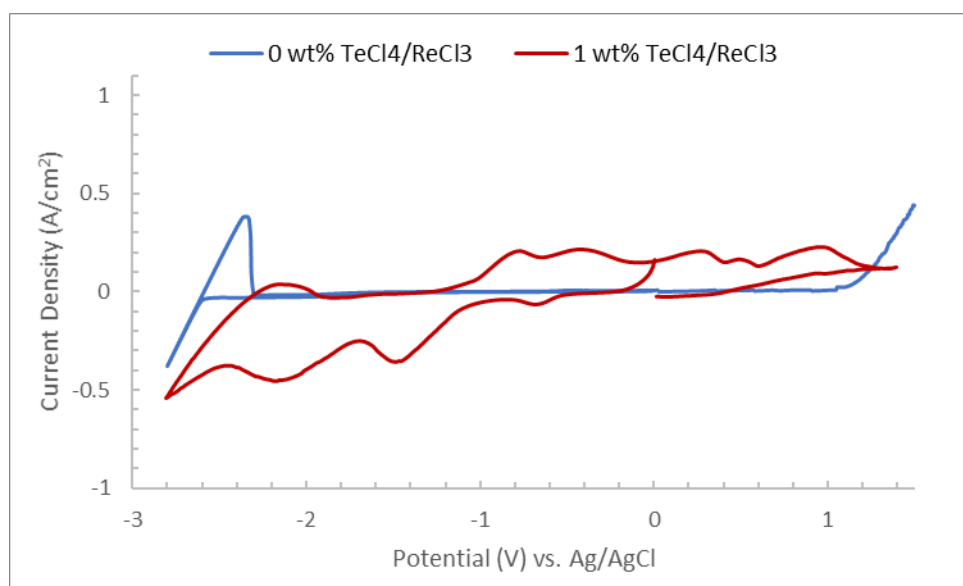


Figure 49: Cyclic voltammogram (CV) in $\text{LiCl}+\text{KCl}$ eutectic with the addition of 0 and 1 wt% $\text{TeCl}_4/\text{ReCl}_3$ at 450°C using molybdenum as a working electrode at a scan rate of 100 mV/s

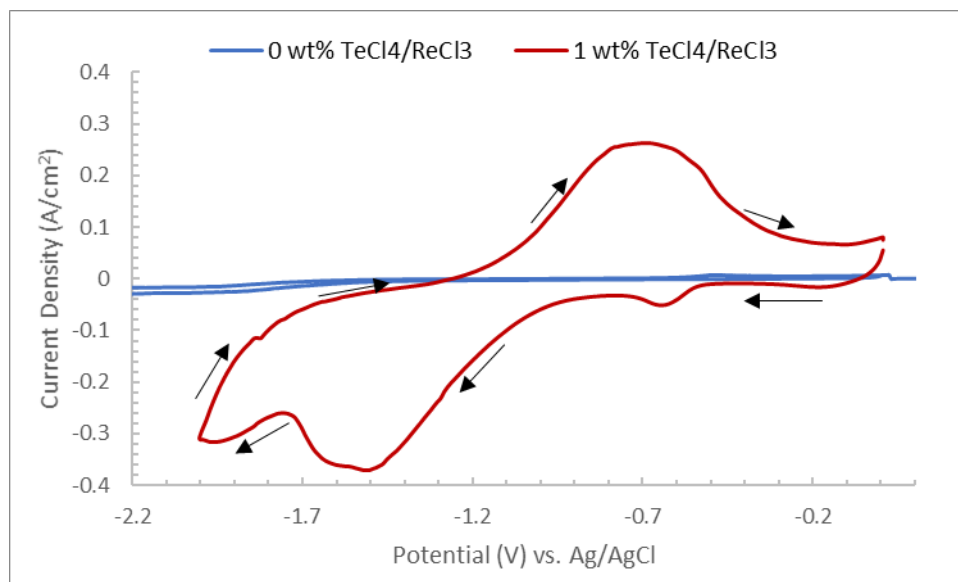


Figure 50: Cyclic voltammogram LiCl-KCl eutectic with and without 1 wt% $\text{TeCl}_4/\text{ReCl}_3$ addition at 450 °C. Reduction and oxidation waves of Re and Te species are revealed. Test conditions: scan rate: 100 mV s^{-1} , WE: Molybdenum

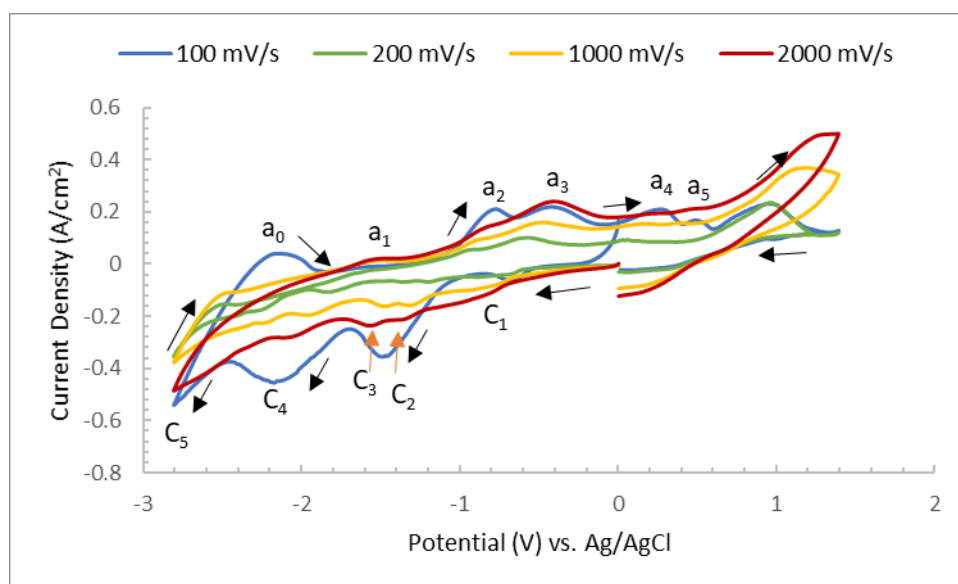


Figure 51: Cyclic voltammograms in LiCl-KCl eutectic with 1 wt% $\text{TeCl}_4/\text{ReCl}_3$ addition at 450 °C at different scan rates, WE: Molybdenum Rod

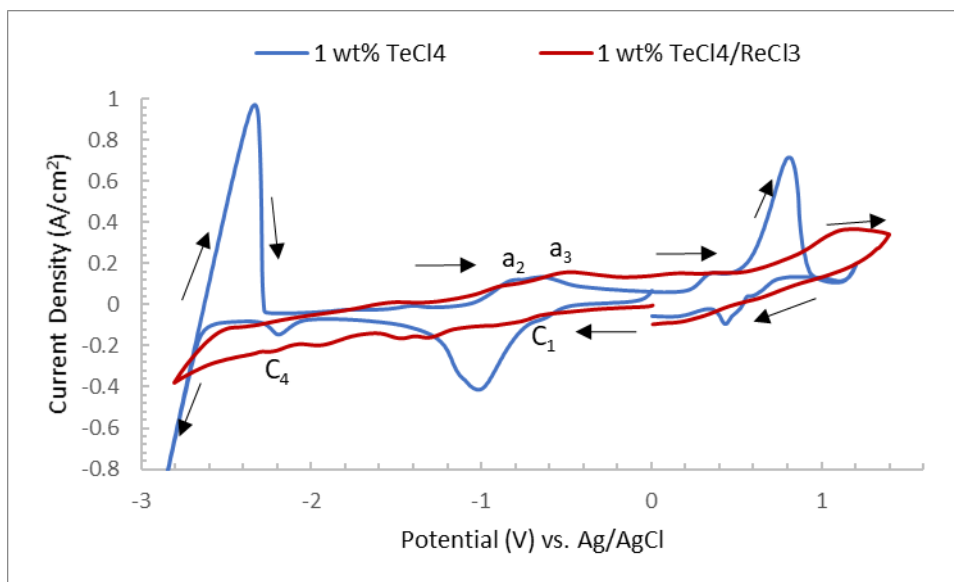


Figure 52: Cyclic voltammograms in LiCl-KCl eutectic comparing 1 wt% TeCl₄ with 1 wt% TeCl₄/ReCl₃ addition at 450 °C at 1000 mV/s, WE: Molybdenum Rod

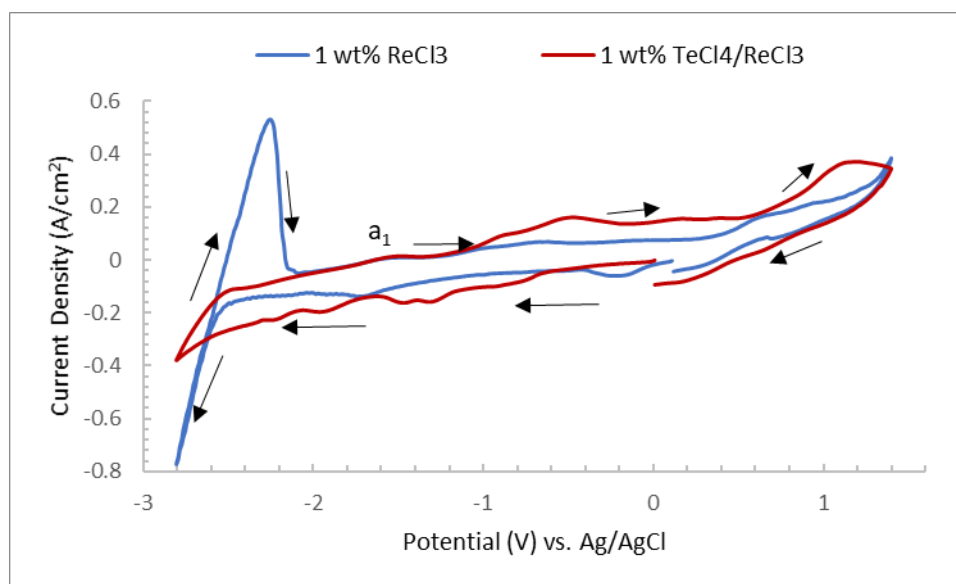


Figure 53: Cyclic voltammograms in LiCl-KCl eutectic comparing 1 wt% ReCl₃ with 1 wt% TeCl₄/ReCl₃ addition at 450 °C at 1000 mV/s, WE: Molybdenum Rod

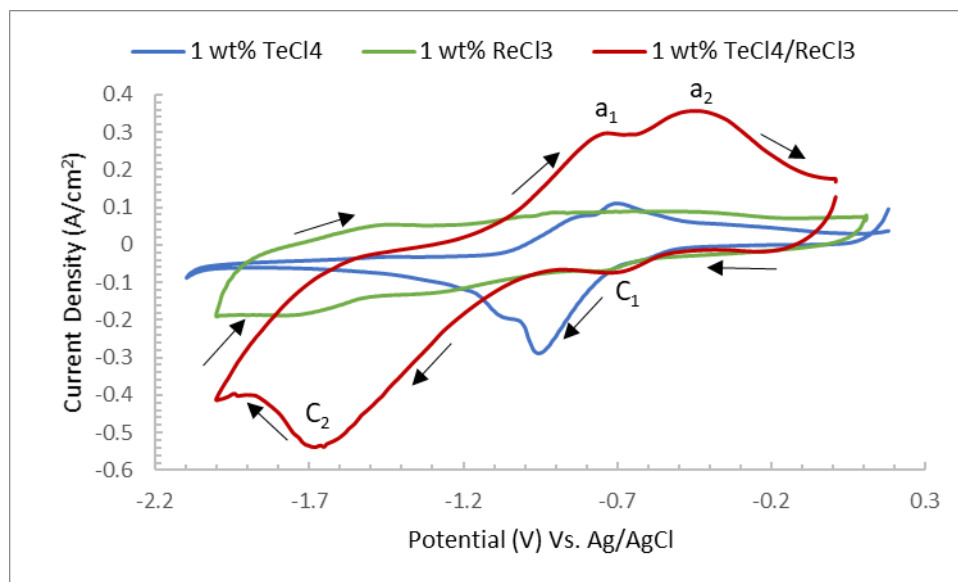


Figure 54: Cyclic voltammograms in LiCl-KCl eutectic comparing 1 wt% TeCl_4 and 1 wt% ReCl_3 with 1 wt% $\text{TeCl}_4/\text{ReCl}_3$ addition at 450 °C Scan Rate $\text{TeCl}_4/\text{ReCl}_3$: 200, Scan Rate 1 wt Te and 1Re: 1000 mV/s, WE: Molybdenum Rod

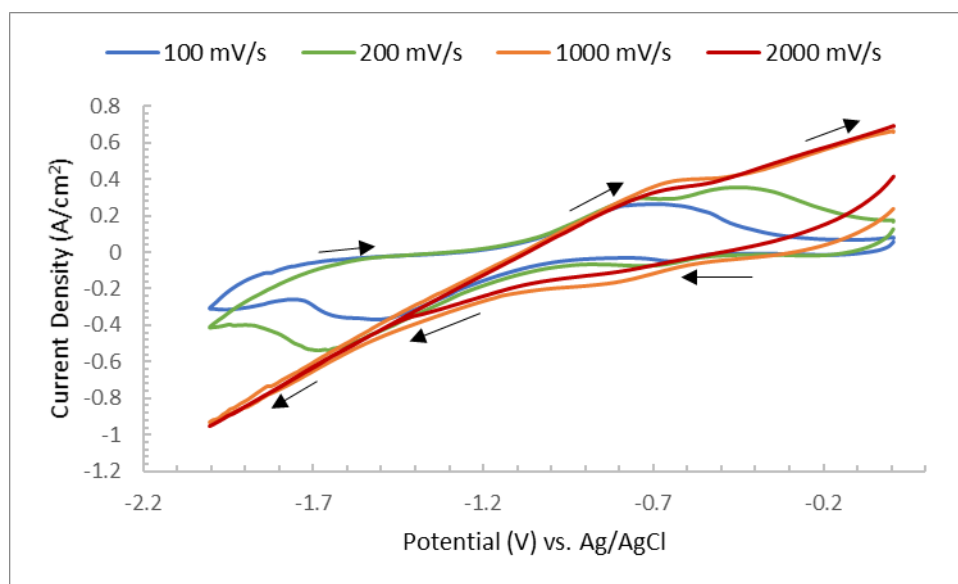


Figure 55: Cyclic voltammograms in LiCl-KCl eutectic comparing varying scan rates of 1 wt% $\text{TeCl}_4/\text{ReCl}_3$ addition at 450 °C, WE: Molybdenum Rod

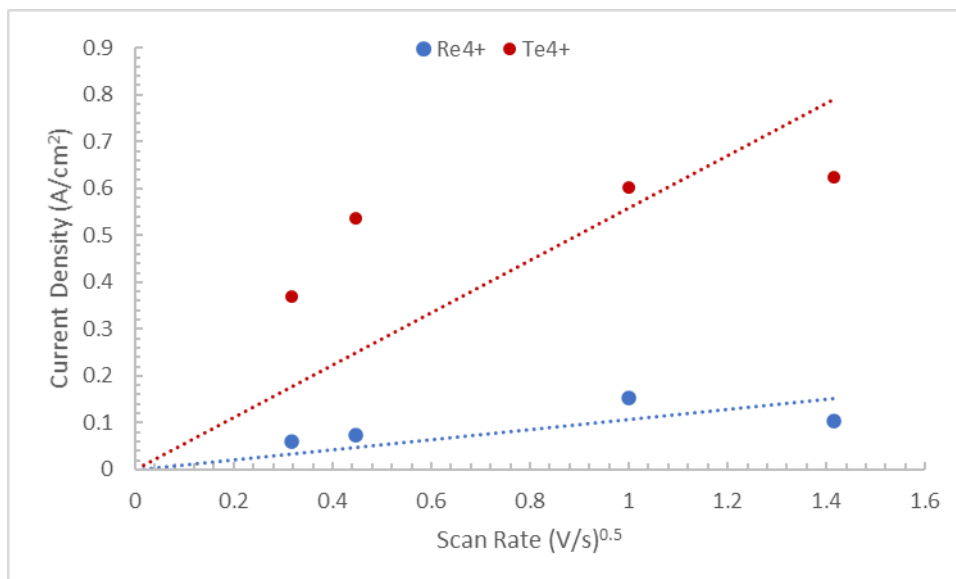


Figure 56: Plots of peak current density versus square root of scan rate in 1 wt% $\text{TeCl}_4/\text{ReCl}_3$ containing LiCl-KCl melt at 450 °C

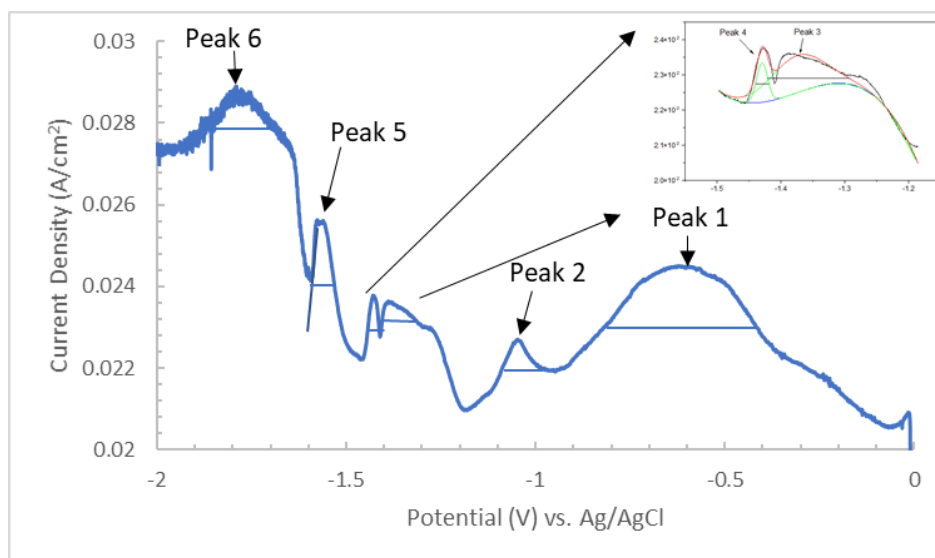


Figure 57: SWV 1 wt% $\text{TeCl}_4/\text{ReCl}_3$ in LiCl-KCl molten salt at 450 °C, Working Electrode Molybdenum Rod

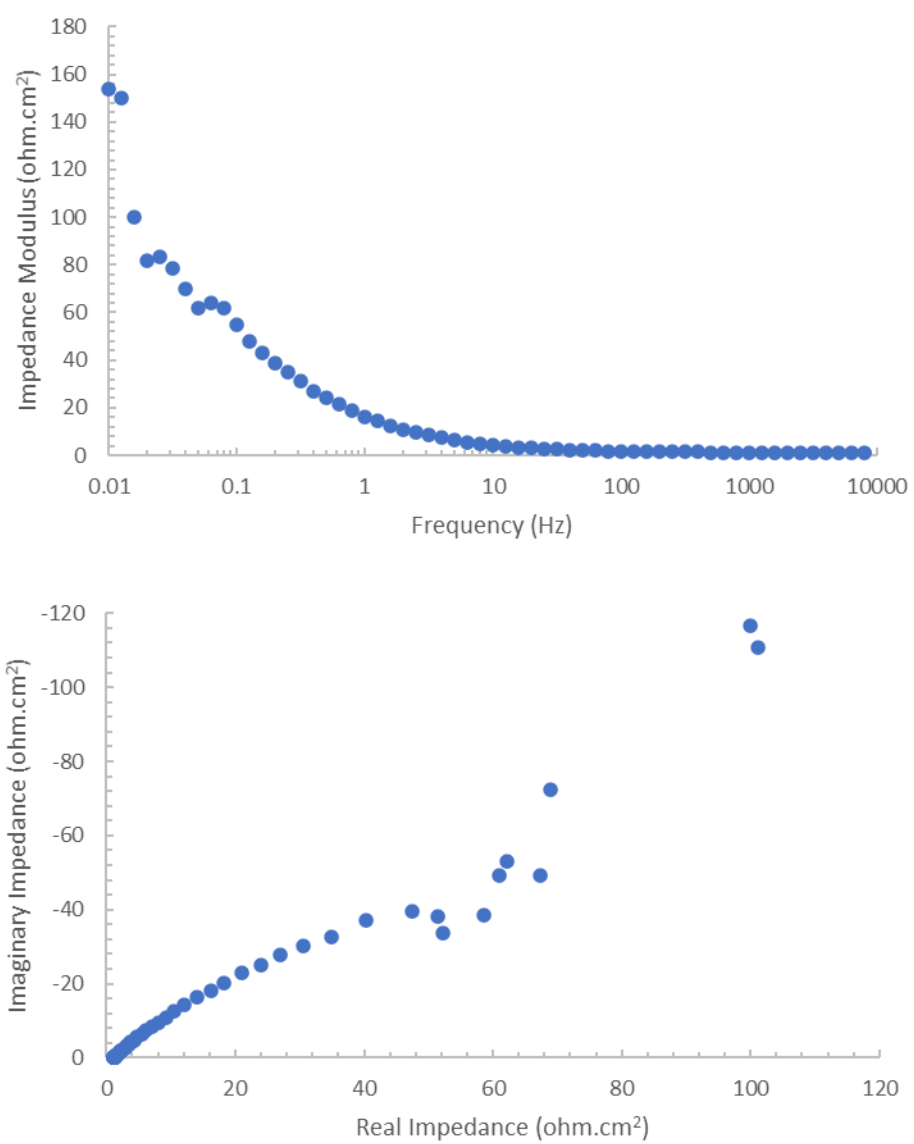


Figure 58: EIS of 1 wt% $\text{TeCl}_4/\text{ReCl}_3$ at Open Circuit Potential for 450 °C: a) Bode Plot, b) Nyquist, WE: Molybdenum

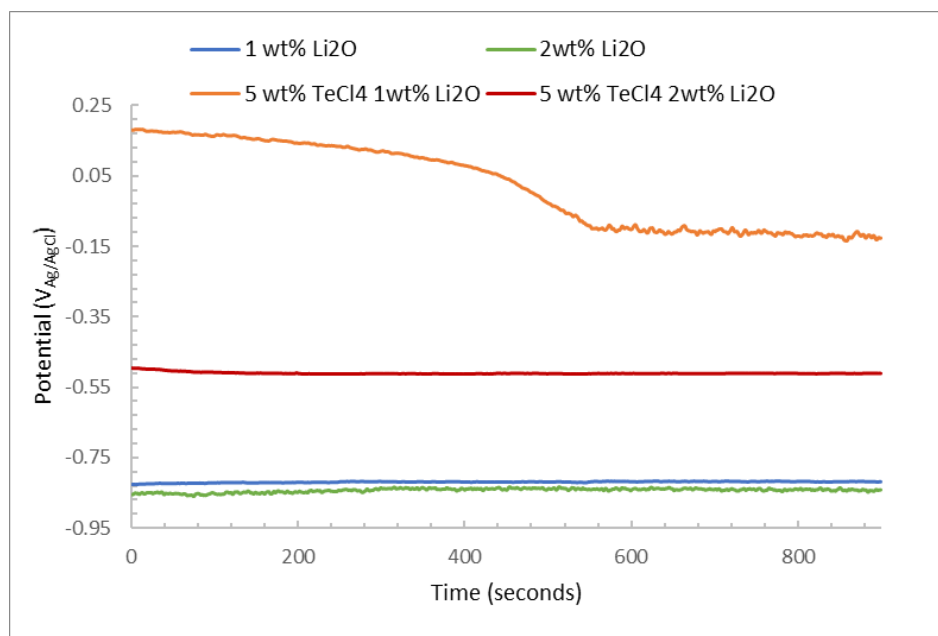


Figure 59: OCP of glassy carbon (GC) electrode in LiCl-KCl eutectic containing 5wt% TeCl₄ with varying concentration of Li₂O at 550 °C.

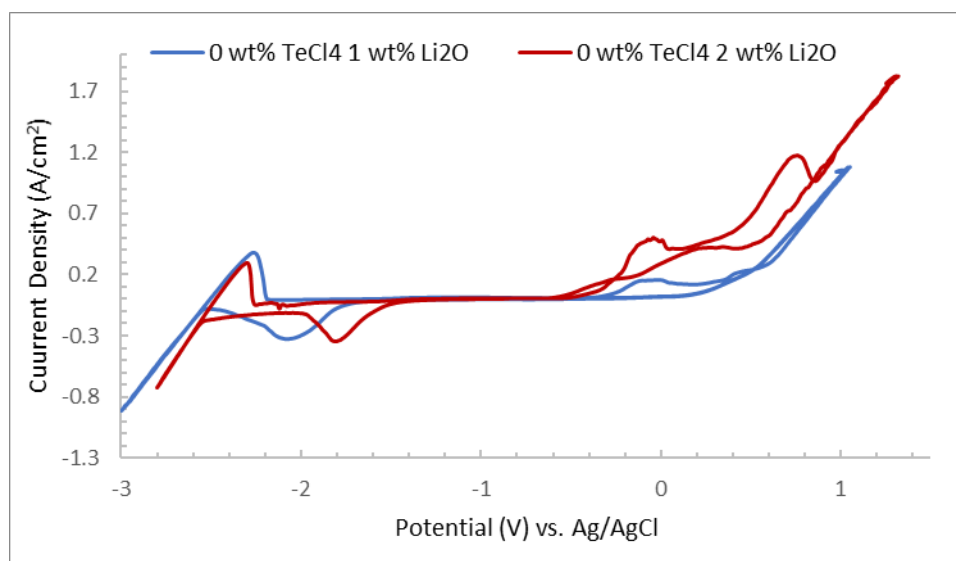


Figure 60: CV of tungsten electrode in LiCl-KCl eutectic comparing without 5wt% TeCl₄ with varying concentration of Li₂O at 550 °C

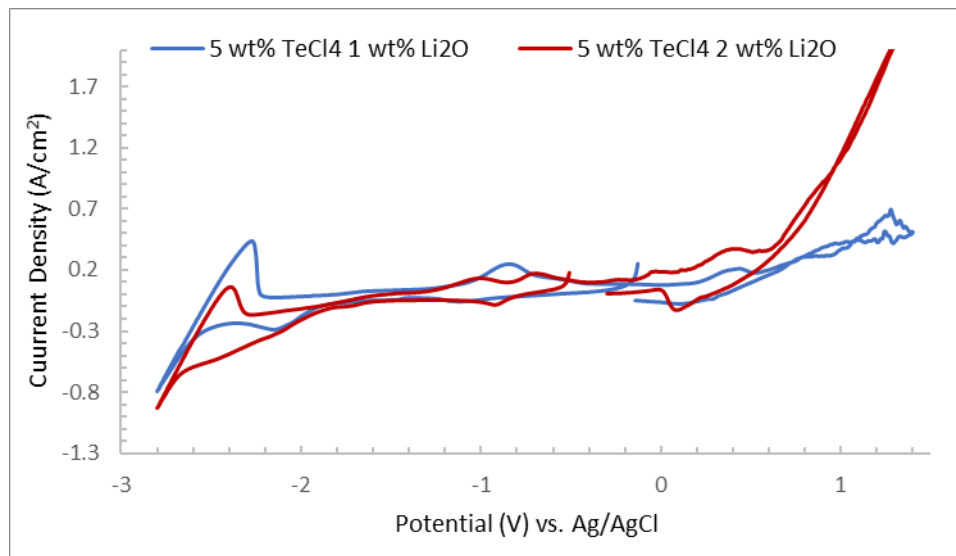


Figure 61: CV of tungsten electrode in LiCl-KCl eutectic comparing with 5wt% TeCl₄ with varying concentration of Li₂O at 550 °C

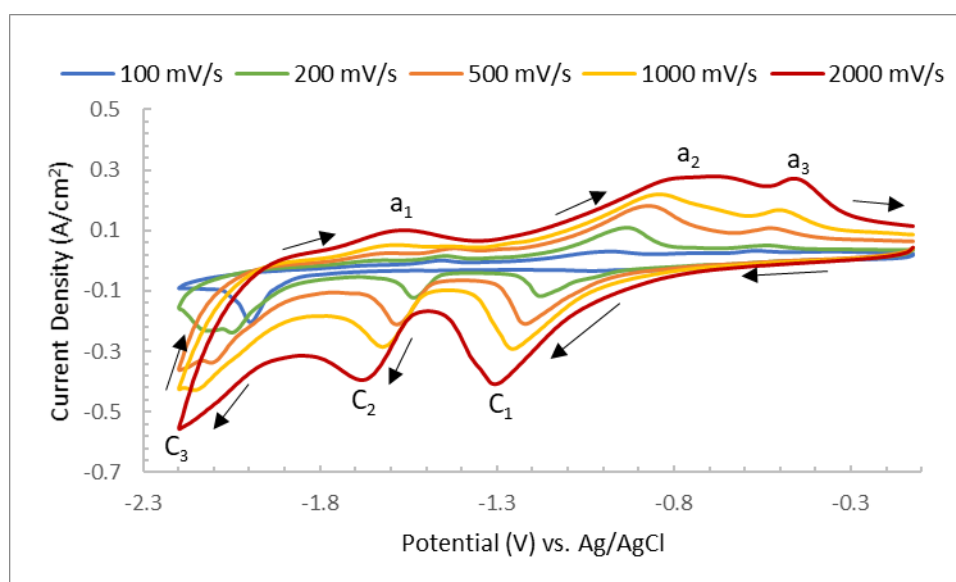


Figure 62: CV of LiCl-KCl eutectic molten salt comparing various scan rates with 5wt% TeCl₄ with 1 wt% Li₂O at 550 °C, WE: Tungsten Rod

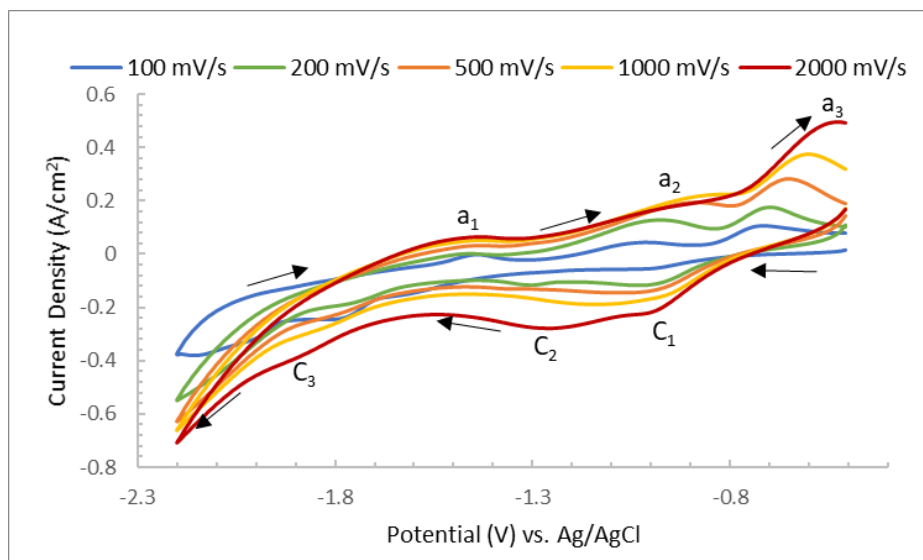


Figure 63: CV of LiCl-KCl eutectic molten salt comparing various scan rates with 5wt% TeCl₄ with 2 wt% Li₂O at 550 °C, WE: Tungsten Rod

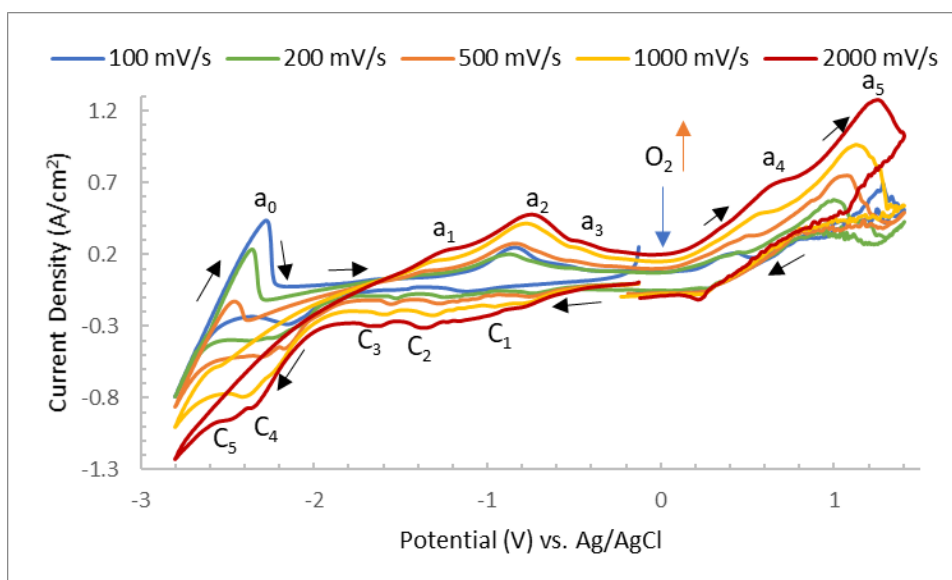


Figure 64: CV of LiCl-KCl eutectic molten salt comparing various scan rates with 5wt% TeCl₄ with 1 wt% Li₂O at 550 °C, WE: Tungsten Rod

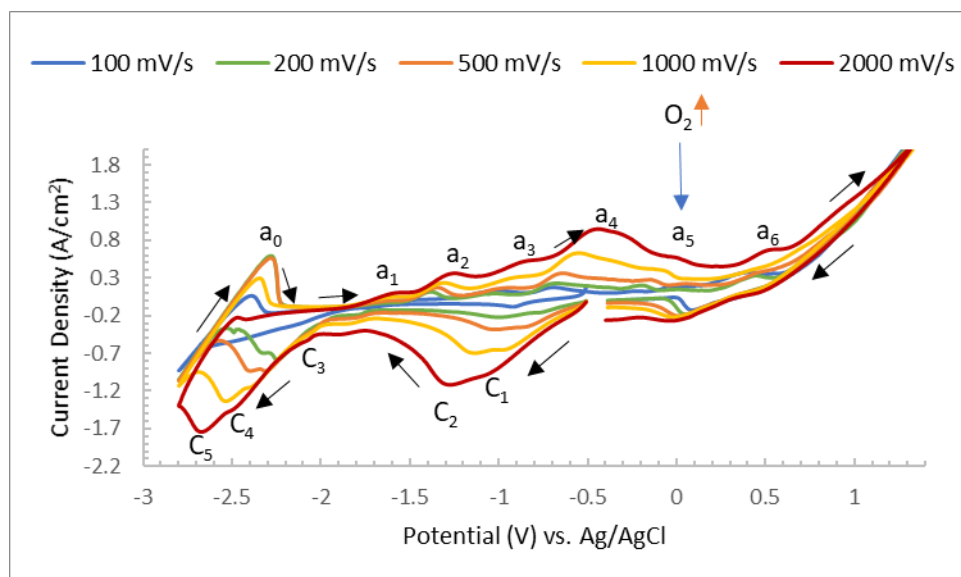


Figure 65: CV of LiCl-KCl eutectic molten salt comparing various scan rates with 5wt% TeCl₄ with 2 wt% Li₂O at 550 °C, WE: Tungsten Rod

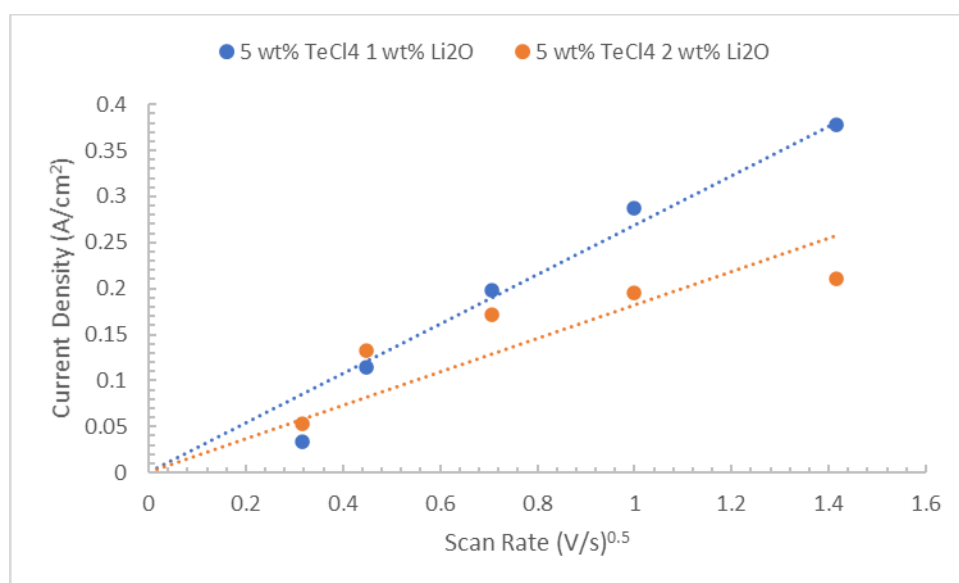


Figure 66: Comparing Square Root of Scan Rate vs. Peak Current Density for 5 wt% TeCl₄ with 1 and 2 wt% Li₂O at 550 °C, Working Electrode: Tungsten

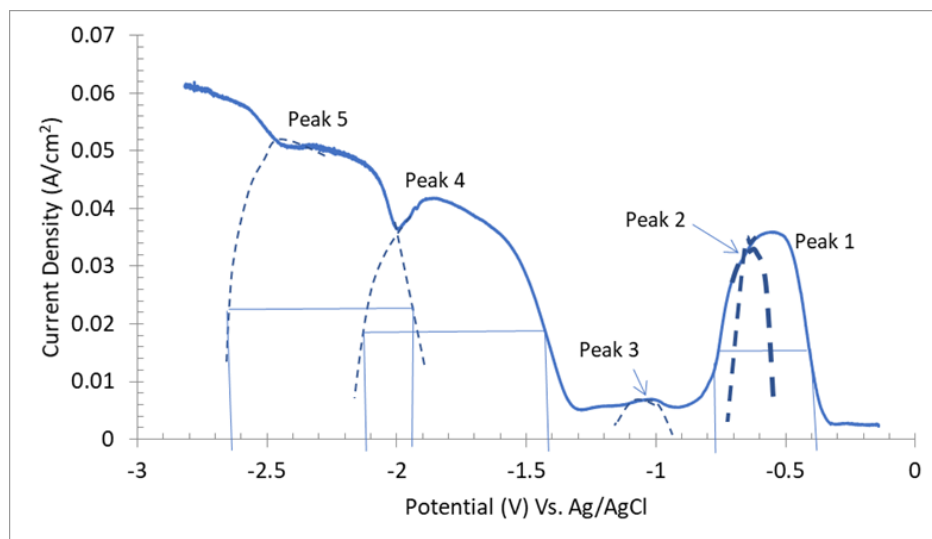


Figure 67: SWV 1 wt% Li_2O with 5 wt% TeCl_4 in LiCl-KCl molten salt at 550 °C, Working Electrode: Tungsten Rod

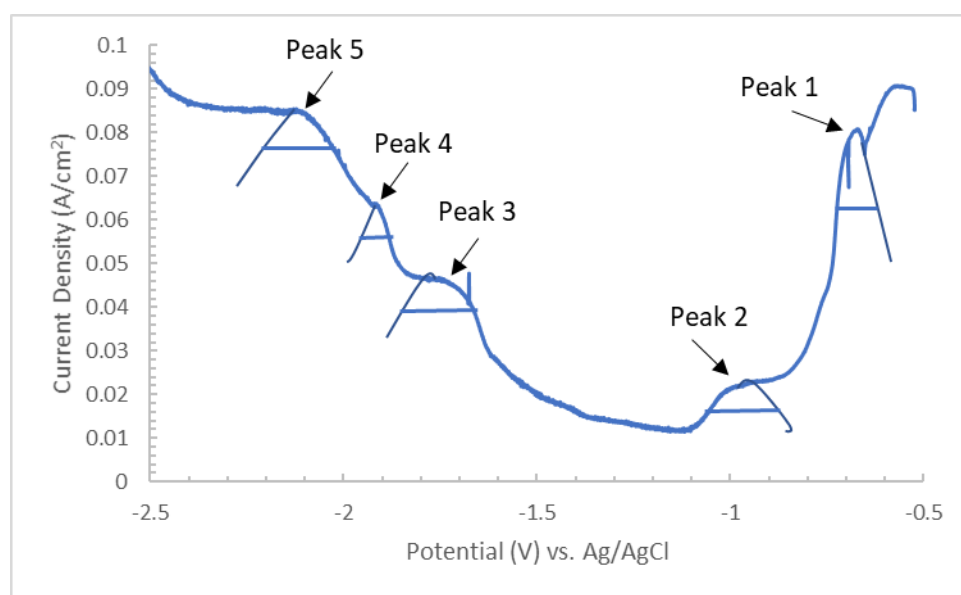


Figure 68: SWV 2 wt% Li_2O with 5 wt% TeCl_4 in LiCl-KCl molten salt at 550 °C, Working Electrode: Tungsten Rod

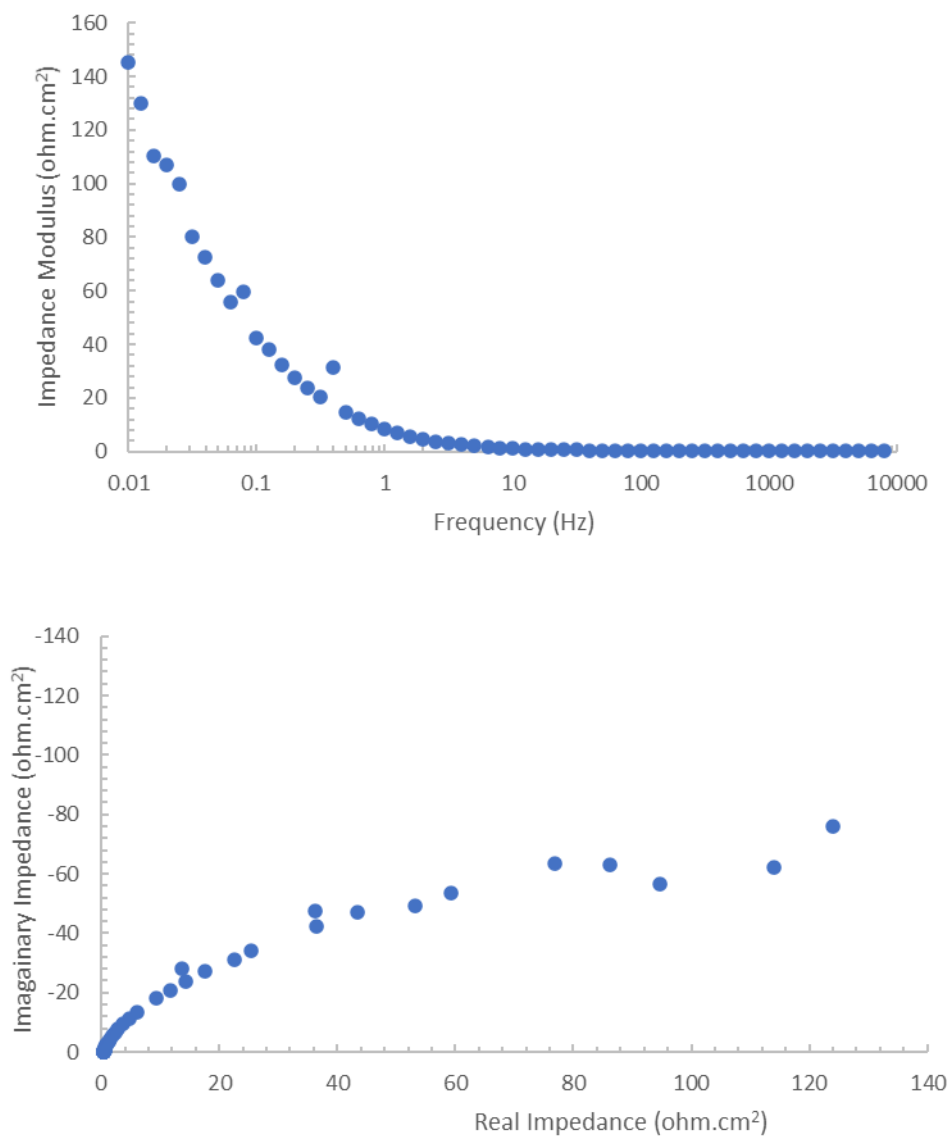


Figure 69: EIS of 5 wt% TeCl_4 with 1 wt% Li_2O at Open Circuit Potential for 550°C : a) Bode Plot, b) Nyquist, WE: Tungsten

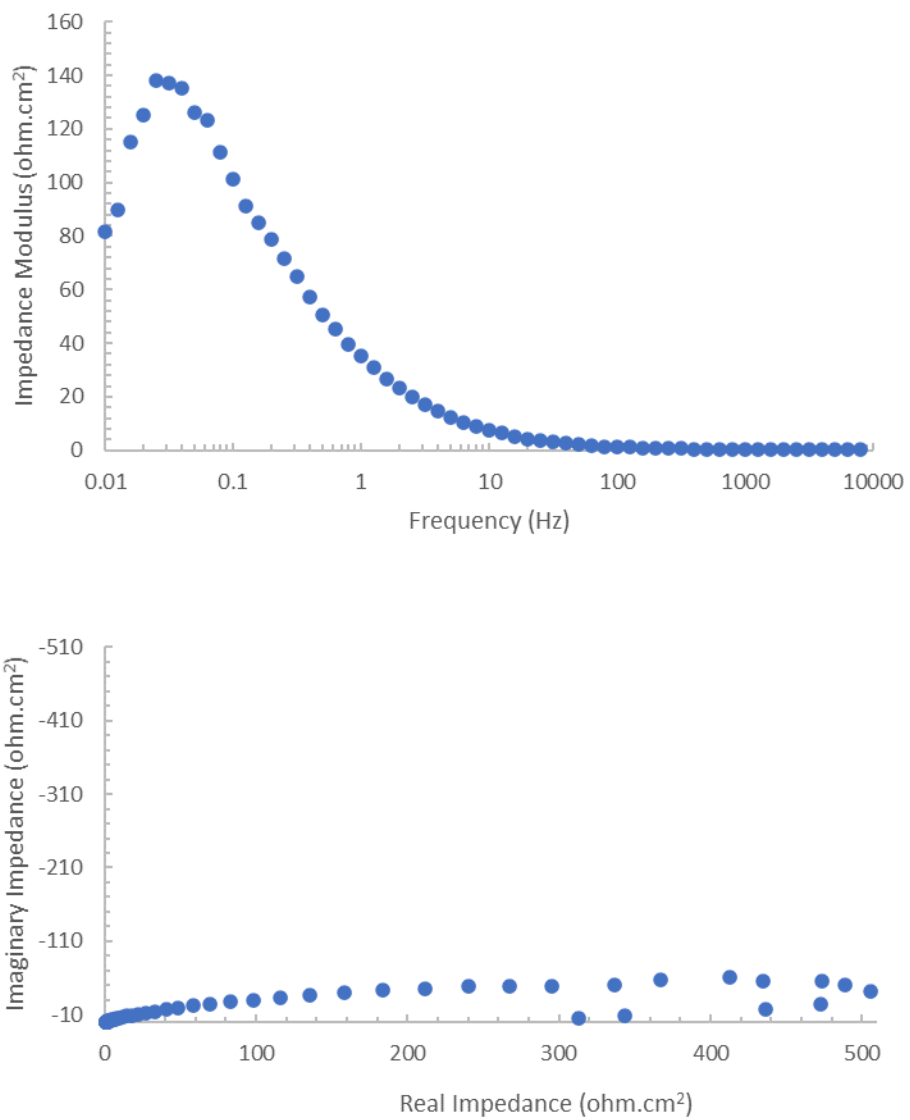


Figure 70: EIS of 5 wt% TeCl_4 - with 2 wt% Li_2O at Open Circuit Potential for 550 °C: a) Bode Plot, b) Nyquist, WE: Tungsten

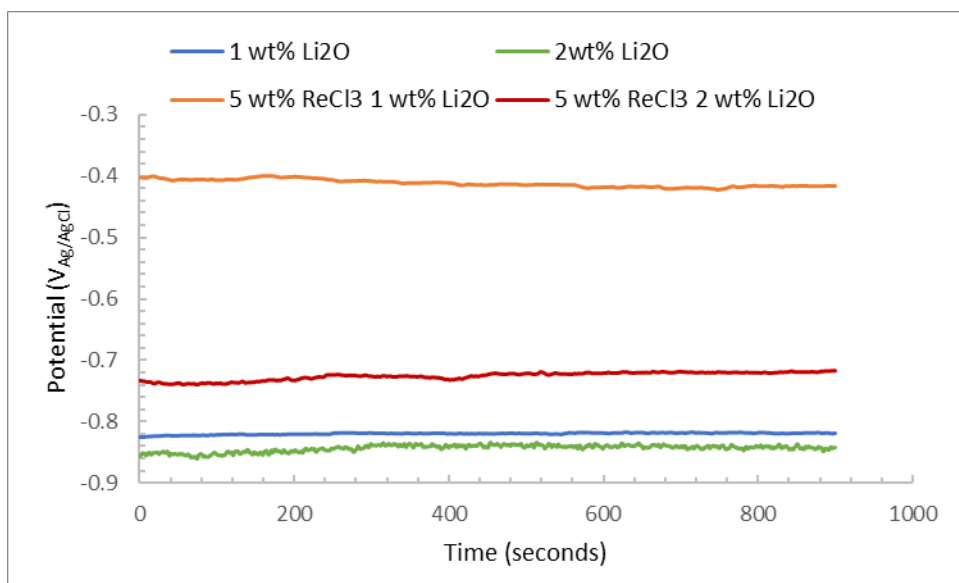


Figure 71: OCP of tungsten electrode in LiCl-KCl eutectic containing different concentration of Li_2O with 5 wt% ReCl_3 at 550 °C

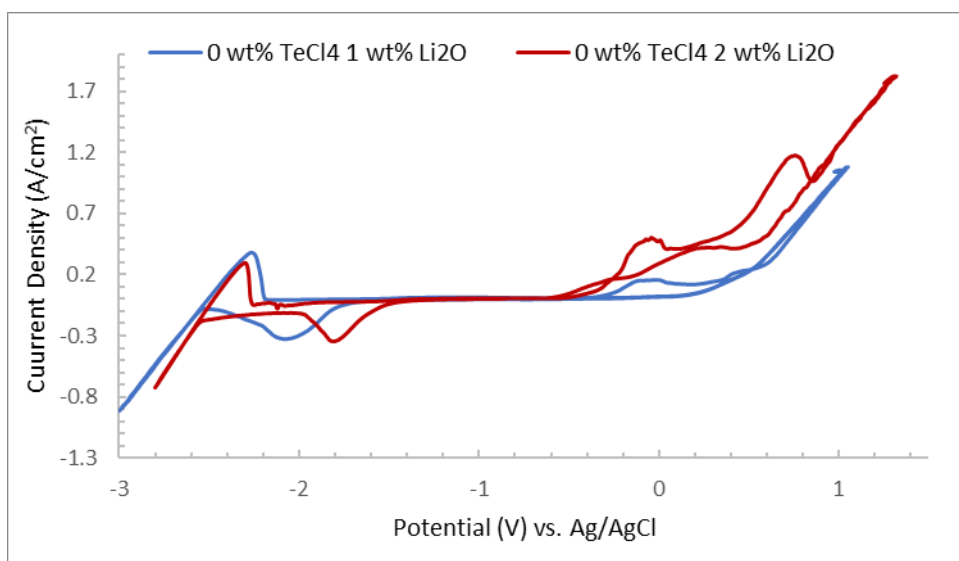
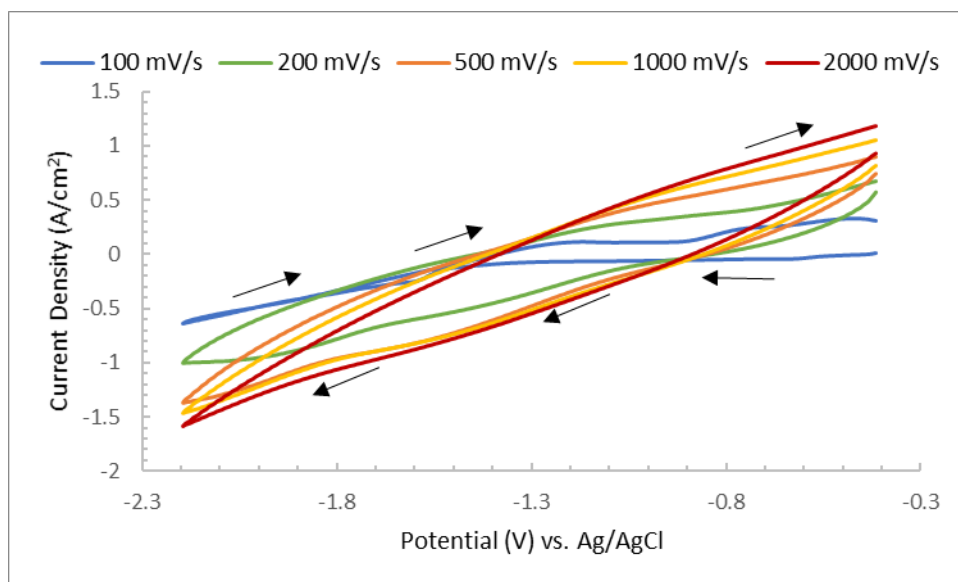
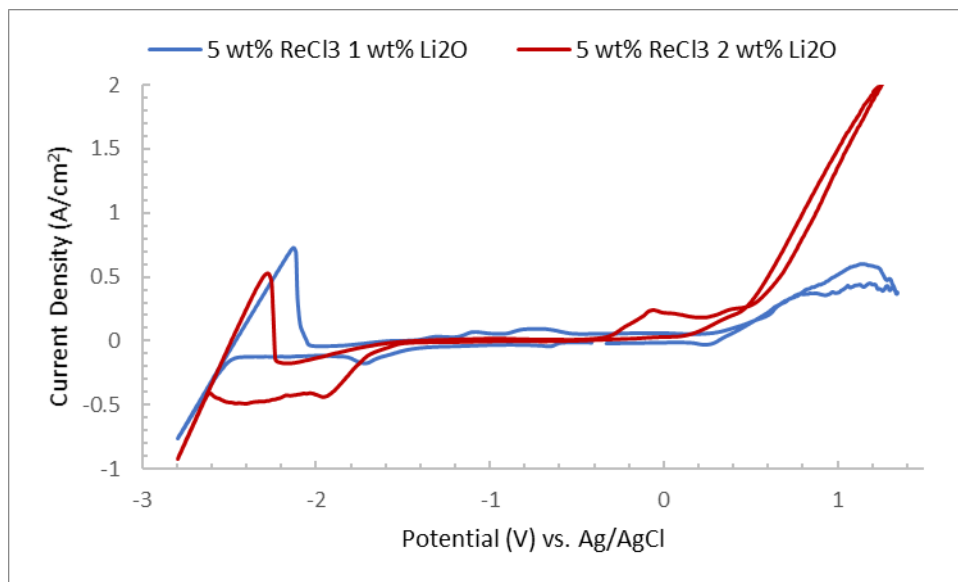


Figure 72: CV of tungsten electrode in LiCl-KCl eutectic comparing without 5wt% ReCl_3



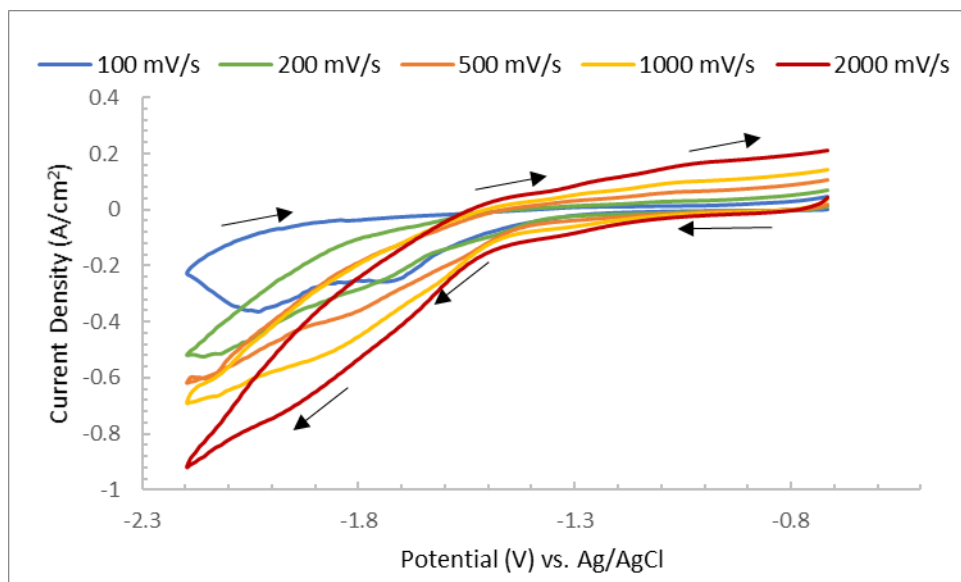


Figure 75: CV of tungsten electrode in LiCl-KCl eutectic comparing varying scan rates of 5wt% ReCl_3 with 2 wt% Li_2O at 550 °C

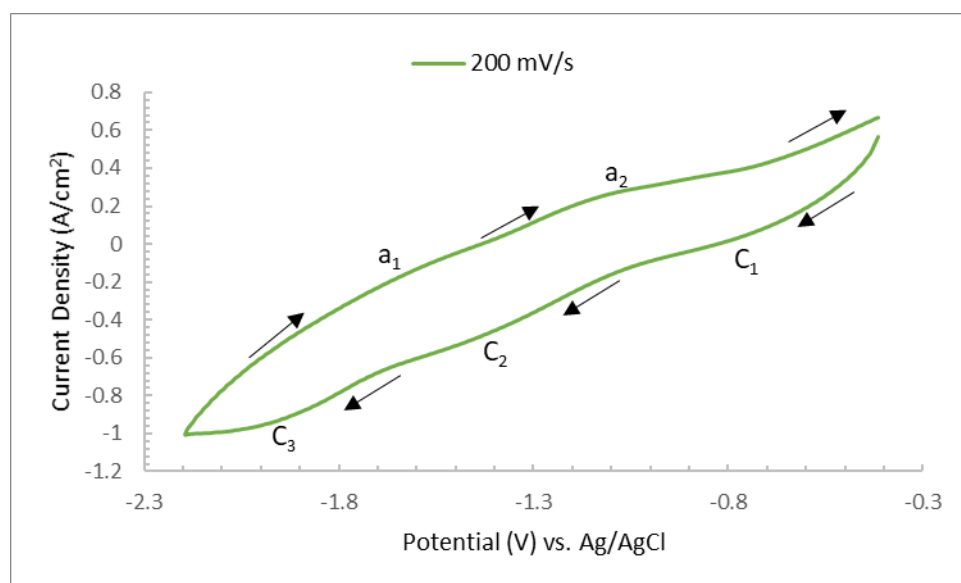


Figure 76: CV of tungsten electrode in LiCl-KCl eutectic of 5wt% ReCl_3 with 1 wt% Li_2O at 550 °C

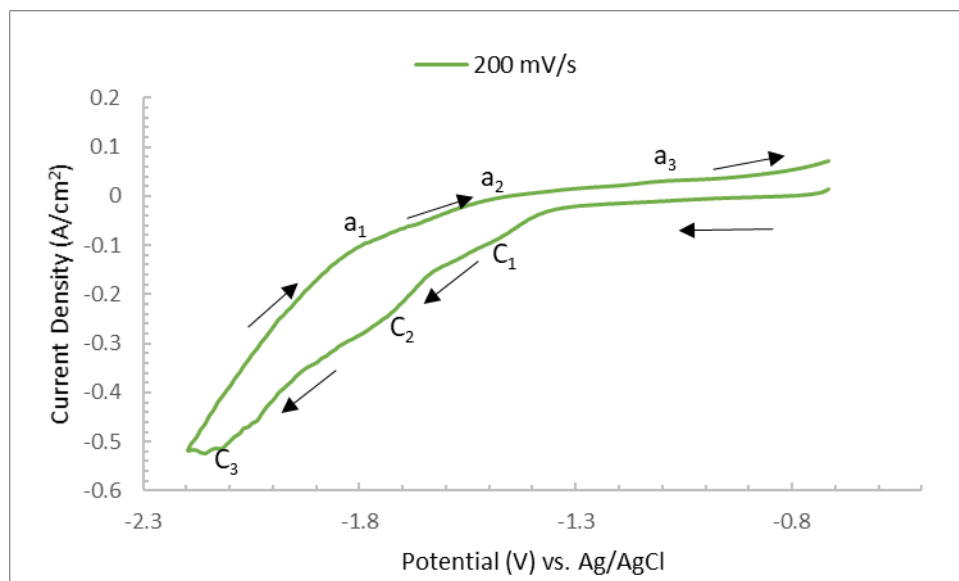


Figure 77: CV of tungsten electrode in LiCl-KCl eutectic of 5wt% ReCl_3 with 2 wt% Li_2O at 550 °C

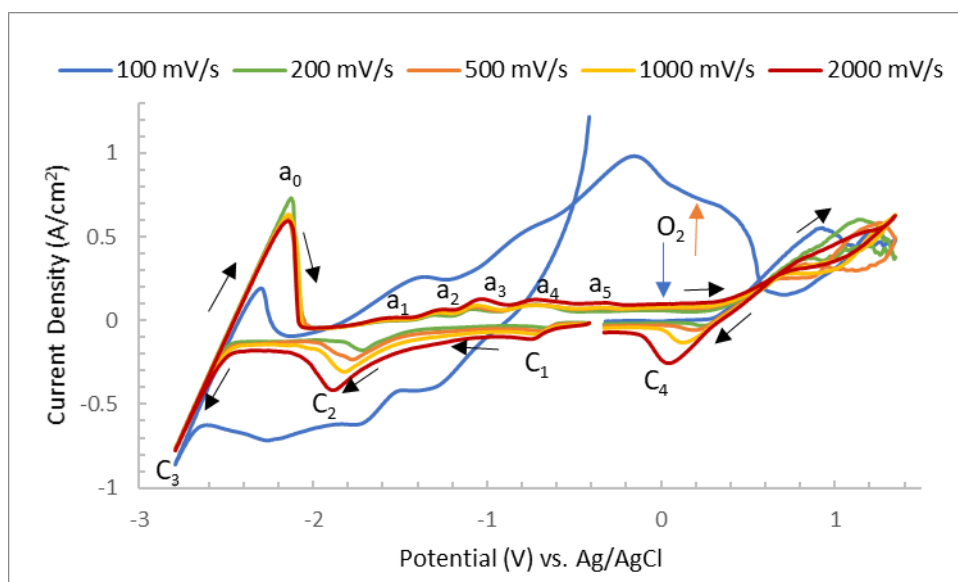


Figure 78: Full window CV of tungsten electrode in LiCl-KCl eutectic of 5wt% ReCl_3 with 1 wt% Li_2O at 550 °C

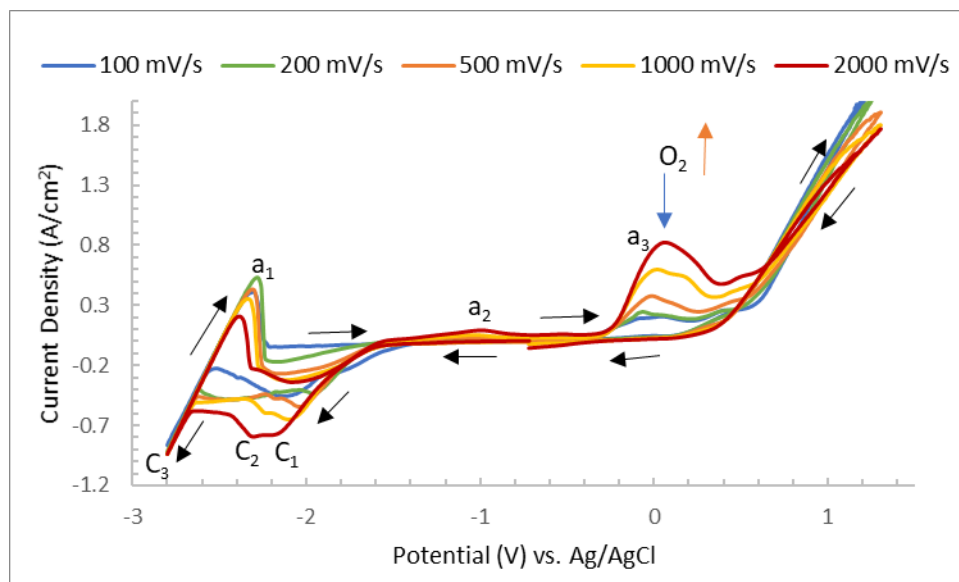


Figure 79: Full window CV of tungsten electrode in LiCl-KCl eutectic of 5wt% ReCl₃ with 2 wt% Li₂O at 550 °C

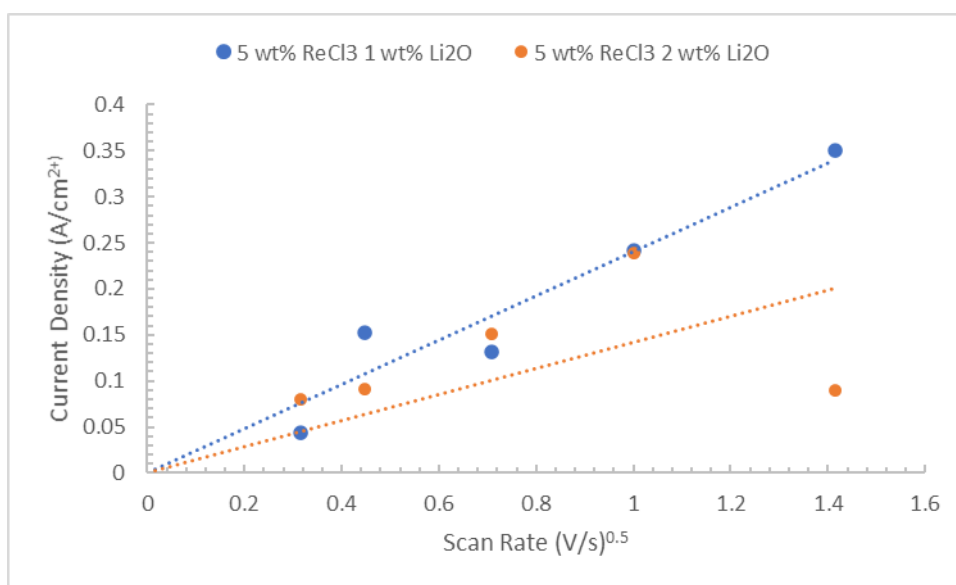


Figure 80: Comparing Square Root of Scan Rate vs. Peak Current Density for 5 wt% ReCl₃ with 1 and 2 wt% Li₂O at 550 °C, Working Electrode: Tungsten

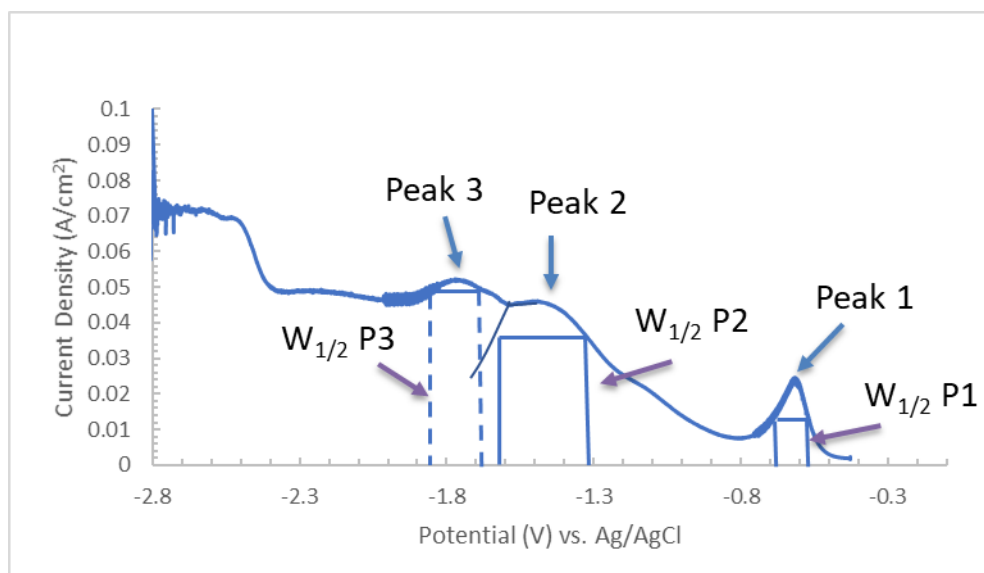


Figure 81: SWV 1 wt% Li₂O with 5 wt% ReCl₃ in LiCl-KCl molten salt at 550 °C, Working Electrode: Tungsten Rod

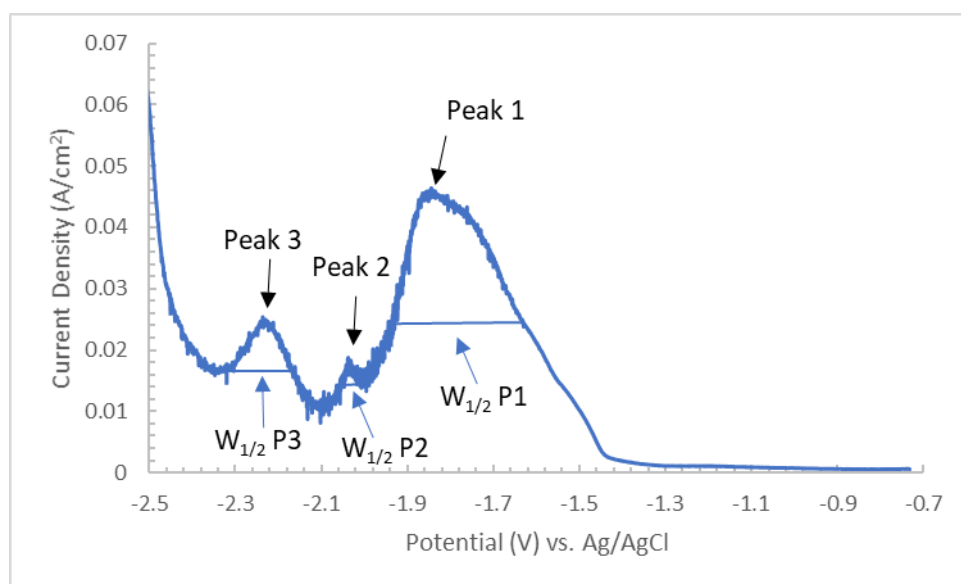


Figure 82: SWV 2 wt% Li₂O with 5 wt% ReCl₃ in LiCl-KCl molten salt at 550 °C, Working Electrode: Tungsten Rod

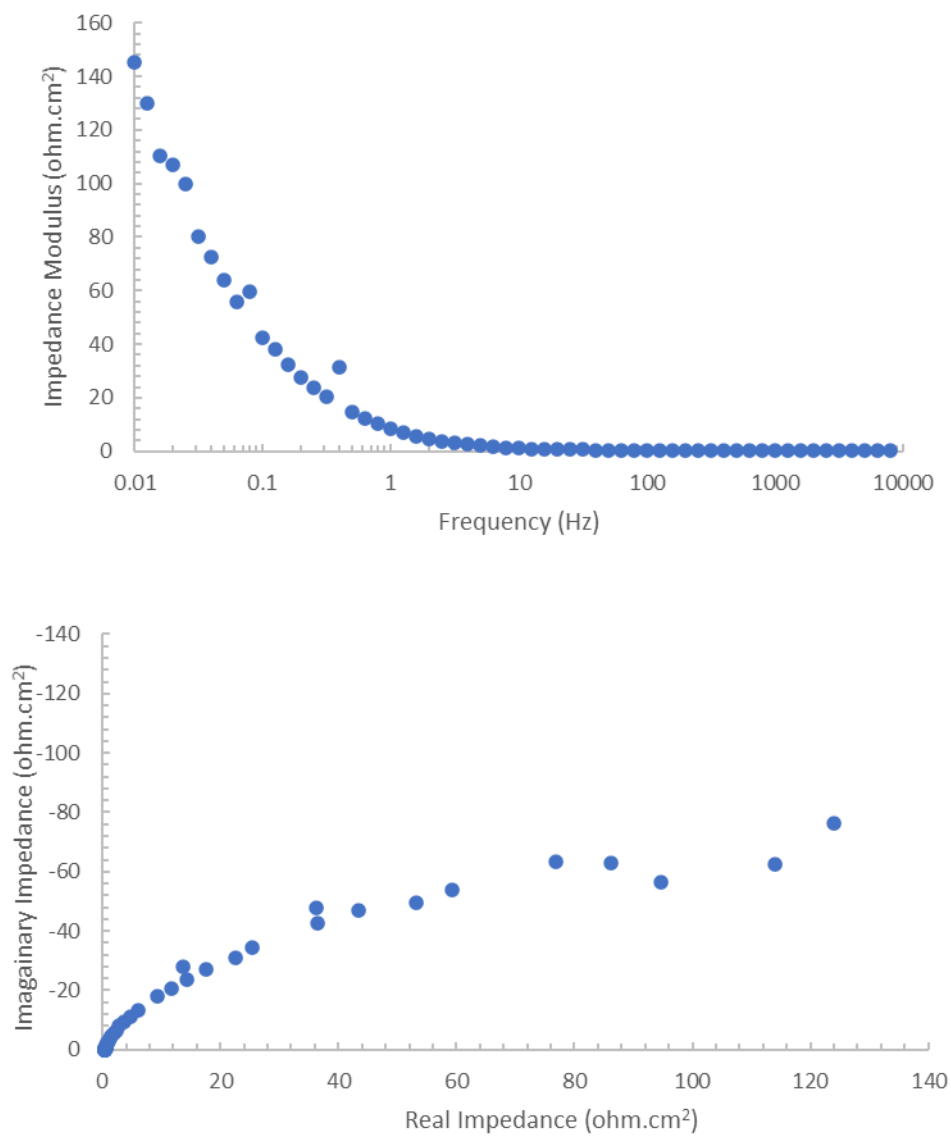


Figure 83: EIS of 5 wt% ReCl_3 with 1 wt% Li_2O at Open Circuit Potential for 550°C : a) Bode Plot, b) Nyquist, WE: Tungsten

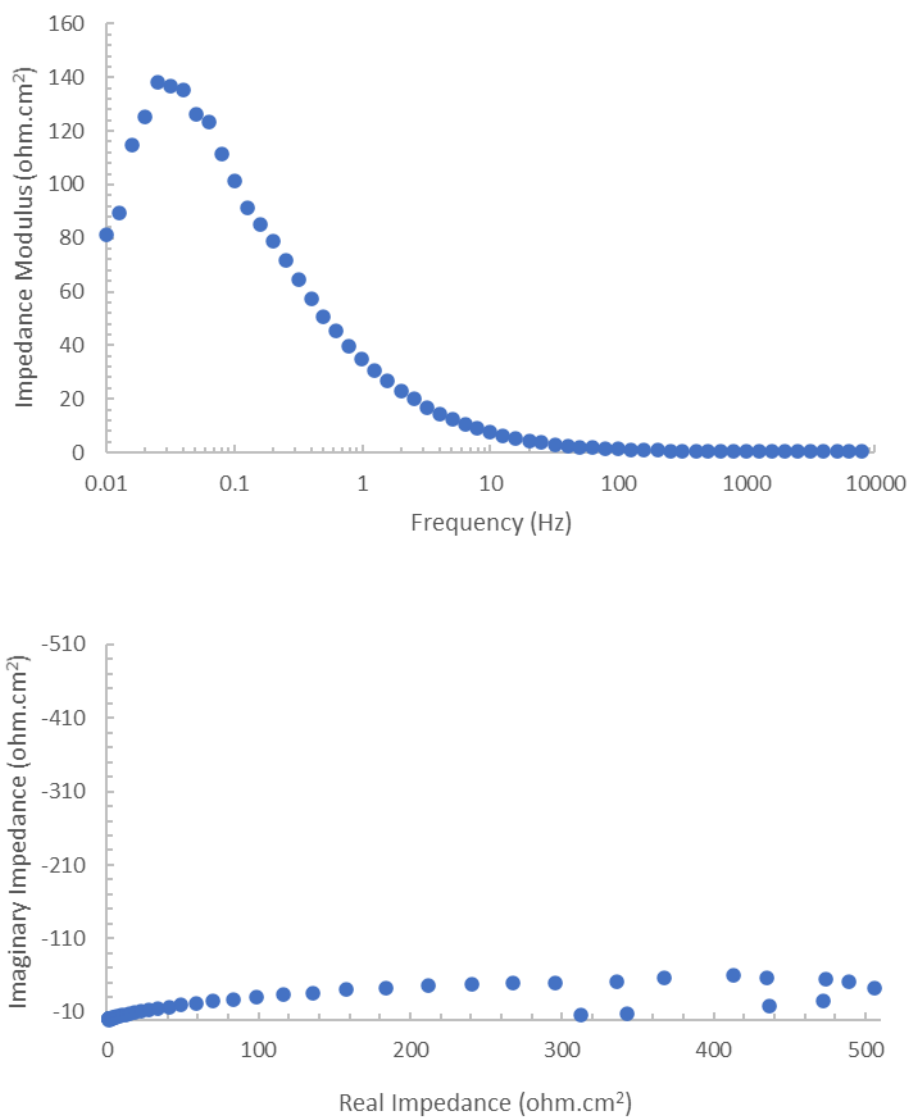


Figure 84: EIS of 5 wt% ReCl_3 with 2 wt% Li_2O at Open Circuit Potential for 550 °C: a) Bode Plot, b) Nyquist, WE: Tungsten